Novel Nanocomposites Integrating Metal-Organic Frameworks (MOFs) for Biomedical Engineering

Bárbara Emanuella Souza

St John's College

University of Oxford

A thesis submitted for the degree of

Doctor of Philosophy

Trinity 2020

Preface

This thesis is submitted for the degree of Doctor of Philosophy in the University of Oxford, United Kingdom. The research presented in this work was carried out by the author between October 2017 and September 2020 in the Department of Engineering Science, under the supervision of Professor Jin-Chong Tan.

To the best of my knowledge, the work described in this dissertation is original, except where due reference has been made, acknowledging the work of others. Nothing has been included that is the outcome of work done in collaboration with others, except where explicitly noted. No part of this dissertation, or any similar to it, has been, or is currently being submitted for any degree at this, or any other university. This thesis is less than 250 pages in length.

The work presented herein has been partially published in the following journal papers:

1. **B.E. Souza**, S. Rudić, K. Titov, A.S. Babal, J.D. Taylor and J.C. Tan, "Guest-Host Interactions of Nanoconfined Anti-Cancer Drug in Metal-Organic Framework Exposed by Terahertz Dynamics", *ChemComm*, 55, 3868–3871 (2019)

2. **B.E. Souza**, L. Donà, K. Titov, P. Bruzzese, Z.X. Zeng, Y. Zhang, A.S. Babal, A. Möslein, M.D. Frogley, M. Wolna, G. Cinque, B. Civalleri, and J.C. Tan, "Elucidating the Drug Release from Metal-Organic Framework Nanocomposites *via in situ* Synchrotron Microspectroscopy and Theoretical Modelling", *ACS Applied Materials & Interfaces*, 12, 5147-5156 (2020)

3. **B.E. Souza**, A.F. Möslein, K. Titov, J.D. Taylor, S. Rudic, and J.C. Tan, "Green Reconstruction of MIL-100 (Fe) in Water for High Crystallinity and Enhanced Guest Encapsulation", *ACS Sustainable Chemistry & Engineering*, 8, 8247-8255 (2020)

4. **B.E. Souza** and J.C. Tan, "Mechanochemical approaches towards the *in situ* confinement of 5-FU anti-cancer drug within MIL-100 (Fe) metal-organic framework", *CrystEngComm*, 22, 4526 - 4530 (2020).

Barbara Emanuella Souza
Oxford
September, 2020

This thesis is dedicated to my partner Natasha,
to my parents and sisters, Marta and Ademir, Brenda and Iasmim,
and to my family in Brazil.

. . .

Their endless love and support are what made me the person that I am today.
I would not be standing at the end of this long journey if it were not for them.

Acknowledgements

Personal

The last three years have passed like a blink of an eye. During this time I have grown as a scientist and as a person, not only due to the academically stimulating environment I have been privileged to be in, but also thanks to the experiences and people I have met along my way.

Firstly, I would like to thank my supervisor, Professor Jin-Chong Tan, for the continuous patient guidance, encouragement, and advice he has provided throughout my doctorate studies. I am especially grateful to Professor Tan for giving me the chance to study at the University of Oxford, for encouraging me to be the best that I can, and for his constant motivation with my research. Thank you JC, for introducing me to the amazing nano-sized world of MOFs and, through that, helping shape the scientist that I am today.

During my time in Oxford, I have been fortunate to be sheltered by families of friends that made my days outside the lab full of joy and happiness. To my Castle Mill family, I would like to thank Cornelia, Kaspar, and T. for their continuous friendship that warmed my days. To Razia and Diala, my St. John's College (Dolphin Quad) family, I thank you for the countless adventures around college that felt like a hug at the end of a long day. To my friends from the department, Ciara, Ice, Caroline, and Annika, thank you for being part of my everyday life. To my Brazilian friends, Eduardo, Vinicius, and Natalia, thank you for been the connection I needed to things that only us Brazilians can understand. To all of you, thank you for the laughs, advice, and friendship.

I am also thankful to my College Advisor, Alice Cicirello, for her enthusiasm, guidance, and inspirational spirit. I also have enormous gratitude for all the scientists in ISIS Neutron and Muon Source and Diamond Light Source, with whom I have learned so much about the dedication needed to achieve great science. In special, Dr Svemir Rudić, Dr Gianfelice Cinque, and Dr Mark Frogley, whose hard work and motivation continue to inspire me.

I am also grateful to all my colleagues in the Multifunctional Materials and Laboratory lab not only for the instigating scientific conversations, but also for the numerous happy moments we have shared in the lab. Special thanks go to Dr Mario Gutierrez, Arun Babal, Dr Zhixin Zeng, and Kirill Titov. I thank Yang Zhang, Dr Abhijeet Chaudhari, and Dr Yueting Sun for their companionship.

Institutional

I would like to thank Fapemig (Fundação do Amparo a Pesquisa de Minas Gerais) for the doctorate scholarship that allowed me to pursue my studies at the University of Oxford.

I would also grateful to ISIS Neutron and Muon Source and Diamond Light Source for providing excellent facilities in which beamtime experiments were conducted to the completion of this thesis.

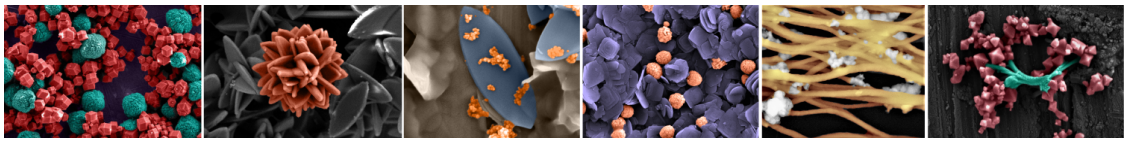

To be Young, Gifted, and Black . . .
— Nina Simone

Abstract

Metal-organic frameworks (MOFs) are fascinating hybrid materials, considered as promising nanocarriers for drug delivery. Their tailorability sets MOFs apart from their porous inorganic (zeolites and silica) and organic (carbon nanotubes) counterparts. To enable the use of MOFs for biomedical applications, new developments of sustainable MOF fabrication and characterization methodologies are sought. In this work, a detailed study the fundamental potential of MOFs as a 'host' to encapsulate various 'guest' drug molecules was carried out. Mechanochemistry and water-based approaches were systematically applied for the preparation of two model systems - the copper-based HKUST-1 and the iron (III) carboxylate MIL-100 (Fe), and their feasibility for the fabrication of drug@MOF assemblies was demonstrated.

First, by leveraging two different mechanochemical approaches (*i.e.* manual grinding *versus* automated vortex grinding), the effects of different mechanochemical environments on the drug confinement were investigated. The outcomes were reflected in the release kinetics of 5-FU from the MIL-100 host, in which different guest–host interactions yielded from each technique led to variations in the release rate. Secondly, the mechanochemical preparation of drug-loaded MIL-100 (Fe) systems, comprising 5-FU, caffeine, or aspirin as guest molecules revealed the undocumented 'modulator' effect presented by 5-FU and caffeine. These molecules can be used to replace highly toxic mineralizers (*e.g.* hydrofluoric acid) in the preparation of crystalline MIL-100 (Fe). Thirdly, a novel water reconstruction process was developed to acquire highly crystalline MIL-100 (Fe). This approach was harnessed for the facile fabrication of the drug@MIL-100 systems, accomplishing up to ∼65 wt.% of drug cargo. Both strategies, mechanochemical and water-based synthesis, elucidated much-needed pathways towards an environmentally friendly and energy efficient preparation of MOF and guest@MOF systems, with improved cargo encapsulation capabilities.

New possibilities presented by high-resolution inelastic neutron scattering were brought to light for the characterization of drug-MOF interactions and structural changes arising from nanoscale confinement. Finally, this work presented the innovative application of synchrotron microspectroscopy to track the release of 5-FU molecules from a (5-FU@HKUST-1/PU) composite. Using experimental time-resolved infrared spectra, jointly with newly developed density functional theory calculations, the detailed dynamics of vibrational motions underpinning the dissociation of 5-FU bound to the framework of HKUST-1 upon water exposure were revealed.

Overall, this work contextualizes future developments of MOFs as efficient drug delivery systems and expands the portfolio of synthetic and characterisation techniques applicable to the large realm of guest@MOF systems.

Contents

List of Figures

List of Tables

List of Abbreviations

1D	One-dimensional
2D	Two-dimensional
3D	Three-dimensional
MOF	Metal-organic framework
DDS	Drug delivery systems
IRMOF	Isoreticular metal-organic framework
ZIF	Zeolitic imidazolate framework
HKUST	Hong Kong University of Science and Technology
MIL	Materials of Institute Lavoisier
UiO	University of Oslo
5-FU	5-Fluorouracil
CAF	Caffeine
ASP	Aspirin
Cu	Copper
Fe	Iron
Zn	Zinc
Ag	Silver
Cr	Chromium
Cl	Chloride
Ni	Nickel
Co	Cobalt
C	Carbon
N	Nitrogen
F	Flourine
O	Oxygen
H	Hydrogen
ZnO	Zinc oxide
$CuNO_3$	Copper (II) nitrate

$FeNO_3$	Iron (III) nitrate
H_3BTC	Benzene-1,3,5-tricarboxylic acid
BTC	Benzene-1,3,5-tricarboxylate
H_2O	Water
D_2O	Deuterated water
Fe-ASP	Iron-aspirin complex (tetraaquosalicylatroiron (III) complex)
PU	Polyurethane
Drug@MOF	Drug-loaded MOF system
MOF/Polymer	MOF composites supported by a polymeric matrix
MG	Manual grinding process
VG	Vortex grinding process
IN	*In situ* encapsulation
EX	*Ex situ* encapsulation
REC	Water reconstructed method
MeOH	Methanol
EtOH	Ethanol
THF	Tetrahydrofuran
HF	Hydrofluoric acid
HNO_3	Nitric acid
DI water	Deionized water
PXRD	Powder X-ray diffraction
SEM	Scanning electron microscope
AFM	Atomic force microscope
TGA	Themo-gravimetric analysis
BET	Brunauer–Emmett–Teller
UV-Vis	Ultraviolet visible
ATR-FTIR	Attenuated total reflectance Fourier transform infrared spectroscopy
SR-microFTIR	Synchrotron radiation Fourier transform infrared microspectroscopy
INS	Inelastic neutron scattering

QENS	Quasi-elastic neutron scattering
IR	Infrared
DFT	Density functional theory
B3LYP	Becke, 3 parameter, Lee Yang Parr
SCF	Self-consistent field
TSE	Twin-screw extrusion
LAG	Liquid assisted grinding
ILAG	Ion and liquid assisted grinding.
ZnSe	Zinc selenide
^{3}He	Helium-3
CUS	Coordinatively unsaturated metal sites
SBU	Secondary building units
FWHM	Full width at half maximum
ESP	Electrostatic potential map
PBS	Phosphate buffered saline
ET	Energy transfer
Q	Scattering vector
THz	Terahertz
CCR	Closed cycle refrigerator

List of Symbols

λ	Wavelength
θ	Bragg angle
Δ	FWHM
δ	In-plane bending mode
γ	Out-of-plane bending mode
ν	Symmetric stretching mode
ω	Wagging mode
τ	Twisting mode
A	Absorbance
c	Concentration
D	Crystalline domain size
°C	Degrees Celsius
K	Kelvin
m	Meters
cm	Centimeters
mm	Milimeters
µm	Micrometers
µL	Microliters
nm	Nanometers
Å	Angstroms
g	Grams
mg	Miligrams
min	Minutes

We must have perseverance and above all confidence in ourselves. We must believe that we are gifted for something and that this thing must be attained

— Marie Curie

1 Introduction

Nanoparticle delivery systems are modern technologies engineered for the target and controlled release of therapeutic agents. These delivery platforms are envisioned to minimize side-effects of conventional treatments and reduce dosage frequency with maximization of drug efficacy. Recently, metal-organic frameworks, or MOFs, have gained attention as novel materials for drug delivery and theranostic applications. This class of hybrid materials has evolved from been purely the object of chemists' curiosity, intrigued by their unmatched chemical composition and structural characteristics, to landing on the hands of engineers and material scientists who have envisioned and developed real-world applications for this multifunctional framework materials. There is a rising interest in the employment of MOFs as porous 'hosts' to afford the adsorption and subsequent release for the delivery of drugs confined as 'guest' molecules. Great efforts have been made in recent decades to propel the use of MOFs in the biomedical field. Despite the recent developments, there are still several challenges hindering the full realization of MOFs for bioapplications. This thesis aims to contribute to the ongoing efforts on engineering smart drug delivery platforms for the controlled and extended-release of different therapeutic molecules. Specifically, the results comprised in the following chapters seek to aid the discussion of MOFs as drug delivery systems (DDS), focusing on the development of green encapsulation approaches, the unravelling of guest host molecular interactions, and the understanding of the dynamics of guest release from

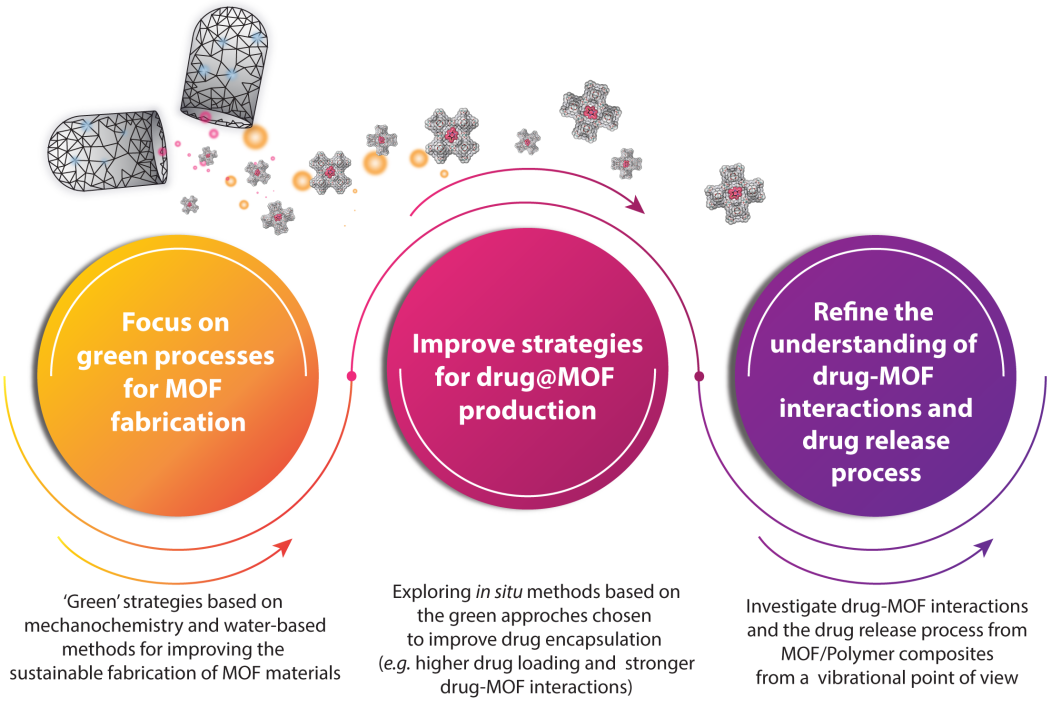

Figure 1.1: Challenges in the field and research goals explored in this thesis

multifunctional MOF/Polymer composites[1], as summarized in Figure 1.1.

This thesis is composed of 9 chapters, interconnected as summarised in Figure 1.2. A brief introduction sets off with an exploration of the primary goals and accomplishments presented by each chapter. With the review of literature in Chapter 2 setting a detailed overview of the past advances in the use of MOFs as DDS, Chapter 3 details the synthetic methods, characterization techniques, and theoretical models employed for the elucidation of structural properties of the samples. Each of the results chapter then expands on a thorough analysis and scientific discussion and contextualizes the significance of the results herein achieved.

Overall, this thesis can be perceived as a combination of three layers. The outer one concerns the development of environmentally friendly MOF fabrication and drug encapsulation approaches. Due to the intrinsic complexity of these supramolecular networks, MOF synthesis conventionally entails long reactions under

[1] Throughout this thesis, a MOF/Polymer composite is considered to be a material which contains a MOF supported by a nanoscaled polymeric matrix. Conversely, herein a guest@MOF system is not considered a MOF-composite, but an assembly formed between the 'hosts' MOF and different 'guest' molecules that occupy the MOF pores.

harsh conditions (*i.e.* high pressure/temperature in boiling organic solvents). This can impair the material biocompatibility and result in a large environmental impact from certain synthesis procedures. Thus, simple and green large-scale methods are desired. Chapters 4-7 demonstrate the application of 'green' synthetic routes (*e.g.* mechanochemistry methods and water-based synthesis) for the fabrication of MOF and guest@MOF systems. *Via* these sustainable methods, it was possible to achieve the following:

I. Reduce the amount of toxic organic solvents (*e.g.* methanol and ethanol) used in the fabrication of MIL-100 (Fe) and HKUST-1, model MOF systems employed in this work. This is important from both environmental and biological perspectives

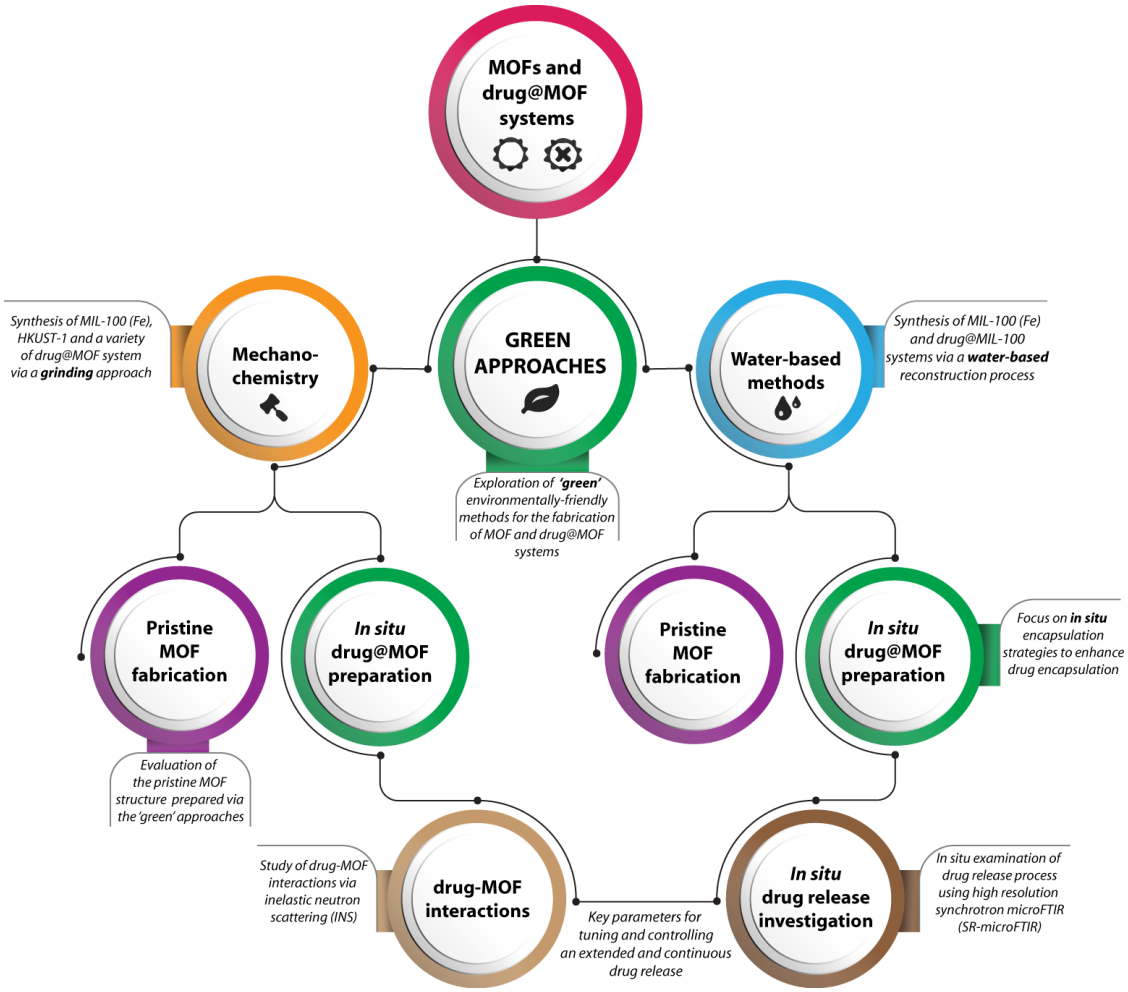

Figure 1.2: Flowchart summarising the scope and interconnection of the chapters presented in this thesis.

since in conventional synthesis, solvent molecules can remain trapped inside the porosity of the MOFs, and therefore increase its inherited toxicity.

II. Simplify the synthesis by reducing the preparation time and eliminating the use of harmful mineralizing agents and modulator, applied to improve material crystallinity. This contributes to a reduction of synthesis cost and material toxicity.

III. Favour the encapsulation of drug molecules by eliminating the competition they face with organic solvent for the active binding sites in the host MOF. This can, therefore, help to accomplish the full hosting potential of different MOFs (*i.e.* achieve higher drug loadings) and lead to stronger guest-host interactions.

The second layer of this thesis seeks to unravel the guest-host intermolecular interaction at the atomic level. In the preparation of guest@host systems, two scenarios are possible. After the encapsulation step is performed, the guest molecules can either be effectively confined into the pores of the host structure or adsorbed onto the pores external surface. Each of these possibilities will ultimately yield different guest-host interactions that can be studied to pinpoint the location of the guest molecules within the MOF structure. Understanding these interactions and the positioning of the guest within the guest@host assembly is central not only for establishing pathways to control the binding of drug molecules to different MOFs carriers but also to achieve a stable and sustained drug release. However, it remains a big unexplored challenge in the field of guest@MOF systems. Chapters 5-7 tackle this problem by demonstrating how high resolution inelastic neutron scattering (INS) spectroscopy offers new insights on drug-MOF interactions, and more generally, on the guest@MOF confinement effects from a vibrational point of view.

In the last layer, the nuances of the drug release process are explored. For that, Chapter 8 delves into the fabrication of composites comprising drug@MOF systems embedded in a biocompatible polymeric matrix. The presence of the MOF particles gives the composites the capability to deliver drugs and growth agents to accelerate tissue regeneration, which makes them relevant materials for wound dressings devices. The dynamics of the drug molecules release from drug@MOF/Polymer was

investigated. Understanding the release of drug molecules from 'host' frameworks is, generally, carried out using *ex situ* techniques (*e.g.* sample and separate, continuous flow, dialysis membranes) that are more appropriate for establishing the drug release kinetics. However, to gain a deeper understanding of the drug release process itself, it is necessary to observe both the chemical and physical changes in the drug-loaded samples *in situ*, thereby revealing physicochemical phenomena not yet documented. The scarcity of studies on the dynamics of the drug release process is a result of the difficulty in continuously monitoring such changes, which can occur in an accelerated manner not easily probed by conventional techniques. Observing the transformations of the host MOFs during the release of confined drug molecules is, however, central to devising better ways for the controlled release of therapeutic agents. In Chapter 8, the efficacy of synchrotron microspectroscopy to track the *in situ* release of anticancer drug molecules from drug@MOF/Polymer composites is demonstrated. The experimental results are further substantiated by *ab initio* density functional theory (DFT) calculations for additional insights into drug-MOF interactions and their energetics.

The last and concluding chapter provides an overview of the results and discoveries made and presents perspectives of future areas for exploration in the field. Together, the results compiled in this thesis offer a platform for further developments in the fields of material science and engineering and take important steps towards practical biomedical applications of MOF materials.

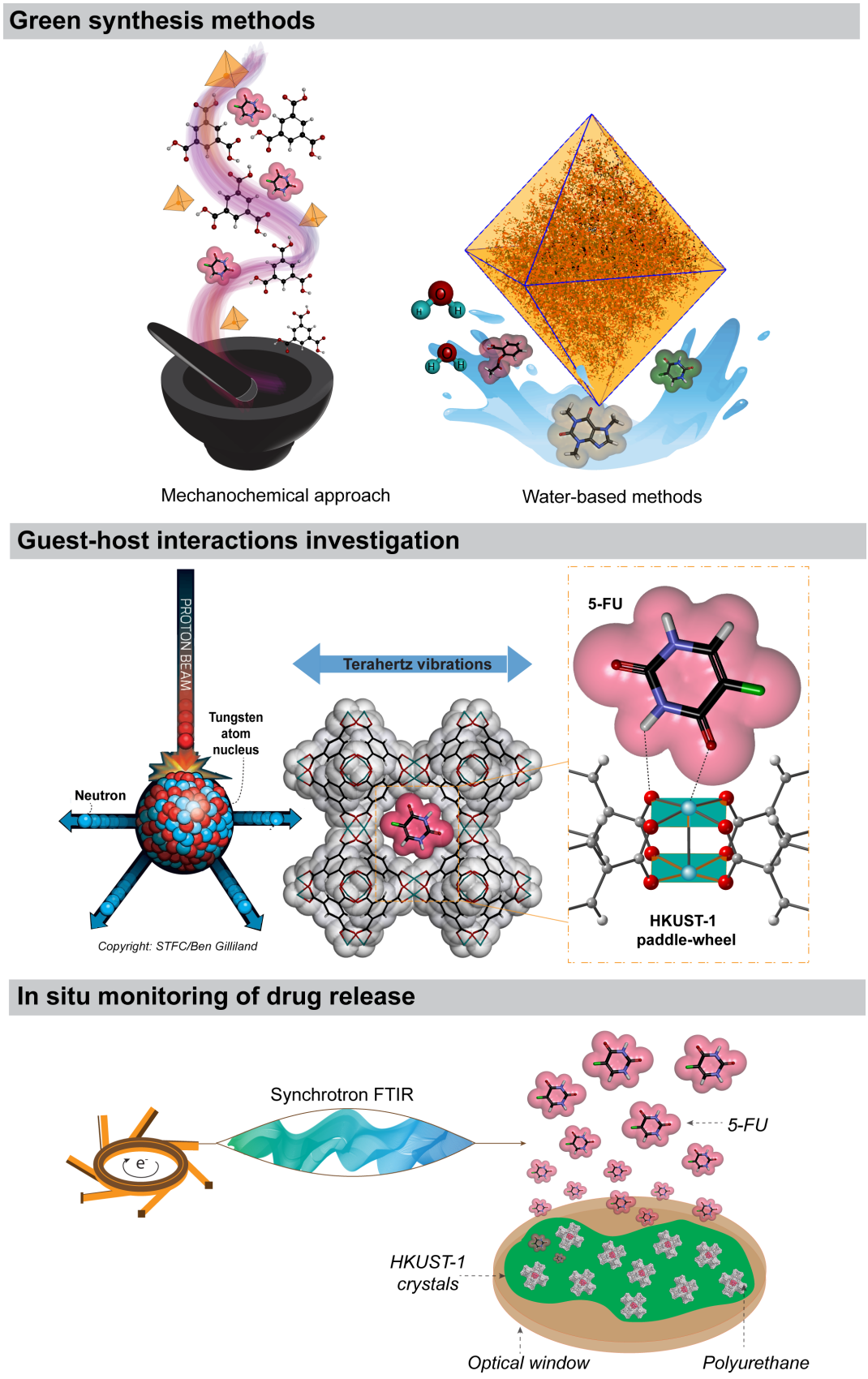

Figure 1.3: Graphical summary of the thesis contents, presenting the novel contributions of this work to the field of MOF materials and guest@host assemblies.

All intelligent thoughts have already been thought;
what is necessary is only to try to think them again.

— Johann Wolfgang von Goethe

2

Review of Literature

Contents

2.1 The prospective biomedical applications of MOFs

MOFs are an emergent class of nanoporous materials placed among the most fascinating and compelling topics of research in nanotechnology. They are porous crystalline solids with a hybrid framework architecture, comprising inorganic metal ions or metal-cluster coordinatively connected by organic 'linkers' to form secondary building units (SBU). These come together to give rise to 1D, 2D, and 3D structural networks that possess characteristics at the intersection of various categories of well-known materials [1–4].

The most obvious use of porous structures in biomedicine consists of taking advantage of their large pore volume to encapsulate appreciable amounts of active molecules, providing them protection from instabilities, and perform their delivery in a controlled manner [5]. Therefore, MOFs have been largely investigated as novel platforms to be used in drug delivery [6, 7], biosensing [8, 9], cosmetics [10], and bio-molecules encapsulation [11]. On account of their flexible structural design and tunable internal pore volume, MOFs enable higher cargo loadings in comparison to traditional carrier systems for a variety of guest molecules (*e.g.* drug and active agents) [10], presenting a loading capacity of as high as 2 g of drug per g of empty MOF (*i.e.* over 66 wt.%) [12, 13]. Progress has been made to overcome existent barriers to the wider application of MOFs in biomedicine. A few examples include the mitigation of the rapid and uncontrolled release of the encapsulated drug molecules commonly encountered in drug delivery (*i.e.* burst-release) [14, 15], the advancement of synthesis to modulate optimal particle size for drug delivery [16], the reduction of toxicity [17, 18], and strategies to develop triggered release mechanisms [19–21]. The rapid development of the field is illustrated by an exponential growth in the number of scientific papers and reviews available in the literature in the past decades.

Despite the significant advances made towards utilizing MOFs as DDS in recent years, their use as biologically- and medically-oriented devices is still at its infancy. Currently, there are no MOF-based formulations that approved by drug agencies. There are still more than a few challenges to be tackled before

moving closer to a practical application in biomedicine. The need for improved biocompatibility of MOF materials and further *in vivo* tests, optimization of synthesis procedures to facilitate scalability and reduce environmental impact, expansion of cargo encapsulation strategies with an enhanced understanding of the guest-host (*i.e.* drug-MOF) interactions and the guest release mechanism are a few examples of persisting barriers.

The research focused on harvesting MOFs properties to engineer new drug delivery vehicles is driven by the need for improvement of currently available treatments [22, 23]. Cancer, in particular, is a burden that continues to grow globally, being the second leading cause of death after cardiovascular disease. In 2018 it accounted for 18.1 million new patients, including 9.6 million deaths [24]. Despite continuous advances in early detection, diagnosis and cancer therapy, existing treatments include surgical procedures and aggressive radio and chemotherapy. Besides the associated unwanted side effects, challenges of the currently available treatment options include insufficient drug delivery to the tumour site, low cell membrane permeability, drug degradation, and off target accumulation [25]. The development of MOF carriers has the potential to improve methods of protection of the organism from these toxic side effects and increase drug efficiency [5].

One strategy to further enhance MOFs features is their combination with supportive matrices (*e.g.* metal nanoparticles, polymers, and carbon nanotubes) to engineer MOF-composites that will maintain the multifunctional properties of MOFs while mitigating the shortcomings of both components [26–30]. Consequently, the composites resulting from the blend of MOF and other auxiliary components make them suitable for a large range of applications, including controlled drug release *via* cutaneous administration. The delayed or improper healing of wounds is today a global health issue that affects millions of people suffering from cancer and ulcerating diabetic lesions. It has an enormous negative impact not only on the patient's quality of life but also on the world economy, where, in 2006, 30% of the total costs in dermatology were linked to the treatment of wounds. In the United Kingdom alone, an estimated expenditure of £3 billion was registered in 2001,

jumping to £5 billion in 2015 [31, 32]. Therefore, the design of novel multifunctional nanocomposites combining wound protection and active disease treatment has higher market value and application prospects in the field of wound care.

In this context, there is scope to investigate the application of MOF-composites, and especially the MOF/Polymer composites, to engineer bioactive wound dressings; that is to say, systems capable of effectively aiding the healing process, by the slow release of drugs and active agents to the wound site, while forming a barrier to stop the penetration of bacteria to the wound environment [33, 34]. In fact, MOFs have recently been investigated for their antimicrobial activities, generally attributed to their metallic ions (*e.g.* Cu, Fe, Zn, and Ag) [35].

This chapter will review the specific parameters that make MOFs a prospective material to overcome some existing obstacles in the fields of drug delivery and personalized therapeutics. At the same time, it will additionally highlight specific areas in MOFs and MOF-composites research that require supplementary development to propel the practical application MOF materials in biomedicine and related fields. To conduct novel exploratory studies, two prototypical MOF structures and three model drug molecules have been used to address the existing limitations of current techniques and methods, as described in the following sections.

2.1.1 MIL-100 (Fe)

The iron (III) carboxylate MOFs are promising given their biologically and environmentally favourable characteristics, large surface areas, and high porosity. They offer numerous coordinatively unsaturated metal sites (CUS) [36], which not only potentializes their application as DDS but also holds great promise as adsorbents and catalysts agents [37, 38]. Specifically, MIL-100 (Fe) exhibits a highly ordered structure with large mesoporous cages (∼3 nm) accessible through pentagonal and hexagonal windows (5 and 8.5 Å) that enable the entrapment of large amounts of functional guests and drug molecules (Figure 2.1). As a functional material targeting biomedical applications, MIL-100 (Fe) features improved biocompatibility in contrast to a variety of MOFs, including its other metal counterparts, namely MIL-100

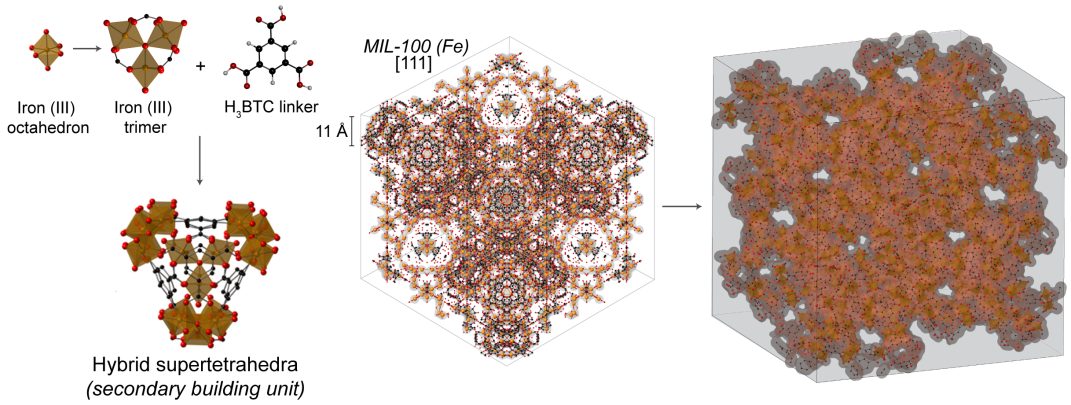

Figure 2.1: Schematic representation of MIL-100 (Fe) building units: tetrahedral hybrid units formed by four iron trimers of octahedra linked by four BTC molecules. Colour code: O in red, C in black, H in gray

(Cr, Ni, Cu, and Co) [6], highly desired for biomedical applications [5, 6, 39]. In addition to its potential as DDS, it has also been studied as contrast agents for NMR imaging because of its favorable *in vivo* detection [6], and extended stability under physiological conditions [40].

2.1.2 HKUST-1

The Cu-based MOF called HKUST-1 $[Cu_3(BTC)_2]$ is one of the first porous MOFs discovered and, as a consequence, has been a reference material for the study of many general properties of MOFs. With its three typical microporous sites (5, 11, and 13.5 Å in diameter) [41, 42], the 3D framework structure of HKUST-1 is composed of copper paddle-wheel building units connected by trimesic acid organic linkers (Figure 2.2). This framework has also been explored as a viable host for the creation of bio-oriented guest@MOF composite systems [43–45]. Upon activation at low pressure and gentle heating (∼90 °C), HKUST-1 forms a chemically activated structure with exposed Cu^{2+} sites. Notably, the CUS in the pores of HKUST-1 are highly accessible, characterizing strong binding sites for guest molecules [46, 47]. HKUST-1 has been considered as a prominent platform for biomedical applications due to its controlled release of many chemotherapy drug cargos, effective antibacterial and antifungal activity, and enhanced wound healing properties, attributed to the Cu ions [45, 48].

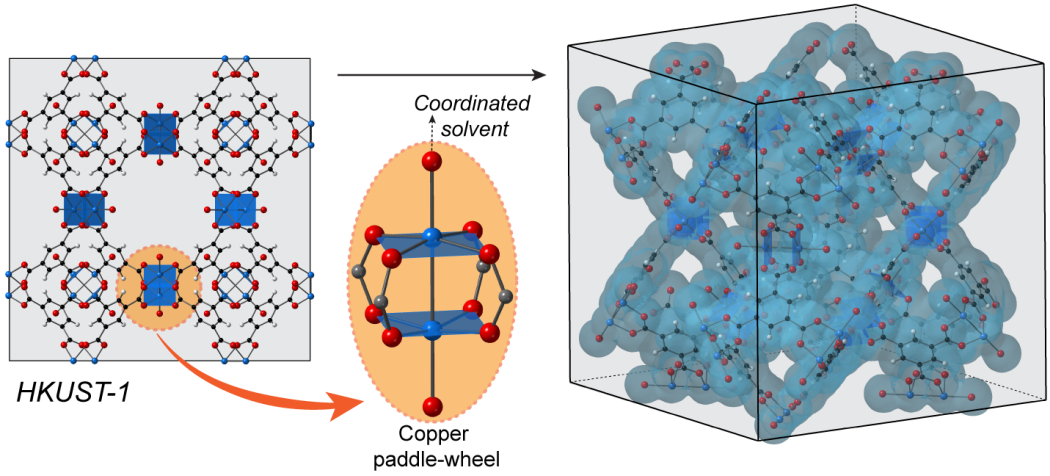

Figure 2.2: Schematic representation of HKUST-1 structure: copper (II) paddle-wheel and BTC linker coordinated to form the open framework structure of HKUST-1. Colour code: Cu in blue, C in black, O in red, H in gray.

2.1.3 Guest drug molecules

The three guest drug molecules used in this thesis were chosen based on ongoing interest in their pharmaceutical applications, yet not fully realized due to existing drawbacks.Specific chemical features of each one of these molecules (*e.g.* pKa values and proton/donor acceptor sites) have also been important factors considered for their application. These characteristics are discussed in details in the respective results chapters.

- 5-Fluorouracil is a long standing anti-cancer drug with an hydrophilic character, which restricts its passage through cell membranes without the aid of a DDS [49].
- Caffeine is widely applied as an active ingredient in many cosmetic and pharmaceutical formulations. Increasing the loading percentage of caffeine within host carriers can hugely increase its bioavailability [50].
- Aspirin is commonly used as an analgesic and anti-inflammatory drug. However, many side effects (*e.g.* stomach bleeding and gastrointestinal ulcers) associated with its oral administration, can potentially be prevented by the use of a DDS [51].

2.1.4 Defining the concept of guest@MOF

The MOF structure itself is determined by the strong coordination between the metal ions and linkers that are tunable to afford the rational design and modification

of the structure. This strong coordination bonding can be extended to the guest molecules, especially if CUS sites are present in the MOF pore structure [46]. Therefore, guest@MOF can be defined by the functionalization of the 'host' MOF nanoporous cavities with the inclusion of the functional 'guest' molecules (*e.g.* drug molecules), for the creation of guest@MOF assemblies.

2.2 Synthetic strategies towards the fabrication of MOF and drug@MOF materials

The synthesis of MOFs attracted enormous attention in the first three decades beyond MOFs discovery. The improvement of synthetic routes and the preparation of new structures were the primary focus of MOF research before the investigation of potential applications for these materials was put under the spotlight. The central aim in MOF fabrication is the definition of conditions that lead to a defined and stable structure. The synthetic method applied has a major impact on the material properties, as it dictates important parameters of the final architecture and controls the morphology of particles produced to suit specific applications [52]. Conventionally, the synthesis of MOFs involves supplying heat to a mixture of organic ligands and metal salts in hydro/solvothermal conditions. Otherwise, energy can also be introduced *via* other means, such as electric potential, electromagnetic radiation, mechanical waves, or mechanical forces. Figure 2.3 showcases the evolution of the synthetic methods applied to the preparation of MOFs in the last two decades [53]. Alternative routes include, for example, microwave-assisted synthesis (microwave irradiation), electrochemistry (electric potential), sonochemistry (ultrasound), and mechanochemistry (mechanical force)[54].

When a MOF is identified as a potential candidate for biomedical application, it is often necessary to optimize the synthesis conditions to ensure good biocompatibility *via* a green fabrication process. On top of that, the increasing global need for sustainability pivots the research of manufacturing processes towards methods with a low environmental impact. One clear way of achieving these goals within the MOF fabrication research is with the reduction of toxic organic solvents involved in

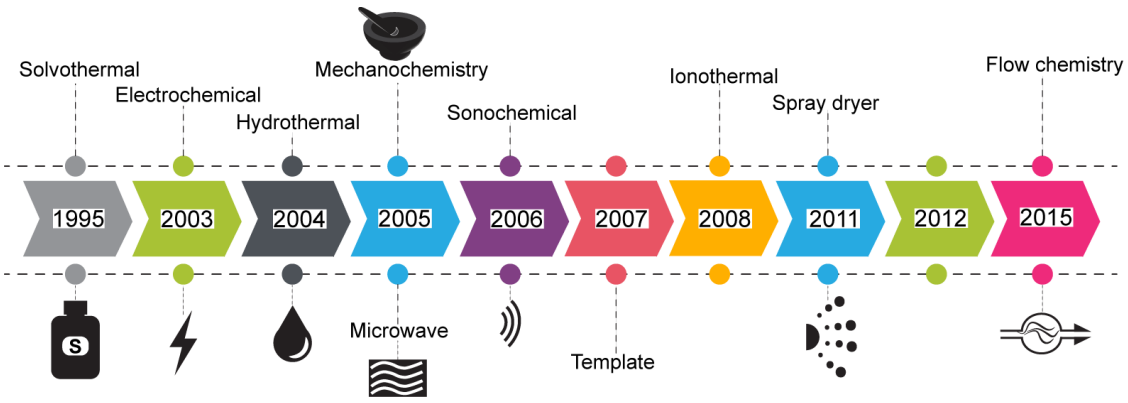

Figure 2.3: Timeline of the most commonly used synthetic approaches for MOF fabrication [53].

the synthesis. This not only represents a step forward in a sustainable synthesis path, but it can also yield MOF carriers with lower toxicity. With that in mind, the next section describes alternative synthetic methods for the fabrication of MOFs of industrial and biomedical interests [55].

2.2.1 Mechanochemistry applied to MOFs production

Mechanochemistry is characterized by reactions, normally of solids reactants, initiated and/or sustained by the application of mechanical energy by grinding or milling in "solvent-free" conditions [56]. As stated by James *et al.* [57] there is controversy in the meaning behind "solvent-free" when associated with a mechanochemical process since such process can also occur in the presence of solvents. In this context, however, it is meant to simply indicate that no bulk solvent has been purposely added to the reaction, and, therefore, highlights the advantage of the approach. It is worth noting that, in spite of a solvent-free synthesis, purification steps that utilize solvents might still be required. Nevertheless, mechanochemistry is considered to be the most environmentally friendly process to produce MOFs, presenting great prospect to reduce the costs of fabrication [58].

One of the first reports of synthesis by manual grinding of an extended coordination polymer likely dates back to 1968 [59]. Almost four decades later, in 2006, Pichon *et al.* [60] reported for the first time the mechanochemical synthesis of a highly crystalline microporous MOF, followed by the fabrication of an archetypal

MOF HKUST-1 *via* dry milling of copper (II) acetate and H_3BTC [61]. In 2009, Friščić and co-workers made great progress and broke synthetic paradigms by showing the use of metal oxides, normally avoided in solution-based synthesis due to their low solubility, for the synthesis of Zn-based MOFs [62].

From this point onwards, numerous MOFs have been synthesized through the different variations of mechanochemical routes. For example, MIL-100 (Fe) and MIL-101 (Cr) have been successfully produced by a neat grinding process assisted by the application of heating for subsequent coordination driven polymerization (grinding-annealing) without the use of hydrofluoric acid (HF) [63, 64]. Other iron-carboxylate MOFs have also been successfully synthesized by a liquid-assisted grinding (LAG) process to assist the mechanochemical reaction (*i.e.* the addition of a very small quantity of solvent - on the order of microliters - during the grinding step) [65]. An ion and liquid assisted grinding (ILAG) has also been applied to the synthesis of MOF crystals. This variation of mechanochemistry used a small amount of catalytic ionic salt to induce and direct the mechanosynthesis starting from metal oxides [56]. For instance, HKUST-1 crystals were produced with the addition of NaCl as a solid solvent assisting the reaction [66]. A zeolitic MOF with a sodalite topology, called ZIF-8, has also been successfully synthesized in a salt-assisted process using ZnO [67].

Innovative research has been conducted to examine the use of well-developed continuous techniques as a means to perform mechanochemical synthesis in a large scale and efficient manner. This is highly appealing for the successful industrial application of MOFs. As an example, ball milling has allowed the synthesis of tens of grams of magnetic Fe-BTC and Cu-BTC (HKUST-1) [61, 68, 69]. Hot-pressing and roll-to-roll approaches have been used to produce HKUST-1 and ZIF-8 coatings distributed over large areas [70–72]. Creative solutions, such as the use of a kitchen grinder for the preparation of MIL-100 (Fe), HKUST-1, and ZIF-8 or the adaptation of a lab vortex mixer for the fabrication of a Cu-based MOF, have been explored in a lab-scale production [73, 74]. A breakthrough came, however, in 2005, when James and co-workers demonstrated the use of twin-screw extrusion (TSE) for

the preparation of various MOF materials [75]. TSE had been traditionally used for the processing of polymeric materials. They have elucidated the synthesis of HKUST-1, ZIF-8, MAF-4, and Al(fumarate) (OH) MOF with a high production rate (4 kg/h) and space-time yield (144 000 kg/m^3 day). Following up on this strategy, Karadeniz *et al.* [76] have presented the synthesis of a series of zirconium-based MOFs: UiO-66, UiO-66-NH2, MOF-801, and MOF-804 in a production rate of 1.4 kg/h. Limitations imposed by ball milling, such as the lack of temperature control, can be overcome with the use of TSE.

2.2.2 Water-based methods for MOFs fabrication

Water-based methods (*i.e.* the use of water as the only solvent) have also been explored as an alternative to accomplish the optimization of MOF fabrication while addressing the related safety hazards, environmental impact, and related costs of the synthesis procedures. Hydrothermal methods can be employed under similar conditions of conventional solvothermal approaches, in which the use of increased temperatures throughout the synthesis is required. They can also be performed at room temperature, which is preferred due to the resulting reduction on the energy cost of the synthesis [77].

The water-based fabrication of MOFs has been demonstrated for a variety of known systems as well as new structures not previously achieved *via* conventional synthetic routes. For example, Chen and co-workers [78] have reported the production of a new ZIF structure named ZIF-L, prepared in deionized water at room temperature. ZIF-L presents one unique cushion-shaped cavity, which is well suited to accommodate functional molecules (Figure 2.4). Similarly, Jian *et al.* [79] have systematically studied the formation of ZIF-8 in water from different metal precursors and various metal/linker molar ratios. They have revealed how changing these synthesis parameters in an aqueous environment yields a large number of crystal topologies and structures, going from the known ZIF-8 configuration, passing through intermediate structures, until reaching the leaf-like ZIF-L structure discovered by Chen *et al.*

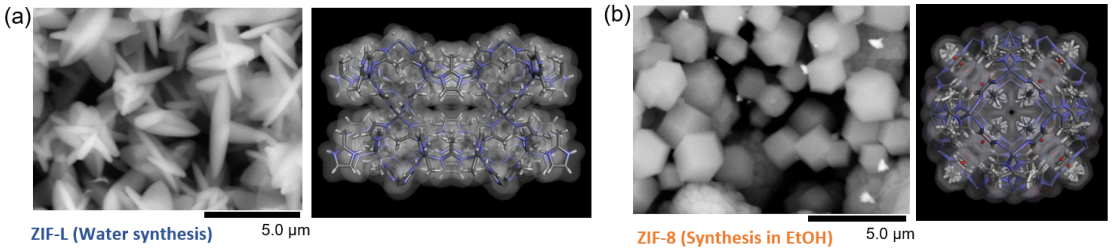

Figure 2.4: (a)ZIF-L prepared *via* a water-based synthesis and (b) ZIF-8 synthesized under solvothermal conditions accompanied by respective schematic crystal structures.

Aqueous methods have also been successfully used for preparing Zr-MOFs and several members of CPO-27/MOF-74 family, resulting in materials with high surface areas and elevated space-time yields (up to 18 720 kg/m^3 day) [77–79]. MIL-100 (Fe) has also been fabricated in a fluoride-free aqueous solution at ambient pressure [80]. The development of water-based approaches, obviating the use of harmful organic solvents, is highly desirable considering that MOF activation (*i.e.* evacuation at high temperature and low pressure) can often be insufficient to eliminate noxious solvent molecules coordinated to the MOF pores. Reducing the amount of organic solvent used during the synthesis and post-synthetic procedures is therefore important as it leads to the production of MOF particles with a lower degree of toxicity and consequently facilitates their biomedical use.

2.2.3 Cost analysis of MOF production

DeSantis *et al.* [81] have conducted a very appealing cost analysis of large scale production of MOFs, considering manufacturing (*i.e.* synthesis, filtration, and drying) and material costs (*i.e.* precursors and solvent used). The baseline solvothermal synthesis has been compared to liquid-assisted grinding and aqueous synthesis to evaluate the cost impact of solvent reduction. The cost breakdown for the synthesis of Mg-MOF-74, for example, was US$48.52 per kg for the solvothermal synthesis method, US$17.96 per kg for the aqueous synthesis method, and US$11.88 per kg for the LAG mechanochemical synthesis method. Therefore, mechanochemical and aqueous methods lead to significantly lower material and manufacturing costs compared to the solvothermal approach. The authors conclude that minimizing the

use of solvent is recommended to equally reduce material cost and cut down the size of reactors, with the consequent reduction to manufacturing cost [82].

2.3 MOFs as DDS: drug molecules incorporation and release

2.3.1 Confining guest molecules within MOF pores

Different strategies have been explored to incorporate guest drug molecules into the porous MOF structure. The following sections describe the most commonly used approaches for the preparation of drug@MOF systems. If combined with previously described mechanochemical and water-based synthesis, the following approaches could help to mitigate existing barriers to the application of MOFs as drug delivery platforms.

Two step *ex situ* encapsulation. In this method for guest encapsulation, the *ex situ* confinement of drug molecules in MOF pores is performed by the immersion of activated MOF particles in a solution containing the guest molecule to be encapsulated (Figure 2.5a). It is certainly the most commonly used process due to its simplicity, being applicable to many different types of drugs and functional molecules, and resulting in a large variety of drug@MOF systems [83, 84]. However, in this process, limitations are imposed by the immersion time, solvent dependency, and the reliance on diffusion processes not yet entirely elucidated for MOF systems [85]. It involves the synthesis of the host MOF, its activation to eliminate coordinated solvent, immersion into the guest drug solution for encapsulation, followed by a final washing step, and subsequent drying. Similar to factors governing any adsorption process (*i.e.*the diffusion mechanisms and the guest-host interactions), the competition between the adsorption of the guest molecules and the solvent molecules used for the impregnation needs to be considered in the two-step encapsulation. This is vital when the MOF structure contains CUS centres that act as primary adsorption sites in the host structure [46].

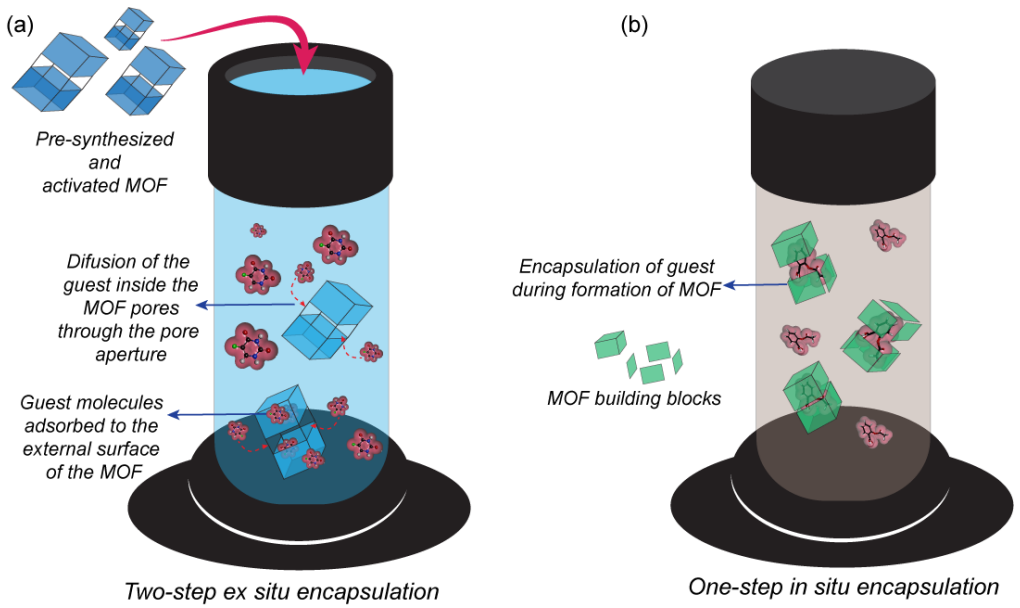

Figure 2.5: Schematic representation of techniques commonly used for guest confinement into the host MOFs. (a) *ex situ*, (b) *in situ* encapsulation.

The choice of the appropriate solvent for the loading of the drug molecules is therefore crucial. For instance, a study by Cunha *et al.* [86] has shown how caffeine is loaded more efficiently into the pores of functionalized UiO-66 (Zr) when water is used as a solvent. On the other hand, the same drug can be encapsulated at higher amounts in MIL-88 (Fe) when ethanol is used. They have further explored the influence of hydrophilicity/hydrophobicity and functionalization of the MOF on the *ex situ* encapsulation [13], which was followed by Rojas and co-workers' study about hydrophobic/hydrophilic balance between drug molecules and MOF during drug encapsulation [87].

Another important factor to consider during the application of a post-synthetic encapsulation method is the dependence on the sizes of the drug molecule and the pore aperture. The improper match between these two dimensions can limit the encapsulation of large guest molecules even if they could be easily accommodated within the MOF pores. Due to the MOF chemical structure, however, this impediment can favour the surface adsorption of the drug molecules onto the pores' exterior walls (*i.e.* weak physisorption) where van der Waals forces, π–π stacking, and hydrogen bonding are the resulting dominant interactions. Therefore,

the weaker interactions and the absence of physical barriers imposed by the MOF cages might lead to leaching problems and the premature release of the encapsulated drug molecules [88].

One step *in situ* encapsulation. The *in situ* method eradicates the post-synthetic steps of drug encapsulation by allowing the guest confinement to take place concomitantly with the MOF formation (Figure 2.5b). As a result, the drug loading becomes independent of the size of the accessible pore aperture and only reliant on the guest/pore dimensions. However, it is essential that the guest remains stable under the conditions for the MOF synthesis, which might limit the number of drug-MOF combinations compatible with this strategy. From an environmental and economic point of view, the one-step encapsulation can be highly beneficial to the fabrication of drug@MOF systems. It also present new frontiers to achieve higher loadings and more efficient drug encapsulation by eliminating the dependence on the drug concentration in solution [89]. To apply this strategy, it is important to consider MOFs that can be prepared under soft conditions (*e.g.* low temperature under atmospheric pressure).

So far, this methodology has been applied to the encapsulation of different types of therapeutic molecules within the MOF structure for subsequent release. For example, ZIF-8 has been successfully used to host the 3-methyladenin anticancer drug [90]. The system was prepared under ambient conditions in which dropwise additions of a linker solution were performed to a drug/metal stock solution. *In vivo* experiments demonstrated higher antitumor efficacy of 3-methyladenin in HeLa cells after its encapsulation into the ZIF-8 pores. Other examples of *in situ* encapsulation are given in the confinement of caffeine [50, 89], curcumin [91], and doxorubicin [92] in ZIF-8, and ibuprofen in HKUST-1 and in a zinc-based MOF [93]. In addition to anticancer drugs, the encapsulation of biomolecules is also achievable *via* this strategy. One example of this is the one-step encapsulation of glucose oxidase and horseradish peroxidase into ZIF-8 crystals, exhibiting high stability and catalytic efficiency [94].

The *in situ* and *ex situ* encapsulation methods present inherently different performance, strengths, and shortcomings in relation to the confinement of guest molecules. These two differential pathways need to be carefully and systematically contrasted to define the most appropriate strategy for specifically desired applications. Chapter 7, then, presents a detailed comparison between these two strategies and measures their influence on the resulting guest-host interactions.

2.3.2 The understanding of guest-host interactions

Guest-host interactions are of fundamental importance in many chemical and biological processes. They represent non-covalent interactions arising from the complexation of guest-host systems [95]. Regardless of the type of drug delivery vehicle employed, the understanding of the interactions between the drug and the carrier is crucial for engineering and controlling the release process. The chemical and structural complexity of MOFs leads to a variety of possible guest-host interactions (*e.g.* van der Waal forces, hydrogen bonding, coordination, π–π stacking) driven by the guest chemistry and diversity of possible host adsorption sites [96, 97]. Earlier studies on the controlled release of active molecules have given less consideration to these important guest-host interactions. This could have been influenced by the difficulty encountered in the investigation of the formation and decomplexation of guest-host systems at the molecular and atomic level [98].

Specifically considering the high and tunable porosity possessed by MOFs and the many types of functional molecules that can be accommodated inside their pores, one ever-lasting challenge is confirming the successful pore encapsulation of the guest molecules (versus their adsorption onto the external surface of MOF cages). Pinpointing the location of drug molecules within the framework structure is central to their realization as drug delivery platforms. Excessively weak interactions arising from the unsuccessful entrapment of these molecules might lead to a rapid release from the host carriers. Excessively strong interactions can prevent the drug from leaving the pores of the MOF. Unambiguously, proving the encapsulation is far from a trivial task. The careful examination of guest-host interactions combined

with computational modeling of the assemblies is, however, a possible path towards assessing the precise encapsulation of guest molecules.

The ordered crystalline environment presented by MOFs is highly advantageous to the study of guest-host interactions since it allows the detailed evaluation of interatomic spacing and distances. For example, Allendorf *et al.* [82] developed an analogy between the supramolecular structure of MOFs and the well-known complex structure of proteins (Figure 2.6) [99]. Four structural elements (primary, secondary, tertiary, and quaternary structures) are classified. The primary structure relates to the coordination environment of metals and linkers and if often referred to as the SBU, the building blocks that give rise to the MOF topology. The secondary structure comprises the assembly of the SBU to form a network. The representative length scales are the pore dimensions and unit cell. The tertiary structure describes the arrangement of the network and lattices to form a supramolecular structure while the quaternary structure denotes interpenetrating network structures. Particularly in what concerns the study of guest-host interactions, the primary and secondary structures are the most significant parts as their length scale directly represents the accommodation of these interactions within the structure.

In the literature, it is possible to find several studies highlighting the investigation of guest-host interactions formed during the adsorption of gases into MOFs. For instance, Gonzalez *et al.* [100] have characterized the interactions of a Co-MOF bearing a multiplicity of CUS with various types of gases (*i.e.* carbon monoxide, carbon dioxide, nitrogen, oxygen, methane, and argon). Using gas sorption and single crystal diffraction, they revealed the physisorptive character of the interactions between the gases with the cobalt open metal site, where all gas molecules presented non-covalent interactions, apart from carbon monoxide, which established weak covalent bonding with the framework. A systematic study by Hobday *et al.* [96] provided a full characterization of the response to adsorption of small molecules (specifically methane, argon, oxygen, and dihydrogen) in ZIF-8 and the underlying guest-MOF interactions using high-pressure crystallography and computational modeling. They unravelled all the gas adsorption sites within

the framework. Several other studies have similarly highlighted the interactions between framework and other functional molecules [101–103].

Although limited, a few studies exposing the guest-host interactions present in drug@MOF systems can be found in the literature. In such studies, the interactions are exposed by different experimental techniques, often combined with theoretical calculations. For example, Hu *et al.* [104] have examined the release of 5-FU from a Mg-MOF. They used microcalorimetry to measure the energy of guest-

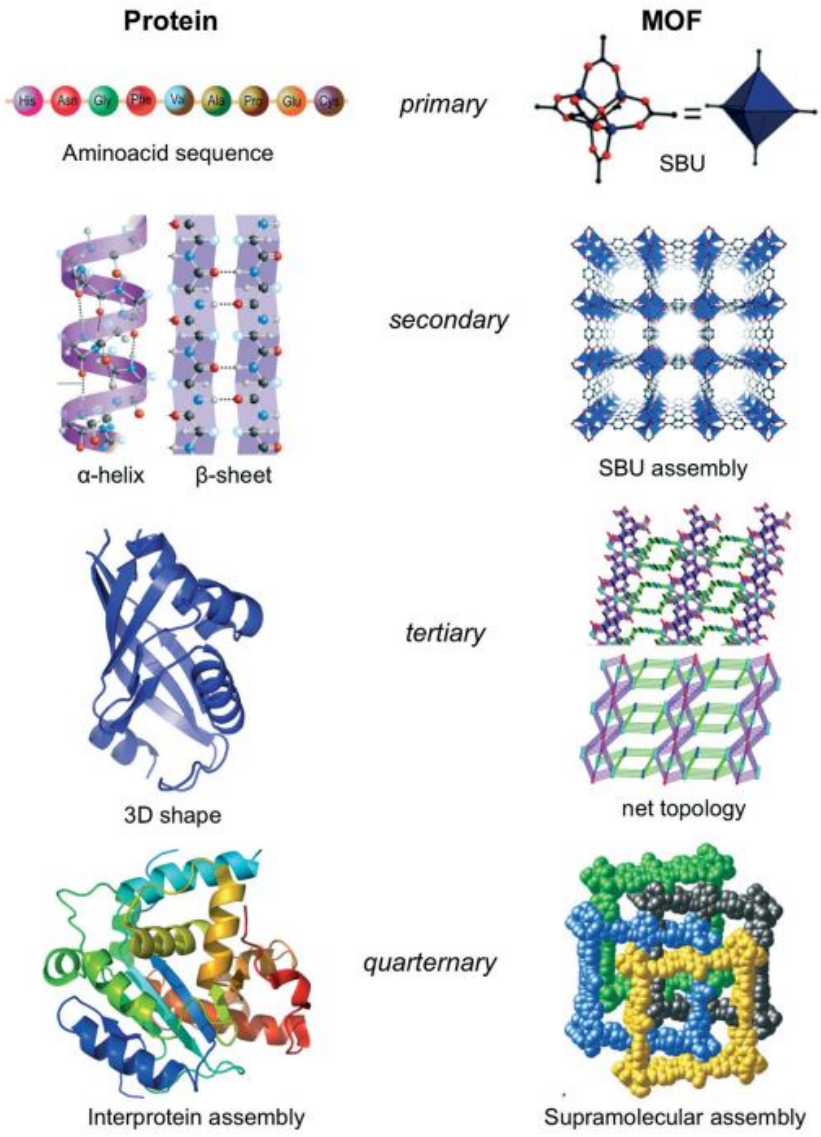

Figure 2.6: Hierarchical structure of proteins and MOFs. Republished with permission of Royal Society of Chemistry, from Crystal engineering, structure–function relationships, and the future of metal–organic frameworks, Mark D. Allendorf and Vitalie Stavila, 17, 2015; permission conveyed through Copyright Clearance Center, Inc.

host interaction during the release process and showed how a hydrogen-rich pore environment led to strong guest-host bonding and a medically reasonable release rate. However, this synergetic approach does not convey specific information about guest-host coordination bonds. Anand *et al.* [105] presented the use of UV-Vis absorption and fluorescence to assess the interactions between doxorubicin and MIL-100 (Fe). They revealed the formation of guest-host interactions *via* coordination between hydroxyl groups in the drug and the iron CUS, forming a doxorubicin-MOF cross-linked coordination network. Rojas and co-workers [87] have conducted a comprehensive study to gain more details behind drug and MOF features during drug encapsulation and release. They have examined the relationship between UiO-66 (Zr), MIL-100 (Fe), and MIL-127 (Fe) with aspirin and ibuprofen, focusing on molecules affinity and pore size. Complementary, theoretical studies have been carried out to study the interactions of the guests with the appropriate MOF carrier to select the best candidates for drug delivery applications [106–109].

Despite multiple experimental attempts to encapsulate therapeutic molecules into MOFs accompanied by detailed characterization of drug loadings and release kinetics, the understanding of the guest confinement and release mechanisms is still very limited. The use of MOF as DDS could, therefore, further benefit from systematic studies that examine the effects of drug confinement at the molecular and atomic levels. Inelastic neutron scattering (INS), as described in the following sections, could be used to probe the underpinning guest-host mechanisms of drug@MOF systems.

2.4 INS as a tool to reveal structural intricacies of MOFs and guest@MOF systems

2.4.1 Contextualizing neutron scattering

Neutrons are used as a high resolution probe in the field of material science due the unique nature of their interaction with condensed matter. They possess wavelengths and energy that are very similar to interatomic spacings and excitations, respectively. This contrasts with other optical probes (*e.g.* IR, Raman, and X-rays) that normally

present either specific wavelengths or energy ranges [110, 111]. Since they possess energy and have mass, neutrons also present measurable momentum. The change in momentum during interaction with the nuclei of matter can also be used to assess different material properties, targeting for example advanced materials [112], life sciences [113], chemistry and energy [114, 115], materials engineering, and a variety of industrial applications [116].

The scattering of neutrons can be formally classified into different categories, such as elastic and inelastic scattering, and coherent and incoherent scattering [117]. The coherent scattering functions, in which the scattered neutron waves interact constructively, offer evidence on collective motions (*i.e.* phonons - the ordered and correlated motion of a lattice). Meanwhile, the incoherent scattering function, which depends on the spin and isotopic incoherence, produces insights into the system's self-correlations (*e.g.* diffusion processes) [118]. The number of neutrons scattered by a given sample is based on the so-called scattering cross-section of the probed atom, which expresses the likelihood of interaction between an incident neutron and a target nucleus (Figure 2.7). In addition to scattering, one should also consider the possible absorption of neutrons, a process governed by the absorption cross-section that varies irregularly throughout the periodic table. The low absorption cross-sections of most elements make neutron a highly penetrating probe that allows the examination of bulk samples in a non-destructive fashion.

Upon scattering, a neutron may change its energy and wavevector when colliding with the nuclei of the sample. The phenomena involved in the transfer of energy between neutrons and nuclei can then be examined in a scattering experiment. Depending on the energy transfer spectrum, the scattering can be classified as the elastic, quasi-elastic, or inelastic scattering (Figure 2.8) [118]. The elastic scattering ideally happens when the scattering function is centred at 0 energy transfer, indicating the absence of dynamics in the sample. The quasi-elastic neutron scattering (QENS) is represented by a broadening of the elastic scattering spectrum and presents shreds of evidence of diffusion processes within the sample. Importantly, it is still centred at 0 energy transfer, the reason why it is called

quasi-elastic. Last, the inelastic scattering is represented by the spectrum peaks centred at energy transfer values different than zero, which are associated with the sample vibrational modes.

2.4.2 Using INS for vibrational spectroscopy

The fundamental differences between the interactions of neutrons beams and optical probes are especially relevant for the study of internal vibrations of molecules in a crystal. The use of INS as a vibrational spectroscopy tool is akin to IR absorption and Raman scattering spectroscopy, and the main variance lies in the probe-scatterer interactions. As mentioned previously, while neutrons interact with the nuclei of

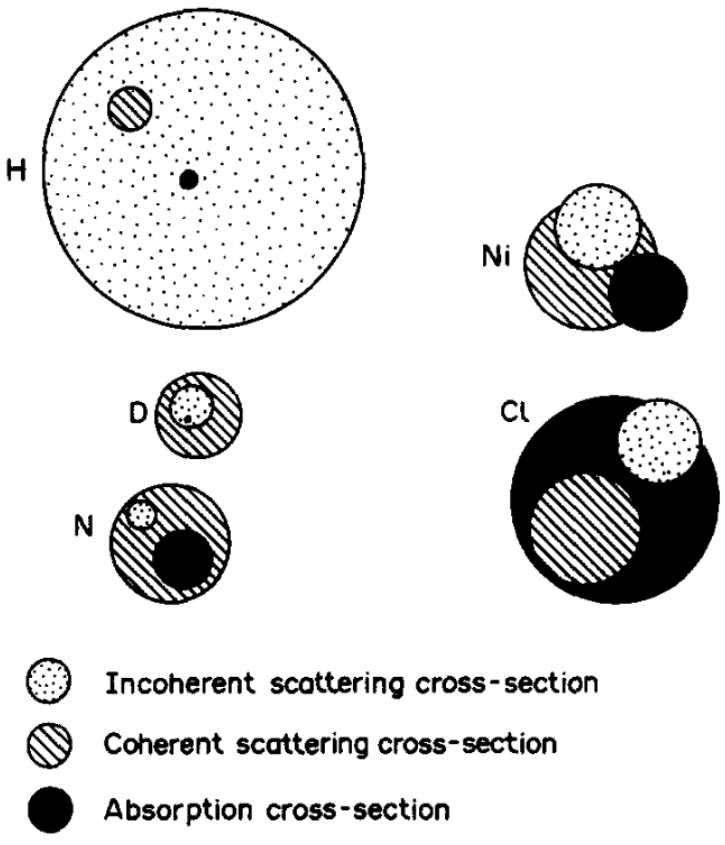

Figure 2.7: Neutron scattering and absorption cross-sections for various elements and isotopes of interest in chemistry. Values for the natural elements are given for Ni, Cl, and N. The magnitude of the cross-section is represented by the area of the circle. Reprinted from Spectrochimica Acta Part A: Molecular Spectroscopy, Vol 48A, No. 3, Juergen Eckert, Theoretical Introduction to Neutron-Scattering Spectroscopy, 271-283, Copyright (1992), with permission from Elsevier

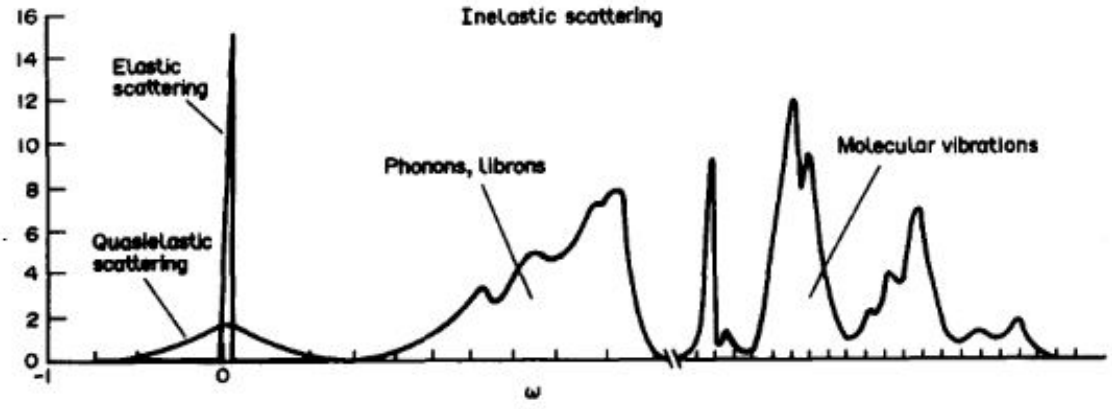

Figure 2.8: Generalized incoherent inelastic neutron scattering spectrum for a hypothetical molecular crystal: elastic and quasielastic scattering near w = 0, inelastic scattering from the external modes of the molecular crystals (phonons and librons), and at higher frequencies (note the break and change in the frequency scale) of the internal vibrational modes. The latter were chosen to be well separated from the lattice modes. The relative intensities of the different parts are arbitrary. Reprinted from Spectrochimica Acta Part A: Molecular Spectroscopy, Vol 48A, No. 3, Juergen Eckert, Theoretical Introduction to Neutron-Scattering Spectroscopy, 271-283, Copyright (1992), with permission from Elsevier

the sample, allowing the analysis of intensity and frequency data, IR and Raman spectroscopy depend on the interaction of photons with the electronic cloud found around the nuclei of the molecules, which are more complex in nature [117]. For example, the optical selection rules (*e.g.* possible transitions of a system from one quantum state to another) dictate that vibrations are only IR active (*i.e.* are present in an IR spectrum) if the molecule presents a dipole moment change during the vibration [119]. Therefore, for instance, the symmetric stretching of a carbon dioxide molecule is IR-inactive while the asymmetric stretching is IR-active, as illustrated in Figure 2.9. However, since the measure of neutron-sample interactions is based on energy transfer, both vibrations of this carbon dioxide molecule would be present in a INS spectrum. Therefore, unlike optical spectroscopic techniques, INS is, in principal, not subject to the optical selection rules, meaning all transitions are in principle active in the INS spectra. This makes INS spectroscopy a more sensitive test of intermolecular forces that rule molecular vibrations, specifically when the molecule is bound to a crystal or adsorbed on its surface [117].

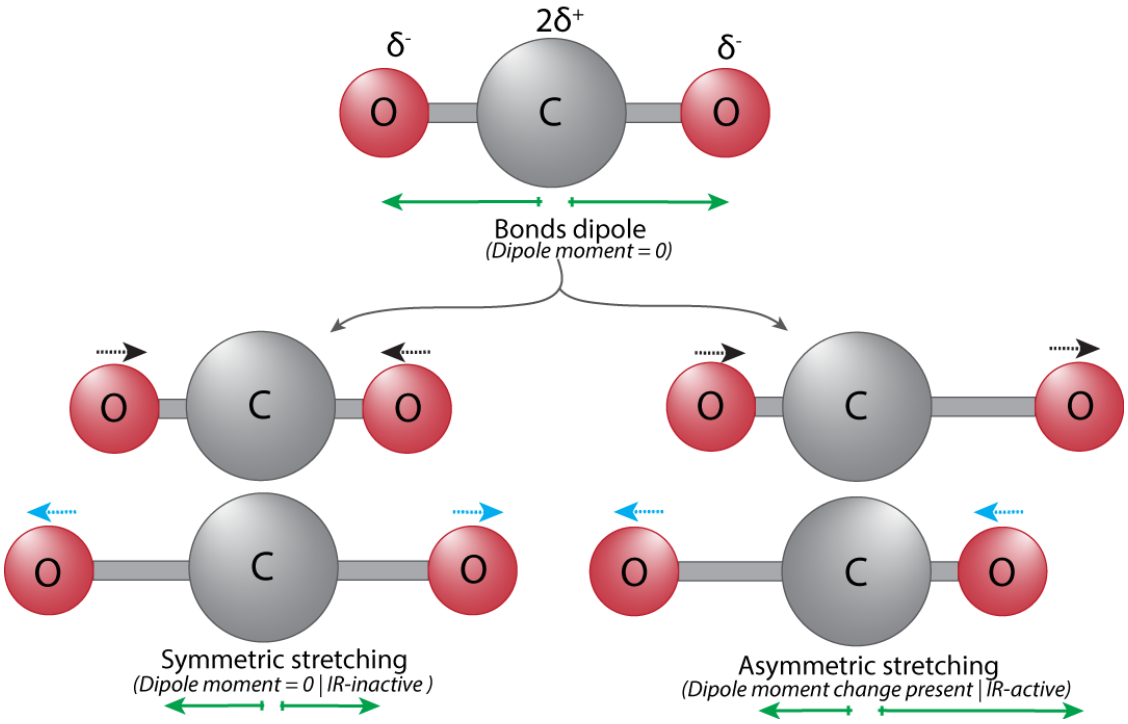

Figure 2.9: Schematic representation of carbon dioxide symmetric and asymmetric vibrations. The analysis of the molecular dipole moment change reveals the IR character of each vibrational mode

The absence of selection rules additionally gives INS the unique ability to examine all the collective vibrational modes (phonons) observed in the low energy THz region (<500-600 cm^{-1}, where 1 THz = 33.3 cm^{-1}). Unlike high-frequency vibrations, arising from molecular vibrations of small functional groups, THz vibrations encompass the collective motions associated with the lattice dynamics of the framework structure [120]. Consequently, INS spectroscopy is a highly sensitive probe for the examination of MOFs structural dynamics and guest-MOF interactions from a vibrational point of view.

2.4.3 Obtaining an INS spectrum

High-resolution INS experiments can be conducted in a nuclear reactor, where a continuous neutron beam is produced by nuclear fission, or by spallation, in which a pulsed neutron beam is generated. The ISIS Neutron and Muon Source, for example, is a spallation source based in Oxfordshire, United Kingdom. In the facility, protons are accelerated in a synchrotron and emitted to collide with a tungsten target.

Upon collision, the high energy protons drive neutrons out of the nuclei of the target atoms. The high intensity neutron pulse is slowed down by an array of hydrogenous moderators and then directed to neutron instruments, such as the TOSCA INS spectrometer in ISIS, where the spectra of different samples can be collected [121].

2.4.4 The application of INS spectroscopy to the study of MOF and guest@MOF structures

Given the resolution presented by INS spectroscopy and the specific sensitivity to different atoms (especially hydrogen), it is not surprising to see the use of this technique in the examination of MOFs structural features as well as their interaction with adsorbed molecules. More often than not, the spectroscopy evaluation of these systems is accompanied by computational studies that take advantage of the highly symmetric structure presented by MOFs to simplify the computational models and to aid the understanding of the resulting INS spectra.

Employment of INS spectroscopy to the study of MOF system was reported for the first time by Yaghi *et al.*, in 2003 [122]. They have exploited INS high sensitivity to hydrogens motions to scrutinize the dihydrogen sorption properties of MOF-5 and the potential to control the dihydrogen binding for energy storage applications. They have determined the importance of the organic linker in determining dihydrogen uptake levels. Shortly after, the same group has expanded their investigation of dihydrogen sorption to other MOF systems including IRMOF-8, IRMOF-11, and MOF-177 to investigate the role played by the organic ligand on hydrogen bonding [123]. Following the pioneering work by Yaghi and co-workers, the use of INS to assess the dihydrogen sorption and interactions with the host MOF has been conducted by many researchers for a variety of MOF systems, including purely experimental studies [124–128] and their combination with theoretical predictions to facilitate the interpretation of some of the complex collective MOF motions [129–133].The technique has also been applied to the study of methane [134], carbon dioxide [135], nitrogen, argon, oxygen, and carbon monoxide adsorption [136, 137], to reveal structural properties of the host MOF,

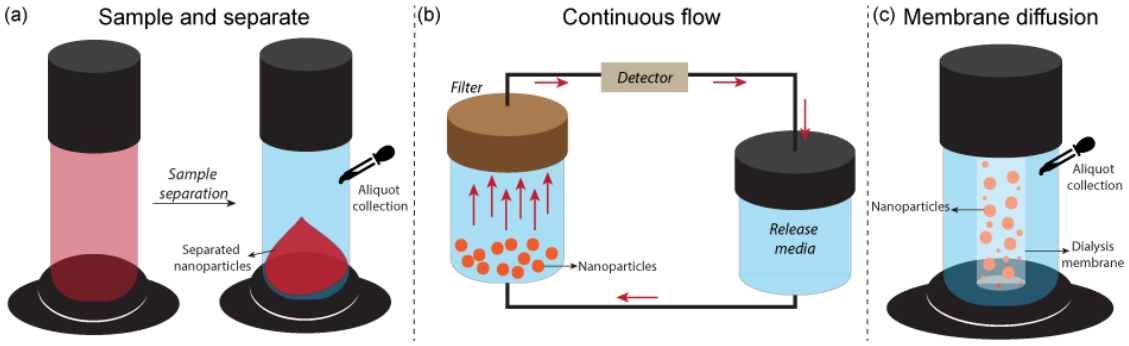

Figure 2.10: Most commonly applied methods for the *in vitro* study of drug release from nanocarriers. (a) sample and separate, (b) continuous flow, and (c) membrane diffusion.

such as a negative thermal expansion in MOF-5 [138], examination of the THz modes and lattice dynamics of HKUST-1 andMIL-140A [120, 139], including gate opening phenomenon in ZIF-8 [140], and structural determination in a Pb@OX-1 system [141]. As highlighted by the aforementioned studies, great focus has been given to using INS for the study of gas sorption in MOF structures. A lack of literature on the use of this powerful technique to examine drug@MOF systems underlines an unrealized potential of INS to the study of drug@MOF structural properties. Chapters 5-7, then, attempt to demonstrate the application of INS to tackle the long-standing challenge of scrutinizing guest-host interactions in the drug@MOF systems.

2.5 Drug release studies: *in vitro* release methods

The natural progression after examining the encapsulation process and the resulting guest-host interactions is to dive into the drug release process itself. Determining the quality and performance of a drug delivery vehicle is a crucial aspect during the development of a new DDS. For that, *in vitro* experiments have been designed and used as a predictor for *in vivo* behaviour for a variety of delivery platforms. *In vitro* drug release kinetic studies are the most commonly employed assays to determine the efficacy of MOF systems in the release of drug cargos. The most commonly applied methodologies, illustrated in Figure 2.10, can be divided into the following categories [142–144].

Sample and separate. In this method (Figure 2.10a), the nanoparticle carriers are added directly into the chosen release media, which are kept under specific temperature and agitation conditions. Sample separation techniques are applied, such as centrifugation and filtration, to separate the suspended nanoparticles. The drug release is assessed by sampling the release media *via* the collection of aliquots at different time intervals. The agitation conditions, choice of the release media, temperature, and separation technique are a few of the parameters influencing the drug release process in this method.

Continuous flow. As shown in Figure 2.10b, drug release is induced by the constant circulation of the release media through the nanoparticles in a closed-loop configuration. The release can be assessed by sampling from the release media or having a detector attached to the line of media flow. While the flow method allows the continuous real-time monitoring of the drug release process, it suffers from disadvantages such as instrument cost, filter clogging, and dependence in the flow rate applied. However, it shows advantages in better simulating the *in vivo* environment. It has been widely used to monitor the drug release from microspheres, but it presents challenges when using particles smaller than 100 nm, which can either induce filter clogging or adulterated results by passing through the filter.

Membrane diffusion. In diffusion techniques (Figure 2.10c), a physical separation between the particles and the release media to be sampled is achieved with a dialysis membrane, allowing the ease of sampling at periodic intervals. In the simplest set-up, the sample is placed inside a dialysis bath, which is immersed in a larger container. Normally, the volume enclosed in the dialysis bag is much smaller to ensure that the drugs released from the nanoparticles diffuse through the interface to the outer compartment, where it is sampled and analysed. The results obtained *via* this method are highly influenced by the choice of the media, the ratio between the cell volumes, and especially the molecular weight cut-off of the dialysis membrane, which will determine the size of molecules that can diffuse through it. The potential of the drug binding to the polymeric membrane also needs to be checked. It is necessary to

ensure appropriate size compatibility between the drug and membrane so the former can flow freely. The ease in setting up this method and sampling the release media makes it an attractive technique applied to the study of many nano-sized carriers.

2.5.1 The drug release process in drug@MOF systems

Sample and separate has been the most commonly applied method for the investigation of drug release from MOF carriers. Horcajada's and Férey's team has extensively explored this method, in combination with UV-Vis spectroscopy and liquid chromatography, for determining drug release concentrations, especially from MIL-type materials (*i.e.* MIL-100, MIL-101, MIL-53). *Via* the sample and separate method, they have been able to obtain release kinetics information of ibuprofen departure from MIL-100 (Fe), MIL-53 (Fe) and MIL-53 (Cr), MIL-101, and MCM-41 [87, 145, 146]. They have also assessed the release of nicotinic acid *via* the degradation of BioMIL-1 [147], and the discharge of anticancer and antiviral drugs azidothymidine triphosphate, cidofovir, and doxorubicin from MIL-100 (Fe) [6]. More recently, Rojas *et al.* [148] employed the sample and separate technique to examine the detoxifying effect of MIL-127 (Fe) over aspirin intoxication.

Although less common, diffusion methods have also been applied to examine the drug release process from MOF carriers. Sun *et al.* [149] have used it for assessing the release of a gold complex and zinc ions from a zinc-based MOF. They have highlighted how the agitation process can accelerate the release, significantly affecting the drug release profile. Orellana-Trava and co-workers [15, 150] have examined the release of calcein and an anticancer drug from a family of Zr-based functionalized MOFs. By applying a dialysis bag, they have demonstrated how the amorphization of the host structure leads to a slower drug release. Gao *et al.* [151] have verified the release of 5-FU from ZIF-8 using this method and have shown how the acidity drop in the release media induces a faster release process. Diffusion methods have been also applied to track the release of ibuprofen from amine-functionalized UiO-66 [152] and antioxidant ferulate MFM-300 MOF [153]. Even though it has been routinely applied to other classes of nanocarriers, (*e.g.* emulsion formulations [154], lipid-core

nanoparticles [155], and liposomes [156]) the continuous flow method has not been systematically used to assess drug release from MOF carriers.

2.5.2 Challenges posed to the study of drug release from nanocarriers

The methods discussed in this chapter focus on providing information on the kinetics of the drug release process from the DDS, resulting in the construction of drug release profiles. From those, it is possible to obtain release rates that can be optimized to ensure drug availability to the target site for the appropriate time and duration. By aiming at drug release kinetic studies, these commonly used in vitro approaches overlook the changes happening in the DDS themselves. This is far too often ignored when full attention is devoted to examining the kinetic and biological effects of the release. It is paramount to understand the guiding factors behind the drug release from multifunctional MOFs, which due to their varied chemical structure can present different release characteristics and mechanisms. The desire to fill this gap has instigated the experiments presented in Chapter 8.

2.5.3 *In situ* FTIR micro-spectroscopy applied to the elucidation of drug release

FTIR is a commonly used technique applied to the analysis of various types of materials. It is employed to obtain a vibrational spectrum of the IR-active modes across a wide spectral range, covering different infrared domains (*i.e.* near infrared, 12800-400 cm^{-1}, mid-infrared, 4000-400 cm^{-1}, and far-infrared, 400-10 cm^{-1}). MicroFTIR, a more recent development of this technique, has enhanced the potential of vibrational spectroscopy for local analysis on a microscopic scale. It has been applied to the careful study of different types of samples, such as microplastics [157], DNA [158],and environmental science and heritage materials [159].

Specific set-ups can be designed for collecting microFTIR spectra, which permit the use of a versatile suite of sample environments and sampling methodologies. As an example, it is possible to combine it with a high-resolution synchrotron source for real-time *in situ* measurements. Its versatility makes microFTIR

well suited for assessing the complex physical and chemical phenomena taking place within MOF structures. For instance, studies utilizing static/flow fluid-cells in the Multimode Infra-red Imaging and Microspectroscopy B22 beamline in Diamond Light Source (UK) have been carried out for the examination of MOF systems. Greenaway *et al.* [160] have demonstrated how the technique enabled the determination of kinetics and thermodynamics of carbon dioxide adsorption in single microcrystals of a functionalized MOF. Savage *et al.* [161] have used the technique to demonstrate the selective adsorption of sulfur dioxide in the robust MFM-300 MOF. Numerous studies have continued to focus on leveraging microFTIR to monitor gas uptake processes within MOF pores [162–164]. Even though it has primarily been applied within the MOF realm to elucidate adsorption routes, microFTIR technique has an unexplored potential to monitor the drug departure process from drug@MOF assemblies. This IR spectroscopic technique, therefore, can be leveraged to overcome the existing challenges described in section 2.5.2.

2.5.4 Theoretical predictions of structural properties in drug@MOF systems

Vibrational spectroscopy, as described in the previous sections, is an extremely powerful tool to investigate the structural properties of MOF systems. Challenges arise, however, with the interpretation of spectroscopic data and vibrations assignment in these complex systems. In such case, one can refer to theoretical models that will assist the decoding of the experimental spectra.

Research concerning the nature of structural vibrations in MOFs has traditionally been focused on gas adsorption, as evidenced in section 2.5.3. Civalleri's group has been one of the pioneers in the use of density functional theory (DFT) for the theoretical investigation of vibrational frequencies of MOF materials. They have demonstrated the use of the CRYSTAL DFT code for the *ab initio* study of crystal properties, to predict the vibrational modes of the well-known MOF-5 structure [165]. This work has been expanded by Zhou *et al.* [166], who investigated the lattice dynamics of MOF-5, leveraging DFT calculations and INS to present

excellent agreement between the experimental data and theoretical predictions. Ryder *et al.* [139] have demonstrated how the interpretation of the THz vibrations of MOFs can significantly benefit from DFT calculations. Theoretical spectra were applied to attain new insights into the structural dynamics of MOFs determined from the far-IR and INS experiments. The potential of combining theoretical calculations and vibrational spectroscopy can be harnessed to understand on a deeper level the structural effect of drug-MOF coordination. This will be revealed in Chapter 8.

2.6 Summary and challenges

This chapter briefly honed in a few fundamentals behind the design of novel MOF-based platforms for the controlled release of drug molecules. By outlining some of the existing challenges, which will be explored in the results chapters, this review takes a slice through the rich MOF literature and gives particular attention to the following points:

I. The environmentally friendly fabrication of guest@MOF systems should be further pursued. Mechanochemistry and water-based methods, already proven to be efficient for the preparation of various MOF materials, need to be more extensively explored for the preparation of drug@MOF assemblies.

II. The nature of the interactions arising from the confinement of drug molecules into host MOFs has not yet been sufficiently interrogated. This investigation can benefit from employing vibrational spectroscopy, specifically using INS spectroscopy, for the examination of the host structure. The deployment of this powerful technique can unveil the long-standing challenge of determining the guest interactions with the framework.

III. Insufficient attention has been dedicated to the dynamic changes undergone by drug@MOF assemblies during drug release. *In situ* methodologies that allow an improved understanding of the mechanisms is fundamental for the design of MOF-based release formulations.

As always in life, people want a simple answer . . .
and it's always wrong.

— Susan Greenfield

3

Experimental and Theoretical Techniques

Contents

3.1 MOF and drug@MOF systems preparation

3.1.1 Mechanochemistry

Mechanochemistry of MIL-100 (Fe). For the studies of mechanochemical synthesis of MIL-100 (Fe) and drug@MIL-100 assemblies presented in this thesis, adaptations were made to the synthesis procedure reported by Han *et al.* [63]. One main variation employed in the fabrication methods described in the following sections focus on the annealing step of the synthesis. First, similar procedure of that of Han and co-workers was followed for the fabrication of manual and vortex grinding samples, in which a sealed teflon flask was used during the annealing step, allowing the direct obtainment of crystalline MIL-100 (Fe) (*Adaptation 1*). Secondly, the sealed jar used for the annealing step was removed for the preparation of pristine MIL-100 (Fe) in the water reconstruction method and drug@MIL-100_IN assemblies (*Adaptation 2*). This change was made to investigate the optimization of the synthesis method aiming at large scale production (kg of material) of MIL-100 (Fe) and guest@MIL-100 systems.

Adaptation 1 was used to produce the materials presented in Chapter 4.
Adaptation 2 was used to prepare the samples discussed in Chapters 5 and 6.

Manual and Vortex grinding. Two different mechanochemical-annealing approaches were used towards the fabrication of pristine MIL-100 (Fe) material (*Adaptation 1*). First, MIL-100 (Fe) MG[1] was synthesized *via* a manual mechanochemistry process (Figure 3.1a). 1.2 g of $Fe(NO_3) \cdot 9H_2O$ [iron(III) nitrate 9-hydrate] (3 mmol) was combined with 420 mg of H_3BTC [benzene-1,3,5-tricarboxilic acid] (2 mmol) in a agate mortar and manually ground for 10 min. Secondly, for the synthesis of MIL-100 (Fe) VG[2] sample a similar procedure was followed (Figure 3.1b-g). The same amounts of initial reactants were placed in a polypropylene tube (⌀23 mm × 85 mm) together with three ⌀4 mm stainless steel spheres

[1] MG = MOF and guest@MOF assembley produced *via* manual grinding approach
[2] VG = MOF and guest@MOF assembley produced *via* vortex grinding approach

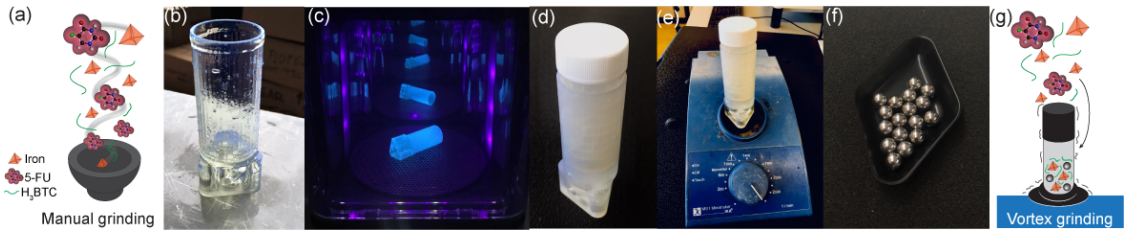

Figure 3.1: *In situ* encapsulation of 5-FU in MIL-100 (Fe). (a) Schematic representation of the manual grinding process used to fabricate 5-FU@MIL-100_MG. (b) 3D printed holder designed for the vortex grinding process which was cured under UV light (c) to enhance mechanical properties. (d) A propylene container was inserted into the holder and the assembly (e) was installed on a vortex mixer. (f) 4 mm diameter stainless steel spheres used for the fabrication of 5-FU@MIL-100_VG as schematically represented in (g).

(ball bearings). The tube was covered with a lid and secured to a standard IKA Mixer Vortex Shaker using a 3D-printed holder and then agitated at 1200 rpm for 10 min.

The resulting material from both grinding processes was placed in a sealed autoclave flask and heated in oven at 160 °C for 4 h, to complete the annealing process. The product was washed by centrifugation (8000 rpm for 10 min) with methanol and deionized water to remove any unreacted components. Pristine MIL-100 (Fe) was then dried at room temperature and activated under vacuum at 150 °C for 12 h. The product of this synthesis produced an overall yield of ∼500 mg of MOF.

5-FU@MIL-100 preparation *via* manual and vortex grinding. Two different guest@MOF samples were synthesized as follows (*Adaptation 1*). For the (one-pot) *in situ* encapsulation of 5-FU, analogous procedure was followed to the fabrication of pristine MIL-100 (Fe) with the addition of ∼540 mg of 5-FU (3.0 mmol) during the grinding process, producing the 5-FU@MIL-100_MG particles *via* manual grinding and 5-FU@MIL-100_VG particles *via* vortex grinding. The drug-loaded samples were washed by centrifugation (8000 rpm for 10 min) with methanol and then activated at 150 °C for 12 h in a vacuum oven.

Drug@MIL-100_IN assemblies preparation. The drug@MIL-100_IN systems were synthesized as follows. For the (one-pot) *in situ* encapsulation of drug molecules (*e.g.* 5-FU, caffeine, and aspirin), a similar procedure to the synthesis

of pristine MIL-100 (Fe) MG with a few adaptations (*Adaptation 2*) was followed. 3.0 mmol of the chosen drug molecule were added during the grinding process. The drug-loaded samples were washed by centrifugation (8000 rpm for 10 min) and then activated at 130 °C for 12 h in a vacuum oven.

3.1.2 Water-based preparation

Mechanochemistry of MIL-100 (Fe) and crystallinity reconstruction. For the reconstruction studies, pristine MIL-100 (Fe) was synthesized *via* a manual grinding-annealing process analogous to the one followed for the preparation of drug@MIL-100_IN assemblies (*Adaptation 2*). To perform the structural reconstruction and crystallinity studies, MIL-100 (Fe) particles were immersed into deionized water and kept under stirring at room temperature. After different immersion times, the samples were separated by centrifugation (8000 rpm for 10 min) and the supernatant was collected to measure the pH values of the reconstruction solution. Finally, the recovered MIL-100 (Fe) samples were dried at room temperature and reactivated under vacuum at 150 °C for 12 h. The reconstruction process was repeated to ensure reproducibility of results acquired with reconstruction and the product obtained *via* the manual grinding method.

Drug@MIL-100_REC assemblies preparation during reconstruction. For the fabrication of drug@MIL-100_REC systems[3], encapsulation during the reconstruction process was performed by immersion of pre-activated MIL-100 (Fe) samples in a saturated aqueous drug solution (*i.e.* 12 mg mL^{-1} for 5-FU, 20 mg mL^{-1} for caffeine, and 3.3 mg mL^{-1} for aspirin) under continuous stirring for 7 days at room temperature. The drug-loaded drug@MIL-100_REC particles were separated by centrifugation (8000 rpm for 10 min) and then activated under vacuum at 130 °C for 12 h.

Mechanochemistry of HKUST-1. HKUST-1 particles were synthesized *via* a

[3] REC = guest@MOF assembley resulting from encapsulation during the structural reconstruction of the MOF

manual grinding process. ∼560 mg of $Cu(NO_3)_2 \cdot 3H_2O$ [copper(II) nitrate trihydrate] (3.0 mmol) and ∼420 mg H_3BTC [benzene-1,3,5-tricarboxylic acid] (2.0 mmol) were combined in the agate mortar and manually ground for 10 min. The product was washed with methanol and separated by centrifugation (8000 rpm for 10 min). The product of this synthesis produced an overall yield of ∼100 mg of MOF.

5-FU@HKUST-1 systems preparation. Two 5-FU@HKUST-1 systems were synthesized as follows. For the (one-pot) *in situ* encapsulation of 5-FU, an analogous procedure to the preparation of pristine HKUST-1 was followed with the addition of ∼540 mg of 5-FU (3.0 mmol) during the grinding process, producing the 5-FU@HKUST-1_IN[4] particles. *Ex situ* encapsulation of 5-FU was performed by immersion of pre-activated HKUST-1 in a saturated methanolic 5-FU solution under continuous stirring for 48 h. The drug-loaded 5-FU@HKUST-1_EX[5] particles were separated by centrifugation. Pristine HKUST-1 and drug loaded samples were washed by centrifugation (8000 rpm for 10 min) with methanol and then activated at 90 °C for 12 h in a vacuum oven. The amount of 5-FU used was selected to maintain a 2:3 molecular ratio of H_3BTC:5-FU to maximize the deprotonation of the organic ligands by the drug molecules and to favour the formation of a highly crystalline host framework (as discussed in Chapters 4 and 5)

3.2 MOF and MOF/Polymer preparation for SR-microFTIR

MOF powder samples. Pre-synthesized HKUST-1 and 5-FU@HKUST-1_IN powder samples, together with 5-FU powder (used as acquired from Fisher Scientific, UK), were dispersed in methanol and drop casted onto the ZnSe window (substrate) for SR-microFTIR measurements (Figure 3.2). 5-FU@HKUST-1_IN were prepared according to *in situ* encapsulation approach described in Section 3.1.

[4] IN = guest@MOF assembley produced *via in situ* encapsulation
[5] EX = guest@MOF assembley produced *via ex situ* encapsulation

MOF/PU samples. Polyurethane (PU) solution was prepared by dissolving poly [4,4'-methylenebis(phenyl isocyanate)-alt-1,4 butanediol/di(propylene glycol)/polyurethane] pellets (purchased from Sigma Aldrich and used without further alterations) in THF for 24-48 hours until complete dissolution of polymer pellets. 85 wt.% MOF/PU composites integrating 5-FU@HKUST-1, HKUST-1 (corresponding to wt.% Equation 3.1) and pristine PU composites were produced by dispersion of a certain amount of previously synthesized MOF particles in a small amount of THF (30 mg of MOF per 1 mL of THF) before their incorporation into the PU-THF solution. The dispersion was performed by a combination of sonication (5 min) and magnetic stirring (5 min, 80 rpm). The set of samples used in the SR-microFTIR experiments were designed to provide a meaningful response during the relatively short period of time allocated on the synchrotron (i.e. maximizing the loading of 5-FU@HKUST 1 powder in the composite).

14 wt.% 5-FU/PU membrane was produced by following an analogous procedure. This strategy, reported by Cohen *et al.* [167], has proven to be a versatile approach for the preparation of homogeneous MOF/polymer composites. Subsequently the membranes were fabricated by drop casting the solution onto the substrates (one drop of ∼40 µL), inclined at an angle of 60°, allowing it to flow until the edge of the substrate (Figure 3.2). The drop casting procedure was done at room temperature with subsequent evacuation of samples at 65 °C for the removal of remaining solvents.

$$\text{MOFwt.\%} = \frac{\text{m}_{\text{MOF}}}{\text{m}_{\text{MOF}} + \text{m}_{\text{PU}}} \times 100\% \tag{3.1}$$

where m_{MOF} is the weight of MOF nanoparticles (dispersed in THF) and m_{PU} is the weight of PU (pellets dissolved in THF).

3.3 Materials characterization

3.3.1 Powder X-ray diffraction (PXRD)

The powder samples were analyzed by PXRD using the Rigaku MiniFlex diffractometer with a Cu Kα source (1.541 Å). Diffraction data were collected from 3° to 30°,

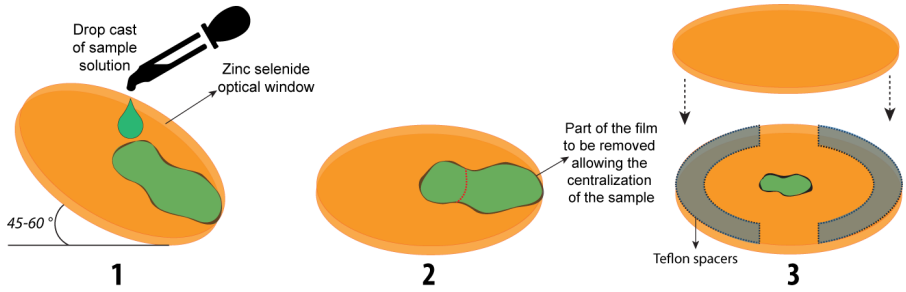

Figure 3.2: MOF and MOF/PU preparation for SR-microFTIR experiments.

using a 0.02° step size and 1.0° min^{-1} step speed for HKUST-1 and drug@HKUST-1 samples and 2θ=3° to 13°, using a 0.02° step size and 0.1° min^{-1} step speed for MIL-100 (Fe), drug@MIL-100, and polymeric composite samples. The diffraction patterns were then normalized with respect to the most intense peak and used for phase identification, except for decomposition studies in which the absolute intensity was used to analyze the decomposition of materials.

3.3.2 Thermogravimetric analysis (TGA)

TGA was performed using TGA-Q50 (TA instruments). Approximately 4 mg of each sample were placed in a platinum pan (maximum volume 50 µL) and heated from 50 °C to 500-650 °C. The measurements for MOF samples were performed at a heating rate of 10 °C.min^{-1} and under a dry nitrogen flow of 40 mL.min^{-1}. The measurements for drug@MOF samples were conducted under an air flow of 40 mL.min^{-1} to ensure complete decomposition of the guest molecules and accurate guest loading determination.

The drug loading was calculated from the TGA analysis *via* Equation 3.2:

$$\text{Drug loading(wt.\%)} = \frac{m_{loss(drug@MOF)} - m_{loss(MOF)}}{m_{loss(drug@MOF)}} \quad (3.2)$$

where $m_{loss(drug@MOF)}$ and $m_{loss(MOF)}$ represent the mass lost in the selected temperature range for the drug@MOF and the MOF samples, respectively.

TGA was selected as the main technique to estimate drug loading in order to establish a direct comparison between the different encapsulation strategies herein applied (*i.e.* conventional solution impregnation *versus in situ* mechanochemical encapsulation). Conventionally used techniques, such as UV spectroscopy, could

not be broadly applied for drug loading estimation in all samples due to the varied nature of the different encapsulation techniques.

3.3.3 Scanning electron microscope (SEM) and atomic force microscope (AFM)

Analysis of the surface topography of the MOF particles and composite membranes was carried out by SEM and AFM imaging. SEM images were obtained using Carl Zeiss EVO LS15 at 15 keV under high vacuum. AFM was performed using the Veeco Dimension 3100 AFM under the tapping mode, equipped with a Tap300G silicon probe with a resonance frequency of 30 kHz (spring constant 40 Nm^{-1}, tip radius $<$ 10 nm).

3.3.4 Specific surface area measurements

The Brunauer-Emmett-Teller (BET) specific surface areas of samples were determined from nitrogen adsorption-desorption isotherms at 77 K, measured with Quantachrome Nova 1200. The isotherms were obtained using a ⌀9 mm sample cell containing 60-100 mg of samples under study. The degassing temperature was 150 °C for MIL-100(Fe) samples and 90 °C for HKUST-1 samples during sample activation under vacuum.

3.3.5 Attenuated total reflectance Fourier transform infrared spectroscopy (ATR-FTIR)

ATR-FTIR spectra were acquired at room temperature with a Nicolet iS10 FTIR spectrometer with an ATR sample holder. The spectra were collected in the range of 650-2000 cm^{-1} with a resolution of 0.5 cm^{-1} and normalized with respect to the most intense vibrational peak to facilitate comparison across the different samples under study.

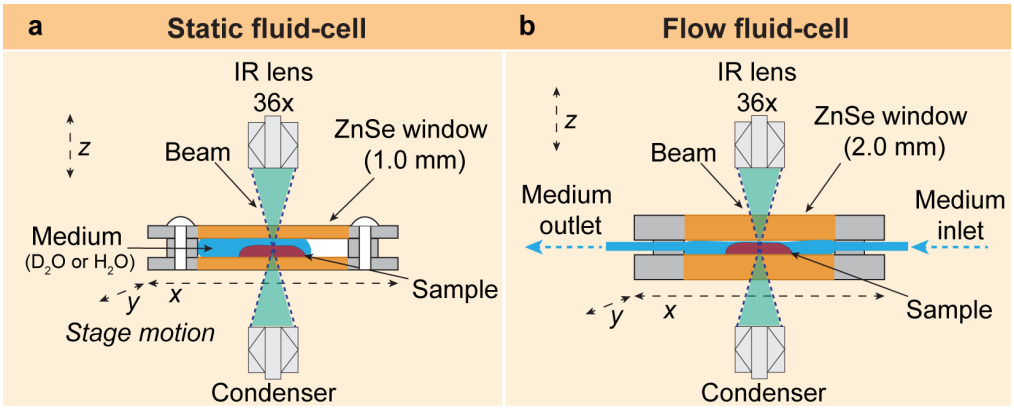

Figure 3.3: Experimental setup for SR-microFTIR spectroscopy measurements. Schematic of the (a) static and (b) flow-cells and sample arrangement (not to scale).

3.3.6 Synchrotron radiation Fourier transform infrared microspectroscopy (SR-microFTIR)

SR-microFTIR spectra were acquired in Beamline B22 MIRIAM at the Diamond Light Source (Oxfordshire, UK). The spectra were collected in transmission mode by employing an IR microscope (Bruker Hyperion 3000) equipped with a 36× objective lens, from spot areas delimited by the IR microscope slits comprising a ~10×10 µm^2. The spectra of different regions in the sample were collected in the mid IR region encompassing the broad spectral range of ~650-4000 cm^{-1}, using a spectral resolution of 4 cm^{-1} and 256 scans resulting in data acquisition time of ~40 s per spectrum. Two key experiments have been carried out with different variations of the *in situ* experimental setups. Because of the difference in the frequency of the bending modes of deionized water (H_2O) and deuterated water (D_2O) and the overlap of these modes with important vibrational bands of the drug molecule present in the drug@MOF samples, the monitoring of drug release was carried out with a combination of experiments performed in H_2O and D_2O to fully establish the evolution of drug peaks within the broad spectral range.

Static-cell. For static-cell SR-microFTIR measurements (Figure 3.3a), powder and polymer composite samples were loaded into a customized liquid cell, sandwiched between two zinc selenide (ZnSe) circular windows (1 mm thickness, ⌀= 25 mm) separated by a 10-µm thick Teflon spacer. Liquid measurements were conducted with the addition of 2 µL of deuterated water (D_2O), placed within the cell confinement.

The sample under study was only partially in contact with D_2O in order to enable the collection of dry and wet backgrounds as reference spectra. The IR spectra were collected in the range of 650-4000 cm^{-1}, at a resolution of 4 cm^{-1}.

Flow-cell. A range of pre-experimental tests were performed in order to optimize the use of the dynamic flow-cell to enable SR-microFTIR measurements (Figure 3.3b). Samples were loaded into a liquid cell sandwiched between two ZnSe circular windows (2-mm thick, ⌀= 25 mm), separated by a 10-µm thick gold spacer. Measurements were performed with provision for medium exchange (D_2O and deionized water (H_2O)) *via* an automatic syringe pump. A flow-rate of 100 µL.min^{-1} was used to fully replace media in the sample chamber throughout the experiment. For measurement in D_2O flow, the media were allowed to flow for approximately 25 minutes before starting data collection, thus allowing the system to reach D-H equilibrium. The enhanced magnification allowed data collection in a 10×10 $µm^2$ scanning window, obtaining good signal-to-noise through the aqueous media. Data were collected in the range of 650-4000 cm^{-1}, at a resolution of 4 cm^{-1}. The dynamic flow study permitted the acquisition of over 180 individual IR spectra at different timepoints, over a period of ∼2 hours. By taking advantage of the possibility to maintain sample to media contact for long periods of time in the flow environment, spectra with high signal to noise ratio and excellent spectral quality were acquired.

SR-microFTIR data processing. Pre-processing of spectral data was performed using the OPUS software version 7.2 (Bruker Optics). FTIR spectra was initially truncated to separate the spectral region of 700-1800 cm^{-1}. "Concave rubberband correction" from the OPUS software was applied with 4000 points followed by max-min normalization in the range of 1680-1760 cm^{-1} (polyurethane peak).

3.3.7 Inelastic neutron scattering (INS) spectroscopy

Inelastic neutron scattering. INS measurements were performed using the TOSCA [168] spectrometer at the ISIS Pulsed Neutron and Muon Source, Ruther-

ford Appleton Laboratory (Chilton, UK). The high resolution (ΔE/E$\sim$1.25%) and broadband (0-4000 cm^{-1}) spectra of each sample ($\sim$1 g) were acquired at $\sim$10 K. TOSCA is an indirect geometry time-of-flight spectrometer where a pulsed, polychromatic beam of neutrons collides with the sample at a distance of $\sim$17 m from the source. The neutrons scattered from the sample were Bragg reflected by a pyrolytic graphite analyzer, while higher order reflections beyond (002) were blocked by a cooled (T < 30 K) Beryllium filter in order to define the final energy. Neutrons with final energy of $\sim$32 cm^{-1} were passed towards the detector array composed by thirteen ^{3}He tubes with effective length of 250 mm. Five banks were located in forward direction (scattering angle $\sim$45°) and five in backwards direction ($\sim$135°). The use of a low final energy translated into a direct relationship between energy transfer (ET, cm^{-1}) and momentum transfer (Q, $Å^{-1}$) such that ET $\approx 16Q^2$. Energy transfer and spectral intensity, *i.e.* S(Q, ω), were then obtained using the Mantid software [169]. Each sample was wrapped in 4 cm × 4.8 cm aluminium sachet and placed into a 2.0 mm spaced flat aluminium cell, which was sealed with indium wire. Sample preparation and cell loading into the cell took place in a glovebox to avoid moisture uptake by the sample. To reduce the effect of the Debye-Waller factor on the experimental spectral intensity and allow comparison with the theoretical spectra, the sample cell was cooled to $\sim$10 K by a closed cycle refrigerator (CCR). The INS spectra were collected under vacuum over a duration of 4-6 hours. The neutron guide upgrade of the TOSCA spectrometer, completed in 2017, has increased the neutron flux at the sample position by as much as 82 times. This upgrade improves the performance through faster measurements and by reducing the required sample mass [170].

Calculation of area under INS curve. The Integrate Gadget in OriginPro was used to perform the numerical integration on the INS spectra to determine the area under the curve of specific vibrational modes. The range of data was selected to include the peaks of the vibrational modes of interest, using the x axis as the baseline.

3.3.8 *Ab initio* density functional theory (DFT) calculations

Composite methods in CRYSTAL 17.[6] DFT calculations of HKUST-1 and its complexes with 5-FU (*i.e.* 5-FU@HKUST-1 adducts A-D) and water were performed using the *ab initio* periodic code CRYSTAL17 [171]. A PBEsol0-3c composite method recently devised for cost effective solid state calculations was employed. All calculations referred to a ferromagnetic unit cell. Model structures were fully optimized by means of an unconstrained relaxation of both lattice parameters and atomic positions. Interaction energies were computed through a supermolecule approach and for adduct A and D they were validated against the more costly benchmark Becke, 3 parameter, Lee Yang Parr (B3LYP) method [172, 173] augmented with the D3 dispersion correction including two- and three-body terms [174] and combined with a TZVP basis set [175] (*i.e.* B3LYP-D3(ABC)/TZVP). Because of the good tradeoff between cost and accuracy of the PBEsol-3c method, vibrational frequencies at the Γ point and their IR intensities were calculated on the optimized geometry by means of a mass-weighed Hessian matrix, obtained by numerical differentiation of the analytical nuclear gradients with a three-point formula [176, 177]. The Pack-Monkhorst/Gilat shrinking factors for the reciprocal space sampling were set to 2, corresponding to 6 to 8 k-points at which the Hamiltonian matrix was diagonalized. The condition for the Self-Consistent Field (SCF) convergence was set to 10^{-8} and 10^{-10} Hartrees during structure optimization and vibrational frequency calculations, respectively.

Gaussian. DFT calculations to determine the theoretical vibrational spectra of H_3BTC, 5-FU, caffeine, aspirin, and the Fe-ASP complex (tetraaquosalicylatroiron (III) complex) were performed using the Gaussian software [178]. The vibrational calculations were carried out at the B3LYP level of theory and 6-31G basis set. The DFT output files of these molecules were used to generate their INS spectra

[6] The calculation performed in this section were developed in collaboration with scientists Professor Bartolomeo Civarelli and Ph.D. student Lorenzo Donà (University of Turin), developers of the composite DFT method used in the calculations of 5-FU@HKUST-1 assemblies.

using the Mantid software [169] through the AbINS extension [179]. During the spectrum generation a total cross section was considered with a quantum order events number of 1.

3.3.9 PXRD peaks height and FWHM of ATR-FTIR peaks

The Integrate Gadget in OriginPro software was used to perform the numerical integration on the PXRD patterns to determine the full width at half maximum (FWHM) of two of the most intense diffraction peaks in the MIL-100 (Fe) samples (*i.e.* $2\theta = 4°$ and $11°$) that correspond to the (022) and (357) planes. The range of data was selected to include the diffraction peaks of interest, using the (horizontal) diffraction angle axis as the baseline. The same approach was used for obtaining the FWHM of ATR-FTIR vibrational bands. To facilitate the comparison between the effect of the reconstruction process (Chapter 6, the ratio between the peak heights [(022):(357)] was taken and the FWHM values were normalized against the largest value presented within a set of samples.

3.3.10 Crystallinity determination from FWHM measurements

Assessment of changes in sample crystallinity was performed by analysing changes to the FWHM of selected diffraction peaks, used as an indication of peak sharpening and/or broadening.

This methodology has been applied to examine MIL-100 (Fe) host stability during the time period of drug release experiments (Chapter 4) and the effect of the reconstruction of MIL-100 (Fe) samples (Chapter 6) as a function of the sample immersion time.

The Scherrer law allows one to determine the size of the crystalline domains D [180]:

$$D = \frac{K \times \lambda}{\Delta \times \cos \times \theta} \tag{3.3}$$

where λ is the wavelength, Δ = FWHM, K is a constant, and θ is the diffraction angle of the corresponding diffraction peak.

As the samples might present different particle sizes and different packing configurations, the best representation to establish the cross comparison of such samples was the "crystallinity" defined as:

$$\text{Crystallinity} = \frac{D_{\text{initial}}}{D_{\text{final}}} \tag{3.4}$$

Then:

$$\text{Crystallinity} = \frac{\frac{K\times\lambda}{\Delta_{\text{initial}}\times\cos\times\theta}}{\frac{K\times\lambda}{\Delta_{\text{final}}\times\cos\times\theta}} = \frac{\Delta_{\text{final}}}{\Delta_{\text{initial}}} \tag{3.5}$$

A small adaptation of Equation 3.5 was used to calculate the crystallinity of samples that have undergone water reconstruction, as described in Chapter 6:

$$\text{Crystallinity} = \frac{D_x}{D_{\text{initial}}} \tag{3.6}$$

with x referring to the different immersion times

3.3.11 Acidity measurements of water reconstruction solutions

The pH values of the immersion solutions recovered after the water reconstruction process (Chapter 6) were determined using a Fisherbrand pH indicator paper stick that was compared against a pH scale and across all the samples in the study.

3.3.12 Proton acceptor/donor sites and electrostatic potential surface map determination

The proton acceptor/donor sites present in the guest drug molecules (*e.g.* 5-FU, caffeine, and aspirin) were determined using BIOVIA Discovery Studio [181]. The electrostatic potential (ESP) surface maps of drug molecules were generated using GaussView. During the map generation, the electron density was calculated from a Total SCF density with isovalue of 0.000400 electrons per unit volume (au^3).

3.3.13 Fabrication of pellets

MIL-100 (Fe) samples. Pellets were prepared on a manual hydrostatic press (Specac) with a die diameter of 13 mm and under a constant axial force that varied from 0.5 to 10 ton. Each pellet was produced using 175 mg of the MIL-100 (Fe) material.

HKUST-1 samples. Pellets were prepared on a manual hydrostatic lab press (Specac) with a stainless steel die of 13 mm and under a constant axial force of 1 ton. The nominal density of each pellet was determined by weighing each one of them and dividing this quantity by its nominal volume. The dimensions of the pellets were determined using a micrometer. Each pellet was produced using 175 mg of the HKUST-1 material.

3.3.14 Drug release experiments

Release of 5-FU from MIL-100 (Fe). Experiment to study of the 5-FU release from MIL-100 (Fe) MG and VG (Chapter 4) were carried out at 37 °C with magnetic agitation, using phosphate buffered saline (PBS, 0.04 M pH 7.4) to simulate physiological conditions. 10 mg of the drug-loaded samples were immersed in 5 mL of PBS. At different incubation times, 1 mL of supernatant was recovered by centrifugation and replaced with the same volume of fresh PBS at 37 °C. The amount of 5-FU released was determined by UV-Vis adsorption spectroscopy at 266 nm. The accurate concentration of 5-FU released was determined using the calibration curve expressed in Equation 3.7, which was constructed by correlating the absorbance and concentration of various measured 5-FU solutions.

$$A = 0.05275 \times c \tag{3.7}$$

where A is the measured absorbance and the c the concentration (in $\mu g.mL^{-1}$) of the collected aliquot

Release of 5-FU from HKUST-1. To perform the release of the 5-FU from the host HKUST-1 described in Chapter 7, 20 mg of the drug-loaded samples were

immersed in abundant MeOH and constantly stirred at room temperature for a period of 72 hours. The material was recovered and washed by centrifugation twice with methanol (8000 rpm for 10 min) to guarantee complete removal of guest molecules present in the final composite sample. Being HKUST-1 a water sensitive MOF, MeOH was applied for the release studies to avoid the decomposition of the structure by the release media (*e.g.* water or PBS). This allowed to study the isolated effects of the release of the guest molecule on structure of the host MOF

3.3.15 Contact angle measurements

Contact angle measurements were performed by the addition of small droplets of deionized water (10 µL) on top of HKUST-1/PU and PU membranes. A monochrome CMOS camera (6×6 µm^2) integrated with a Navitar 12× zoom lens was used to obtain images used for the measurements. ImageJ software [182] was then applied to compute the contact angle values.

3.3.16 Swelling experiments

Swelling behavior of composites was measured by a gravimetric method. PU and HKUST-1/PU membranes were immersed in deionized water at room temperature until the swelling equilibrium was reached. Samples were removed and blotted with filter paper to remove the excess water on the surface, and then weighed. The immersion time and drying procedure were repeated until the weight of the swollen samples became constant. The swelling ratio and the swelling water content as a percentage were defined by Equation 3.8:

$$\text{Swelling ratio}\% = \frac{\mathrm{m_{swollen}} - \mathrm{m_{dry}}}{\mathrm{m_{dry}}} \times 100\% \tag{3.8}$$

where $\mathrm{m_{swollen}}$ is the mass of the swollen polymer/composite and $\mathrm{m_{dry}}$ is the mass of the dry polymer/composite collected before immersion into water.

Se a educação sozinha não transforma a sociedade,
sem ela tampouco a sociedade muda.

Educação não transforma o mundo.
Educação muda as pessoas.
Pessoas transformam o mundo.

— Paulo Freire

4

The mechanochemical confinement of 5-FU within MIL-100 (Fe)

Contents

4.1 Background and motivation

Although the mechanochemical synthesis of pristine MIL-100 (Fe) material has been demonstrated before, one-pot encapsulation of guest molecules into this Fe-based MOF *via* mechanochemistry is less understood. Specifically, for MOFs such as MIL-100 (Fe) possessing highly accessible coordinatively unsaturated metal sites (CUS) that act as a strong binding site for guest drug molecules, the solvent free encapsulation method can eliminate the competition drug molecules might face against the polar solvents for the active binding sites, as explained in more details in Chapter 2.

This chapter reports the detailed fabrication of a drug-encapsulated MIL-100 (Fe) systems, designated as 'drug@MIL-100', using an annealing assisted mechanochemical approach. Two different methods were employed (*i.e.* manual grinding (MG)

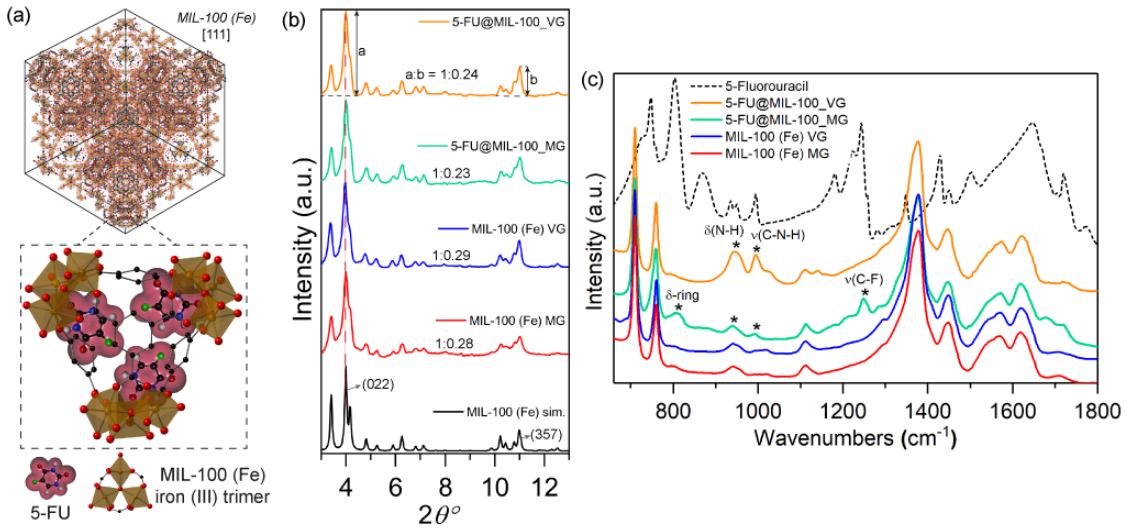

Figure 4.1: *In situ* encapsulation of 5-FU and structural characterization of MIL-100 (Fe) and drug@MOF systems. (a) Schematic representation of guest–host interaction of 5-FU to the unsaturated iron sites of MIL-100. (b) Normalized PXRD patterns of MIL-100 (Fe) and drug-loaded counterparts. (c) Normalized FTIR spectra of MIL-100 (Fe) samples measured in ATR mode. Asterisks mark the position of the 5-FU peaks. Colour scheme: iron in orange, carbon in black, oxygen in red, hydrogen in white, nitrogen in purple, and fluorine in green.

vs. automated vortex grinding (VG)) to accomplish the *in situ* encapsulation of guest 5-FU within the pores of the MIL-100 (Fe) host framework, producing the 5-FU@MIL-100 systems. The results in this chapter demonstrate this method feasibility as a facile solvent free one-pot strategy. The manual and vortex grinding strategies were adapted from Han *et al.* [63] and Stojakovic *et al.* [74], previously used for the synthesis of pristine MOF, to enable *in situ* drug encapsulation, not yet demonstrated in the former studies.

4.2 Examination of 5-FU@MIL-100 systems

Figures 3.1a-g in Chapter 3 illustrate the *in situ* encapsulation process. The samples fabricated are described in Table 4.1. For the manual grinding approach, all reactants (*i.e.* organic linker H_3BTC, iron nitrate, and 5-FU) were manually ground using a mortar and pestle. A customized holder was designed and 3D-printed to couple a standard polypropylene container to an automatic vortex mixer (Figures 3.1b-e). This setup allowed the application of a higher number of rotations

Table 4.1: MIL-100 manual and vortex grinding derived samples - description and details

	Samples	**Synthesis method**	**Guest**
Mechanochemical method	MIL-100 (Fe) MG MIL-100 (Fe) VG	Manual grinding Vortex grinding	- -
In situ encapsulation	5-FU@MIL-100_MG 5-FU@MIL-100_VG	Manual grinding Vortex grinding	5-Fluorouracil

per minute *via* the vortex mixer, increasing the number of collisions induced between the solid reactants and the stainless-steel spheres (Figures 3.1f-g).

Figure 4.1a shows a schematic representation of the encapsulation of the drug guest molecules, yielding guest-host interaction of 5-FU with the CUS located on the iron trimers of MIL-100 (Fe) host to form the $C = O \cdots Fe$ coordination. Indeed, similar interactions involving organic molecules binding to the CUS of MIL-100 (Fe) have been reported [105]. Figure 4.1b shows the PXRD patterns of pristine MIL-100 (Fe) and drug@MIL-100 systems, confirming the successful synthesis of crystalline MIL-100 (Fe) through both annealing assisted mechanochemical approaches. The effect of the different synthesis/encapsulation technique on the material crystallinity has been monitored *via* analysis of the PXRD data. The evolution of the relative peak intensity corresponding to the two most intense Bragg peaks [*i.e.* (022):(357) ratio] (Figure 4.1b) and the changes in the FWHM of the (022) peak at 2θ=4° (Figure 4.2) have been monitored as a function of the grinding technique used. The ratios of the relative intensity of the (022):(357) planes showed consistency across all samples. There was no significant difference found between the pristine samples of MIL-100 (Fe) MG and MIL-100 (Fe) VG. Similar results were observed for the drug-loaded counterparts. However, further assessment of the samples crystallinity *via* analysis of the FWHM of the (022) peak (Figure 4.2a) shows that 5-FU@MIL-100_MG and 5-FU@MIL-100_VG present relatively sharper peaks (higher crystallinity) compared with their pristine counterparts. This might be attributed to the role played by 5-FU molecules in the deprotonation of the H_3BTC organic linkers due to the presence of proton acceptor sites in 5-FU (see Figure 4.2b).

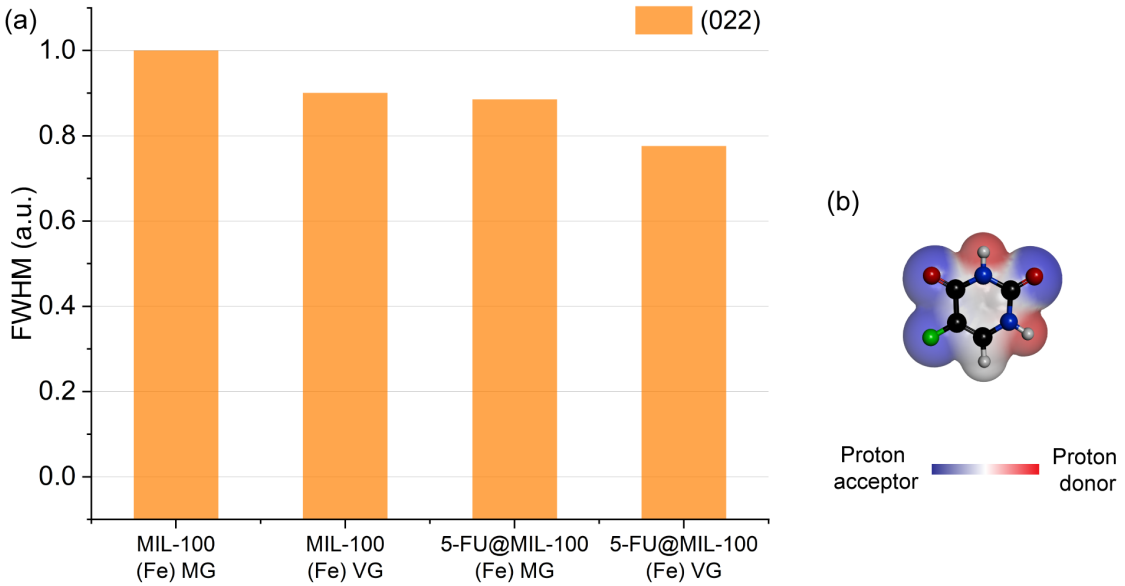

Figure 4.2: (a) FWHM values of (022) peak of MIL-100 (Fe) MG and MIL-100 (Fe) VG and their drug-loaded counterparts. (b) Schematic representation of 5-FU molecules showing the proton acceptor and donor sites. Colour code: O in red, C in black, H in grey, N in navy blue, and F in green.

This effect is examined and discussed in deeper details in Chapter 5. The PXRD patterns of the MG and VG samples before and after the annealing step are shown in Figure 4.3. The comparison reveals that the mechanical stress from grinding was responsible for the formation of MIL-100 (Fe) structure, while the subsequent heat treatment by annealing only helps to enhance the sample crystallinity. Noteworthy, these results are different from those reported by Kuroda *et al.* [183]. who used the annealing step after mechanochemical grinding (of a coordination polymer) to yield a new phase with a different crystalline structure. Conversely, the basic structure of MIL-100 (Fe) has remained unaltered after annealing Figure 4.3).

The ATR-FTIR spectra of all the samples are presented in Figure 4.1c. The vibrational data allow us to investigate in detail the chemical structure of the samples in the mid-IR region. The characteristic bands of MIL-100 (Fe) (*i.e.* ν(C−H) in the organic linker at 707 cm^{-1} and 760 cm^{-1}, ν(O−C−O) and δ(O−H) at 1371 cm^{-1} and 1441 cm^{-1}, and ν(C=O) in the carboxylic group at 1623 cm^{-1} were detected[1] [184], confirming retainment of the chemical bond integrity after 5-FU loading by both encapsulation techniques. The collection of the spectrum

[1] Molecular vibrations: δ = in-plane bending, ν = symmetric stretching

of the unencapsulated 5-FU enabled the identification of the drug bands in the drug@MOF systems from experiments and theory (DFT calculations) (Figure 4.4). The spectra of 5-FU@MIL-100_MG and 5-FU@MIL-100_VG display changes in the regions of 800-1300 cm^{-1} and 1680-1800 cm^{-1}, in comparison to the spectrum of pristine MIL-100 (Fe), confirming the presence of drug molecules in the drug@MOF assemblies. However, there are salient differences between the spectra of the two different drug-loaded systems, indicating distinct guest-host interactions resulting from the two encapsulation techniques. In 5-FU@MIL-100_VG spectrum the modes at 945 cm^{-1}, 995 cm^{-1}, and 1140 cm^{-1} associated with δ(N−H) and ν(C−N−H), respectively, are evident. In contrast, in the 5-FU@MIL-100_MG spectrum these modes are more suppressed while the vibrations at 810 cm^{-1}, 1210 cm^{-1}, and

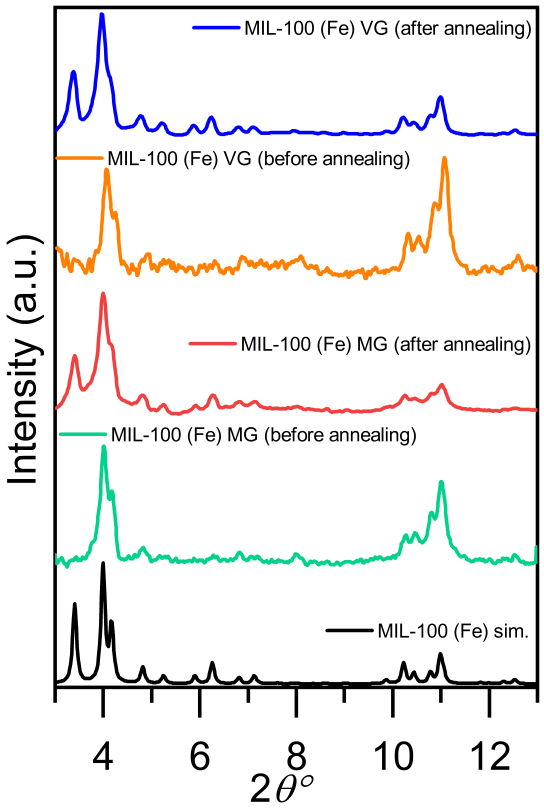

Figure 4.3: Normalized PXRD patterns of MIL-100 (Fe) before and after the annealing step after the mechanochemical grinding (MG and VG) process. The contrast between the patterns before and after annealing for the manually and vortex ground samples revealed that the mechanical stress (from grinding) have resulted in framework formation prior to the annealing step. Annealing is therefore used to enhance material crystallinity.

$1247\,\mathrm{cm}^{-1}$, associated with δ-ring and ν(C−F), respectively, are apparent (see Figures 4.4 and 4.5 for details and schematic representation of the vibrational modes). These observations suggest the higher efficacy of the manual grinding encapsulation process towards the successful confinement of 5-FU drug molecules within the MIL-100 (Fe) pores.

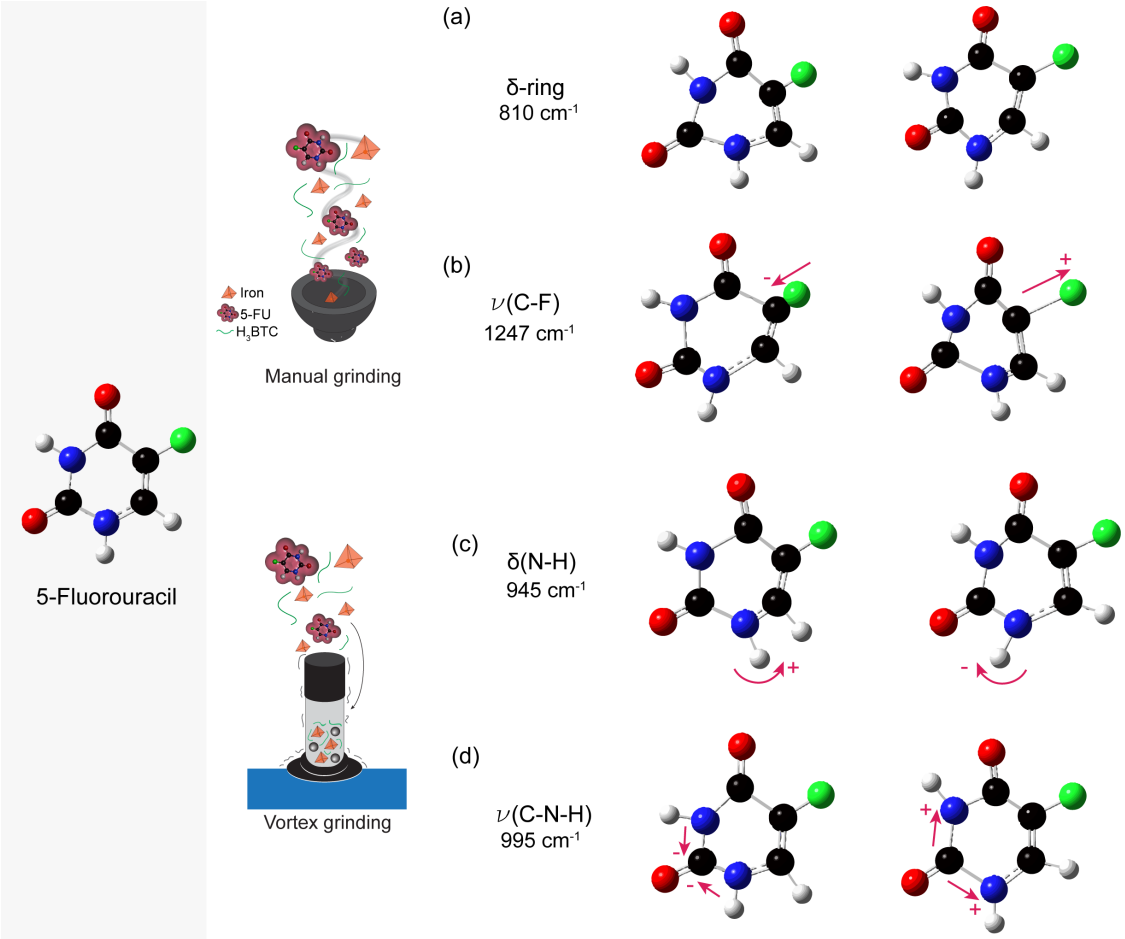

Figure 4.4: Schematic representation of the molecular vibrational modes of 5-FU at different wavenumbers. (a) Bending mode of the uracil ring. (b) Stretching of C−F bond. (c) Bending of N−H bond. (d) Stretching C−N−H bonds. Arrows indicate the directions of the collective deformations with +/- amplitudes computed by DFT (B3LYP level of theory and 6-31G basis set).

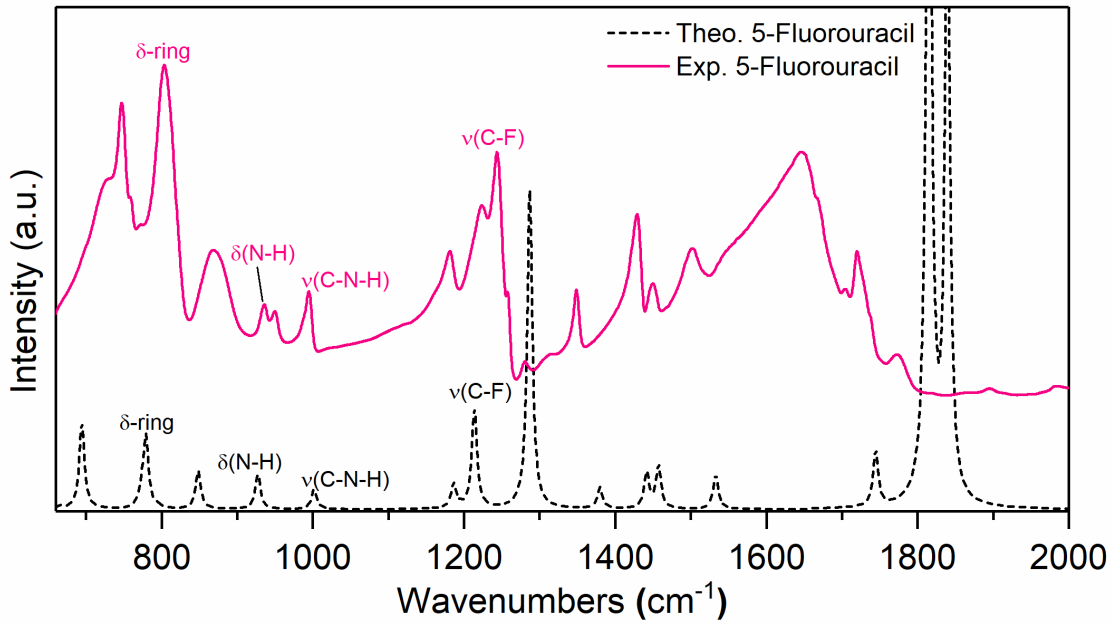

Figure 4.5: Comparison between theoretical and experimental vibrational spectra of 5-FU used to identify the specific vibrational modes marked in the plot. A reasonably good match between the experimental and theoretical spectra was observed, where the mismatch between the theoretical and experimental frequencies is a common shift resulting from the *ab initio* calculations.

4.3 5-FU loading and resulting guest-host interactions

The level of guest encapsulation was evaluated by BET surface area from N_2 adsorption isotherms (Figure 4.6a) and further estimated by TGA using Equation 3.2 (Figure 4.6b). The surface area of the pristine MIL-100 (Fe) MG ($793\,m^2\,g^{-1}$) and MIL-100 (Fe) VG ($753\,m^2\,g^{-1}$) are in good agreement with the values of other reported mechanochemically synthesized MIL-100 (Fe) samples (Table 4.2). The drug loading registered by TGA for 5-FU@MIL-100_MG and 5-FU@MIL-100_VG were determined to be 20.2 wt.% and 18.3 wt.%, respectively. The BET surface area of the drug@MOF samples was found to be greatly reduced to $333\,m^2\,g^{-1}$ (reduction of 58 %) and $697\,m^2\,g^{-1}$ (reduction of 7.5 %), respectively. These results further indicate that although the vortex grinding is very effective for the synthesis of pristine MIL-100 (Fe), the manual grinding process appears to be more efficient for the encapsulation of 5-FU within the MOF pores. As indicated by the

Table 4.2: Comparison between the BET surface area of drug@MIL-100 fabricated *via* MG, VG, and conventional methods

Samples	**Synthesis method**	**BET surface area** ($m^2\,g^{-1}$)	**Ref.**
MIL-100 (Fe) MG	Manual grinding	793	This Chap.
MIL-100 (Fe) VG	Vortex grinding	753	This Chap.
5-FU@MIL-100_MG	*in situ* encapsulation	333	This Chap.
5-FU@MIL-100_VG	*in situ* encapsulation	697	This Chap.
MIL-100 (Fe)	Mechanochemistry (liquid assisted grinding - ball mill)	1033	[65]
	Mechanochemical (kitchen grinder)	255	[73]
	Solvothermal (high temperature)	1836	[185]
	Solvothermal (high pressure and temperature)	1750	[186]
	Solvothermal (high pressure and temperature)	1223	[187]
	Solid state synthesis (high pressure and temperature)	110	[188]

ATR-FTIR vibrational data, the hypothesis is that the C = O ⋯ Fe coordination is established between MIL-100 (Fe) CUS and 5-FU molecules. Additionally, the adjacent hydrogens in 5-FU can interact *via* hydrogen bonds with the oxygen atoms surrounding the iron trimers. The C = O ⋯ Fe coordination, therefore, can strongly limit the displacement of nitrogen atoms, thus suppressing the δ(N−H) and ν(C−N−H) modes (proximity to the binding oxygen atom) in 5-FU@MIL-100_MG (Figure 4.1c). Conversely, the identification of drug molecule "free" motions in the 5-FU@MIL-100_VG spectrum suggests that 5-FU molecules could be adsorbed onto the external surfaces of the MIL-100 (Fe) crystals by weaker intermolecular interactions (*e.g.* π-π interactions between 5-FU and BTC linker).

An increase in the thermal stability of the drug-loaded samples was observed when compared to MIL-100 (Fe) MG and MIL-100 (Fe) VG samples. Table 4.3 showcases in detail the decomposition process of MIL-100 (Fe) and drug@MOF samples acquired from TGA. An increase in the initial decomposition temperature of 5-FU@MIL-100_MG and 5-FU@MIL-100_VG in comparison to MIL-100 (Fe) MG

and MIL-100 (Fe) VG (increase of ∼30 °C) was observed. An increase in the rate of decomposition between drug-loaded and pristine MIL-100 (Fe) host was noted. This corresponds to different decomposing amounts as a function of temperature due to the presence of the encapsulated drug molecules. The presence of the guest molecules is also reflected in the temperature at which half of the material has decomposed.

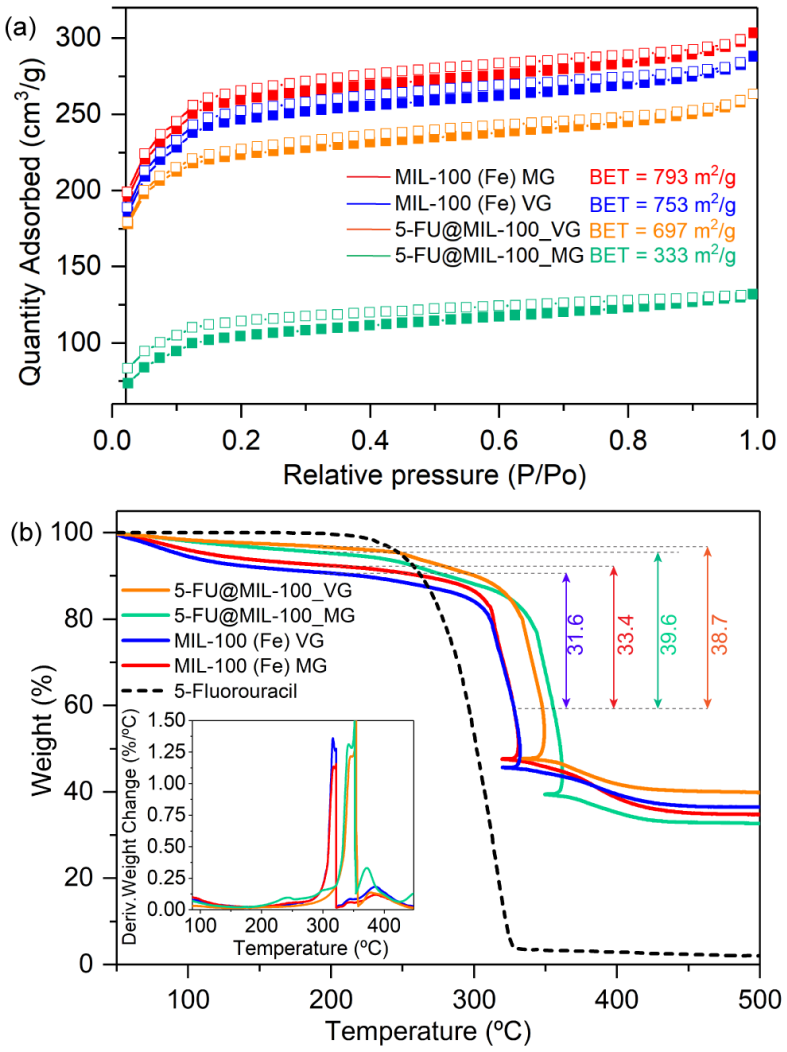

Figure 4.6: Nitrogen adsorption (filled symbols) and desorption (empty symbols) isotherms of MIL-100 (Fe) and drug-loaded counterparts. The comparison between samples under study shows clear decrease in accessible surface area upon guest encapsulation. (b) TGA plots of MIL-100 (Fe) samples and drug@MOF composites showing material decomposition as a function of increasing temperature. Insets show the derivative weight change with respect to temperature. Note that the decrease of the temperature in the TGA plots over 300 °C is due to highly exothermic process related to the departure of the organic linker, exceeding the set program temperature. The furnace temperature thus decreases in order to follow the initial program temperature [13].

Table 4.3: Analysis of thermal decomposition of MIL-100 (Fe) and drug-loaded samples produced *via* MG and VG

	Initial decomposition temperature	Maximum rate of decomposition	Temperature of half decomposition	Final residue (at 660°C)
MIL-100 (Fe) MG	290 °C	-0.266 %/°C	331 °C	36.6%
MIL-100 (Fe) VG	290 °C	-0.238 %/°C	332 °C	34.6%
5-FU@MIL-100_MG	320 °C	-0.429 %/°C	349 °C	32.6%
5-FU@MIL-100_VG	321 °C	-0.403 %/°C	360 °C	38.2%

Meanwhile, the final residue has presented very little change, demonstrating the total decomposition of drug molecules and confirming the accuracy of drug loading calculations. The increase in the thermal stability of drug-loaded samples can be attributed to the improved crystallinity (structural robustness) presented by the drug@MOF systems in comparison to their pristine counterparts (see Figure 4.1b).

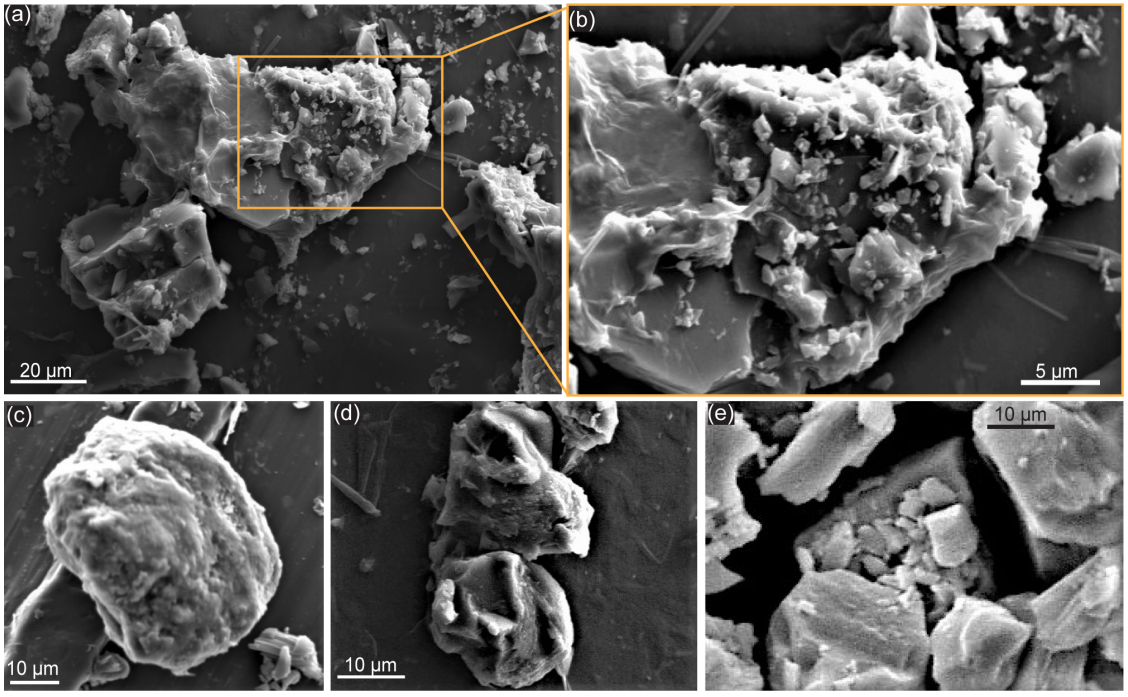

Figure 4.7: SEM images of as synthesized (a-b) MIL-100 (Fe) MG and (c-e) MIL-100 (Fe) VG. The micrographs display a non-uniform particle distribution, due to the grinding nature of the synthesis method leading to particles aggregation.

The samples morphology was examined *via* SEM as presented in Figures 4.7-4.8. SEM images show no significant changes upon 5-FU loading. The nature of the

grinding process appears to favour the formation of fragmented aggregates of MIL-100 (Fe) crystals, with a non-uniform distribution (*ca.* 2-30 µm). Moreover, the low surface potential presented by MIL-100 (Fe) particles (8.6 mV) causes insufficient electrostatic repulsion forces to prevent the aggregation of the particles [189]. Further discussion about the particles aggregation will be presented in Chapter 6.

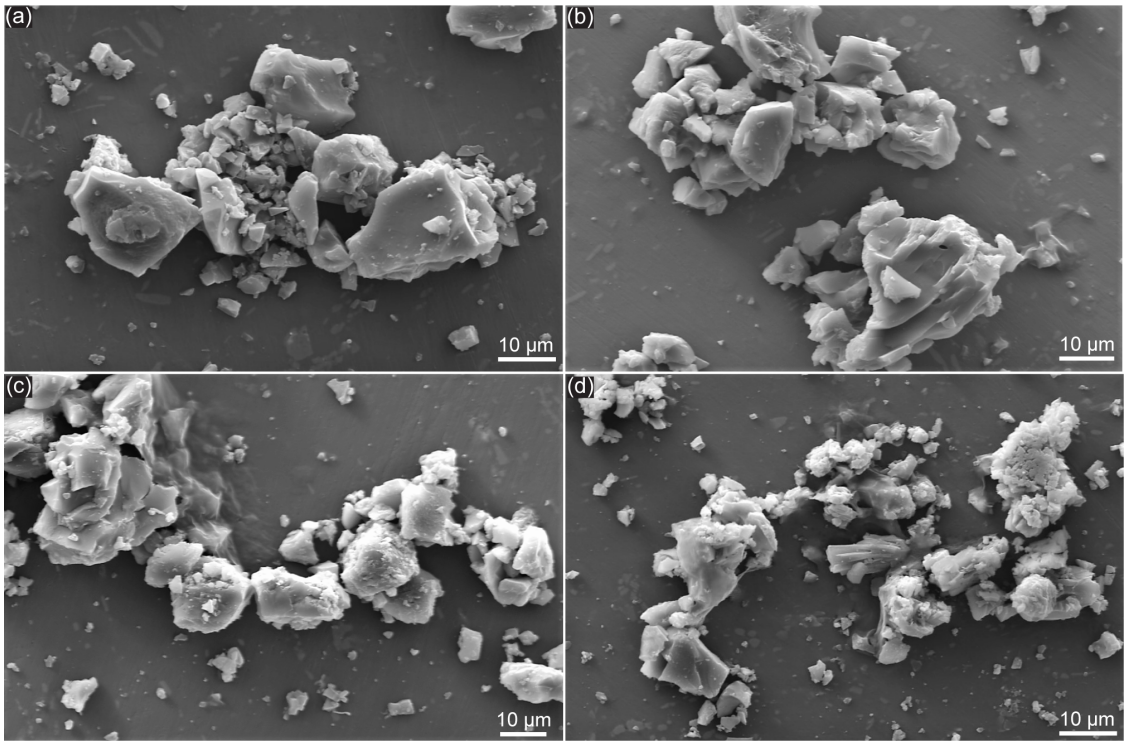

Figure 4.8: SEM images comparing as synthesized (a) MIL-100 (Fe) MG, (b) MIL-100 (Fe) VG, and drug-loaded samples. (c) 5-FU@MIL-100_MG, and (d) 5-FU@MIL-100_VG. The micrographs display the absence of morphological changes upon drug encapsulation.

4.4 Evaluating the kinetics of 5-FU release from 5-FU@MIL-100 assemblies

Figure 4.9 shows the results of the 5-FU release from MIL-100 (Fe), conducted in a phosphate buffered saline (PBS) of pH 7.4, used to simulate physiological conditions. The evolution of the 266 nm absorption band of 5-FU was tracked using UV-Vis to construct a calibration curve (Figures 4.9a-b) used to determine the cumulative release of the drug molecules. Drug release profiles obtained for the drug-loaded samples are presented in Figure 4.9c.

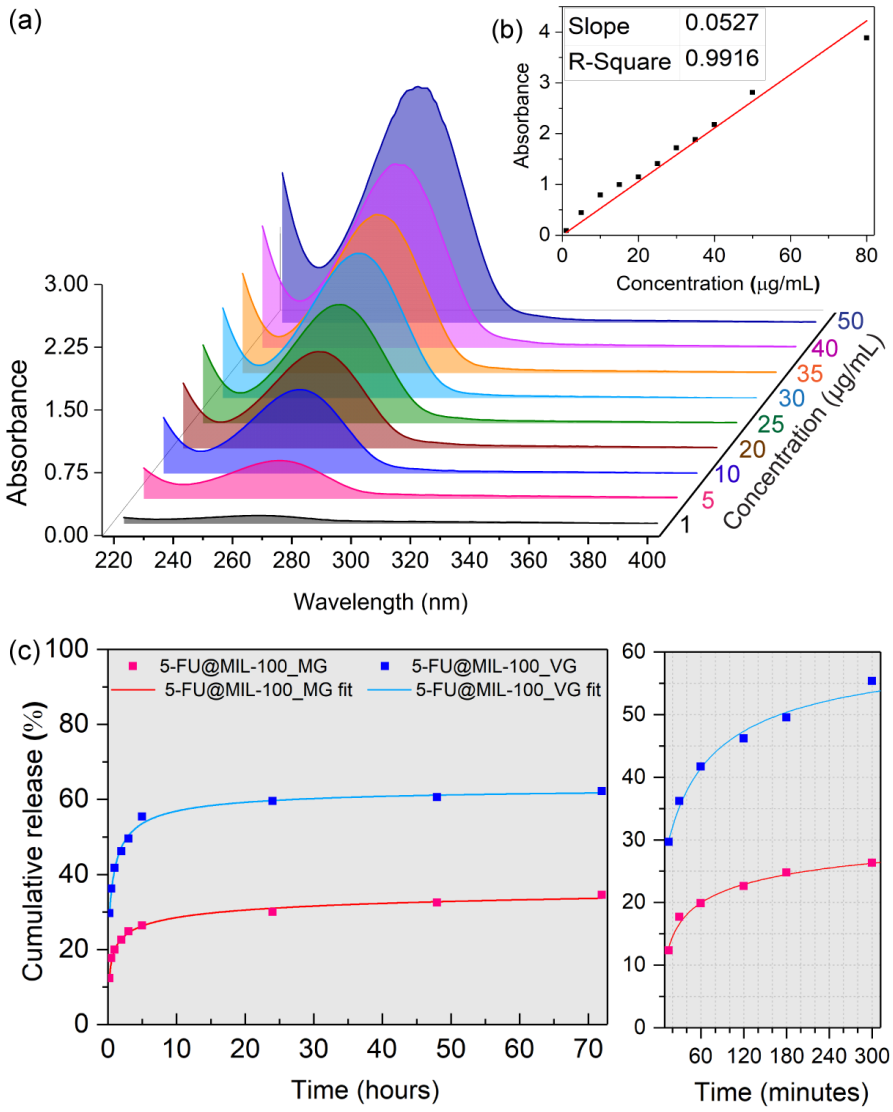

Figure 4.9: Drug release studies. (a) UV-Vis spectra collected for 5-FU solutions at different concentrations, highlighting the 5-FU band at 266 nm used to establish the calibration curve presented in (b). The calibration equation was used to translate the UV-Vis absorbance into the cumulative drug release. (c) Drug release profiles of 5-FU@MIL-100_MG (red trace fit) and 5-FU@MIL-100_VG (blue trace fit) revealing the cumulative release over a period of 72 hours.

Interestingly, 5-FU@MIL-100_MG shows a significantly slower release of 5-FU. During the first release stage (initial 5 hours), drug release of ∼60% was detected from the VG sample in comparison to ∼26% released from the MG counterpart. The percentages were calculated by considering the total loading of the drug in the drug@MOF systems, determined by TGA. The second release stage (*i.e.* up to 72 hours) happened in a considerably slower fashion, which stabilized

Table 4.4: Fitting equations for the 5-FU drug release profiles from 5-FU@MIL-100

Sample	Fitted equation	R^2
5-FU@MIL-100_MG	$5\text{-FU}(\%) = 48.83 - \frac{158.00}{1+41305.08x^{1/6.00}}$	0.99121
5-FU@MIL-100_VG	$5\text{-FU}(\%) = 64.02 - \frac{43.08}{1+1.98x^{1/1.68}}$	0.99364

after 48 hours. 62% and 34% of the 5-FU loaded into 5-FU@MIL-100_VG and 5-FU@MIL-100_MG were released, respectively. Fitted curves of the release profiles revealed that the release process follows a generalized hyperbolic curve for both samples, with high coefficients of determination (R^2) (Table 4.4).

The stability of the host framework during the release experiments was assessed to ensure the ongoing stability of the host material during the release of the guest molecules (Figures 4.10 and 4.11). The initial assessment of MIL-100 (Fe) stability during drug release experiments has been performed *via* analysis of UV-Vis spectrometry and material crystallinity.

As displayed by Figure 4.10a, PXRD patterns of the host collected after the release experiment display no signs of MIL-100 (Fe) degradation. The FWHM

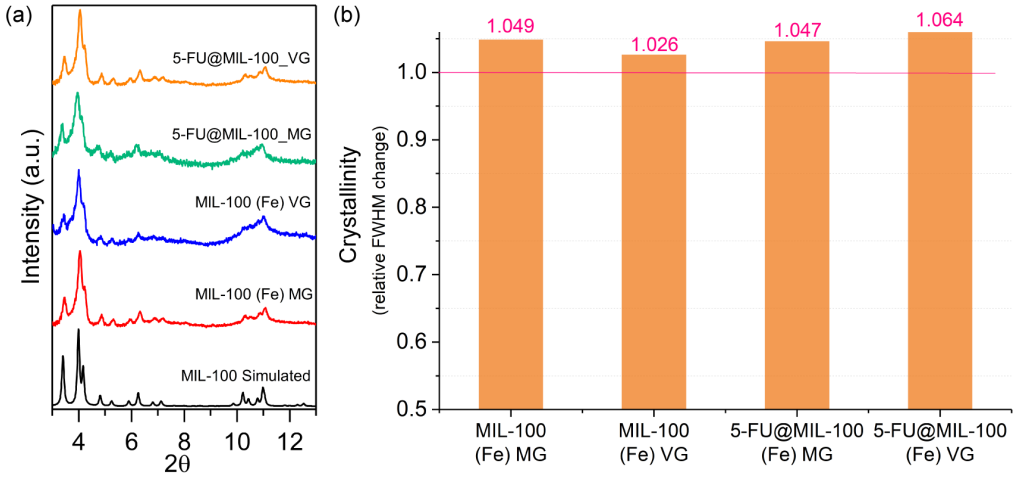

Figure 4.10: Analysis of diffraction data of MIL-100 (Fe) samples after release experiments. (a) PXRD patterns of pristine MIL-100 (Fe) and drug loaded samples, displaying that the materials hold good crystallinity after immersion in PBS during the release experiments. (b) Relative FWHM of samples, the ratio was taken in relation to the initial value for the FWHM of the samples before the release experiments.

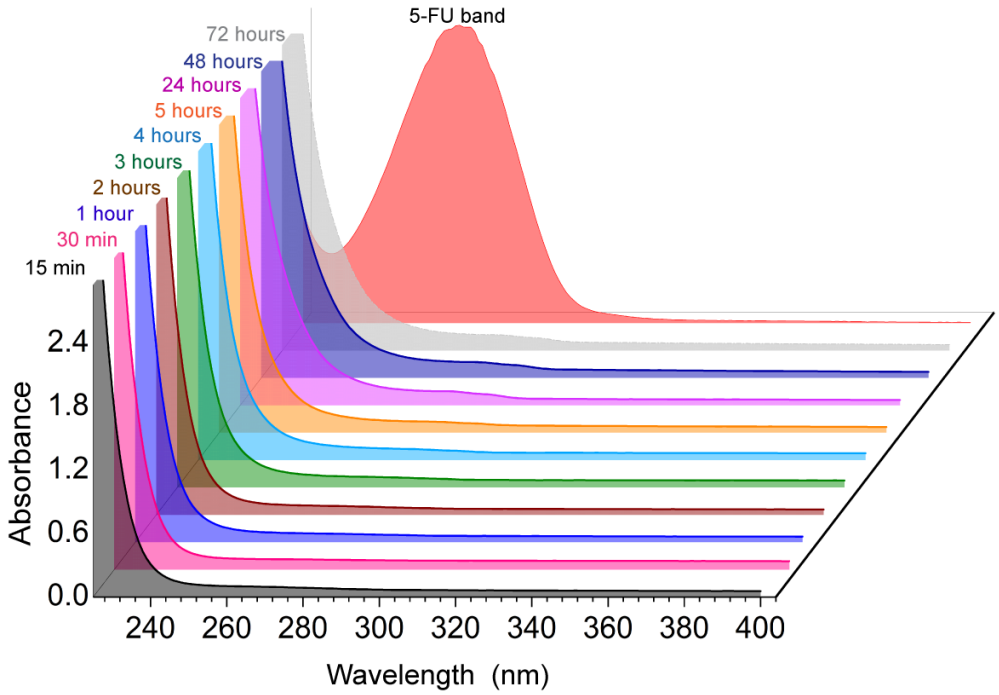

Figure 4.11: UV-Vis spectra of the supernatant of MIL-100 (Fe) in PBS showing the good stability of MIL-100 (Fe) host during the release of 5-FU guest. The contrast with 5-FU spectrum (red trace) highlights the absence of any absorbance associated with decomposition of MIL-100 (Fe) that could interfere with the band at 266 nm used to track the release of 5-FU.

measured before and after the release process shows a slight broadening of the (022) peak (Figure 4.10b) (*i.e.* minor changes to material crystallinity as calculated *via* Equation 3.5). However, no evidence of amorphization was found. The stability of the host framework was further assessed *via* UV-Vis spectroscopy. As shown in Figure 4.11, the supernatant of MIL-100 (Fe) in PBS does not present strong absorbance in the spectral region where the characteristic 5-FU band at 266 nm is found, used for monitoring the drug release. No significant changes to the UV-Vis spectra of MIL-100 (Fe) were observed over a 72 hour period. The data from the 5-FU drug release study indicate that the manual grinding technique provides a more effective nanoconfinement of 5-FU within the pores of MIL-100 (Fe), while the vortex grinding approach appears to yield weaker guest-host interactions due to adsorption of guest molecules outside the cages of the host framework. Even though we can observe a plateau in the drug release profiles for both samples, there is a clear discrepancy in the kinetics and speed of the delivery Specifically exemplified by the

large difference in the amount released in the first hour (doubling that of the manual ground sample). A slower diffusion at the molecular level throughout the pores is usually associated with strong guest-host interactions [13]. Consequently, the slower release kinetics of 5-FU from 5-FU@MIL-100_MG could indicate stronger guest-host interactions, further supporting the notion revealed by analysis of vibrational data from ATR-FTIR (5-FU interactions CUS through $C = O \cdots Fe$ coordination).

The conditions for the establishment of such strong coordination seem to be favoured by the continuous and homogenous grinding provided by the manual grinding approach but disfavoured by the localized collisions that occur during the vortex grinding process. In the manual grinding, the mechanical deformation induced is a result of the shear stress created in the regions of sliding contact between the pestle, reactants, and mortar. It creates a 2D distribution of the grinding force over a larger surface area, which might facilitate the improved formation of multiple MIL-100 SBUs. Since the concept behind an *in situ* encapsulation technique is based on the host cages rapidly forming around the guest molecules, the hypothesis is that the multiplicity of SBU simultaneously and adjacently formed on the manual grinding process could explain the detected higher effectiveness of this method in achieving the confinement of 5-FU guest molecules. In contrast, for the vortex grinding setup used herein (Figure 3.1g), the simultaneous formation of adjacent SBUs is expected to be relatively smaller due the reduced region of contact from the normal stress generated by the impact collision of stainless-steel balls. The results indicate that drug confinement is less effective for the latter process. A continuous shear stress is also present in twin-screw extrusion (TSE) methods, proven to be efficient for the fabrication of different MOF materials [190]. Based on these results, the manual grinding process has been selected as the primary methodology for the fabrication of *in situ* encapsulation of drug molecules in host MOFs, to be described in the next chapters.

4.5 Summary and conclusions

This chapter has demonstrated that mechanochemistry offers new opportunities for the fabrication of complex MOFs such as MIL-100 (Fe), and more specifically it is a promising strategy for the nanoconfinement of guest drug molecules within the MOF porosity. By leveraging two mechanochemical based techniques (*i.e.* manual and vortex grinding) for the encapsulation of 5-FU in MIL-100 (Fe), modifications in the vibrational behaviour of each drug@MOF assembly were detected, revealing the underpinning intermolecular interactions arising from each encapsulation technique. The outcomes are reflected in the release kinetics of 5-FU from the MIL-100 (Fe) host, in which the stronger guest-host interactions of the manually ground system led to a slower release of 5-FU. Finally, it was found that while the vortex grinding approach demonstrated is very effective for the fabrication of pristine MIL-100 (Fe), a manual grinding/milling route yields the enhanced incorporation of drug guest molecules in the MOF pores. Nevertheless, the limitations imposed by the manual grinding process herein utilized, specifically in terms of reproducibility, need to be acknowledged. It is difficult to ensure the same standards (e.g. grinding force and speed) are applied to each individual synthesis when the process is highly dependent on the person executing it. However, the advantages presented by this method and its simplicity (*i.e.* low associated cost and easy accessibility) could be exploited for the rapid fabrication of different guest@host systems in lab scale. The findings herein reported illustrate how different mechanochemical environments can give significantly different outcomes in the quest of fabricating a drug@MOF composite system.

With guns you can kill terrorists,
with education you can kill terrorism

— Malala Yousafzai

5

Drug molecules modulator effect during their encapsulation in MIL-100 (Fe)

Contents

5.1 Background and motivation

To reduce the environmental impact of the synthesis and improve the biocompatibility of the product, many efforts have been put into engineering greener and faster synthetic methods for the fabrication of MOF structures [191]. Thus far, there have been several different reported approaches for the fabrication of MIL-100 (Fe), as described in detail in Chapter 2. Since its discovery [192], procedures have evolved from methods with long reaction time under harsh conditions (*i.e.* high temperature and high pressure coupled with the use of hydrofluoric acid (HF) and concentrated nitric acid (HNO_3)) to high pressure solvent-free procedures [63,

193–195]. On the one hand, the use of toxic substances, such as mineralizing agents, to improve the crystallinity of MIL-100 (Fe) material could affect its applicability in the biomedical field [196]. On the other hand, improved crystallinity is crucial as it determines the material long-range periodicity and impacts its porosity and structural robustness. Today, one of the biggest challenges remains to optimize the synthetic procedures to yield highly crystalline MIL-100 (Fe) under mild conditions, *i.e.* avoiding the use of HF, toxic agents, high pressure and temperature. The harsh methods available not only jeopardize its potential bio-oriented applications, but also limit its scalability to enable commercial production. Developing new synthetic strategies is, however, an enduring challenge due to the high complexity of the skeletal and topological structure of large-pore MOFs such as MIL-100 (Fe). The ideal synthetic route should concomitantly allow the facile encapsulation of different 'guest' drug molecules whilst preserving the structural properties and porosity of the 'host' MIL-100 (Fe) framework.

This chapter expands the results presented in Chapter 4 and presents the application of the mechanochemical *in situ* method for the fabrication of various drug-encapsulated MIL-100 (Fe) systems, designated as 'drug@MIL-100_IN', under ambient conditions. The 'modulating' effect of the drug molecules: 5-FU and caffeine (CAF) on facilitating the formation of highly crystalline MIL-100 (Fe) was reported, akin to the role of a conventionally applied mineralizer. Conversely, aspirin (ASP) leads to the formation of an amorphous MOF phase. The vibrational dynamics of the drug@MOF_IN systems were studied *via* INS, performed at the TOSCA spectrometer [168, 170], gaining further insights into guest-host interactions through the collective vibrational modes. Understanding the underpinning molecular interactions is key to controlling the capture and release of confined drug molecules from the MOF host carriers. The feasibility of this method as a facile one-pot self-assembly strategy was demonstrated, shedding new light on environmentally friendly approaches towards the fabrication of the MIL-100 (Fe) framework and its guest-encapsulated composite systems.

Table 5.1: MIL-100 *in situ* encapsulation samples - description and details

	Samples	**Synthesis method**	**Guest**
Mechanochemical method	MIL-100 (Fe)	Manual grinding	-
Mechanochemical + in situ modulator method	5-FU@MIL-100_IN CAF@MIL-100_IN ASP@MIL-100_IN	Manual grinding *in situ*	5-Fluorouracil Caffeine Aspirin
Commercial grade	Fe-BTC (Basolite F300)	Solvothermal	Used as acquired

5.2 Structural analysis of MIL-100 (Fe) and drug@MIL-100_IN systems

Figure 5.1a schematically illustrates the *in situ* encapsulation process through mechanochemistry. All bulk reactants were manually ground in a mortar and pestle to produce the samples presented in Table 5.1. The crystallinity of the resulting materials was examined *via* PXRD (Figure 5.1b). MIL-100 (Fe) together with 5-FU and caffeine-loaded systems were successfully synthesized. For 5-FU@MIL-100_IN and CAF@MIL-100_IN, the main Bragg diffraction peaks below $2\theta = 5°$ are apparent and a highly ordered structure is confirmed. Conversely, in ASP@MIL-100_IN the sharp Bragg peaks at low diffraction angles are completely absent, substituted by broad peaks located around 2θ = 4-5°, 6-8°, and 10-12°, indicating the amorphous character of this sample. The structural differences between these samples were further assessed by analyzing the relative peak intensity of the (022):(357) planes (*i.e.* the two most intense diffraction peaks in MIL-100 (Fe) pattern) as a function of drug molecule present during the grinding step of the synthesis. Complementarily, the FWHM values of the (022) peak were also calculated (Figure 5.2) and are accompanied by the non-normalized PXRD patterns (Figure 5.3).

By carefully contrasting the as-synthesized MIL-100 (Fe) and its drug-loaded counterparts, two conclusions can be drawn. First, from Figure 5.1b, it is possible to detect the deficiencies in the crystalline structure of pristine MIL-100 (Fe).

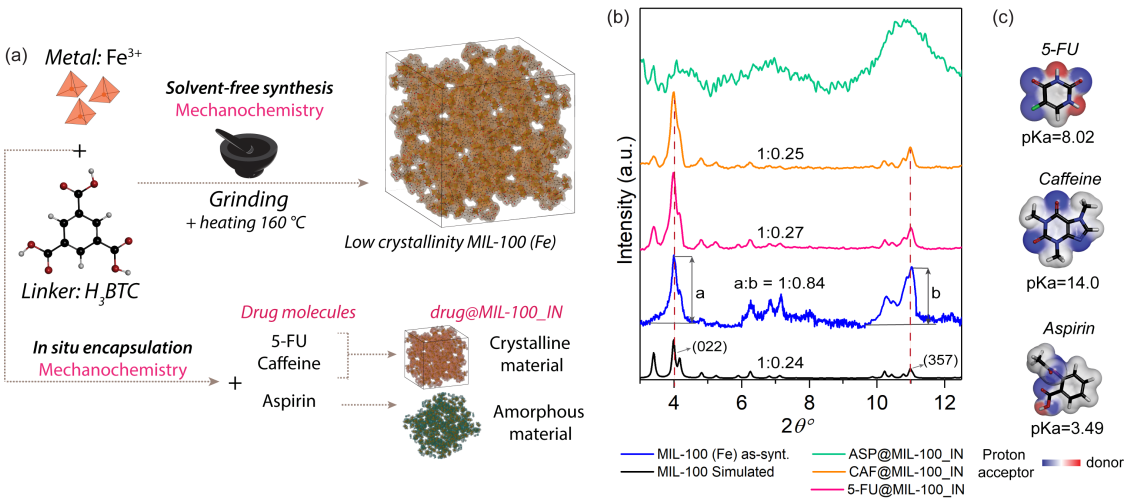

Figure 5.1: Mechanochemical encapsulation and structural characterization of MIL-100 (Fe) and drug@MOF_IN systems. (a) Schematic summarizing the manual grinding process used to fabricate the drug@MIL-100_IN samples (the suffix "IN" denotes guest encapsulation by *in situ* approach) and the respective effect of the different drug molecules on the framework crystallinity. (b) Normalized PXRD patterns of MIL-100 (Fe) and drug@MIL-100_IN assemblies showing the ratios between diffraction planes to assess the material crystallinity. The ratio was not computed for the aspirin loaded system due to the amorphous nature of this sample. (c) Guest molecules of 5-FU, caffeine, and aspirin, highlighting their proton acceptor and donor sites. Colour scheme: iron in orange, carbon in black, oxygen in red, hydrogen in white, nitrogen in purple, and fluorine in green.

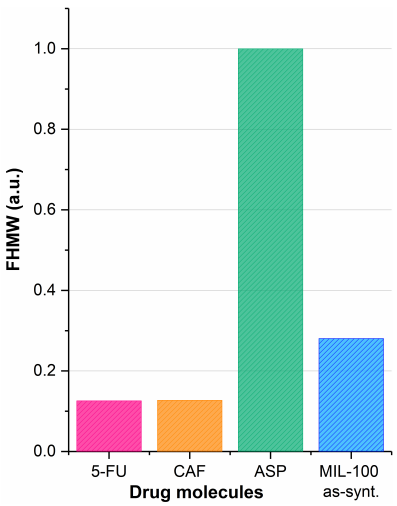

Figure 5.2: FWHM used to assess the sharpening of the (022) peak in the drug@MIL-100_IN systems, contrasting the templating effect of the different guest drug molecules being used. The plot shows the strong negative effect that aspirin has on the material crystallinity in comparison to 5-FU and caffeine molecules, which favor the formation of highly crystalline MIL-100 (Fe). To facilitate the comparison, the values have been normalized in relation to the highest FWHM value in the set of samples.

The absence of the diffraction peak at $2\theta = 3.4°$, the small relative intensity of the (022):(357) planes (*i.e.* ratio of 1:0.84), and the slight broadness of the (022) peak (Figure 5.2) all point to the partial formation of the crystalline framework. Likewise, the reduced relative intensity of the Bragg peaks at the small diffraction angles ($2\theta < 5°$) implies a weak long-range ordering of the MIL-100 (Fe) structure (Figure 5.3). Figure 5.4 shows the ATR-FTIR spectra of all the samples. The typical vibrational bands of MIL-100 (Fe) (*i.e.* ν(C−H) in the organic linker at $\sim$707 cm^{-1} and $\sim$760 cm^{-1}, ν(O−C−O) and δ(O−H) at $\sim$1371 cm^{-1} and $\sim$1441 cm^{-1}, and ν(C=O) in the carboxylic group at $\sim$1623 cm^{-1}) were detected in all samples, confirming the retainment of chemical bonds integrity [1][184]. The presence of the vibrational band at $\sim$1720 cm^{-1} in the spectrum of the MIL-100 (Fe), assigned to the stretching of carboxyl group present in the acidic form of the organic linker

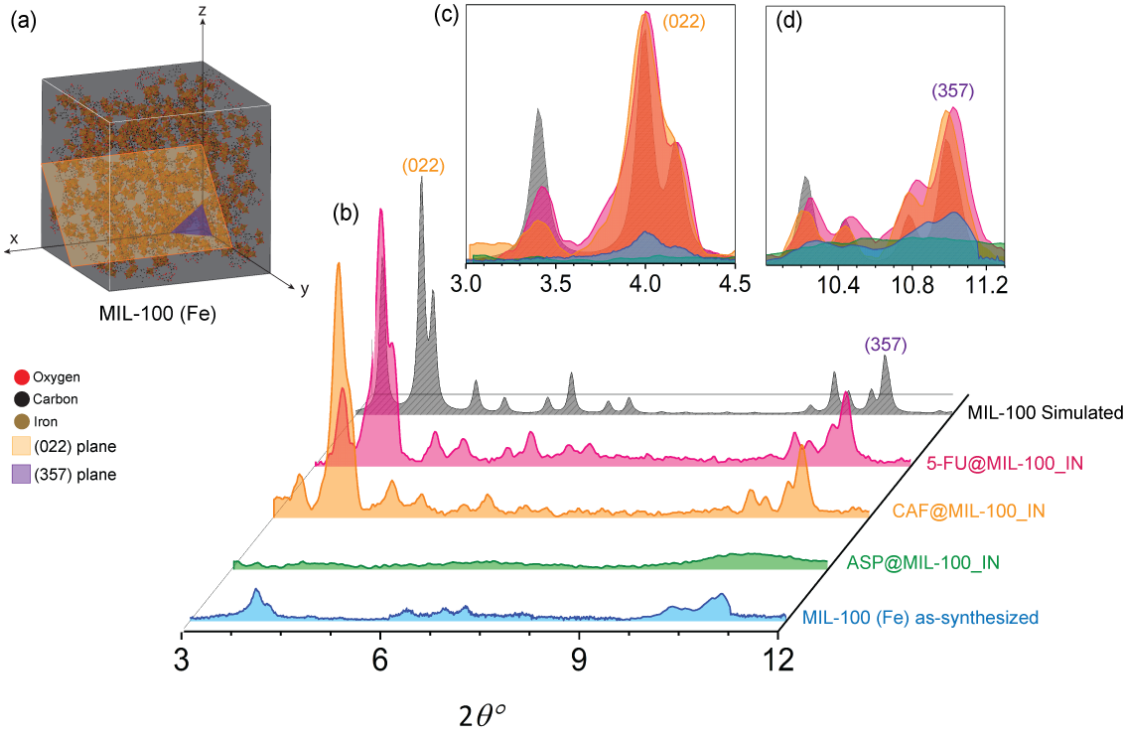

Figure 5.3: Diffraction data of MIL-100 (Fe) and drug@MIL-100_IN systems. (a) Schematic representation of MIL-100 (Fe) crystal structure. (b) Evolution of the absolute intensity of the diffraction peaks (non-normalized) after drug encapsulation, showing the marked improvement in crystallinity in the drug@MIL-100_IN systems in comparison to their pristine counterpart. Overlapping representation of the PXRD patterns with closer look at the peaks at (c) $2\theta = 3°$-$4.5°$ and (d) $2\theta = 10°$-$11.3°$.

[1] Molecular vibrations: δ = in-plane bending, ν = stretching

(*i.e.* H_3BTC), indicates the presence of remaining protonated organic ligand in the structure of MIL-100 (Fe)[194, 197]. Because the full deprotonation of H_3BTC is needed to yield a three dimensional framework with high crystallinity, the incomplete deprotonation of the organic ligand may hinder the complete self-assembly of the SBU. This has resulted in the partially formed (defective) MIL-100 (Fe) mesocages with lower crystallinity (Figure 5.1a).

Secondly, as revealed by the PXRD patterns in Figure 5.1b, *via* the *in situ* strategy, highly crystalline 5-FU@MIL-100_IN (ratio 1:0.27) and CAF@MIL-100_IN (ratio 1:0.25) samples were obtained, while the presence of aspirin resulted in the production of the amorphous ASP@MIL-100_IN product. Contrasting the ATR-FTIR data of MIL-100 (Fe) and drug@MIL-100_IN systems, the sharpening of the band at ∼1355 cm^{-1}, assigned to the stretching of the carboxylate groups present in the BTC organic linker, was observed. The change was characterized by the decrease in FWHM of this band (Figure 5.4). The sharpening by ∼42% and ∼40% was observed for 5-FU@MIL-100_IN and CAF@MIL-100_IN, respectively, suggesting the increase in the structural symmetry of the MIL-100 (Fe) host upon the presence of drug molecules [198]. Conversely, the ASP@MIL-100_IN system remained virtually unchanged (sharpening by ∼4%). The changes to the band at 1355 cm^{-1} were accompanied by the decline in intensity of the band at ∼1720 cm^{-1}. This was quantified by the reduction in the integrated spectral area of this vibrational peak for both 5-FU@MIL-100_IN and ASP@MIL-100_IN systems (Figure 5.4). Such an analysis was not carried out for CAF@MIL-100_IN due to the superposition of the BTC linker band and a vibrational band of caffeine (guest) in the same spectral range. The decline in the intensity of this band implies the decrease in the amount of protonated linker present in the sample.

As the intensity of the diffraction peaks is attributed to the periodic atomic arrangement averaged over the whole polycrystalline sample [199], the total increase in intensity observed in the PXRD patterns of the drug@MIL-100_IN systems in comparison to the as-synthesized MIL-100 (Fe) (Figure 5.3) indicates the increase in long-range ordering of the host MIL-100 (Fe) crystals when 5-FU or caffeine

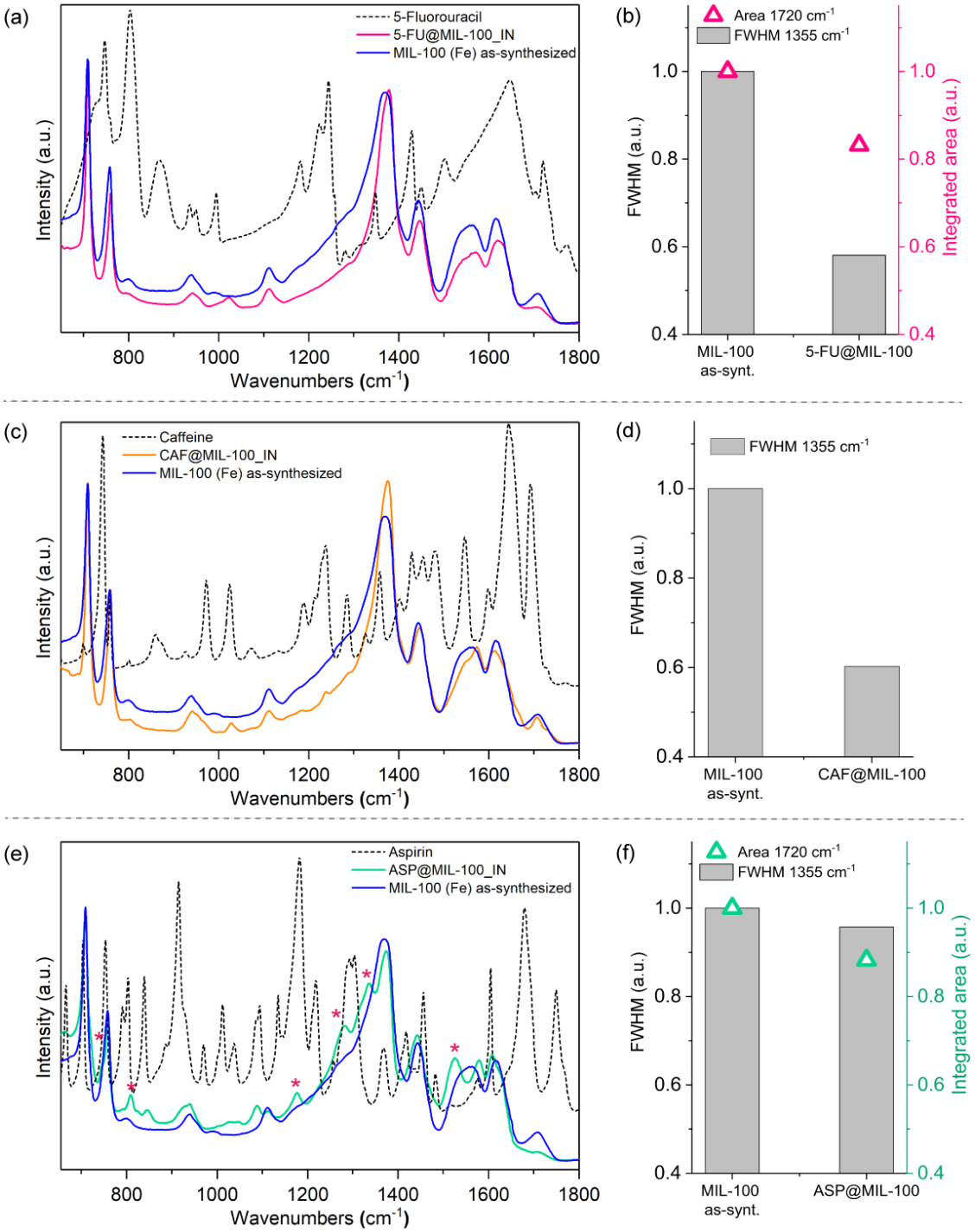

Figure 5.4: Normalized ATR-FTIR spectra of drug@MIL-100_IN samples and FWHM of chosen vibrational bands, displaying the data for (a-b) 5-FU@MIL-100_IN, (c-d) CAF@MIL-100_IN, and (e-f) ASP@MIL-100_IN. For comparison, the IR spectra of the unencapsulated drug molecules are shown in the plots. Asterisks indicate the presence of aspirin-iron complex.

were present during mechanochemical synthesis. As shown in Figure 5.1c, 5-FU, caffeine, and aspirin are molecules possessing proton (H^+) acceptor atoms (especially oxygen and nitrogen), which can potentially facilitate the deprotonation of the H_3BTC organic ligand and aid the formation of MIL-100 (Fe) cages. pKa values are also presented in Figure 5.1c, indicating that among the drug molecules, 5-FU and caffeine are the most likely molecules to act as proton acceptors. Therefore, *via* the *in situ* encapsulation process, 5-FU and caffeine function as 'modulators' by aiding the deprotonation of the organic linkers. This results in formation of highly crystalline MIL-100 (Fe) frameworks, which simultaneously confine the drugs within the mesocages. The templating effect of caffeine on the formation of 3D structures has also been reported [50]. Meanwhile, the high acidity of aspirin molecules (pKa = 3.49) compromises the establishment of the long-range periodicity of the framework and results in the obtained amorphous phase. Strong broadening of the (022) peak was observed when aspirin was present during the *in situ* synthesis (Figure 5.2). This is due to the competition between H_3BTC and aspirin for coordination with the iron ions, resulting in the formation of an amorphous violet aspirin-iron complex (Fe-ASP) known as tetraaquosalicylatroiron (III) complex (Figure 5.5). Vibrational bands attributed to the complex have been identified in the ATR-FTIR spectrum of ASP@MIL-100_IN as shown in Figure 5.6, confirming the complex formation. The nature of these vibrations has been further characterized by DFT calculations and compared with the experimental spectrum presented in Figure 5.6 and Table 5.2.

5.3 Modulator effect of 5-FU and caffeine molecules

To further assess the modulating effect of 5-FU and caffeine, the influence of the drug:H_3BTC molecular ratio on the crystallinity of the resulting material was investigated. To accomplish the complete deprotonation of the organic linker, the dissociation of 3 hydrogen atoms for each H_3BTC molecule is necessary. In principle, both 5-FU and caffeine have the potential to accept 3 protons each, but pKa values

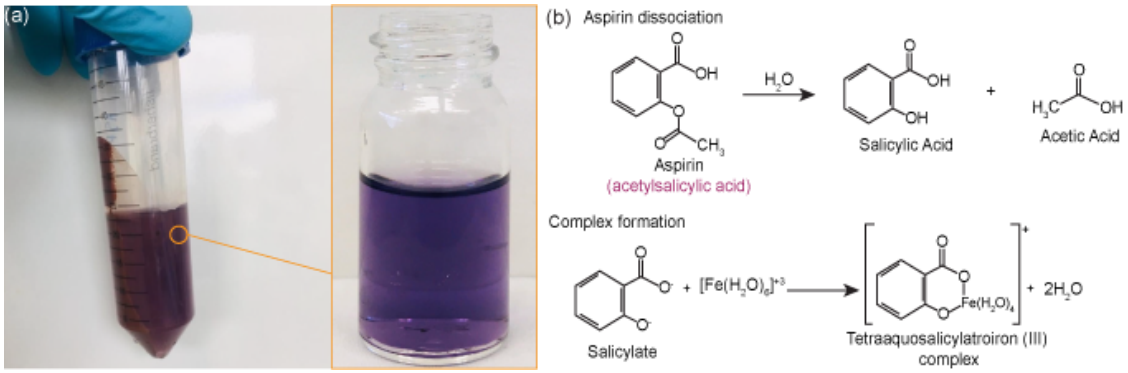

Figure 5.5: (a) Photographs of ASP@MIL-100_IN sample and supernatant collected after the washing step of the synthesis method. The photographs show a distinct purple colour associated with the formation of a violet Fe-ASP complex identified as tetraaquosalicylatroiron (III) complex. (b) Description complex formation. When in contact with moisture, aspirin dissociates into acetic and salicylic acid. The latter can react with acidified iron (III) ions to form the violet complex.

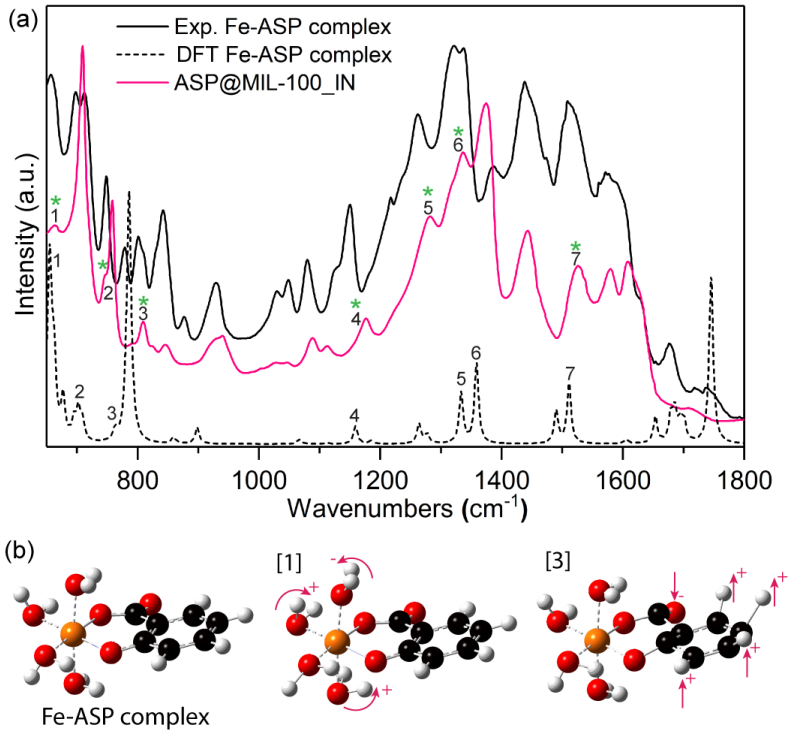

Figure 5.6: (a) ATR-FTIR spectra of Fe-ASP complex (black) and ASP@MIL-100_IN system (pink). The comparison of the spectra highlights the formation of the Fe-ASP complex within this drug@MIL-100_IN system. Marked by asterisks are the vibrational peaks assigned to the Fe-ASP complex in the ASP@MIL-100_IN spectrum. The spectrum of Fe-ASP calculated by DFT (B3LYP, 6-31G basis set), has also been presented to identify the molecular origin of the Fe-ASP complex vibrations identified in the guest@host spectrum. (b) Schematic representation of Fe-ASP complex vibrations, [1] OH wagging of water molecules and [3] out-of-plane bending of OH (aromatic ring) and C=O groups. Arrows indicate the directions of the collective deformations with +/- amplitudes computed by DFT. Colour code: O in red, C in black, H in grey, and Fe in orange.

Table 5.2: Description of vibrational modes of interest in Fe-ASP complex.

Mode no.	**Theo.** (cm^{-1})	**Exp.** (cm^{-1})	**Description**
1	655	663	ωOH (water molecules)
2	703	743	ωOH (water molecules) and γ aromatic ring
3	765	808	γOH and γ aromatic ring
4	1159	1177	νC=O and δ aromatic ring
5 6	1332 1359	1334 1340	νC=O and νC=C
7	1512	1513	γOH (water molecules)

δ = in-plane bending, γ = out-of-plane bending, ν = stretching, ω = wagging

indicate that caffeine has a higher potential to act as a proton acceptor. Normalized PXRD patterns in Figure 5.7 show the effect on the crystallinity of the final samples when different amounts of 5-FU (Figure 5.7a) and caffeine (Figure 5.7b) were added during the grinding process. As the amount of drug molecules increases (*e.g.* from 0.1 to 1.0 mmol of drug/mmol of H_3BTC), an evident increase in the relative intensity of the diffraction peaks was observed. Even with only 0.1 mmol of caffeine per mmol of H_3BTC, improvements in crystallinity of CAF@MIL-100_IN were tangible when compared to MIL-100 (Fe). With 1.0 mmol of both 5-FU and caffeine per mmol of H_3BTC, highly crystalline material has been obtained. The degree of crystallinity of these samples was further assessed by measuring the FWHM of the (022) peak (Figure 5.8), which shows the increase in the crystallinity of the MIL-100 (Fe) host. As anticipated, caffeine presents a slightly better modulator performance due to its relatively higher pKa value (*i.e.* greater proton acceptor potential).

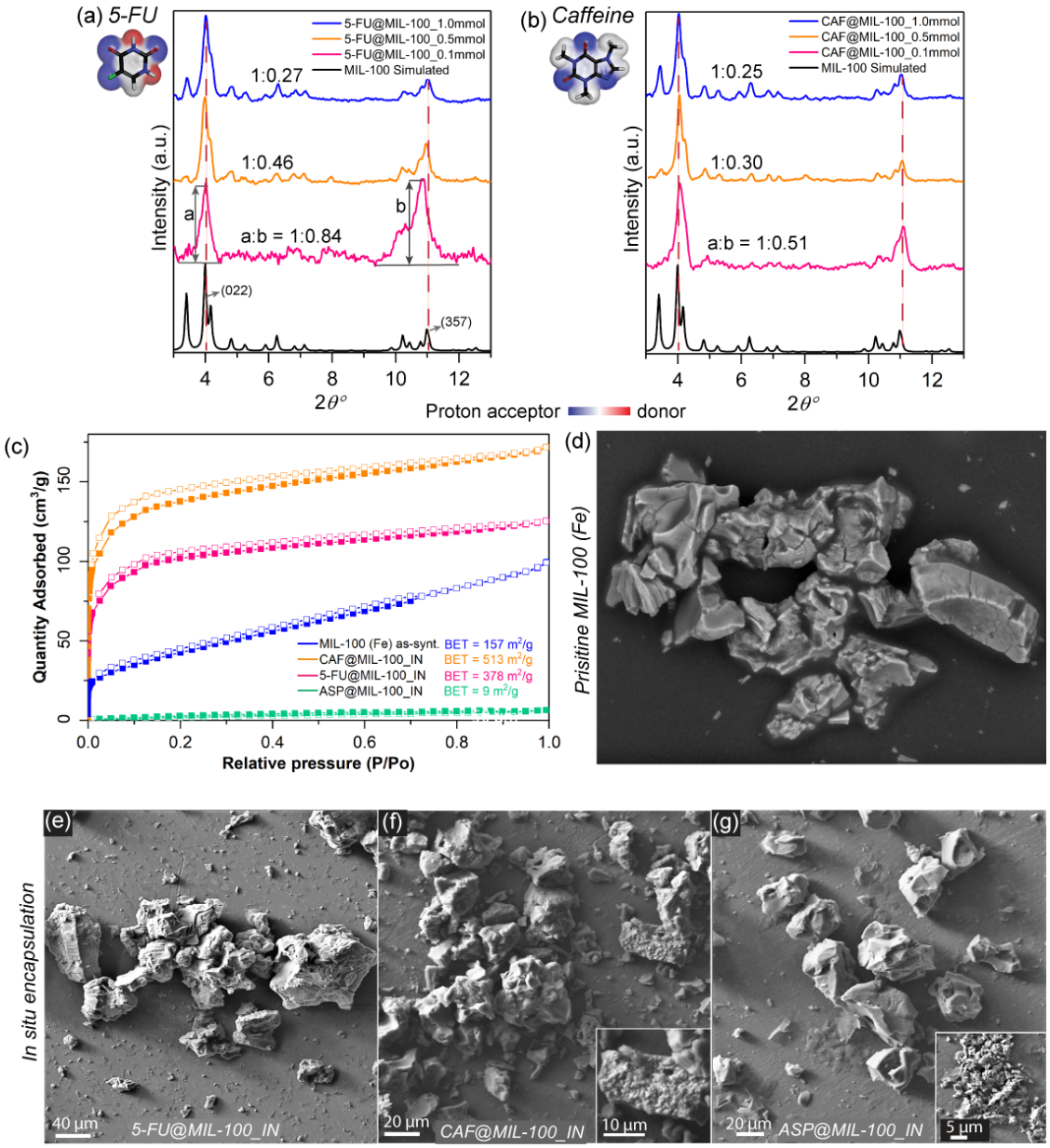

Figure 5.7: Normalized PXRD patterns of (a)5-FU@MIL-100_IN and (b) CAF@MIL-100_IN samples, showing the effect of the drug:linker ratio used during the synthesis (*i.e.* x mmol of drug per 1.0 mmol of H_3BTC) on the final crystallinity of the resulting material. The relative intensity of PXRD peaks was determined from the ratio of (022):(357). (c) Nitrogen adsorption (filled symbols) and desorption (empty symbols) isotherms of MIL-100 (Fe) and drug-loaded counterparts. SEM images of (d) MIL-100 (Fe) and drug@MIL-100_IN systems: (e) 5-FU@MIL-100_IN, (f) CAF@MIL-100_IN, (g) ASP@MIL-100_IN. Colour code: O in red, C in black, H in grey, N in navy blue, F in green.

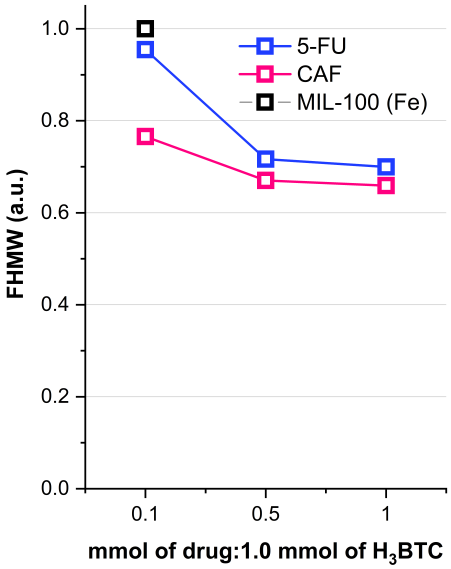

Figure 5.8: FWHM used to assess the sharpening of the (022) peak and evaluate the modulator effect of 5-FU (blue) and caffeine (pink) on the crystallinity of MIL-100 (Fe).

5.4 Drug loadings, textural and morphological properties of drug@MIL-100_IN assemblies

N_2 adsorption isotherms (Figure 5.7c) and SEM images (Figure 5.7d-g) were used to further characterize the drug@MIL-100_IN systems. SEM images, employed to examine the morphology of the samples, show no signs of alterations upon drug encapsulation. The formation of the observed MIL-100 (Fe) crystal aggregates was detected culminating in the non-uniform particles size range observed (*i.e.* 2-100 µm), as reported in Chapter 4. The amorphous ASP@MIL-100_IN product also presented itself in an aggregated form, with an equally large distribution of particle size.

Due to the lack of a noticeable morphological difference between the amorphous and crystalline phases, BET surface areas of MIL-100 (Fe) and drug loaded counterparts were determined from the nitrogen adsorption isotherms to quantify the sample porosity (Figure 5.7c). The isotherms were also used to determine the level of guest encapsulation, which were further quantified by TGA using Equation 3.2 (Figure 5.9).The drug loadings of 20.4 wt.%, 54.8 wt.%, and 9.8 wt.% were determined by TGA for 5-FU@MIL-100_IN, CAF@MIL-100_IN, and ASP@MIL-100_IN,

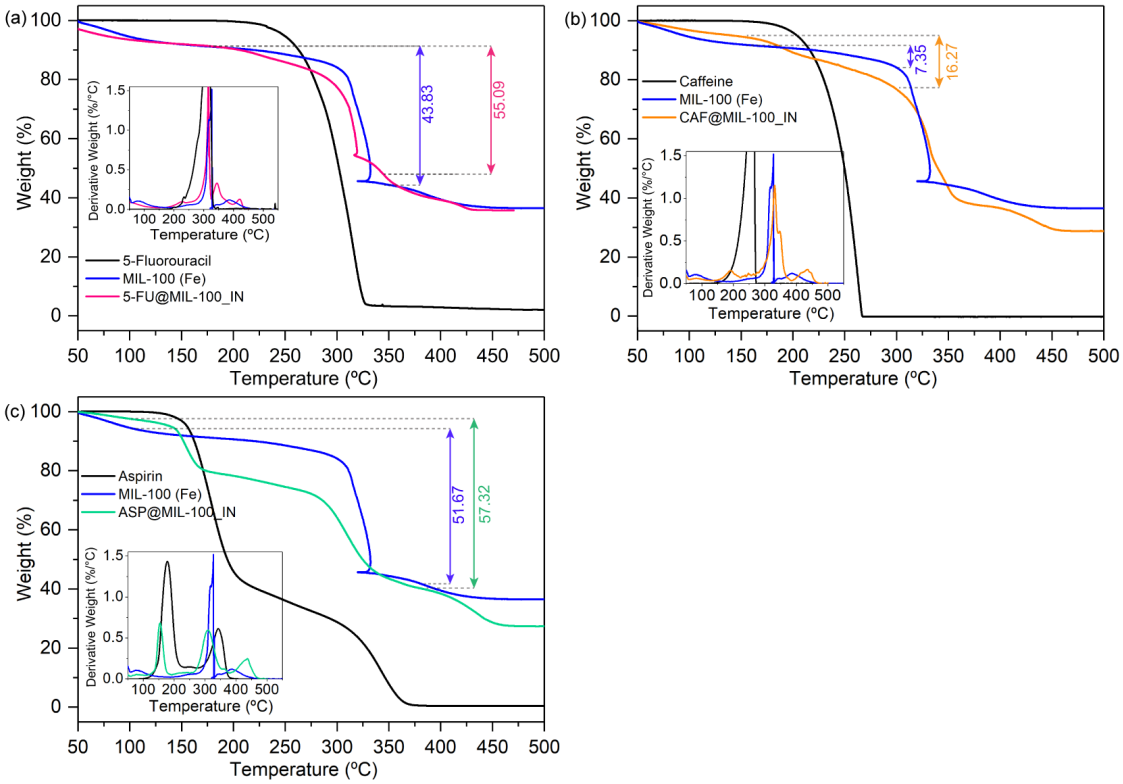

Figure 5.9: TGA of drug@MIL-100_IN systems with insets showing the differential material decomposition behaviour as a function of temperature. (a) 5-FU@MIL-100_IN, (b) CAF@MIL-100_IN, and (c) ASP@MIL-100_IN

respectively. Table 5.3 compares the drug loading herein attained with previously reported results. Sizeable loading found for 5-FU and caffeine is the result of the advantageous formation of the host MIL-100 (Fe) cages around the guest drug molecules, made possible by the *in situ* encapsulation approach applied here. Conversely, the low drug loading of aspirin was attributed to the formation of the Fe-ASP complex, which is mostly removed during the wash steps (see Figure 5.5).

The surface area of the MIL-100 (Fe) (157 $m^2\,g^{-1}$) was largely reduced when compared with values of other reported mechanochemically synthesized MIL-100 (Fe) samples (Table 5.4). The enhanced development of the host framework structure due to the modulating effect of 5-FU and caffeine also had a notable impact on the material surface areas, being 378 $m^2\,g^{-1}$ and 513 $m^2\,g^{-1}$ for 5-FU@MIL-100_IN and CAF@MIL-100_IN, respectively. It is important to note that the surface areas of these drug@MIL-100_IN systems should not be directly compared to the ones presented in Table 5.4. This is because the improvement of MIL-100 (Fe)

Table 5.3: Comparison of drug loading of drug@MIL-100_IN samples achieved *via* various methods.

Drug	MOF	Synt. Method	Drug loading (wt.%)	Ref.
5-FU	MIL-100	Mechanochemical *in situ* encapsulation	20.4	This Chap.
	MIL-100	manual grinding	20.2	Chap. 4
	MIL-100	vortex grinding	18.3	Chap. 4
	MIL-100	Immersion into drug solution	66.0	[200]
	MIL-88		28.0	[200]
	MIL-53		13.1	[200]
CAF	MIL-100	*in situ* encapsulation	54.8	This Chap.
			49.7	[13]
	MIL-100	Immersion into drug solution	24.2	[6]
			52.4	[10]
ASP	MIL-100	*in situ* encapsulation	9.8	This Chap.
	MIL-100	Immersion into drug solution	24.8	[148]
	MIL-100		1.806 *	[51]
	MIL-127		0.14 *	[87]

*: g/g of MOF

porous structure attributed to the modulating effect of the drug molecules occurs in parallel with its partial obstruction, occasioned by pore filling after confinement of drug molecules.

Finally, the isotherm shape and the significantly reduced surface area found in ASP@MIL-100_IN (9 $m^2 g^{-1}$) showcase the non-porous character of this drug-loaded amorphous material. For comparison, the PXRD pattern and ATR-FTIR spectrum of a commercial grade of MIL-100 (Fe), termed Basolite F300 (Fe-BTC), were collected. It displays broad PXRD peaks, suggesting an amorphous structure, but its vibrational spectrum remains intact (Figure 5.10), in a similar fashion to ASP@MIL-100_IN. These observations imply that the aspirin-loaded system retains the basic building blocks and short-range connectivity of the crystalline MIL-100 (Fe), but it lacks long-range periodic order, possibly being impeded by the formation of the tetraaquosalicylatroiron (III) complex.

Table 5.4: Comparison of the BET surface areas of drug@MIL-100_IN samples

Samples	Synthesis method	BET surface area ($m^2\,g^{-1}$)	Ref.
MIL-100 as-synt.	Mechanochemistry (manual grinding)	157	This Chap.
5-FU@MIL-100_IN	Mechanochemical *in situ* encapsulation	378	This Chap.
CAF@MIL-100_IN		513	
ASP@MIL-100_IN		9	
MIL-100 (Fe)	Mechanochemistry (liquid assisted grinding - ball mill)	1033	[65]
	Mechanochemical (kitchen grinder)	255	[73]
	Solvothermal (high temperature)	1836	[185]
	(high pressure and temperature)	1750	[186]
	Solvothermal (high pressure and temperature)	1223	[187]
	Solid state synthesis (high pressure and temperature)	110	[188]

[65] Pilloni et al., [73] Samal et al., [185] Zhang et al., [186] Chen et al., [187] Zhang et al.,[188] Kansal et al.

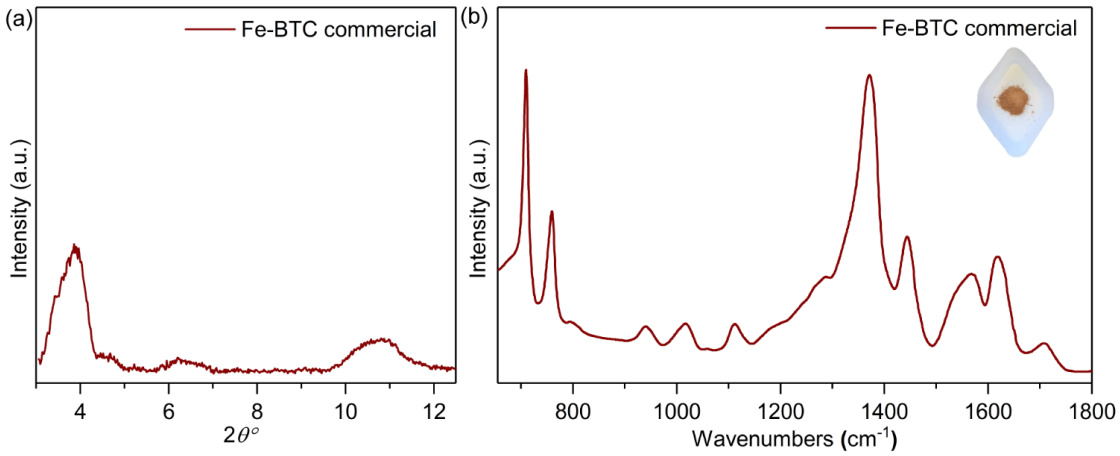

Figure 5.10: Analysis of commercial Fe-BTC. (a) PXRD pattern of the Fe-BTC showing the amorphous character of the sample while the chemical bonds integrity is displayed *via* (b) ATR-FTIR spectrum.

5.5 Examination of the lattice dynamics and low energy vibrations in drug@MIL-100_IN assemblies *via* INS

The vibrational properties of MIL-100 (Fe) and drug@MIL-100_IN systems were characterized by INS spectroscopy, and the results are presented in Figure 5.11. INS spectroscopy of the drug@MIL-100_IN system probes the dynamic properties of the drug-encapsulated MIL-100 (Fe) samples, revealing the modulator effect of the guest drug molecules. The full spectra up to ∼60 THz (2000 cm^{-1}) are shown in Figures 5.12-5.14.

Detailed comparison between the INS spectra of the *in situ* derived samples and the MIL-100 (Fe) reveals an overall lower spectral intensity of 5-FU and aspirin encapsulated MIL-100 (Fe) systems. This can be credited to two main factors. Firstly, the INS spectral intensity at low frequency (*i.e.* low momentum transfer (Q)), as recorded on TOSCA, is proportional to the mean square displacement of the atoms from their equilibrium position. At higher frequency, however, the intensity is suppressed by the Debye-Waller factor [201]. On this basis, the decrease in the scattering intensity in the low energy region of the drug@MIL-100_IN systems, specifically for 5-FU@MIL-100_IN and ASP@MIL-100_IN, suggests the decrease of structural motions. As the periodicity of the MIL-100 (Fe) host is enhanced, stronger constraints are imposed on the lattice modes.

Another factor contributing to the observed reduction of spectral intensity is the decrease in the total amount of hydrogen atoms present within the sample, resulting from the large incoherent neutron scattering cross section of hydrogen [119]. In this case, the increase in the effective deprotonation of the organic linker as detected in ATR-FTIR measurements (Figure 5.4), due to the modulating effect of 5-FU and caffeine, and the consequential reduction of the number of hydrogens present in the samples resulted in the decline of overall spectral intensity. For the amorphous ASP@MIL-100_IN system the decline can be linked to the formation of the aspirin iron complex which reduces the overall number of H_3BTC molecules within the sample. Additionally, despite its amorphous nature, this system still presents all

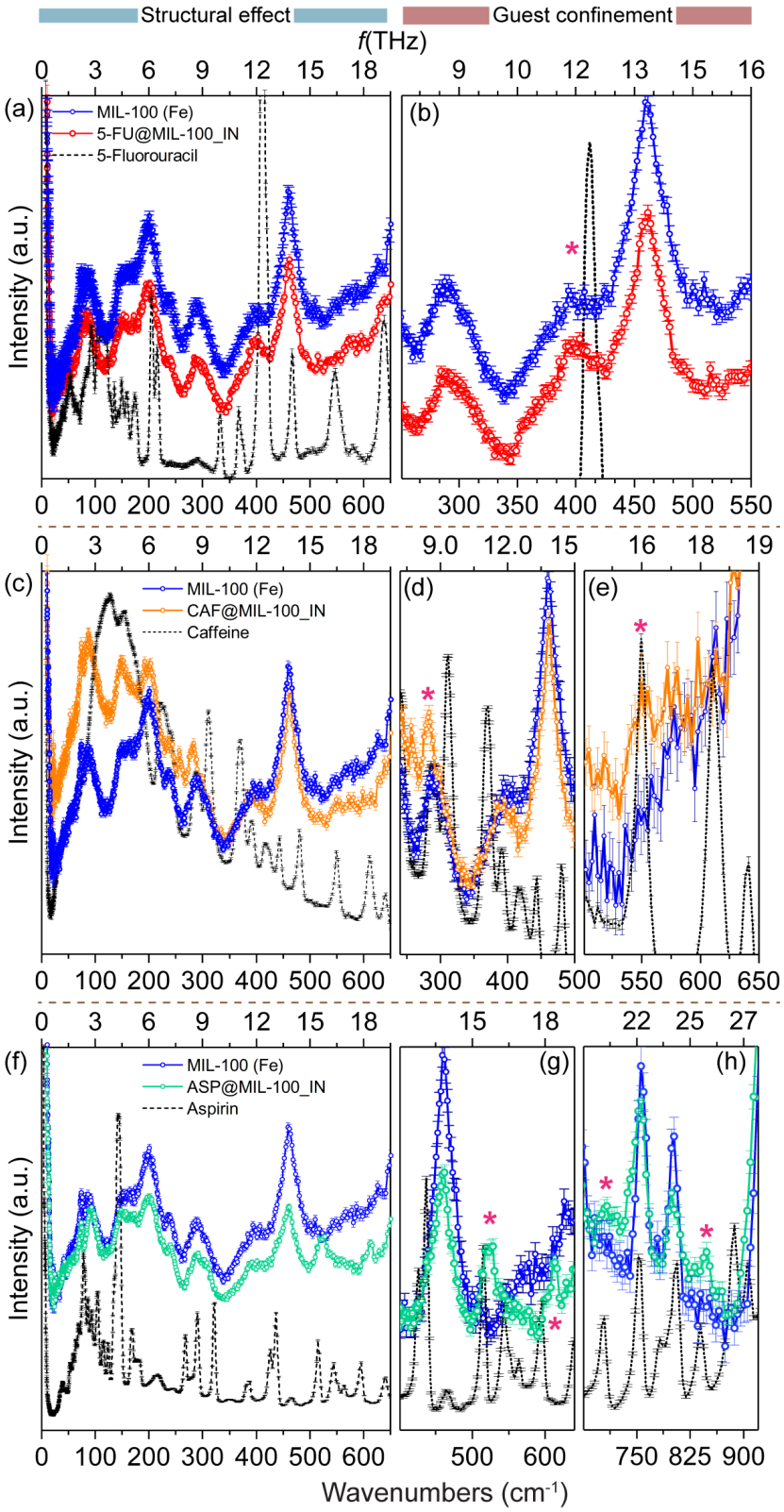

Figure 5.11: INS spectra of (a-b) 5-FU@MIL-100_IN, (c-e) CAF@MIL-100_IN, and (f-h) ASP@MIL-100_IN, with magnified views of the drug peaks present in the drug@MIL-100_IN systems, highlighted with asterisks.

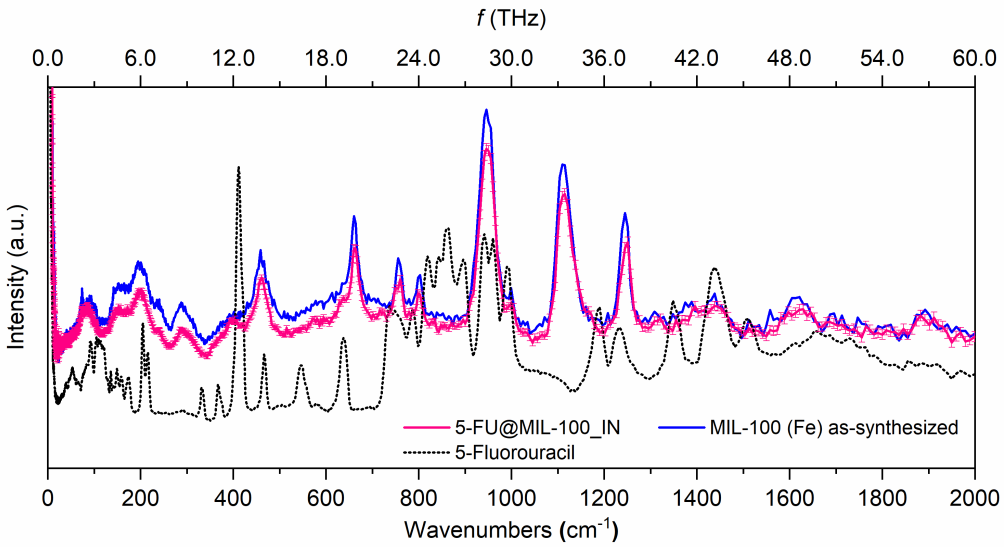

Figure 5.12: INS spectra of 5-FU@MIL-100_IN yielded by *in situ* encapsulation techniques. Spectrum of 5-FU presented in black was scaled down to facilitate the comparison with the guest@MIL-100_IN systems.

the collective modes observed in the MIL-100 (Fe), akin to what was detected in the higher energy vibrational bands of the ATR-FTIR spectra (Figure 5.3).

Analysis of the magnified INS spectra in Figure 5.11 (right panels) shows that in all drug@MIL-100_IN samples, drug vibrational peaks (highlighted with asterisks) were observed. *Ab initio* DFT calculations further revealed details of the specific

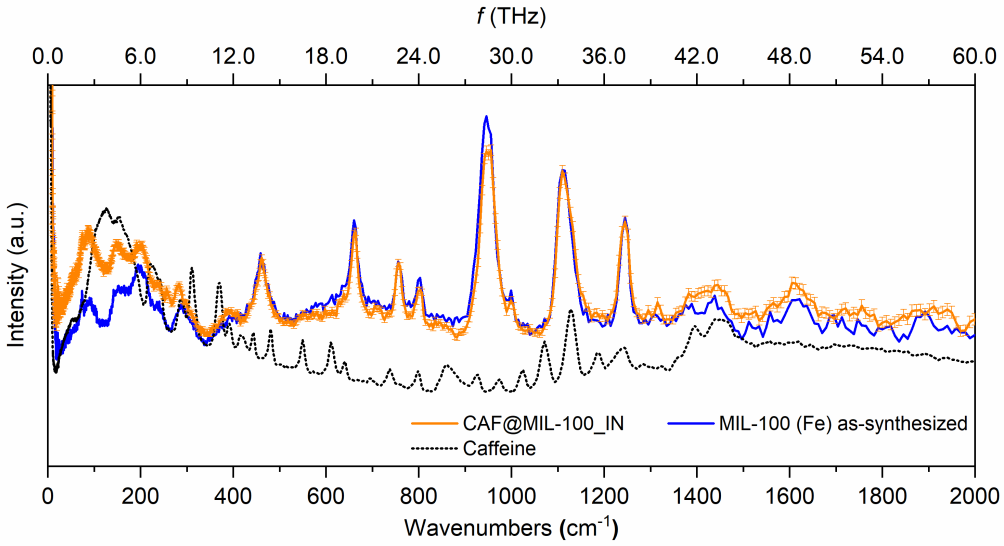

Figure 5.13: INS spectra of CAF@MIL-100_IN yielded by *in situ* encapsulation techniques. Spectrum of caffeine presented in black was scaled down to facilitate the comparison with the guest@MIL-100_IN systems.

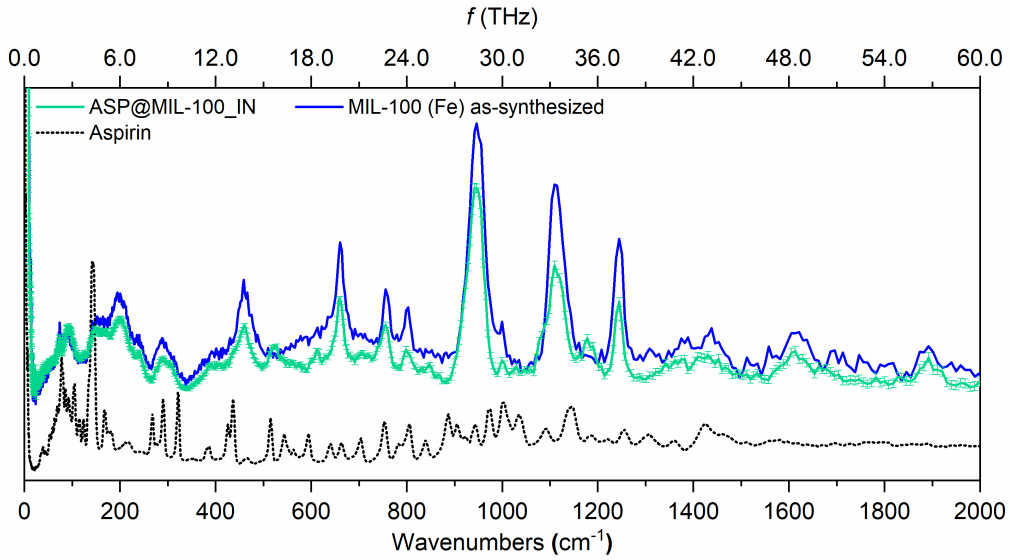

Figure 5.14: INS spectra of ASP@MIL-100_IN yielded by *in situ* encapsulation techniques. Spectrum of aspirin presented in black was scaled down to facilitate the comparison with the guest@MIL-100_IN systems.

drug molecule vibrations (Figures 5.15 and Table 5.5). Scrutiny of the INS spectra provides a deeper insight into the dynamics of the guest-host interaction. The higher intensity observed in the spectra of CAF@MIL-100_IN below 9 THz (300 cm^{-1}) is linked to the combined scattering of the MOF host and the caffeine guest molecule, specifically resulting from the high guest loading (∼55 wt.%) of this system.

Vibrational frequency shifts in the guest vibrational modes after confinement were detected in all the samples (marked by asterisks in Figure 5.11 insets), indicating the presence of constraints to the free motions of the drug molecules due to pore confinement. This effect is clear in the shift and suppression of the vibrational mode of 5-FU at ∼12.3 THz (∼410 cm^{-1}), the caffeine mode at ∼8.6 THz (∼288 cm^{-1}), and the aspirin modes at ∼15.4 THz (∼514 cm^{-1}) and ∼19.2 THz (∼641 cm^{-1}) in the spectra of 5-FU@MIL-100_IN, CAF@MIL-100_IN, and ASP@MIL-100_IN, respectively.

The origin of each of these vibrations has been detailed in Table 5.5. Based on the INS spectra and on the electrostatic potential maps (ESP) of the drug molecules (Figure 5.16) it is possible to conclude that 5-FU, caffeine, and aspirin form strong Fe ⋯ O coordination with the CUS of the MOF, conferred by the *in*

situ encapsulation method applied. The proposed *in situ* approach is advantageous against the conventional post-synthetic drug encapsulation approach as it will be later discussed in details in Chapter 7.

Table 5.5: Description of vibrational modes of interest for 5-FU, caffeine, and aspirin, obtained from ATR-FTIR measurements versus DFT calculations.

Mode no.	**Theo.** (cm^{-1})	**Exp.** (cm^{-1})	**Description**
5-FU			
1	112	30-130	γ ring
2	145	152	δC=O and δC−N
3	380	410	δOCNCO
4	1000	995	νC−H and νC−N
CAF			
1	80-130	50-140	δN−CH_3 and τN−CH_3
2	150	135	γ rings
	180	155	
3	201	174	τN−CH_3
4	242	228	δ rings
5	293	288	δ pyrimidine ring with τN−CH_3
6	552	549	Pyrimidine ring breathing with τN−CH_3 and δN−CH_3
7	1035	1024	δC−N_3
8	1237	1237	
9	1298	1284	νN−CH_3, νC−N, and νC−C in both rings
10	1712	1720	νC=O
ASP			
1	25-121	26-114	ωC−O, ωC=O, and τC−CH_3
2	137	135	ω ring
3	175	142	
4	515	514	γ ring with δC=O
5	640	641	γ ring with δC−O and δC=O
6	819	839	γ ring with δC−H
7	1060	1085	γ ring with νC−H
8	1179	1180	Ring breathing with δC−H

δ = in-plane bending, γ = out-of-plane bending, ν = stretching, ω = wagging
τ = twisting

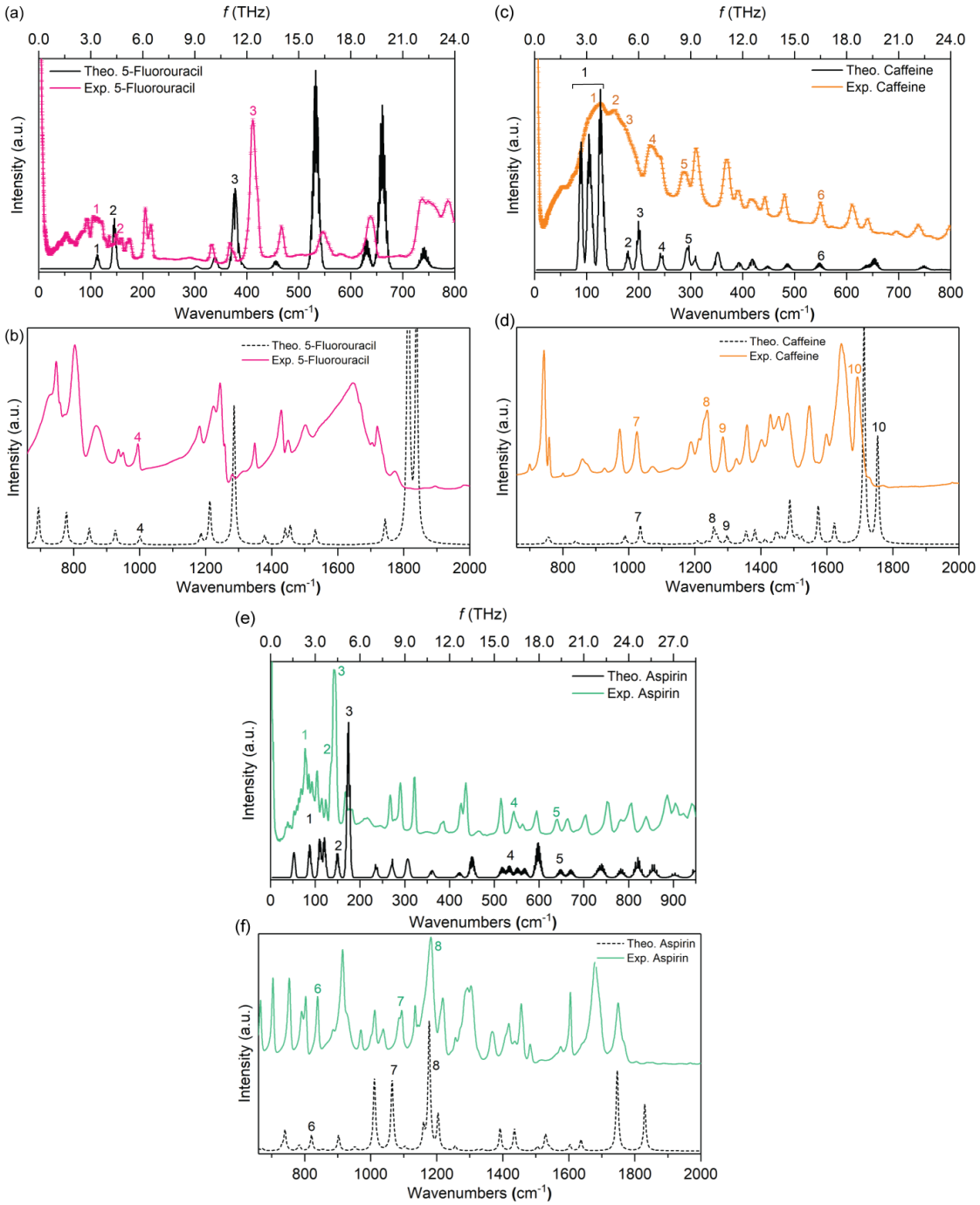

Figure 5.15: Theoretical INs and FTIR vibrational spectra of 5-FU, caffeine, and aspirin calculated by DFT (B3LYP, 6-31G basis set). (a) INS and (b) ATR-FTIR spectra of 5-FU, (c) INS and (d) ATR-FTIR spectra of caffeine, and (e) INS and (f) ATR-FTIR spectra of aspirin, highlighting some of the key vibrational modes.

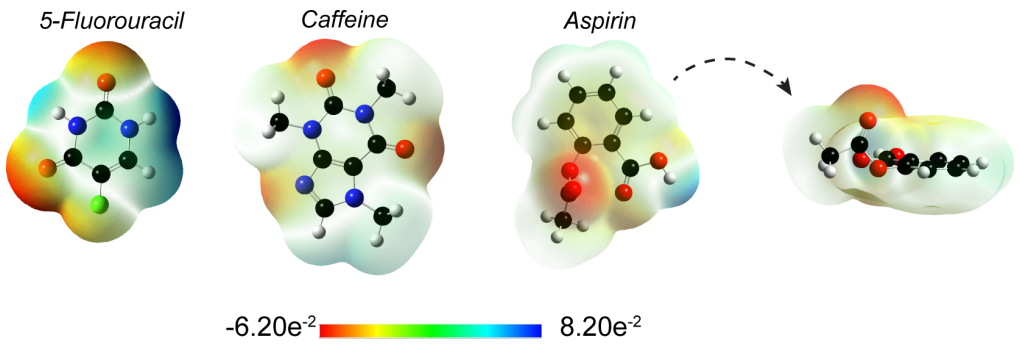

Figure 5.16: ESP of 5-FU, caffeine, and aspirin, for which aspirin is shown in two different angles for better visualization. Colour code: O in red, C in black, H in grey, N in navy blue, F in green.

5.6 Summary and conclusions

This chapter has demonstrated the use of a facile mechanochemical method to achieve pore confinement of various 'guest' drug molecules within MIL-100 (Fe) pores. Notably, this proof-of-concept study shows how 5-FU and caffeine can function as 'modulators' leading to the fabrication of a highly crystalline MIL-100 (Fe) framework. As a counterexample, aspirin molecules were used to illustrate the formation of an amorphous MIL-100 (Fe) phase. It is intriguing that benign modulators such as caffeine could potentially replace highly toxic mineralizers, such as HF commonly used in the preparation of MIL-100 (Fe). The results present in this chapter elucidate a promising pathway towards an environmentally friendly approach to yield MIL-100 (Fe) crystals and guest-encapsulated composites, thereby addressing the continuous search for low cost and scalable synthetic methods. Finally, using INS, clear differences in the vibrational behavior of the isolated drug molecules and the drug@MOF_IN assemblies were established. Neutron vibrational spectroscopy reveals the intrinsic guest-host intermolecular interactions, pointing to the successful confinement of drug molecules due to the *in situ* mechanochemical strategy applied. The facile approach demonstrated herein can advance the future commercial potential of mesoporous MIL-100 material, expanding its usability in the biological and medical fields.

Nothing in life is to be feared;it is only to be understood. Now is the time to understand more, so that we may fear less

— Marie Curie

6

Water reconstruction of MIL-100 (Fe) for enhanced guest encapsulation

Contents

6.1 Background and motivation

In Chapters 4 and 5, mechanochemistry has been successfully applied to the fabrication of different drug@MIL-100 systems. However, as shown in Chapter 5, the pristine MIL-100 (Fe) material, resulting from ambient conditions synthesis, presents itself with a low degree of crystallinity, which could impair its large scale use. This chapter demonstrates how the crystallinity of the material can be significantly improved upon its simple immersion in water, *via* a process termed 'reconstruction'. Notably, the reconstruction method has been shown highly effective for the recovery of time degraded and mechanically amorphized samples, applicable

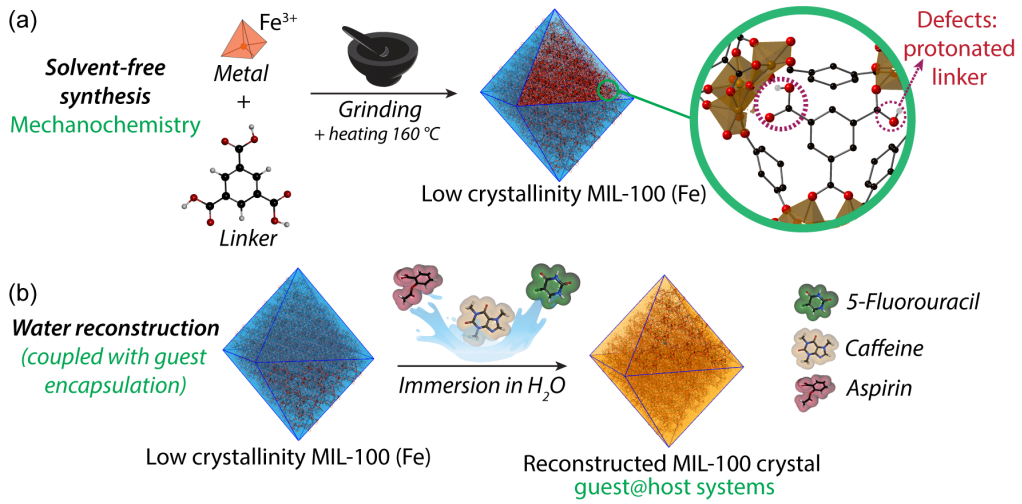

Figure 6.1: Schematic summary of the reconstruction method. (a) Mechanochemical approach applied to the synthesis of low crystallinity MIL-100 (Fe). (b) Reconstruction process to enhance material crystallinity and for the entrapment of different drug molecules within the MOF pores.

as a material regeneration strategy [202]. Additionally, the reconstruction step of MIL-100 (Fe) crystals can be tailored to enable the fabrication of drug@MIL-100 systems, designated as 'drug@MIL-100_REC'. By employing the drug molecules also used in Chapter 5 (*e.g.* 5-FU, caffeine, and aspirin) as guests for confinement in the pores of MIL-100 (Fe), this chapter further expands the study of the vibrational dynamics of the drug@MOF systems *via* INS. Analysis of the collective modes unravels details behind the reconstruction process, casting new light on the guest-host interactions underpinning the controlled drug release from MOF carriers. A summary of the synthetic routes being employed in this chapter and samples being studied are respectively presented in Figure 6.1 and Table 6.1.

Table 6.1: MIL-100 reconstruction samples - description and details

Synthesis method	Samples	Guest
Reconstruction studies	MIL-100 (Fe) Day [x]	-
Encapsulation during reconstruction	5-FU@MIL-100_REC CAF@MIL-100_REC ASP@MIL-100_REC	5-Fluorouracil Caffeine Aspirin

x: immersion time (*e.g.* 1, 2, 3...15 days)

6.2 Reconstruction of MIL-100 (Fe): a green mechanochemical and water-based approach

Figure 6.2 illustrates the changes observed in MIL-100 (Fe) as a function of time throughout the reconstruction process. Upon immersion of the low-crystallinity sample (as-synthesized) into water, it is possible to significantly enhance the material crystallinity. The sample presented a distinctive colour change (Figure 6.2a) that was accompanied by the increase in its crystallinity, confirmed by the PXRD patterns (Figure 6.2b-c). The evolution in the material optical properties suggests the occurrence of microstructural changes in MIL-100 (Fe). A closer look at the diffraction data of as-synthesized MIL-100 (Fe) shows that the Bragg peaks below $2\theta = 5°$ exhibit either very low intensity or are completely absent from the pattern prior to the water reconstruction. Conversely, Bragg peaks within $2\theta = 10°$-$11.5°$ show a less pronounced change before and after reconstruction. The low relative intensity of the Bragg peaks at the smaller diffraction angles of $2\theta < 5°$ signifies a weak long range ordering of the as-synthesized MIL-100 (Fe) framework. Because the intensity of the diffraction peaks is determined by periodic atomic arrangement averaged over the entire polycrystalline sample [199], the overall increase in intensity observed in the PXRD patterns indicates the progressive increase of long-range ordering of the MIL-100 (Fe) crystals during reconstruction.

The structural changes were further assessed by analysing the relative peak intensity data as a function of sample immersion time (Figure 6.2b). The changing relative intensity of the (022):(357) planes, corresponding to the two most intense diffraction peaks, was calculated as the ratio between the peaks intensity. The results reveal a notable rise in intensity of the (022) plane (*i.e.* $2\theta = 4°$), versus a slower increase in intensity of the (357) plane (*i.e.* $2\theta = 11°$). The process can be divided into three stages. Firstly, during the first two days of immersion, the relative intensity of (022):(357) peaks were marginally unaffected. In the second stage (2-7 days), a steep rise in the (022):(357) relative intensity from 0.57:1 to 1:0.27 was observed, indicating a major increase in long-range periodicity of MIL-100 (Fe).

Finally, the relative intensity ratio stabilized, with minimal changes from 7-15 days. Notably, the change in the relative intensity of the peaks is accompanied by narrowing in FWHM of the (022) peak, indicating increasing sample crystallinity, calculated according to Equation 3.6. The narrowing can be also associated to the continuous size increase of the crystalline domain (Figure 6.2a). For comparison, the normalized PXRD patterns are presented in Figure 6.3.

Figure 6.4a shows the ATR-FTIR spectra where the typical vibrational bands of MIL-100 (Fe) were detected in all samples, confirming the chemical bonds integrity even in the low crystallinity material. From the ATR-FTIR spectra, two features can be highlighted. First, the sharpening of the band at ~1355 cm^{-1}, assigned to

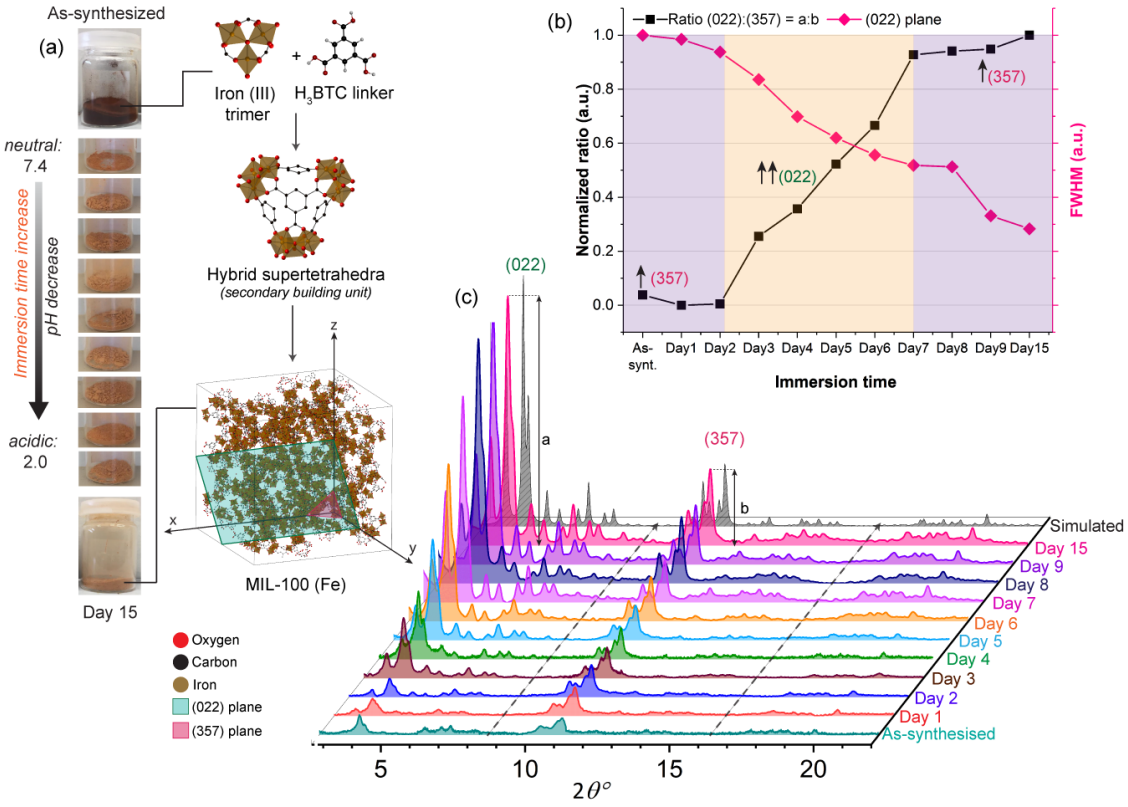

Figure 6.2: MIL-100 (Fe) reconstruction process. (a) Photographs showing evolution of the MIL-100 (Fe) samples collected at different immersion time intervals, and schematics of the associated chemical structure of MIL-100 (Fe) crystals. The images display the colour shift observed upon the increase of the crystallinity of MIL-100 (Fe) material. (b) Ratios of the changing relative intensity of the (022):(357) planes. The plots display a faster increase in peak intensity for small diffraction. The plot also presents the FWHM of the peaks corresponding to the (022) plane, showing a progressive increase in the material crystallinity. (c) Evolution of the absolute intensity of the diffraction peaks throughout the reconstruction process, showing the marked improvement in crystallinity.

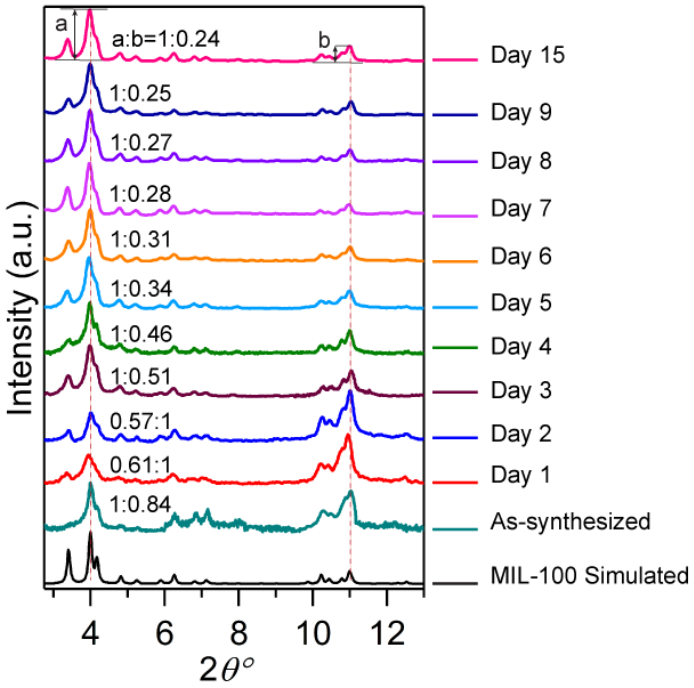

Figure 6.3: Normalized PXRD patterns of MIL-100 (Fe) after different immersion times. Each pattern presents the ratios of the changing relative intensity of the a:b = (022):(357) planes, demonstrating the progressive increase in the relative intensity of the (022) plane.

the stretching of the carboxylate groups present in the organic ligand (BTC), was observed (see Figure 6.5a). This change was quantified by the decrease in FWHM of this band (Figure 6.5b), indicating the increase in the structural symmetry of MIL-100 (Fe) samples [198]. Secondly, the band at ∼1720 cm^{-1}, assigned to the stretching of carboxyl group present in the acidic form of the organic linker (*i.e.* H_3BTC) [194, 197], has shown a progressive decline in intensity, corresponding to the reduction in the spectral area of this vibrational peak (Figure 6.5b). These changes were accompanied by a large rise in the acidity of the solution in which MIL-100 (Fe) crystals were immersed (*i.e.* pH values fell from 7.4 to 2.0), as shown in Figure 6.2a, strongly indicating that a continuous deprotonation of the organic linker took place throughout the reconstruction process (days 1 to 15). As mentioned in Chapter 5, the complete deprotonation of H_3BTC is necessary for the formation MIL-100 (Fe) 3D framework with high crystallinity. The incomplete deprotonation of the organic ligand can impede the self-assembly of the SBU (Figure 6.2a), thereby resulting in the formation of defective mesocages (partially formed). Similar results

have been reported by Fernández-Bertrán *et al.* [203], who obtained partially formed frameworks of Zn(Imidazolate)$_2$ *via* a similar manual grinding process. It is proposed that the presence of water in the reconstruction process, acting as a weak base to form hydronium ions (H_3O^+), will facilitate the deprotonation of H_3BTC and aid in the reconstruction of the defective MIL-100 (Fe) structure resultant from the grinding process.

To acquire a better understanding of the framework reconstruction process,

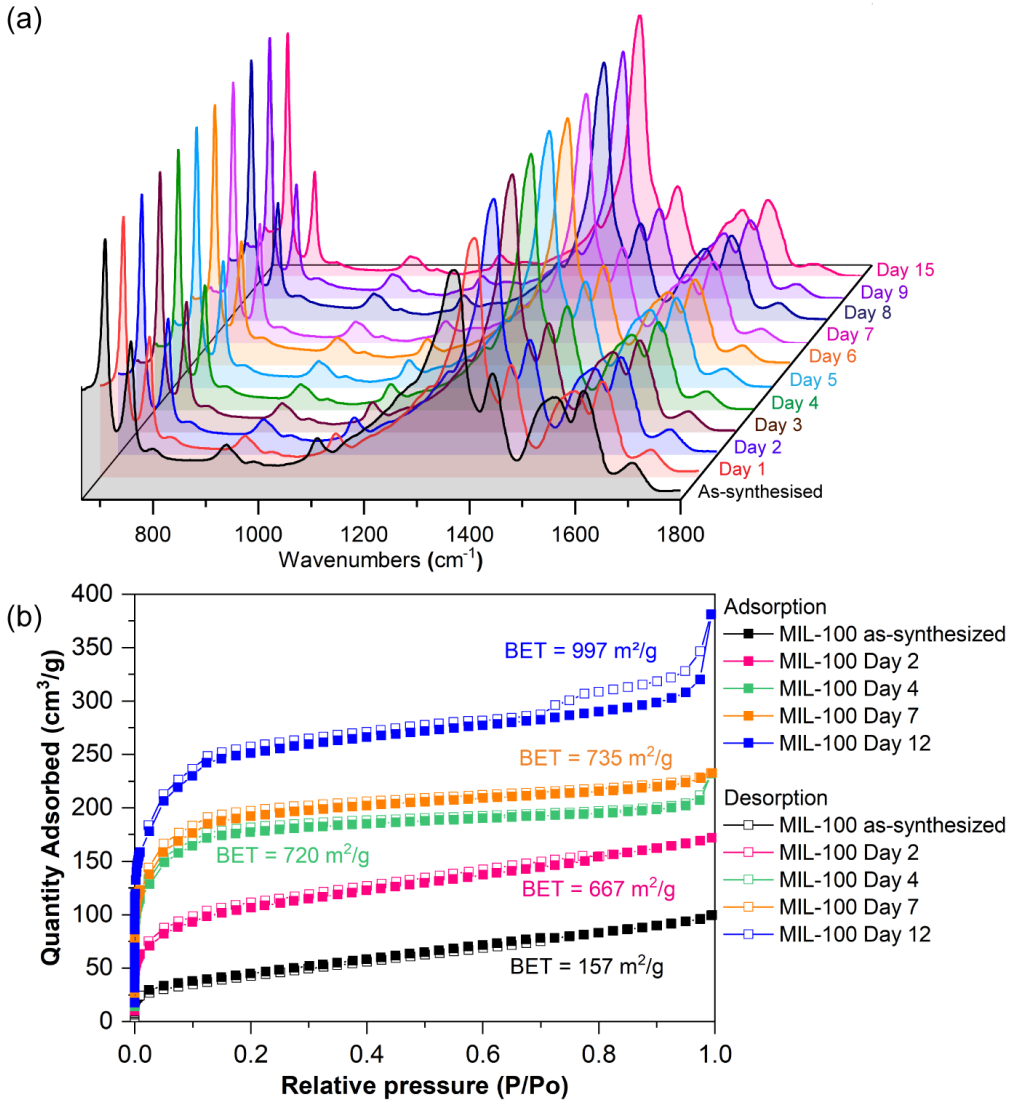

Figure 6.4: (a) Normalized ATR-FTIR spectra of MIL-100 (Fe) samples collected at different immersion time intervals. (b) N_2 adsorption and desorption isotherms of MIL-100 (Fe) samples under reconstruction. Samples were activated at 150 °C under high vacuum for 12 hours prior to N_2 adsorption measurements at 77K.

the Brunauer-Emmett-Teller (BET) surface areas of the samples was determined using N_2 sorption at 77 K. The BET results of four selected samples obtained from immersion times of 2, 4, 7 and 12 days are shown in Figure 6.4b and Table 6.2. A considerable increase (exceeding 500%) in surface area of the Day 12 sample was found when compared with the as-synthesized MIL-100 (Fe). Evolution of the shape of isotherms at P/Po > ∼0.7 demonstrates the reconstruction of MIL-100 cages. From the as-synthesized to Day 12 samples, one can observe the progression from type II isotherm (non-porous materials) to type I, associated with microporous

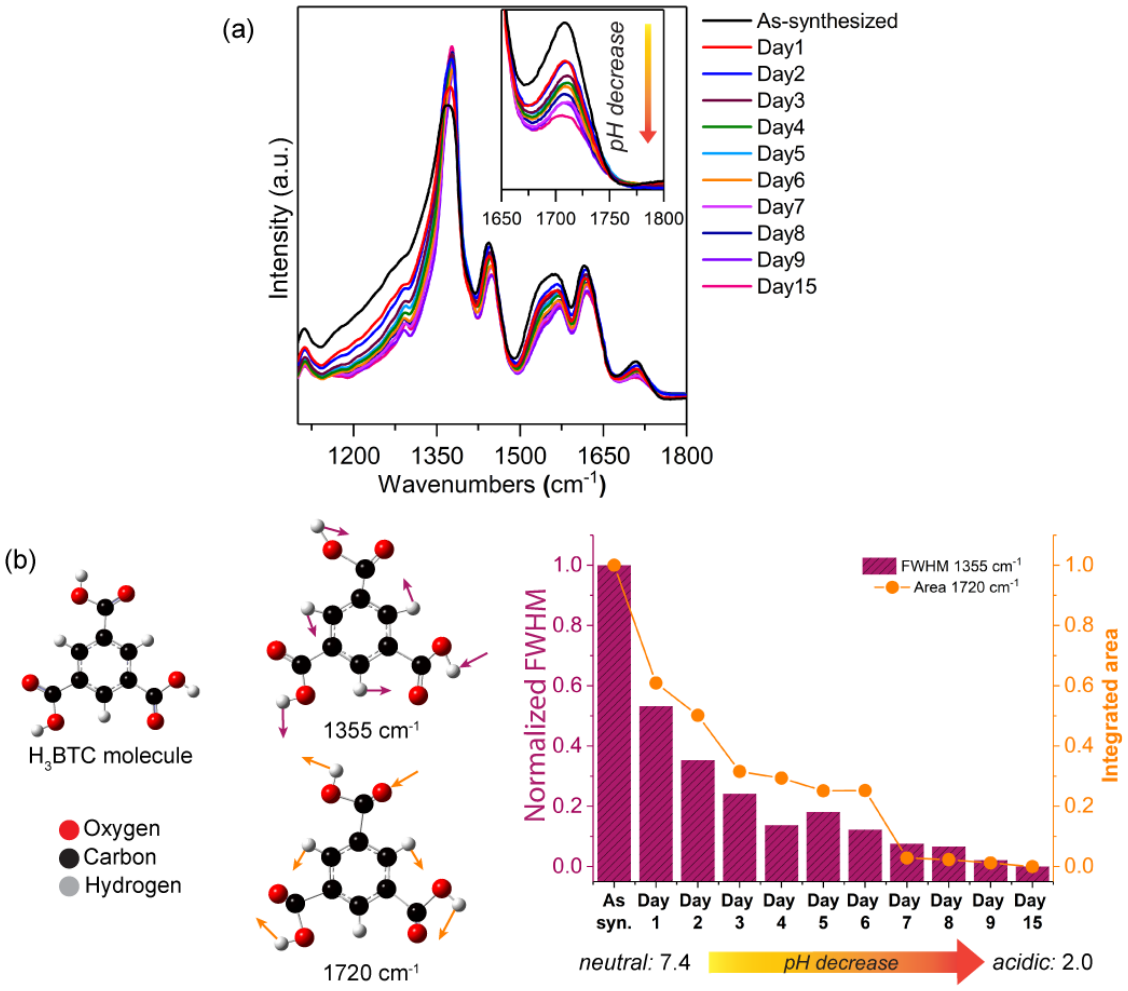

Figure 6.5: Vibrational characterization of reconstructed MIL-100 (Fe).(a) Sharpening of the carboxylate vibrational band at ∼1355 cm^{-1} and the decrease in intensity of the C=O stretching of H_3BTC at ∼1720 cm^{-1}, expressed numerically by (b) FWHM values and integrated area, respectively. To facilitate the comparison, the values have been normalized in relation to the highest FWHM value in the set of samples. Colour code: O in red, C in black, and H in grey.

materials (*i.e.* pore size < 2 nm), and eventually reaching type IV, attributed to mesoporous cages (*i.e.* pore size = 2 - 50 nm)[204]. The hysteresis loop in the N_2 isotherm takes place at very high relative pressure, indicating the low probability that small mesocavities have been obtained with the reconstruction process. It is important to point out the reduced BET surface area of our reconstructed material in comparison with the highest values reported in the literature. This might be due to a lower amount of accessible microporosity, which dominates the structure of reconstructed MIL-100 (Fe) from the reconstruction process.

Synthesis parameters (*i.e.* total synthesis time and required temperature and pressure, and use of corrosive agents) of approaches conventionally used for the

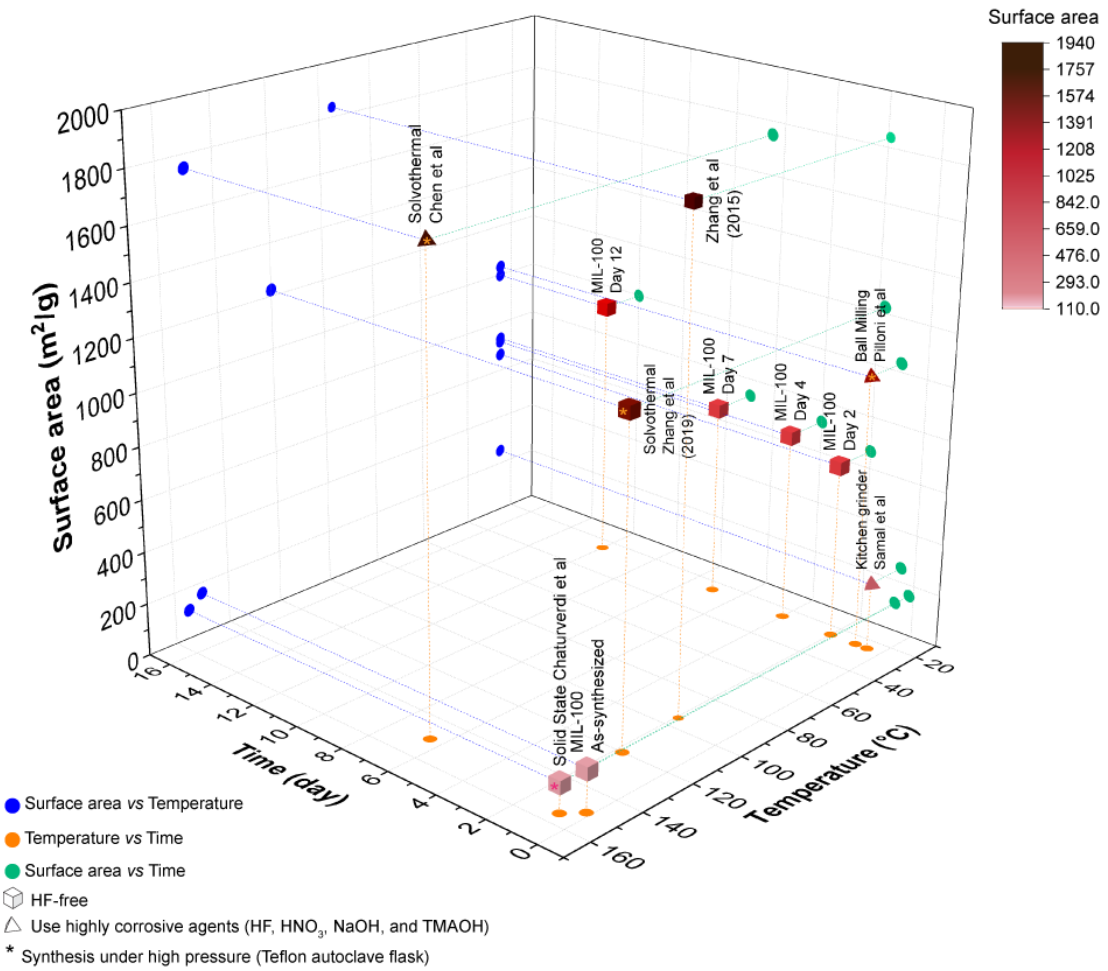

Figure 6.6: Comparison of BET surface area, synthesis temperature and total synthesis time of MIL-100 (Fe) samples prepared in this work *via* the reconstruction technique and the reported BET surface area of MIL-100 (Fe) fabricated via various synthetic methods.

fabrication of MIL-100 (Fe), some newly employed mechanochemical methods and the mechanochemical reconstruction method herein applied were compared based on the resulting BET surface area achieved. As shown in Figure 6.6 in the reconstruction method offers a good trade-off between surface area and ease of synthesis, against other reported mechanochemical, solvothermal and solid-state strategies for synthesizing MIL-100 (Fe).

The as-synthesized MIL-100 (Fe) material has shown higher surface area when compared to the material obtained *via* the solid-state approach [188] conducted under high-pressure conditions. The surface area of MIL-100 (Fe) material is significantly improved after the reconstruction process (*i.e.* MIL-100 Day 12) and is comparable to those obtained by solvothermal and ball milling approaches, which require the use of more extreme conditions (high temperature and pressure) and the use of corrosive toxic agents. For instance, in the work by Pilloni *et al.* [65]. in which a milling approach was used in combination with corrosive tetramethyl ammonium hydroxide, resulted in a material with comparable surface area to the reconstructed MIL-100 (Fe). The former additive can hinder the green production of MIL-100 (Fe) in terms of energy consumption and toxicity of reactant involved in the synthesis method.

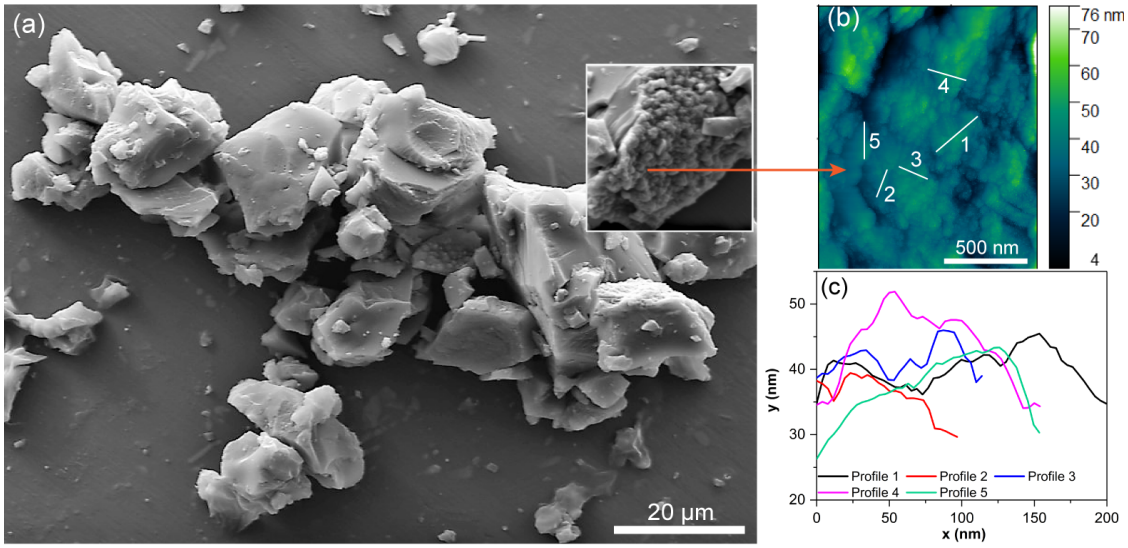

Figure 6.7: (a) SEM images of as-synthesized MIL-100 (Fe) samples. (b) AFM image displaying the surface morphology of as-synthesized MIL-100 (Fe) crystals accompanied by (c) the height profile of the marked regions, showing the formation of large particles by aggregation of nanosized particles.

Table 6.2: Comparison of the BET surface area of reconstructed MIL-100(Fe) samples produced *via* various methods

	Samples	**Synthesis method**	**BET surface area** ($m^2\,g^{-1}$)	**Ref.**
	MIL-100 as-synt.	Mechanochemistry (manual grinding)	157	
Reconstruction process	MIL-100 Day 2	Mechanochemistry followed by water immersion	667	
	MIL-100 Day 4		720	
	MIL-100 Day 7		735	
	MIL-100 Day 12		997	
	5-FU@MIL-100_REC	Encapsulation during reconstruction (7 days)	435	This Chap.
	CAF@MIL-100_REC		223	
	ASP@MIL-100_REC		225	
Time degraded	MIL-100 aged (1.5 years of shelf life)	Mechanochemistry (manual grinding)	521	
	MIL-100 aged reconstructed	Reconstruction	767	
Mechanically amorphized	MIL-100 crushed pellet (10 ton)	Mechanochemistry (manual grinding)	14	
	MIL-100 pellet reconstructed	Reconstruction	276	
MIL-100 (Fe)		Mechanochemistry (liquid assisted grinding - ball mill)	1033	[65]
		Mechanochemical (kitchen grinder)	255	[73]
		Solvothermal (high temperature)	1836	[185]
		Solvothermal (high pressure and temperature)	1750	[186]
		Solvothermal (high pressure and temperature)	1223	[187]
		Solid state synthesis (high pressure and temperature)	110	[188]

[65] Pilloni *et al.*, [73] Samal *et al.*, [185] Zhang *et al.*, [186] Chen *et al.*, [187] Zhang *et al.*,[188] Kansal *et al.*

SEM and AFM were used to characterize the morphology of as-synthesized MIL-100 (Fe) (Figure 6.7a and the reconstructed samples Figures 6.8-6.9). Particles in a large range of sizes were observed, ranging from *ca.* 100s of nm to 10s of µm. The

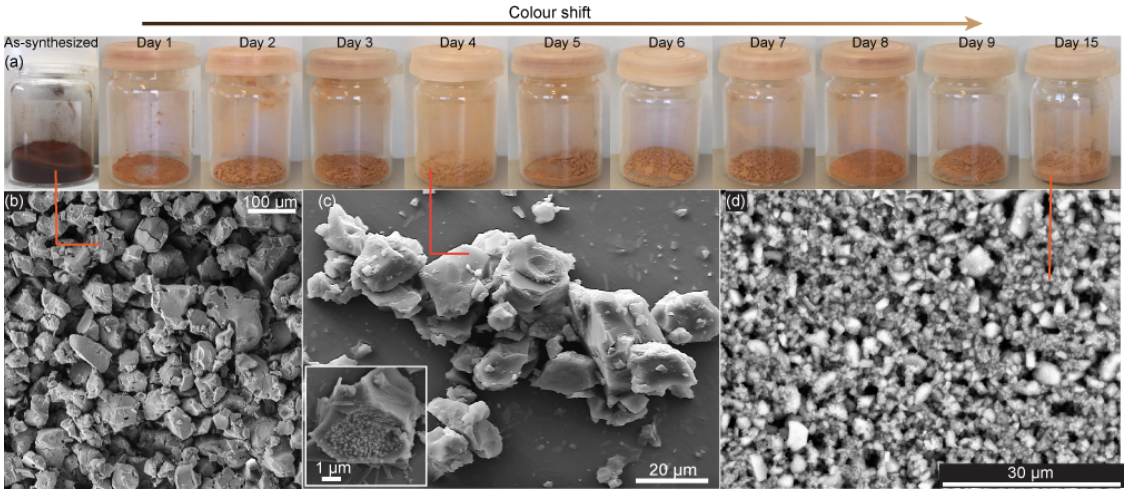

Figure 6.8: SEM images of MIL-100 (Fe) samples under reconstruction. (a) Photographic representation of MIL-100 (Fe) samples collected at different immersion time intervals. The change in the sample color can be associated to changes in the aggregation of particles as observed in (b), (c) and (d), respectively.

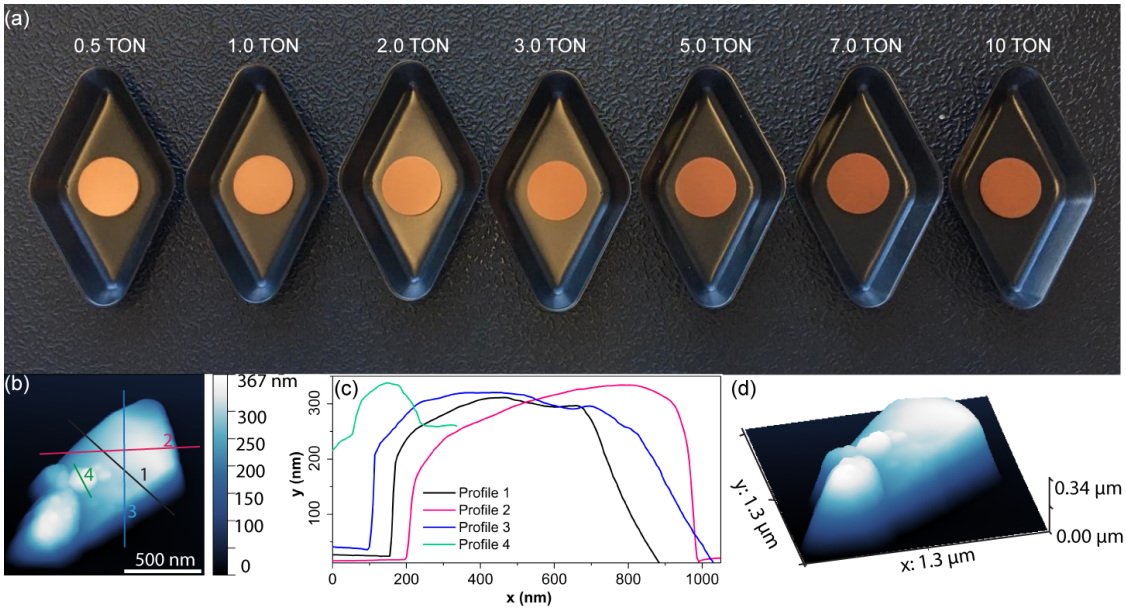

Figure 6.9: SEM images of MIL-100 (Fe) samples. (a) Pellets of MIL-100 (Fe) Day 12 samples produced by the application of various uniaxial forces. The packing of the MIL-100 (Fe) particles demonstrates that shifts in the colour of the pellets, going from light to dark brown, are observed as the particles become more densely packed (*i.e.* subjected to 0.5 to 10 ton). (b) AFM image of MIL-100 (Fe) Day 12 crystals used to produce the pellets displayed in (a). (c) Height profile of crystals revealing the size and shape of MIL-100 (Fe) Day 12 crystals, with a rectangular-like shape of hundreds of nanometers. (d) 3D view of crystal displayed in (b).

grinding process appears to favour the formation of aggregates of MIL-100 (Fe) crystals, culminating in larger particles (Figure 6.7a) constituted from densely packed nanoparticles (Figure 6.7c inset). AFM imaging (Figure 6.7b) revealed the granular nature of the particle surfaces, comprising nanocrystals < 50 nm as depicted in Figure 6.4c (see Figure 6.9 for further details).

6.3 Reconstruction of time degraded and mechanically amorphized MIL-100 (Fe)

Exceptionally, the applicability of the reconstruction process to enable the recovery of time degraded samples, which were aged for 1.5 years (Figure 6.10-6.11) was demonstrated. Throughout the aging time, the samples have been stored in a standard sealed vial. As observed in Figure 6.10a, the aged MIL-100 (Fe) showed signs of decomposition/collapse due to the change in the relative intensity of the planes (022):(357), going from 1:025 to 1:0.99 for the as-synthesized and aged samples, respectively. The (022) plane seemed to suffer the most from the aging of the sample, with large reduction of intensity. As it can be noted from Figure 6.10b, the (022) peak has shown large broadening after aging. *Via* the reconstruction process the crystallinity of the material was increasingly recovered with the increase of immersion time (Figure 6.10c). Not only the relative intensity of the samples presented a massive change (from 1:0.99 back to 1:0.26), but also the FWHM values of the (022) peak were fully restored.

Concomitantly, as shown in Figure 6.11a-b, the broadening of the carboxylate vibration band at 1355 cm^{-1} in the aged sample and the sharpening of this same band after the reconstruction process indicates the increase in the structural symmetry of the sample. Moreover, the BET surface area presented a recovery of 96.7% against the initial value, demonstrating the reconstruction of the material porosity Figure 6.11c.

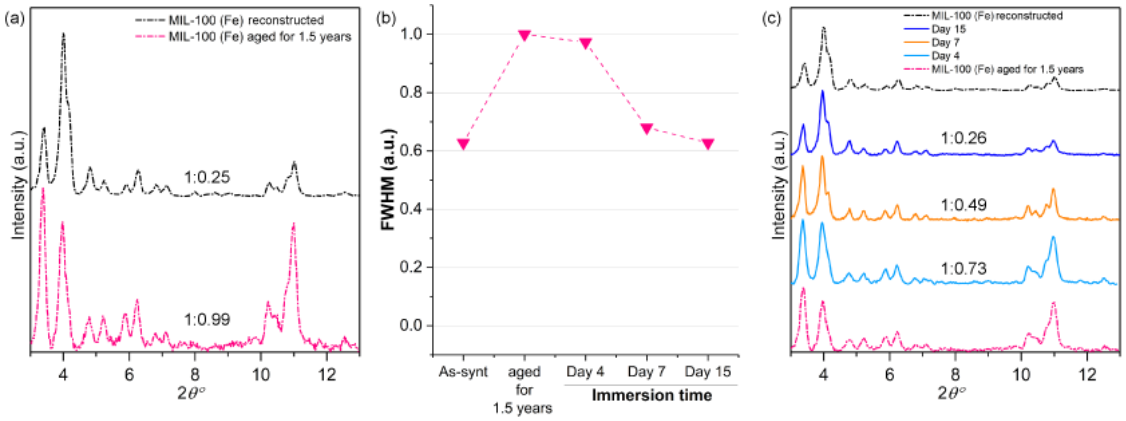

Figure 6.10: (a) Normalized PXRD pattern of fresh MIL-100 (Fe) (black trace) and the aged sample (pink trace). (b) FWHM of the (022) plane. (c) PXRD patterns showing the recovery of crystallinity of the aged sample after immersion in DI water. To facilitate the comparison, the values have been normalized in relation to the highest FWHM value in the set of samples.

Likewise, the reconstruction process has also been successfully applied to the recovery of crystallinity of mechanically amorphized samples (Figure 6.12-6.13. As demonstrated in Figure 6.12a-b, the diffraction peaks at 4° and 11° vanish after the pelletizing process.

After relaxation of the structure (*i.e.* crushing the 10 ton pellet back to powder) some of the most intense diffraction peaks reappeared. However, the relative intensity of (022):(357) peaks is very distinct from the original powder used for the production of the pellets (MIL-100 (Fe) Day 7. The above ratio was almost completely restored after 7 days of immersion in DI water. Figure 6.12c shows the colour shift presented by the samples during the reconstruction process. The original colour is restored, which demonstrates changes in the microstructure/optical properties of the material.

Similar to what was observed during the reconstruction of the aged samples, Figure 6.13a-b shows the broadening of the carboxylate vibration band at 1355 cm^{-1} after pelletizing and the sharpening of the same band after the reconstruction process, indicating the increase in the structural symmetry of the sample. Concomitantly, as it can be seen from Figure 6.13c, the material is almost non-porous with a much reduced surface area of 14 m^2/g. The BET surface area presented a recovery of only 27.7% compared to its initial value, going up to 276 m^2/g. This indicates that

even though recovery of the mechanically amorphized material has been made in terms of crystallinity, the porosity could not be fully restored.

These are important findings that can pave the way to the regeneration and recycling of MIL-100 materials, thereby addressing one of the main challenges preventing their industrial applications [205, 206].

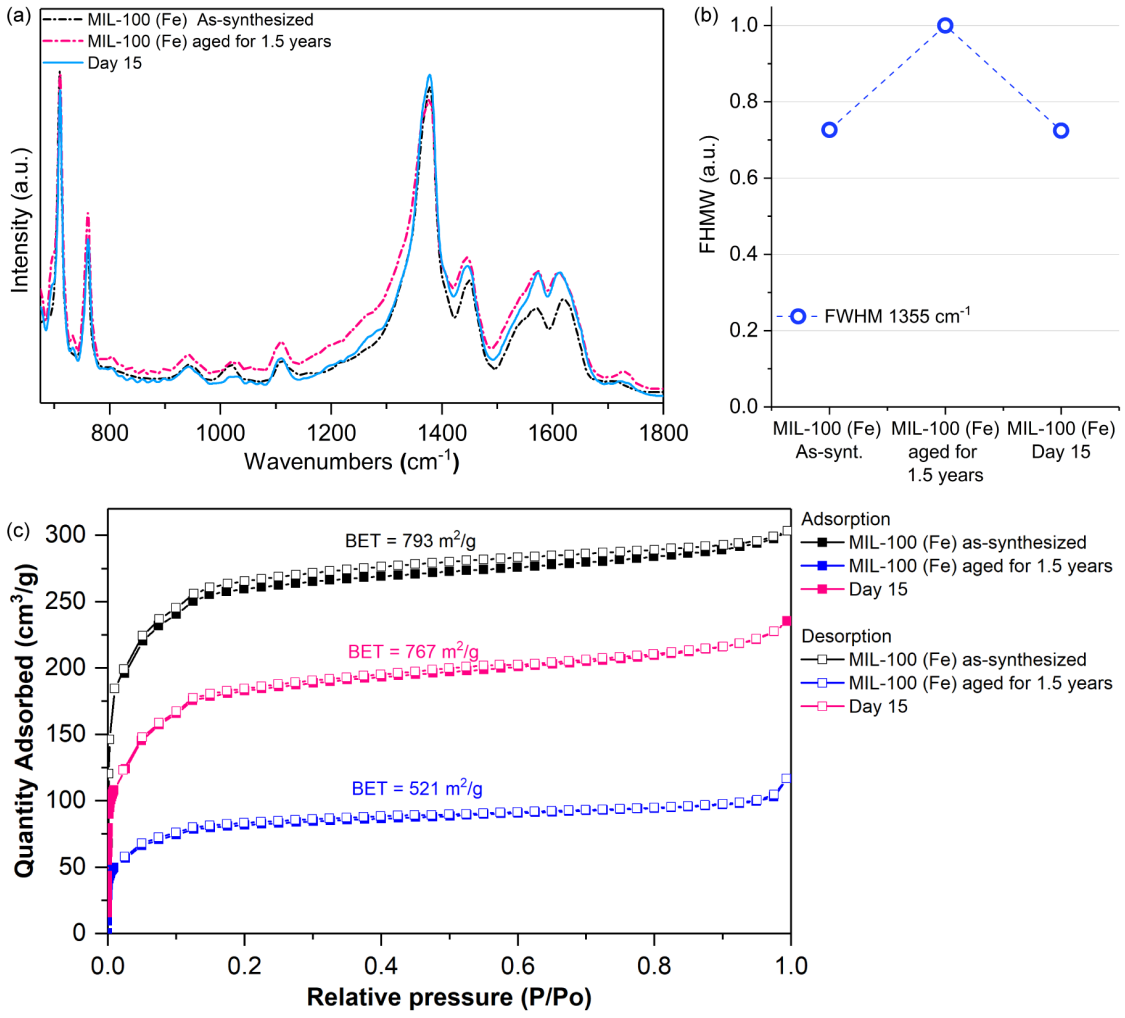

Figure 6.11: Analysis of vibrational data of the reconstructed aged sample. (a) ATR-FTIR spectra of aged samples under reconstruction. The spectra has been normalized in relation to the most intense vibrational peak. (b) FWHM values of vibration band at ~1355 cm^{-1} highlighting the sharpening of carboxylate vibration after the reconstruction process. (c) N_2 adsorption and desorption isotherms of time degraded MIL-100 (Fe) samples under reconstruction. Samples were activated at 150 °C under high vacuum for 12 hours prior to the N_2 adsorption measurements at 77 K. The BET surface area presented a recovery of 96.7% versus the initial value.

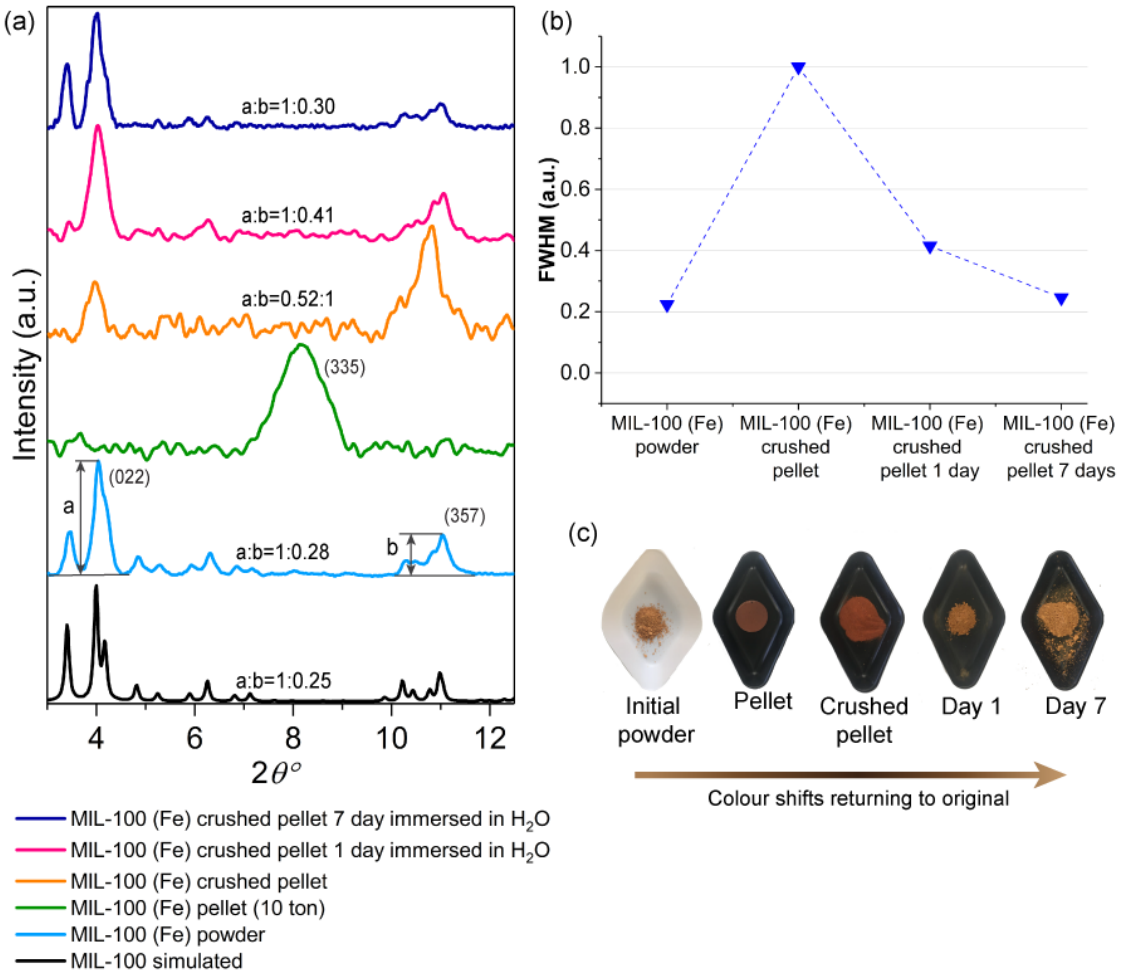

Figure 6.12: Reconstruction of mechanically amorphized samples. (a) PXRD patterns showing the progressive change in the relative intensity of the diffraction peaks. The patterns have been normalized in relation to the most intense diffraction peak. (b) Colour shift presented by the samples during the reconstruction process in which the original colour is restored demonstrating changes in the microstructure/optical properties of the material. (c) FWHM used to assess the sharpening of the (022) peak. As it can be observed, after the pelletizing, the diffraction peak corresponding to the (022) plane becomes very broad. However, the FWHM values are virtually restored to the pristine material values after the reconstruction process.

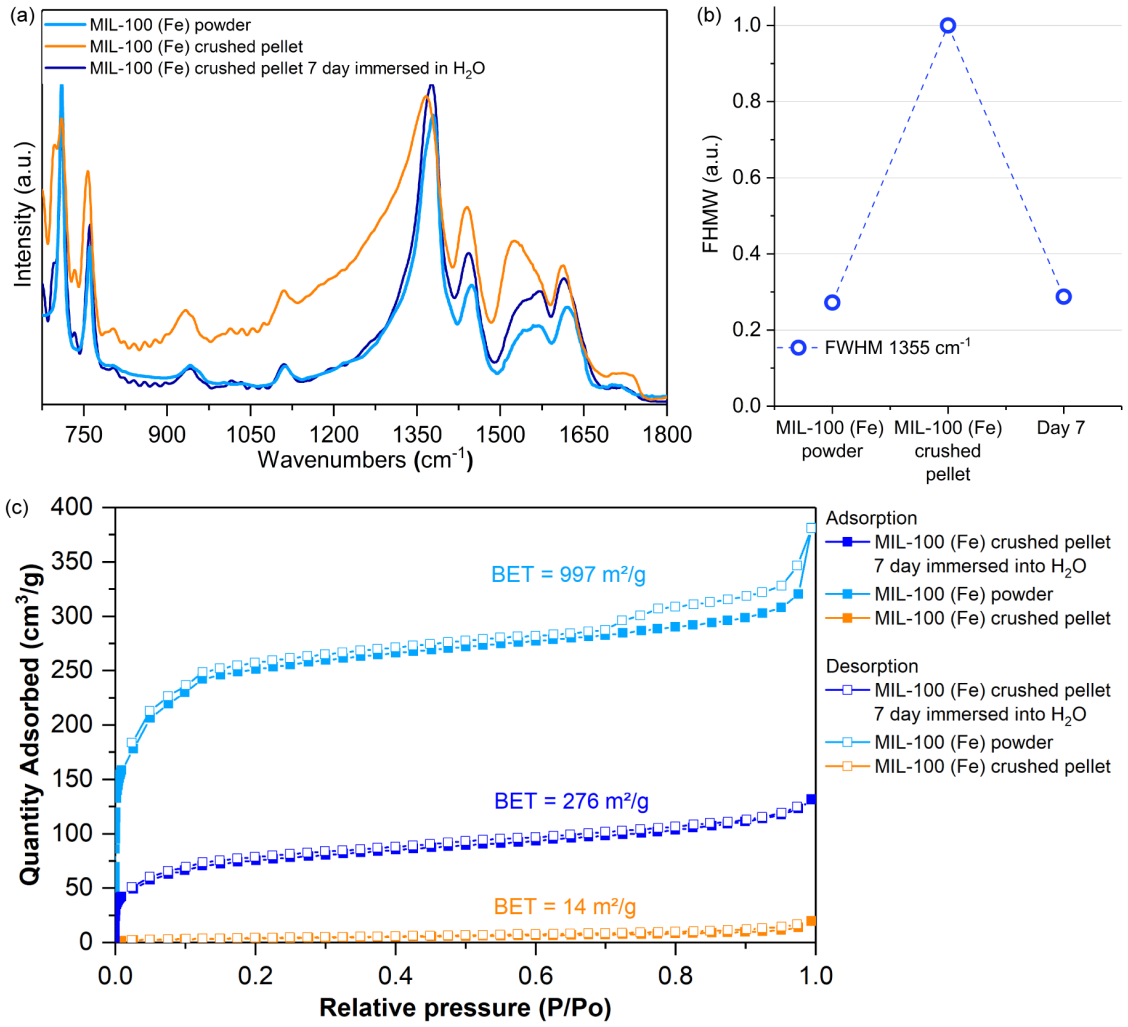

Figure 6.13: Analysis of vibrational data of reconstruction of MIL-100 (Fe) pellet sample. (a) ATR-FTIR spectra of pelletized samples under reconstruction. The spectra has been normalized in relation to the most intense vibrational peak. (b) FWHM values of vibrational band at ∼1355 cm^{-1} highlighting the sharpening of carboxylate vibration after the reconstruction process. (c) N_2 adsorption and desorption isotherms of mechanically amorphized MIL-100 (Fe) samples under reconstruction. Samples were activated at 150 °C under high vacuum for 12 hours prior to the N_2 adsorption measurements at 77 K. The BET surface area presented a recovery of only 27.7% compared to its initial value.

6.4 Analysis of the lattice dynamics and low energy vibrations in reconstructed samples *via* INS

Figure 6.14 displays the INS spectra of MIL-100 (Fe) samples collected after 2, 4, 7, and 12 days of immersion in water. Collective modes vibrations associated

Table 6.3: Description of vibrational modes of H_3BTC (0-800cm^{-1})

Mode no.	Theo. (cm^{-1})	Exp. (cm^{-1})	Description
1	20-133	21-183	γCOOH, γCO, and γring including trampoline like motion
2	218	202	γCO
3	272	273	δCO
4	332	334	
5	361	358	γring and γOH
6	470	464	δCC and δOH
7	505	506	δCO and δOH
8	603	600	γring and δOH
9	635	636	δOH and δCH
10	674	685	
11	714	750	δCO and δCC
12	780	786	

δ = in-plane bending, γ = out-of-plane bending

with the lattice dynamics of the framework structure and their analysis *via* INS spectroscopy can provide further insights into how the structure of MIL-100 (Fe) is rebuilt during the reconstruction process. Due to the difficulty in isolating the origin of each THz vibration in a complex system like MIL-100 (Fe), the INS spectrum of the H_3BTC linker was collected (Figure 6.14a) and correlated with DFT calculations [207]. The complete comparison between experimental and theoretical spectra of H_3BTC accompanied by description of the vibrational modes are found in Figure 6.15 and Table 6.3.

As displayed in Figure 6.14a, the H_3BTC molecules may establish hydrogen bonding interactions *via* –COOH groups. By contrasting the linker and framework spectra, the identification of the modes that are predominantly influenced by the BTC linker within the framework structure of MIL-100 (Fe) was performed. A good agreement between H_3BTC and MIL-100 (Fe) spectra was observed, both in the low and high energy regions (Figure 6.14b and Figure 6.16). It can be seen in Figures 6.14b-d that the overall MIL-100 (Fe) INS spectral intensity declines with a higher sample immersion time. This decay can be attributed to two factors. First, as mentioned in the previous chapter, in the INS spectrum generated on TOSCA,

the intensity at low frequency (*i.e.* low momentum transfer (Q)) is proportional to the mean square displacement of the atoms from their equilibrium position. At higher frequency, however, the intensity is suppressed by the Debye–Waller factor [201]. On this basis, the decline in the scattering intensity in the low energy region, below 9 THz (< 300 cm^{-1}), with the increase of immersion time suggests the reduction of atomic motions. As the periodicity of the MIL-100 (Fe) samples

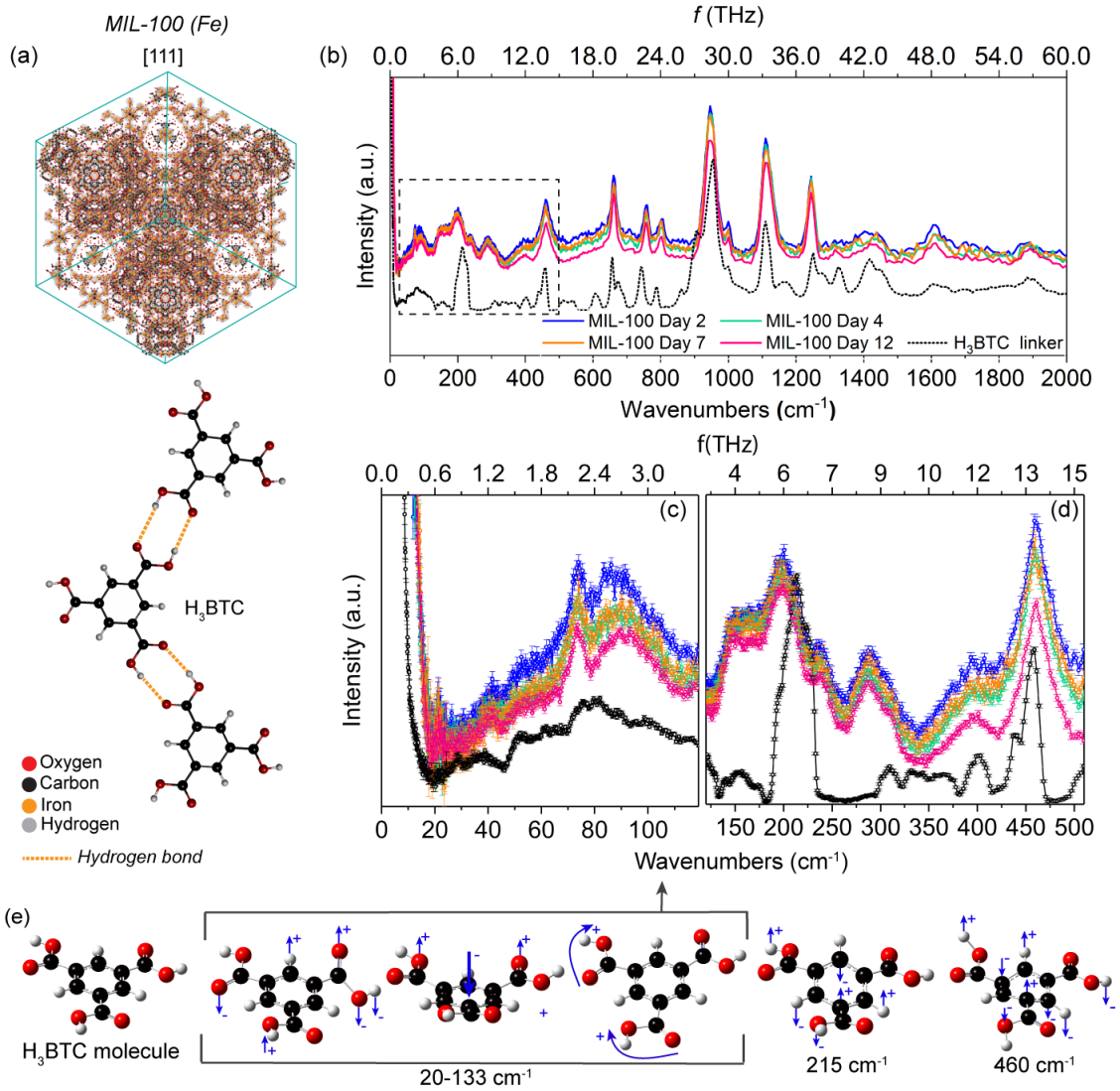

Figure 6.14: INS measurements of reconstructed MIL-100 (Fe) samples. (a) Representation of MIL-100 (Fe) unit cell and H_3BTC molecules interacting *via* hydrogen bonds. (b) INS spectra of MIL-100 (Fe) samples measured after different immersion times are presented against the spectrum of H_3BTC linker (scaled down to facilitate comparison to the MIL framework spectra). Closer look at the (c) low energy region (0-120 cm^{-1}), and (d) 145-510 cm^{-1} range. (e) Schematic representation of H_3BTC molecular vibrations at different wavenumbers, as simulated by DFT (B3LYP, 6-31G basis set).

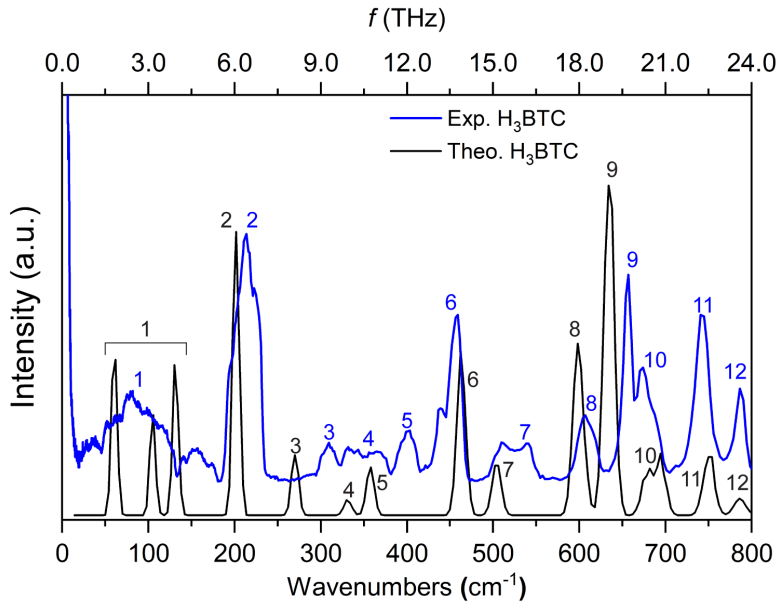

Figure 6.15: Comparison between experimental INS spectrum (blue) and theoretical DFT spectrum of (black) H_3BTC. Numbers were used to facilitate the identification of the vibrational modes. Good agreement between both spectra is observed in the low energy region.

improves, it is reasoned that stronger constraints are imposed onto the atomic movements in the framework.

This result is substantiated by the notable rise in the thermal stability of the reconstructed framework *via* TGA, see Figure 6.17), where an ∼48% increase in the initial decomposition temperature was recorded. Table 6.4 displays details of the decomposition process of MIL-100 (Fe) sample acquired from the TGA plots (Figure 6.17). A large increase in the initial decomposition temperature of the crystalline MIL-100 (Fe) in comparison to the as synthesized material can be observed. A decrease (∼20%) in the rate of the composition between 210-450 °C was also noticed. Meanwhile, the maximum rate of decomposition, the temperature in which half of the material has decomposed and the final residue have remained virtually unchanged.

Another factor that contributes to the overall spectrum intensity is the amount of hydrogen atoms present in the sample, due to the large incoherent neutron cross section of hydrogen atoms, the largest amongst all known elements [208]. The observed decrease in spectral intensity can, therefore, be correlated with the depro-

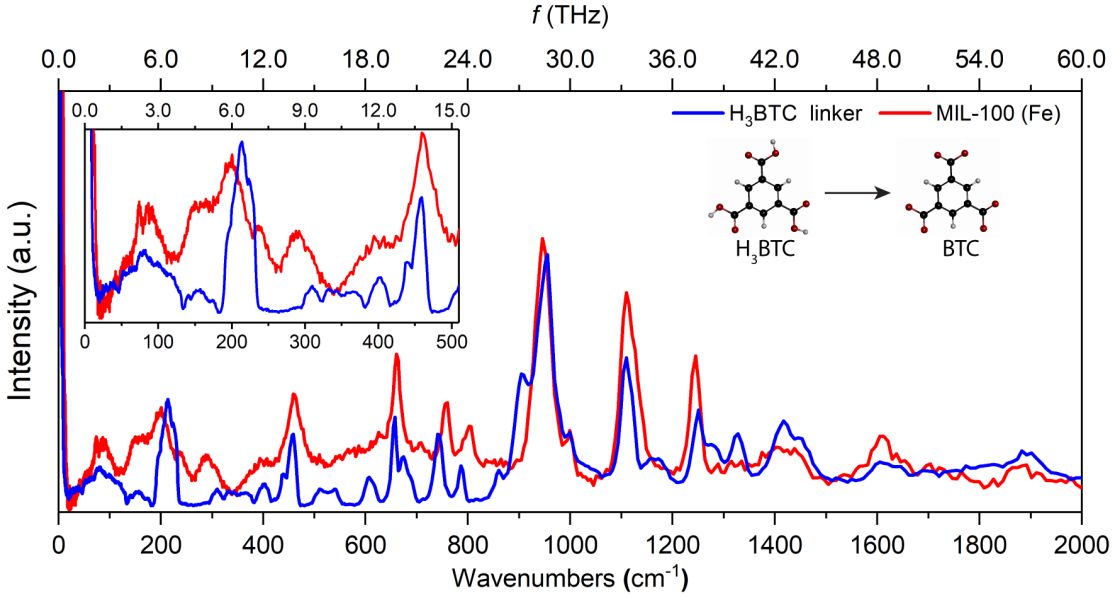

Figure 6.16: INS spectra of pristine MIL-100 (Fe) sample (red) and organic linker H_3BTC (blue). Good agreement is observed between framework modes and organic linker modes, helping us to pinpoint in the MOF spectrum the vibrational modes related to the organic linker. Note that the H_3BTC spectrum was scaled down by a factor of 0.3 to facilitate comparison with the MOF spectrum. Colour code: O in red, C in black, and H in grey.

tonation of the organic linker, previously observed in the ATR-FTIR measurements (Figure 6.5b). As shown in the inset of Figure 6.16, the acidic form of the organic ligand (*i.e.* H_3BTC) has twice as many hydrogen atoms than its deprotonated counterpart (*i.e.* BTC). In the low energy region, H_3BTC vibrations are dominated by the out of plane bending of COOH, including 'trampoline like' motions [120], at 0.6-4.0 THz (20-133 cm^{-1}), out-of-plane CO bending at ∼6.4 THz (215 cm^{-1}), and ring deformation accompanied by OH bending at ∼13.8 THz (460 cm^{-1}), as

Table 6.4: Analysis of thermal decomposition of reconstructed MIL-100 (Fe)

	MIL-100 (Fe) As-synthesized	**MIL-100 (Fe) Day 15**
Initial decomposition temperature	210°C	310°C
Rate of decomposition (210°C-450°C)	-0.076 %/°C	-0.061 %/°C
Maximum rate of decomposition	-0.275 %/°C	-0.289 %/°C
Temperature of half decomposition	574°C	578°C
Final residue (at 660°C)	37 %	38 %

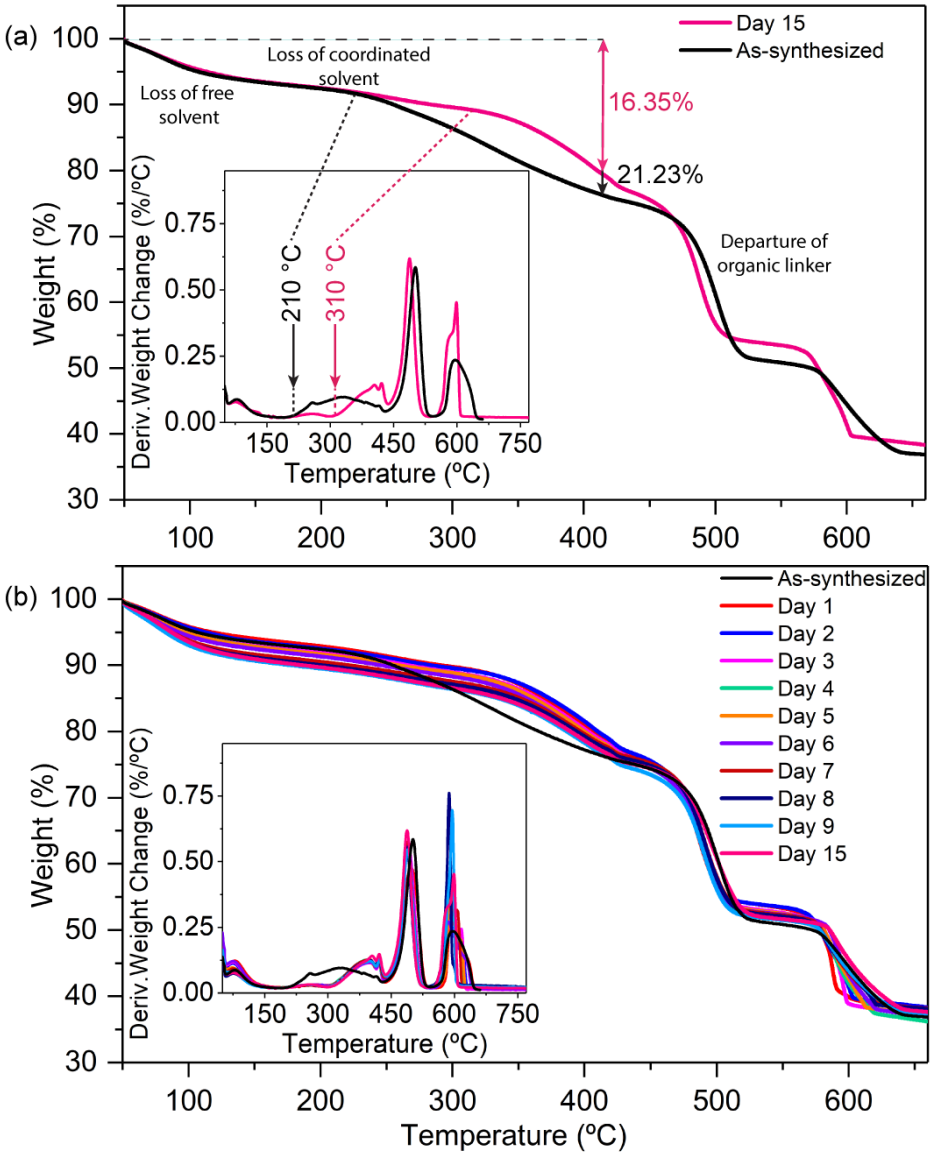

Figure 6.17: TGA of reconstructed MIL-100 (Fe) samples with insets showing the differential material decomposition behaviour as a function of temperature. (a) Contrast between the as-synthesized MIL-100 (Fe) and reconstructed MIL-100 (Fe) after 15 days of immersion time. An increase in the thermal stability of the material is observed (∼100 °C difference in the initial decomposition temperature of the material). (b) Contrast between TGA of the as-synthesized sample and samples subjected to different immersion times.

illustrated in Figure 6.14e and described in Table 6.3[207]. These vibrational modes, involving the large displacement of hydrogen atoms, show a decline in intensity upon the increase of sample immersion time, thus, the INS results support the notion that the reconstruction of MIL-100 (Fe) mesocages is controlled by the deprotonation of the organic linkers.

6.5 Fabricating drug@MIL-100 systems *via* the water reconstruction method

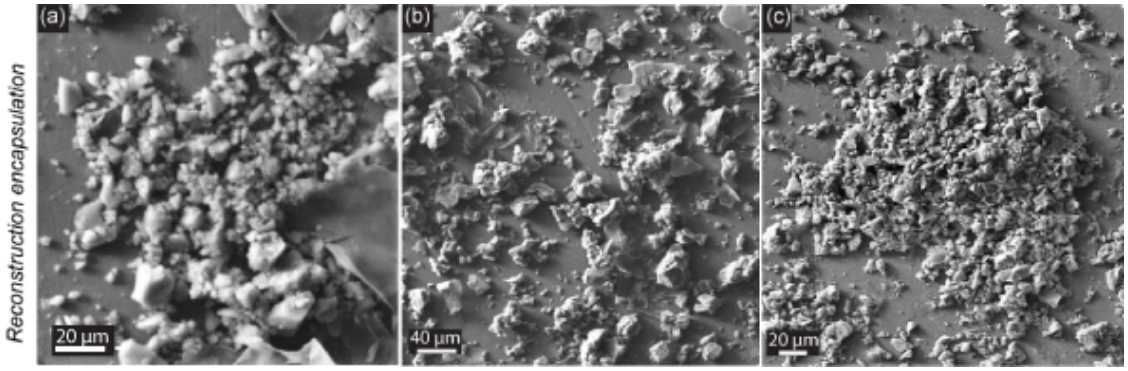

Figure 6.18: SEM images of guest@MIL-100 systems. (a) 5-FU@MIL-100_REC, (b) CAF@MIL-100_REC, and (c) ASP@MIL-100_REC.

The reconstruction approach can additionally be applied to fabricate highly loaded guest@host systems (termed: guest@MIL-100_REC) leading to the encapsulation of different drug molecules (guest = 5-FU, CAF, and ASP) when MIL-100 (Fe) cages are being reconstructed. SEM images of drug@MIL-100 systems reveal that the drug loaded samples produced *via* the reconstruction encapsulation approach have a similar morphology to the reconstructed MIL-100 (Fe) samples (Figure 6.18).

Figures 6.19a-c show the PXRD patterns of drug@MIL-100_REC systems. The relative intensity of (022):(357) planes and the FWHM of the (022) corresponding peak of the drug@MIL-100 systems were calculated and contrasted to assess the effect that the confinement of the different drug molecules have on the crystallinity of the host material. Through the reconstruction process, 5-FU@MIL-100_REC with high crystallinity was successfully obtained. Generally, it can be seen that the relative peak intensity in 5-FU@MIL-100_REC (*i.e.* 1:0.30) agrees well with

reconstructed MIL-100 (Fe) (1:0.27) (Figure 6.19a). The FWHM in Figure 6.20 shows that the confinement of 5-FU within MIL-100 (Fe) pores did not affect the periodicity and crystallinity of the resultant framework. Similar effect was observed in CAF@MIL-100_REC, for which the relative peak intensity (*i.e.* 1:0.37) and the FWHM of (022) peak were slightly larger than in 5-FU loaded counterpart, but still in close agreement with MIL-100 (Fe) pristine material (Figures 6.19a

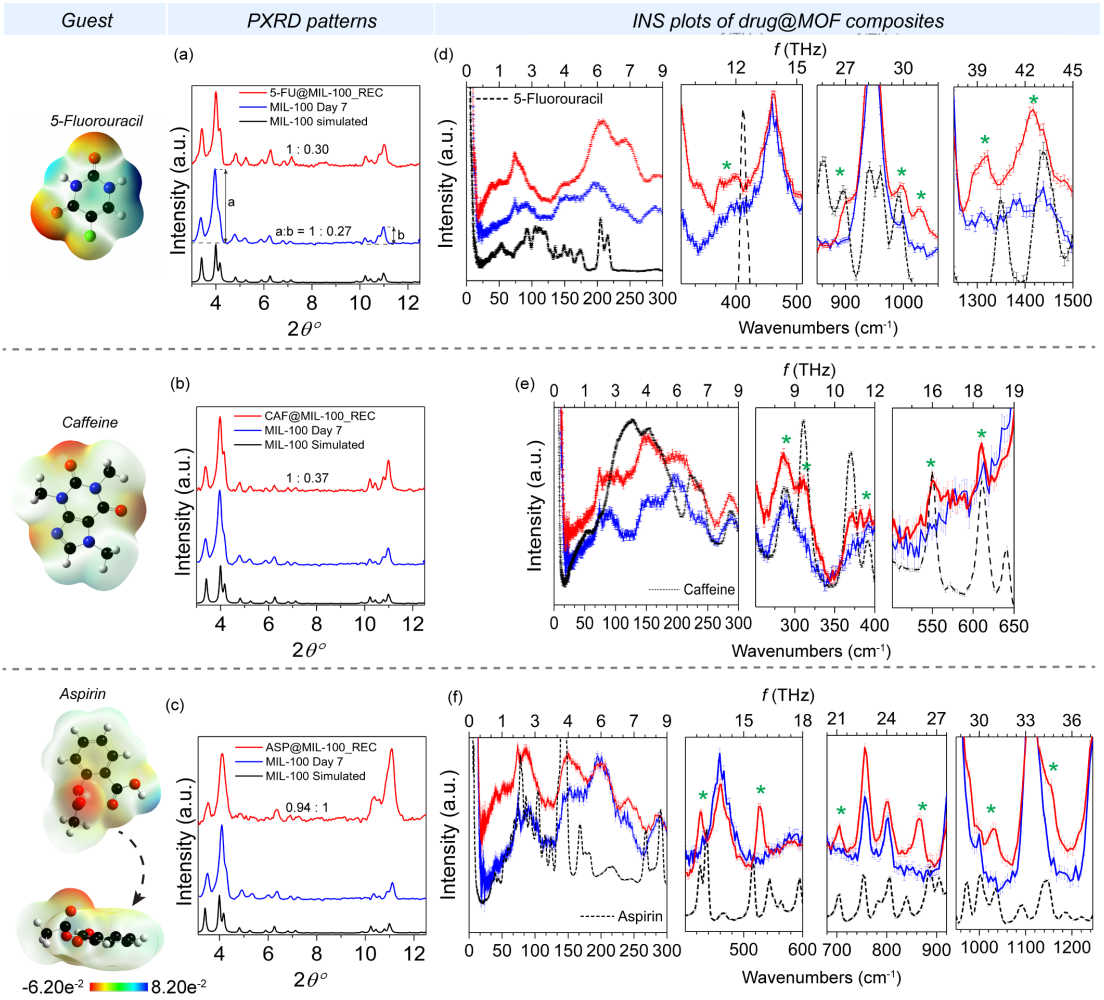

Figure 6.19: Normalized PXRD patterns and INS spectra of drug@MIL-100_REC systems. The diffraction patterns are presented for assessment of the materials crystallinity as (a) 5-FU@MIL-100_REC, (b) CAF@MIL-100_REC, and (c) ASP@MIL-100_REC. INS spectra of (d) 5-FU@MIL-100_REC, (e) CAF@MIL-100_REC, and (f) ASP@MIL-100_REC, with closer look at the drug peaks present in the drug@MIL-100_REC systems, highlighted with asterisks. The guest drug molecules and their respective electrostatic potential maps (ESP) were presented, for which aspirin is shown in two different angles for better visualization. Colour code: O in red, C in black, H in grey, N in navy blue, F in green.

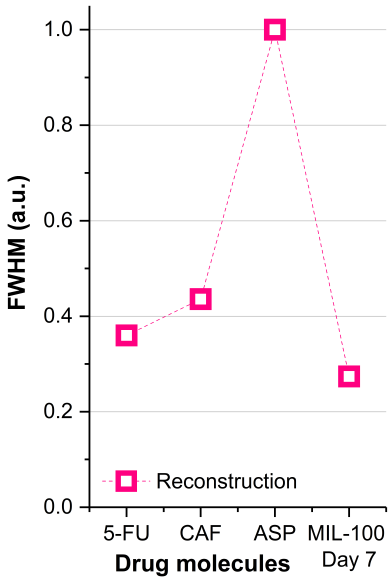

Figure 6.20: FWHM used to assess the sharpening of the (022) peak in the drug@MIL-100_REC systems, contrasting the effect of the different guest drug molecules being used. The plots evidence the strong effect on the material crystallinity that aspirin has in comparison to the other drug molecules when the reconstruction strategy is applied for the encapsulation of the guest molecules. To facilitate the comparison, the values have been normalized in relation to the highest FWHM value among this set of samples.

Figure 6.21: Photograph showing the various MIL-100 (Fe) samples after the encapsulation reconstruction process, showing a distinct colour difference between 5-FU@MIL-100_REC and CAF@MIL-100_REC to ASP@MIL-100_REC. This is due to the formation of a violet aspirin-iron complex known as tetraaquosalicylatroiron (III) complex (inset). When in contact with moisture, aspirin dissociates into acetic and salicylic acid. The latter then can react with acidified iron (III) ions to form the violet complex.

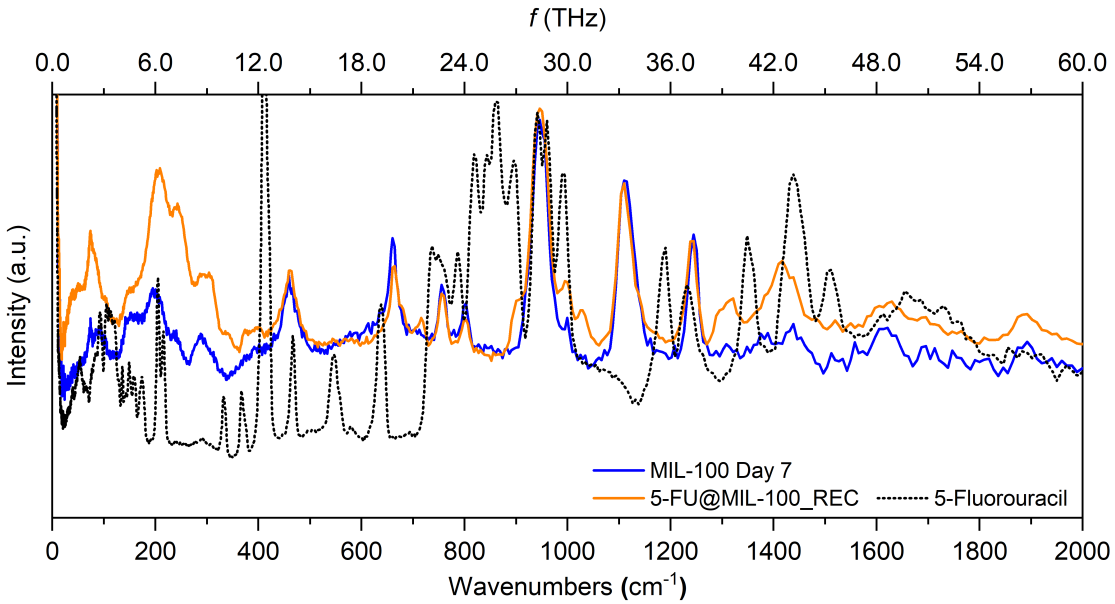

Figure 6.22: INS spectra of 5-FU@MIL-100_REC yielded by the reconstruction encapsulation method. Spectrum of 5-FU presented in black was scaled down by a factor of 0.4 to facilitate the comparison with the guest@MIL-100 systems.

and 6.20). The fabrication of ASP@MIL-100_REC was correspondingly achieved, however, the periodicity of the material was reduced when contrasted to the other drug@MIL-100_REC systems. After the encapsulation of aspirin, the relative intensity of diffraction peaks (*i.e.* 0.9:1) was dissimilar to the value of MIL-100 (Fe) and a large broadening of the (022) peak was detected (Figure 6.20). These results indicate that aspirin, in some degree, interferes with the establishment of long range ordering of the host framework. This is because of the competition between aspirin and the H_3BTC linker molecules for coordination to the iron cations, leading to formation of an amorphous violet Fe-ASP complex known as tetraaquosalicylatroiron (III) (Figure 6.21), which formation has also been described in Chapter 5.

Figures 6.19d-f display the INS spectra of the drug@MIL-100_REC composite systems. The full spectra up to ~60 THz (2000 cm^{-1}) are shown in Figures 6.22-6.24. Scrutiny of the THz vibrations can provide insights on the guest-host interactions and reveal how the encapsulation of the different drug molecules affects the long range dynamics of the host framework structure.[209] The spectra of the pure guest molecules were also collected and used for the assignment of the drug peaks in drug@MIL-100_REC. Analysis of the INS spectra shows that in all

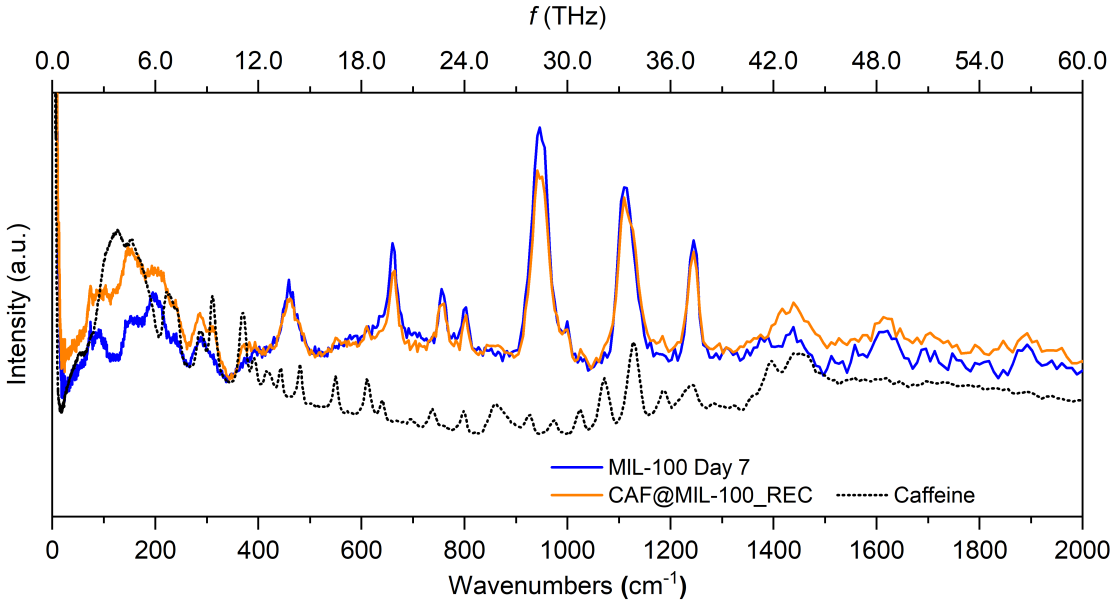

Figure 6.23: INS spectra of ASP@MIL-100_REC yielded by the reconstruction encapsulation method. Spectrum of caffeine presented in black was scaled down by a factor of 0.2 to facilitate the comparison with the guest@MIL-100 systems.

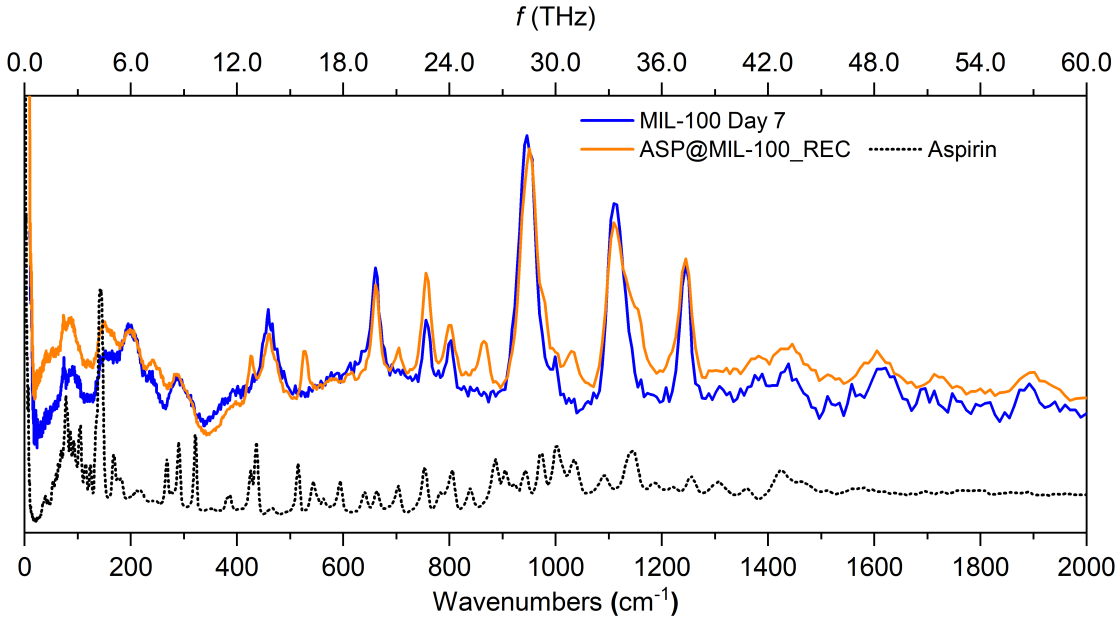

Figure 6.24: INS spectra of ASP@MIL-100_REC yielded by the reconstruction encapsulation method. Spectrum of aspirin presented in black was scaled down by a factor of 0.1 to facilitate the comparison with the guest@MIL-100 systems.

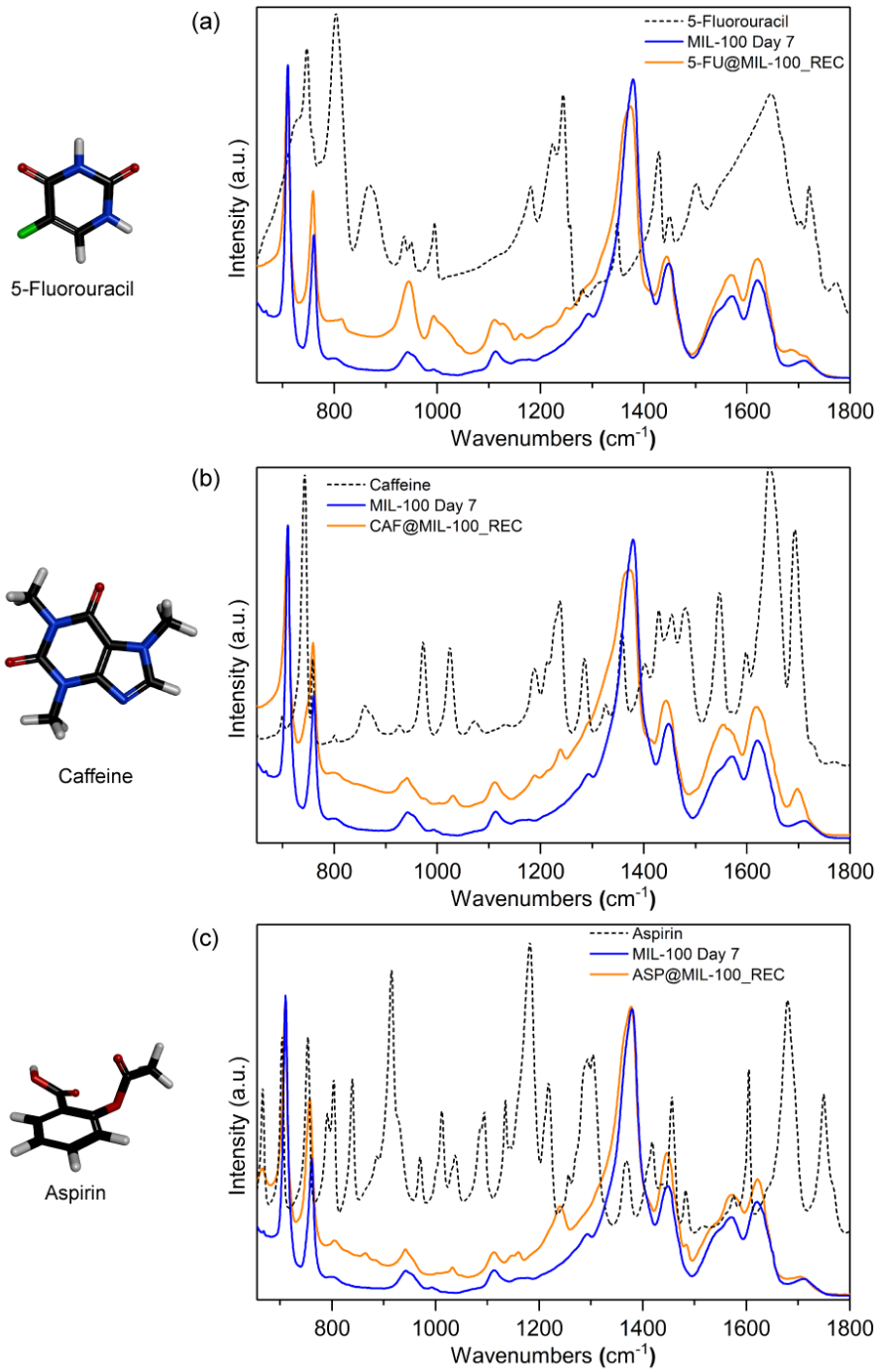

Figure 6.25: Normalized ATR-FTIR spectra of drug@MIL-100_REC systems displaying (a) 5-FU@MIL-100_REC, (b) CAF@MIL-100_REC, and (c) ASP@MIL-100_REC. For comparison, the spectrum of MIL-100 (Fe) after 7 days of immersion time was also presented. Colour code: O in red, C in black, H in grey, N in navy blue, F in green.

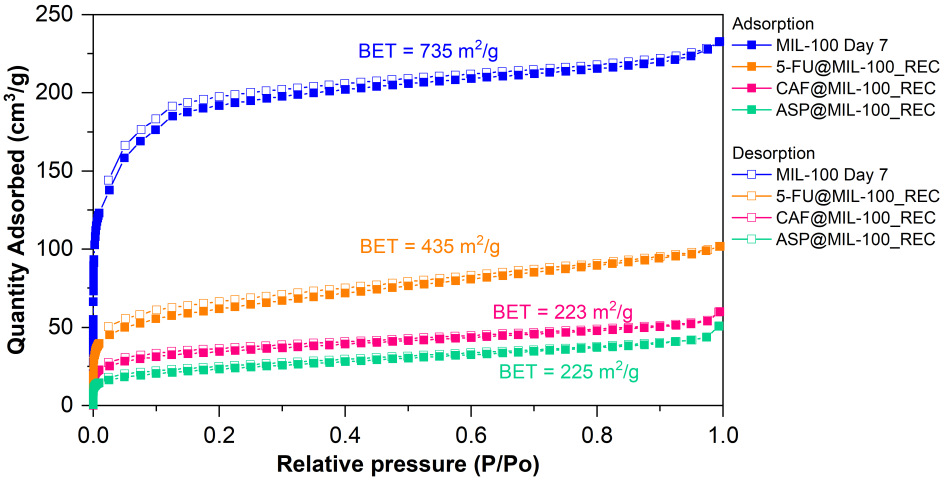

Figure 6.26: N_2 adsorption and desorption isotherms of 5-FU@MIL-100_REC, CAF@MIL-100_REC, and ASP@MIL-100_REC systems.

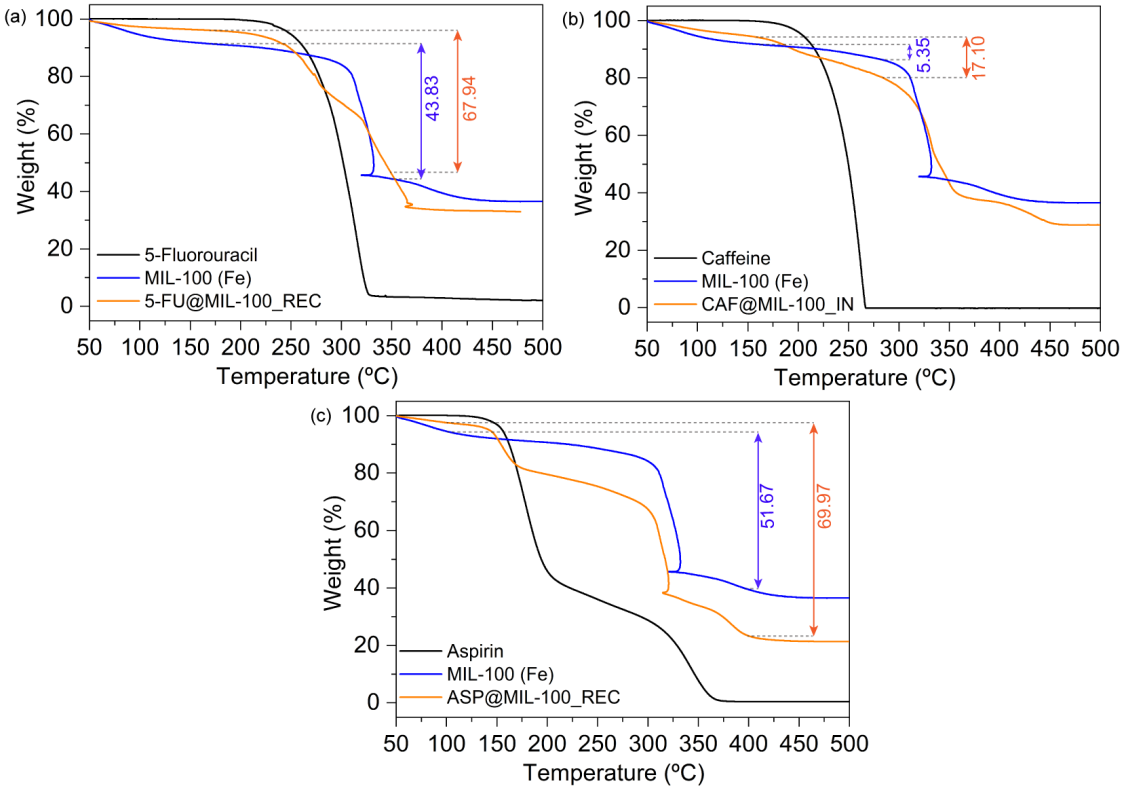

Figure 6.27: TGA of drug@MIL-100_REC systems showing the material decomposition behaviour as a function of temperature. (a) 5-FU@MIL-100_REC, (b) CAF@MIL-100_REC, and (c) ASP@MIL-100_REC.

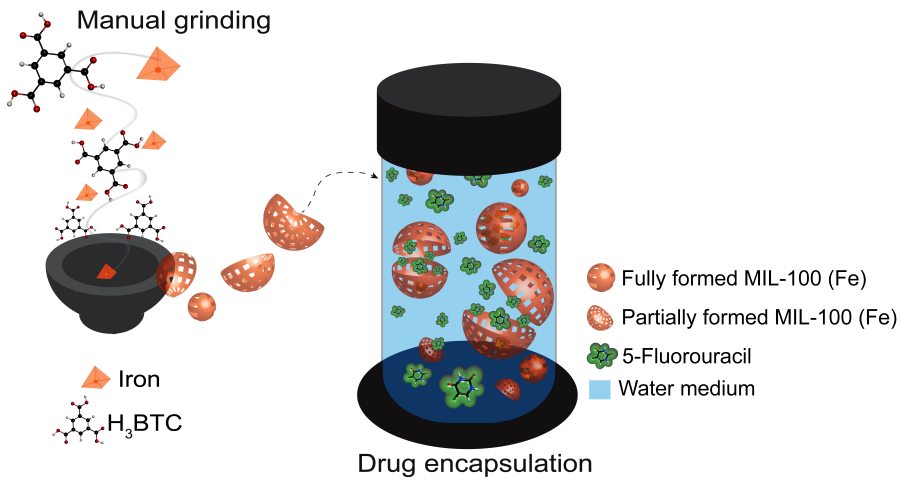

Figure 6.28: Schematic representation of the speculated guest encapsulation mechanism during the reconstruction process immersed in water. The formation of the MOF cages around the drug molecules allows the achievement of high guest loadings.

guest@host systems considered, the distinctive vibrational peaks of guest molecules were detected. This is akin to what was also observed in the high energy region, in which the ATR-FTIR spectra of the drug@MOF systems (Figure 6.25) also display the presence of the drug molecules.

To correlate the influence of the drug:MOF ratio on the drug@MIL-100_REC spectra, the level of guest encapsulation was evaluated by BET surface area (Figure 6.26) and quantified by TGA using Equation 3.2 (Figure 6.27). Overall, remarkably high drug loadings of 35.5 wt.%, 64.7 wt.% and 50 wt.%, were achieved for 5-FU@MIL-100_REC, CAF@MIL-100_REC, and ASP@MIL-100_REC, respectively.

The BET surface areas of the samples were found to be greatly reduced, confirming successful guest encapsulation. In Table 6.5, the guest loadings herein attained are compared against previously reported results. In the work by Cunha *et al.*[13] a theoretical approach has been used to estimate the maximum loading of caffeine molecules in MIL-100 (Fe) mesocages. A theoretical loading capacity of 65.8 wt.% was established when full accessibility of both small and large cages (*i.e.* 25 and 29 Å in diameter) was considered. However, using the conventional impregnation technique (*i.e.* immersion of the host MOF into a saturated drug solution) an experimental loading of only 49.5 wt.% was attained by Cunha and co-workers.

Table 6.5: Comparison of drug loadings achieved in drug@MIL-100_REC samples and systems produced *via* various other methods.

Drug	MOF	Synthesis method	Drug loading (wt.%)	Ref.
5-FU	MIL-100	Reconstruction	35.5	This Chapter
	MIL-100	Immersion into drug solution	66.0	
	MIL-88		28.0	[200]
	MIL-53		13.1	
Caffeine	MIL-100	Reconstruction	64.7	This Chapter
		Immersion into drug solution	49.7	[13]
	MIL-100		24.2	[6]
			52.4	[10]
Aspirin	MIL-100	Reconstruction	50.0	This Chapter
	MIL-100	Immersion into drug solution	24.8	[87]
	MIL-100		1.8 *	[51]
	MIL-127		0.14 *	[148]

*: g/g of MOF

The difference between the theoretical loading capacity and the experimental loading were attributed to the non-accessibility of caffeine molecules (7.6 × 6.1 Å) into the small cages of MIL-100 (Fe) due to the reduced size of its pentagonal window aperture (∼4.5 × 5.5 Å). Conversely, higher experimental loadings were achieved using the water reconstruction methodology (*i.e.* 64.7 wt.%). As illustrated in Figure 6.28, instead of having to overcome the physical obstacle imposed by the narrow pore windows, the guest drug molecules get encapsulated by the formation of the MIL-100 (Fe) cages around them. This improves the occupancy of the small and large cages allowing us to harness the full hosting potential of MIL-100 (Fe). The possibility of confinement of guest molecules in the small cages of MIL-100 (Fe) opens new frontiers to tuning the prolonged release of therapeutic molecules (avoiding burst release effect *via* the slow decomposition of pore cages) and to yield permanent encapsulation of bulky guests, such as fluorescent dyes for photoluminescent devices [210].

Further insights into the dynamics of the guest-host interaction can be drawn by analyzing the INS spectra. The relatively higher intensity observed in the spectra

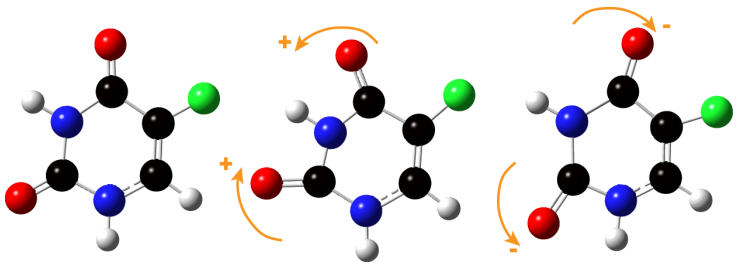

Figure 6.29: Illustration of the in-plane bending of OCNCO at ∼12.3 THz (∼410 cm^{-1}). Arrows indicate the directions of the collective deformations with +/- amplitudes computed by DFT (B3LYP, 6-31G basis set). Colour code: O in red, C in black, H in grey, N in navy blue, F in green.

of the guest@MIL-100_REC, specifically in the 0-9 THz (0-300 cm^{-1}) range, can be associated with a combination of scattering coming from the framework and the drug molecules. As seen in Figures 6.19d-f, the spectra of the drug molecules exhibit a very high scattering intensity in the low energy region, meaning that even low amounts of encapsulated guest can have a large effect on the vibrational spectra of the drug@MIL-100_REC system.

Vibrational frequency shifts were observed in the guest vibrational modes present in the drug@MIL-100_REC spectra (marked in Figures 6.19d-f by asterisks). Such shifts indicate the existence of constraints to free motions of the drug molecule. For example, the effect of the guest confinement is evident on the 5-FU@MIL-100_REC spectrum, in which the very strong 5-FU vibration at ∼12.3 THz (∼410 cm^{-1}) associated with the in-plane bending of OCNCO is highly suppressed (Figure 6.29) [211]. Based on the electrostatic potential surface map (ESP) depicted in Figure 6.19, 5-FU molecules will bind to the CUS *via* one of their oxygen atoms through Fe···O coordination. The same scenario is repeated for caffeine and aspirin molecules, which as shown in the ESP maps in Figure 6.19, can also establish Fe···O coordination to the host MIL-100 (Fe) CUS. Similarly, the suppression and shift of the caffeine modes at ∼10.8 THz (∼360 cm^{-1}) related to C=O bending and the shift of aspirin modes at ∼12.6 THz (∼421 cm^{-1}), ∼16.0 THz (∼533 cm^{-1}) related to the C=O bending, substantiates the formation of Fe···O coordination between caffeine and aspirin to the CUS. Shift of the aspirin modes at ∼25.6 THz (∼855 cm^{-1}) and ∼31.2 THz (∼1040 cm^{-1}), associated

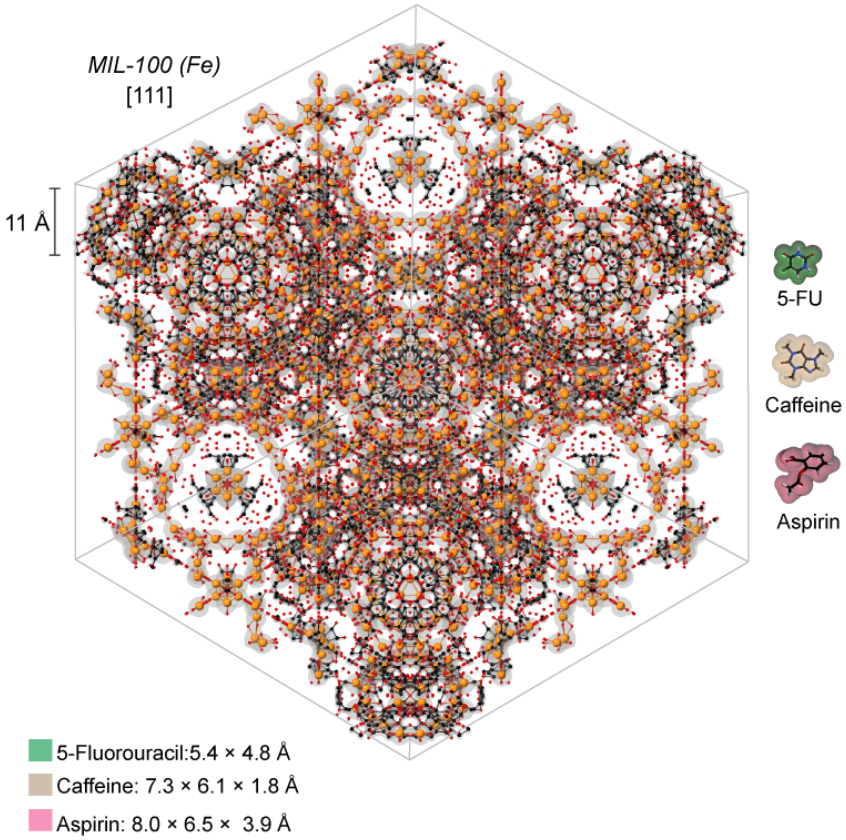

Figure 6.30: Schematic representation of MIL-100 (Fe) and guest drug molecules dimensions. The comparison showcases how the mesocages of MIL-100 (Fe) can accommodate multiple of the chosen drug molecules within the MOF pores.

with benzene ring deformation, suggests that the drug molecules simultaneously form π-π interactions with the organic linker and between drug molecules within MIL-100 (Fe) cages. In fact, comparing the size of MIL-100 (Fe) mesocages (25 and 29 Å in diameter) [192], the chosen drug molecules are considerably small (see Figure 6.30) meaning that the interactions between multiple drug molecules (*e.g.* dimers formation) are expected inside the same pore. The suppression and shifts of high intensity drug molecule modes indicate the strong guest-host interaction yielded by the employment of the reconstruction encapsulation method.

6.6 Summary and conclusions

This chapter has demonstrated the use of a low cost, green mechanochemical method applied to the facile fabrication of highly crystalline MIL-100 (Fe) material, where framework reconstruction in water leads to improved thermal stability. This

approach can be used to achieve guest@MIL-100 systems with a high loading of the encapsulated guest molecules. High-resolution INS spectroscopy aided the understanding of the guest-host interactions through unravelling the vibrational dynamics of the MIL-100 (Fe) phase and its guest-encapsulated composites. This work provides new approaches towards the eco-friendly preparation of MIL-100 (Fe) and guest@MIL-100 systems, avoiding the use of highly toxic agents that are limiting the promising biomedical applications of MIL-100 (Fe). The simple approach demonstrated here could be applied to the large scale synthesis of MIL-100 materials for future commercialization.

All sorts of things can happen when you're open to new ideas and playing around with things.

— Stephanie Kwolek

7

Examining guest-host interactions arising from the 5-FU confinement in HKUST-1

Contents

7.1 Background and motivation

The copper-based framework termed HKUST-1 has been explored as a viable host for the creation of bio-oriented guest@MOF composite systems [43, 45, 212]. Notably, the multiple CUS in the pores of HKUST-1 are highly accessible and can act as strong binding sites for guest drug molecules [46, 47]. There has also been a rising interest in the development of biologically and environmentally friendly synthesis methods to yield HKUST-1 [57].

Various studies have reported the use of mechanochemistry for the synthesis of HKUST-1, where ball milling has been used to accomplish neat or liquid-assisted grinding to fabricate porous frameworks [66, 73, 75, 213]. However, one-pot encapsulation of guest molecules into HKUST-1 *via* mechanochemistry is less common, especially its comparison with post-synthetic encapsulation, has not yet been investigated in detail. While the chemical structure and encapsulation of

certain drug@MOF combinations (guest@host system) have been reported [146, 214], and pioneering studies elucidating the chemical interaction in guest-host MOF systems have been published [108, 215, 216], studies interrogating the different dynamics arising from different encapsulation techniques are scarce.

This chapter reports the detailed characterization of 5-FU@HKUST-1 systems *via* INS. A mechanochemical method (manual grinding) was employed to accomplish *in situ* encapsulation of 5-FU within the HKUST-1 host framework, yielding the 5-FU@HKUST-1_IN composite. Its feasibility as a facile one-pot self-assembly strategy was demonstrated, in contrast to the *ex situ* encapsulation method to yield 5-FU@HKUST-1_EX (*via* immersion of pre-activated host in a saturated drug solution).

7.2 Structural analysis of 5-FU@HKUST-1

Figure 7.1a illustrates the possible guest-host interaction of 5-FU with the CUS located on the copper paddle-wheel of HKUST-1, forming C=O$\cdots$Cu coordination. Indeed, similar interactions involving organic molecules binding to HKUST-1 [47, 102] and other MOFs with open metal centres have been reported [105]. Figure 7.1b shows the PXRD patterns of the activated samples, confirming the successful synthesis of crystalline HKUST-1 through mechanochemistry. While the Bragg peaks of 5-FU@HKUST-1_EX match those of the pristine HKUST-1, the diffraction pattern of 5-FU@HKUST-1_IN is considerably different. It can be seen in Figure 7.1b that the PXRD pattern of 5-FU@HKUST-1_IN exhibits some of the major peaks of HKUST-1 (albeit shifted) and the appearance of several new diffraction peaks. These changes in diffraction pattern suggest that there is deformation to the host framework, causing the formation of a distorted phase of HKUST-1 with reduced symmetry. It is hypothesized that the successful confinement of 5-FU drug molecules within the HKUST-1 pore *via* the *in situ* encapsulation strategy could give rise to structural distortions of the HKUST-1 unit cell.

The coordination of the guest molecule to the CUS also affected the colour of the samples and its nominal density, as summarised in Figure 7.2. Interestingly, the

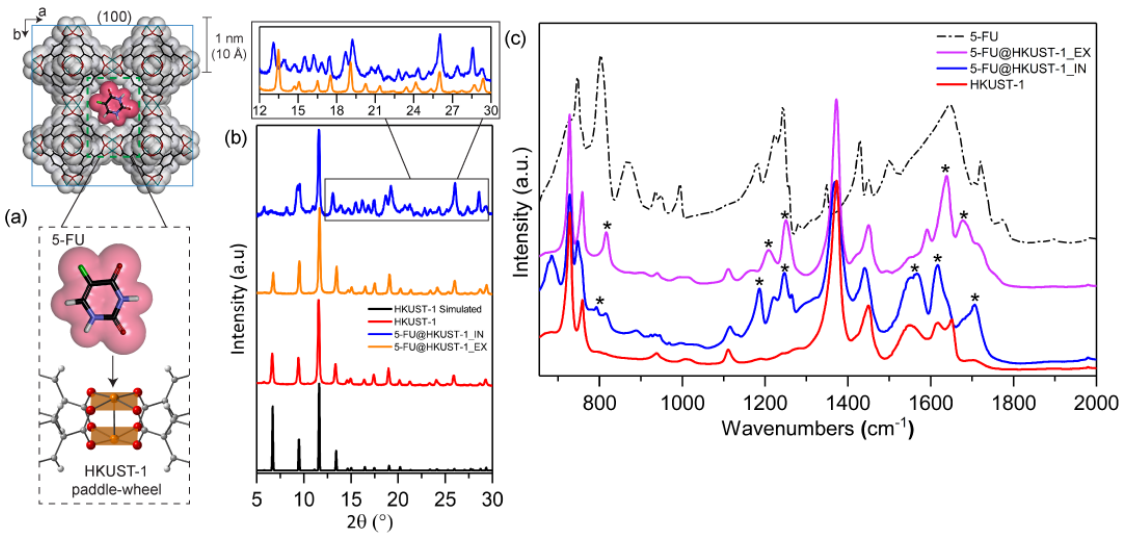

Figure 7.1: Structural characterization of HKUST-1 and drug@MOF systems. (a) Schematic representation of guest-host interaction of 5-FU to the unsaturated metal sites located at the pore apertures of HKUST-1. Colour scheme: copper in orange, carbon in grey, oxygen in red, hydrogen in white, nitrogen in purple, and fluorine in green. (b) Normalized PXRD patterns of manually ground HKUST-1 and its drug-loaded counterparts. Inset shows the additional diffraction peaks emerging in 5-FU@HKUST-1_IN, compared to 5-FU@HKUST-1_EX. c) Normalized FTIR spectra of HKUST-1 samples measured in ATR mode. Asterisks mark the position of the 5-FU peaks. Colour code: O in red, C in grey, H in white, Cu in orange, N in navy blue, and F in turquoise.

cubic structure of HKUST-1 is recoverable upon release of encapsulated guest from the 5-FU@HKUST-1_IN composite (Figure 7.3), evidenced from the emergence of Bragg peaks matching the pristine structure of HKUST-1. The release of the guest drug molecules was performed by immersion of the MOF encapsulated drug into abundant MeOH for three days (refer to Chapter 3 for the complete details). This recovery was also accompanied by the return of the characteristic colour shift of HKUST-1 upon activation, indicating the change in the copper coordination after guest release. On the other hand, 5-FU@HKUST-1_EX maintains its crystal integrity after release of 5-FU, showing no detectable structural changes (Figure 7.4). Importantly, the release of the guest can be confirmed by tracking the disappearance of the 5-FU peak in the ATR-FTIR spectra. 5-FU@HKUST-1_EX shows a nearly perfect recovery (Figure 7.5) towards a pristine HKUST-1, whereas 5-FU@HKUST-1_IN is less complete in 1500-1700 cm^{-1} (Figure 7.6) indicating a stronger guest-host interaction.

The level of guest encapsulation was evaluated by BET surface area determination (Figure 7.8) and quantified by TGA using Equation 3.2 (Figure 7.7). The surface area of the pristine HKUST-1 (1068 $m^2\,g^{-1}$) is in agreement with the values of other reported HKUST-1 samples synthesized *via* mechanochemistry and other conventional techniques (Table 7.1). The drug loadings in 5-FU@HKUST-1_IN and 5-FU@HKUST-1_EX have been determined *via* Equation 3.2 to be 14.6 wt.% and 18.8 wt.%, respectively. The BET surface area of the samples was found to be greatly reduced to 13 $m^2\,g^{-1}$ and 463 $m^2\,g^{-1}$, respectively. SEM and AFM images

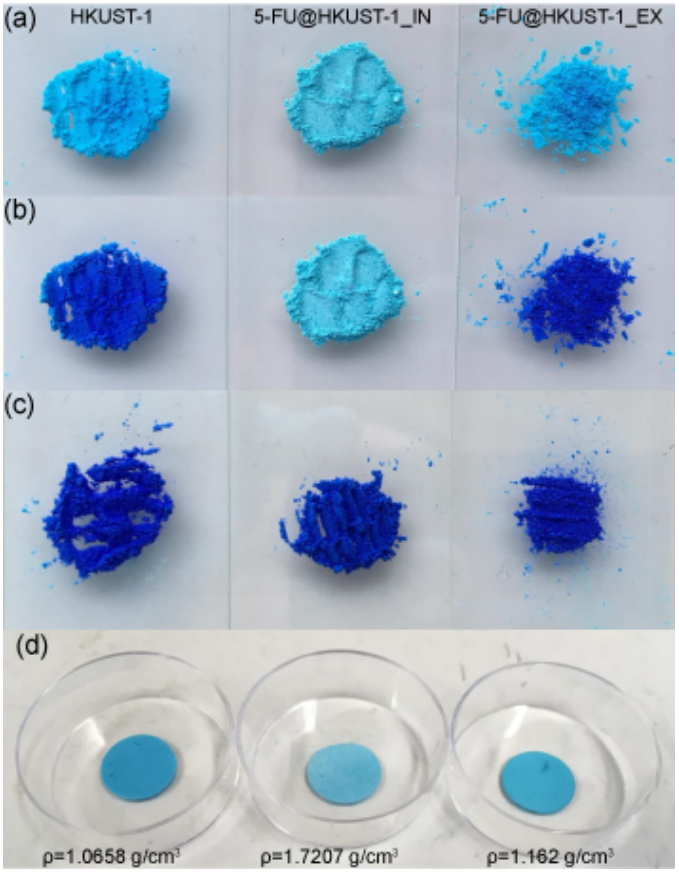

Figure 7.2: Colour change observed in HKUST-1 samples upon heating. (a)HKUST-1 (left), 5-FU@HKUST-1_IN (center) and 5-FU@HKUST-1_EX (right) before sample activation. (b) Colour change observed after samples activation at 90 °C under vacuum. HKUST-1 framework presents a characteristic colour switch from light to dark blue upon heating, linked to the change in coordination of the copper site. 5-FU@HKUST-1_IN did not present the expected colour change, due to the coordination of the guest molecule to the copper metal site [102]. (c) Colour change presented by all samples upon guest release. (d) Pellets produced to estimate nominal density of samples, whose values considerably differ as a result of differences in porosity.

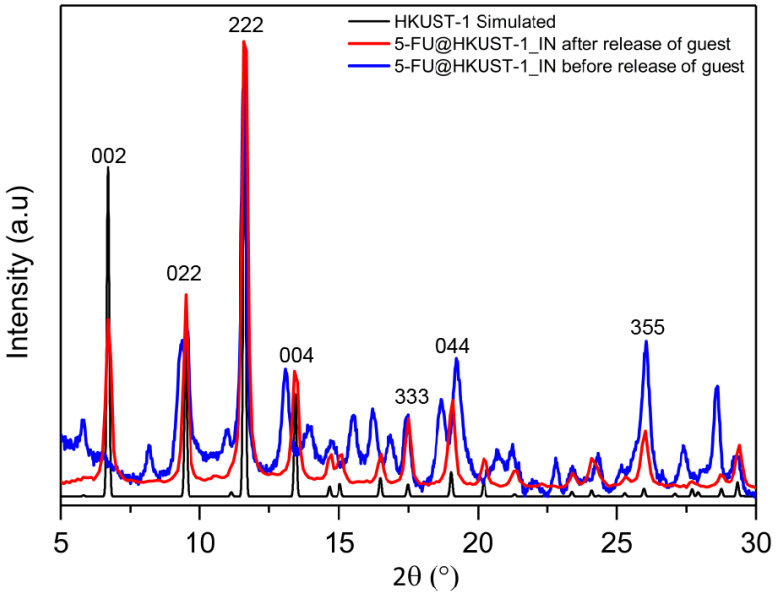

Figure 7.3: Diffraction patterns of 5-FU@HKUST-1_IN before and after the release of 5-FU (guest) drug molecules. Recovery of cubic symmetry is clear when comparison is made between the diffraction pattern of the host framework obtained after guest release and simulated pattern of HKUST-1. Labeling of Bragg peaks accompany the HKUST-1 simulated pattern for reference.

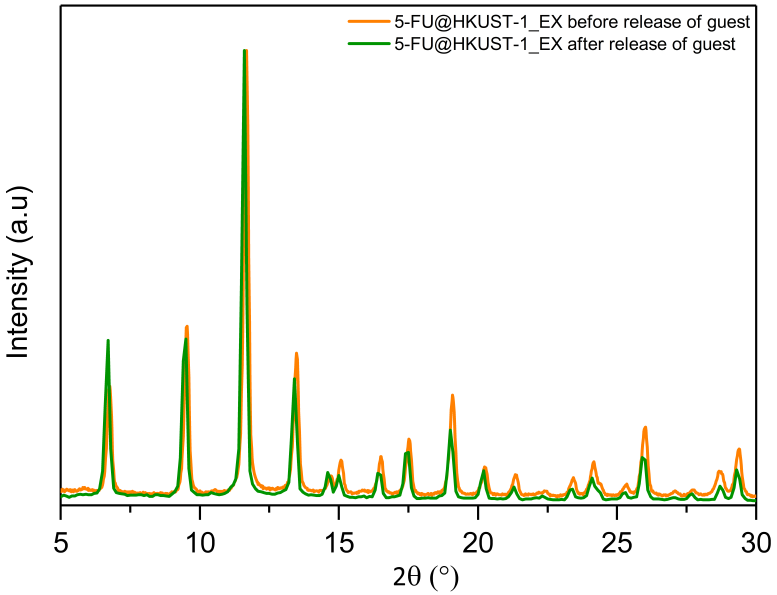

Figure 7.4: Diffraction patterns of 5-FU@HKUST-1_EX before and after the release of guest drug molecule. No apparent structural changes detected upon the release of 5-FU.

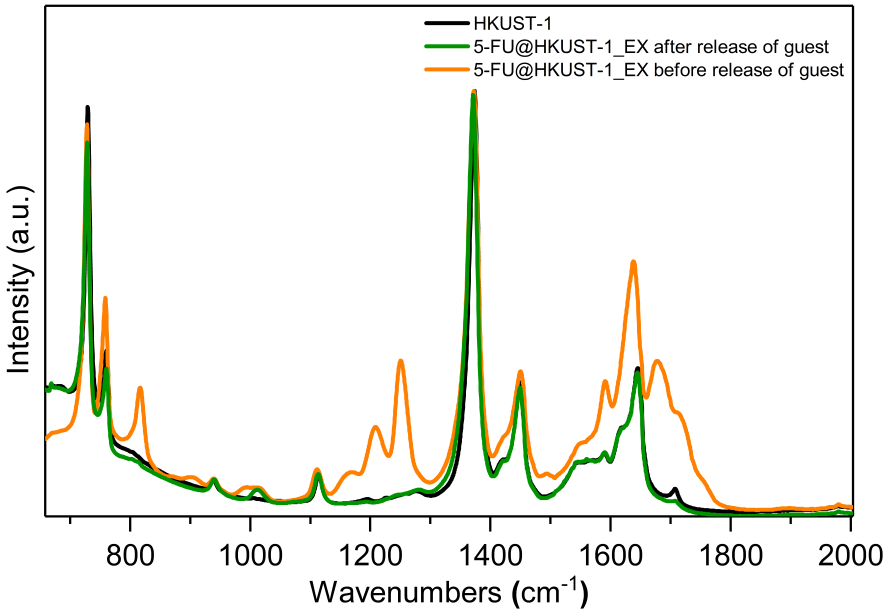

Figure 7.5: ATR-FTIR spectra of 5-FU@HKUST-1_EX before and after the release of the guest drug molecule confirming the release of 5-FU. Asterisks mark the position of the 5-FU peaks.

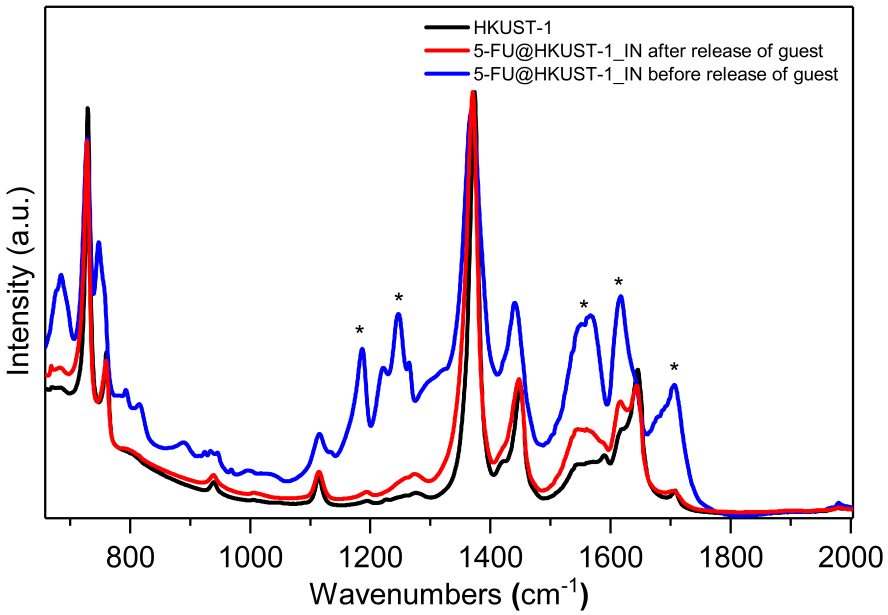

Figure 7.6: ATR-FTIR spectra of 5-FU@HKUST-1_IN before and after the release of the guest drug molecule. The disappearance of the main 5-FU peaks shows the successful release of the drug molecule after sample was immersed in methanol and stirred for 72 hours. Asterisks mark the position of the 5-FU peaks.

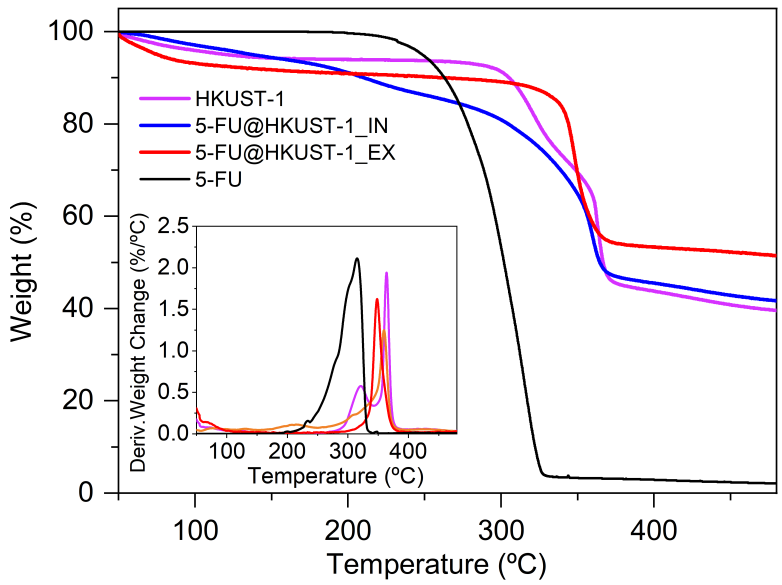

Figure 7.7: TGA plots of HKUST-1 and drug-loaded samples showing different material decomposition behavior as a function of temperature. Inset shows the derivative weight change with respect to temperature.

are presented in Figure 7.9. The AFM topography shows the crystal morphology while SEM images display no sign of major alterations before and after drug encapsulation. The particle size was found to be at 432 ± 83 nm.

In the ATR-FTIR spectra (Figure 7.1c) the characteristic bands of HKUST-1 (*i.e.* ν(Cu−O) at 728 cm^{-1}, ν(C=C) in the benzene ring at 1372 cm^{-1}, δ(OH) bending at 1448 cm^{-1}, ν(C−O) at 1618 cm^{-1}, and ν(C=O) of H_3BTC at 1706 cm^{-1}) were detected in all samples, confirming the retention of the chemical bond integrity upon 5-FU loading [1]. The spectra of 5-FU@HKUST-1_IN and 5-FU@HKUST-1_EX exhibit clear changes in the regions of 1100-1300 cm^{-1} and 1500-1700 cm^{-1}, in comparison to the pristine HKUST-1 spectrum. These modes originate from ν(C−N) and ν(C−F) bonds of 5-FU [211], corroborating the presence of drug molecules in the measured samples. However, there are salient differences between spectra of the two different drug-loaded composite: *in situ* vs. *ex situ*. Differences in the vibrational modes of the composites suggest the specific interactions between 5-FU and HKUST-1. due to guest confined inside the pore versus guest adsorbed

[1] Molecular vibrations: δ = in-plane bending, ν = stretching

outside the host framework. This interactions will be explored in deeper details in the analysis of INS spectroscopy.

7.3 Examination of the lattice dynamics and low energy vibrational bands upon guest encapsulation *via* INS

Examination and comparison of the low energy vibrational bands, termed the terahertz (THz) modes of the *in situ* and *ex situ* derived composite samples, will offer additional insights into the different drug-MOF interactions. Using INS, it is possible to measure the full vibrational spectrum to reveal how the presence of the drug molecule affects THz dynamics of the host framework. Figure 7.10 presents the experimental and theoretical INS spectra of HKUST-1 as well as its drug-loaded

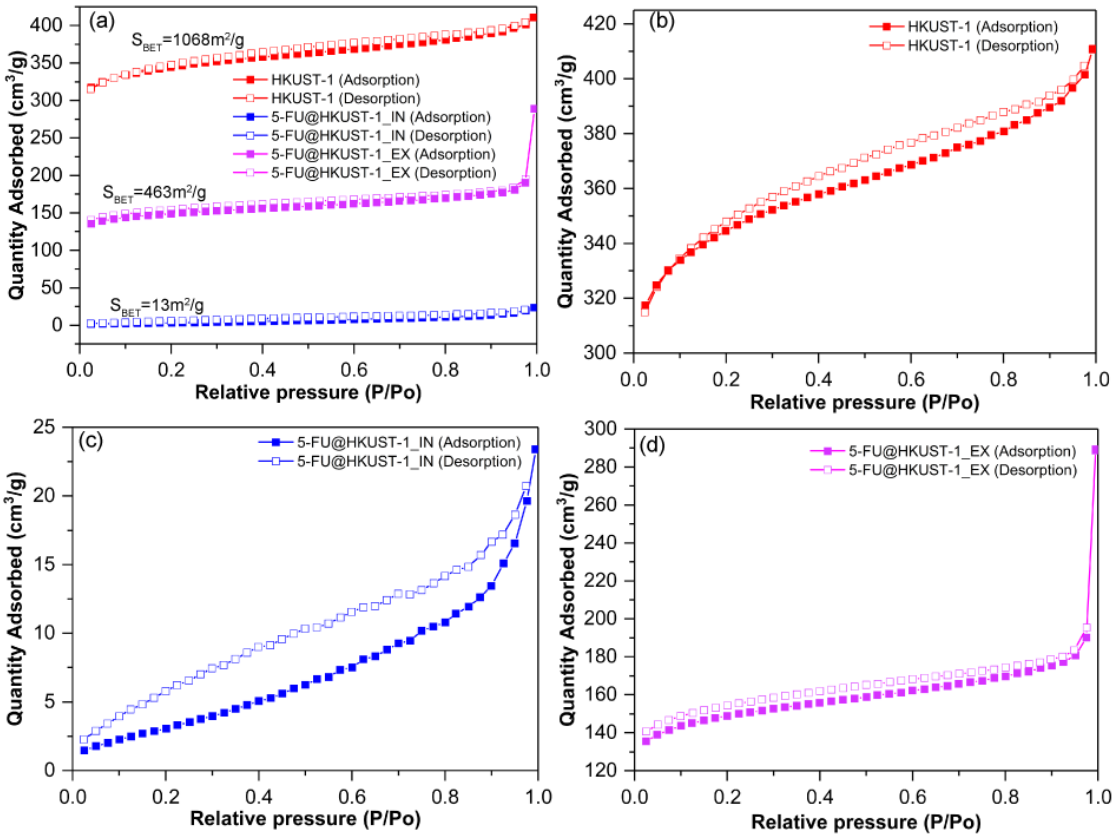

Figure 7.8: Nitrogen adsorption and desorption isotherms of HKUST-1 and drug-loaded counterparts. Individual isotherms of b) HKUST-1, c) 5-FU@HKUST-1_IN and d) 5-FU@HKUST-1_EX. The HKUST-1 samples were activated at 90 °C under high vacuum for 12 hours prior to the N2 adsorption measurements at 77K.

Table 7.1: Reported BET surface areas of HKUST-1 materials synthesized by mechanochemistry and other conventional methods

Sample	**Method**	**Grinding time**	**BET surf. area** ($m^2\,g^{-1}$)	**Ref.**
HKUST-1	Manual grinding	10 min	1068	This Chapter
5-FU@HKUST-1_IN			13	
5-FU@HKUST-1_EX			463	
HKUST-1	Ball milling: neat grinding	30 min	1188	[217]
	Grinding jar: neat grinding	20 min	1119	[218]
	Grinding jar: assisted by solid solvent (NaCl)	20 min	1281	[66]
	Extrusion: liquid assisted	-	1738	[75]
	Ball mill: liquid assisted	25 min	758-1713	[213]
	Kitchen grinder: liquid assisted	5-60 min	707	[73]
	Solvothermal	-	300-1500	[45]
	Solution-based	-	227	[212]
	Solution-based	-	1564	[219]
	Solvothermal	-	629	[220]
	Electrochemical	-	324	[220]

counterparts up to ∼15 THz (500 cm^{-1}); the full spectra up to ∼60 THz (2000 cm^{-1}) are shown in Figures 7.11 and 7.12. Because identification of the origin of the THz vibrations is challenging, the results from *ab initio* DFT calculations [2] were employed to compute the theoretical INS spectrum of HKUST-1 [120]. This enabled the assignment of the peaks observed in the experimental INS data. A reasonably good agreement between theory and experiments is observed in Figure 7.10a.

The THz modes in HKUST-1 can be divided into three regions: (I) below 4.5 THz (<150 cm^{-1}), associated with paddle-wheel deformation and translational motions; (II) 4.5-9 THz (∼150-300 cm^{-1}), which contains asymmetric paddle-wheel deformation with Cu-Cu bond buckling and O-Cu-O bending modes; and (III) 9-18 THz (∼300-600 cm^{-1}) exhibiting in-plane and out-of-plane deformations of aromatic rings. Herein the vibrational modes were designated as no. 1-19 (see

[2] The DFT calculations presented in this section were developed in collaboration with scientists Prof. Jin-Chong Tan and Dr Matthew M. Ryder (University of Oxford), resulting from previously performed and published calculations [120].

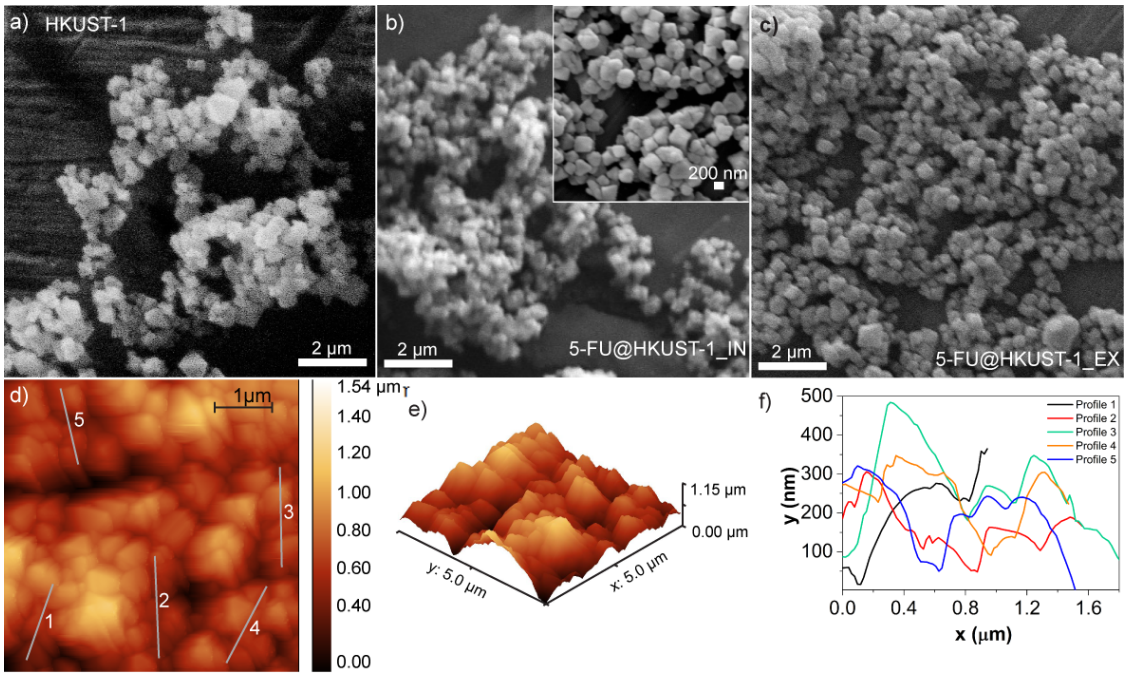

Figure 7.9: SEM images of (a) pristine HKUST-1, (b) 5-FU@HKUST-1_IN, and (c) 5-FU@HKUST-1_EX. The crystals show a uniform particle distribution, similar to the nanoHKUST-1 crystals fabricated *via* solution-based methods [211]. (d-e) AFM images of pristine HKUST-1 crystals for morphology characterization, accompanied by 3D representation of the surface topography. (f) Height profiles from traces marked in (d) for the calculation of crystal size of HKUST-1, which was found to be at 432 ± 83 nm (averaged of 100 measurements).

Figures. 7.10a and 7.13) to facilitate band identification; descriptions of all modes are given in Table 7.2.

In region-I, an overall decrease in the intensity of the INS spectrum of 5-FU@HKUST-1_IN was detected. The decline of the spectral intensity in this sample may be explained by suppression of specific lattice modes, linked to strong guest-host interactions causing the framework distortions detected in the PXRD data (Figure 7.1a). However, inelastic scattering of the 5-FU@HKUST-1_EX sample shows a different behavior. The relatively higher scattering intensity observed in the spectrum of this sample, specifically in the range of ∼2.2-3.7 THz (74-125 cm^{-1}) might be a combination of scattering coming from the framework and the drug molecules, which indicates a weaker guest-host interaction. Likewise, a closer comparison between the spectra of 5-FU@HKUST-1_EX and 5-FU@HKUST-1_IN reveals a lower scattering intensity of the latter up to ∼6.4 THz (213 cm^{-1}),

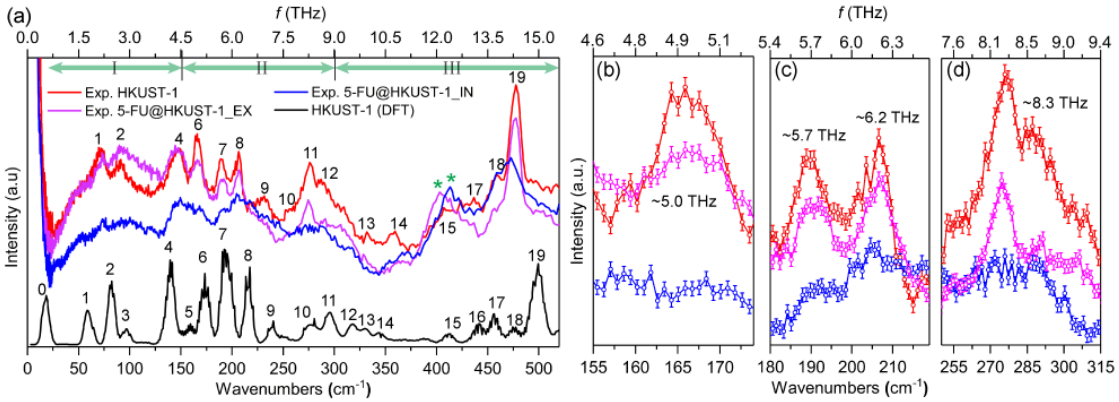

Figure 7.10: (a) Comparison of experimental and theoretical INS spectra of HKUST-1 and its drug-loaded counterparts. The theoretical spectrum was calculated using published DFT calculations. Closer look at THz modes at (b) ∼5.0 THz, (c) ∼5.7 THz and ∼6.2 THz, and (d) ∼8.3 THz, whose lattice dynamics are illustrated in Fig. 3(b)-(e), respectively. Asterisks mark the positions of the 5-FU peaks. (1 THz ≈ 33.36 cm^{-1} ≈ 4.14 meV).

accompanied by reduced integrated area under the INS spectrum.

Within region-II, four THz modes were pinpointed as the most sensitive to 5-FU loading. Differences in the relative scattering intensity of the peaks at ∼5.0 THz (166 cm^{-1}), ∼5.7 THz (190 cm^{-1}), and ∼6.2 THz (207 cm^{-1}), are observed in the spectra of drug-loaded samples (Figure 7.10). These modes are, respectively, associated with paddle-wheel translational motion, asymmetric paddle-wheel deformation with Cu−Cu buckling and O−Cu−O bending accompanied by rocking mode of the organic linkers, whose vibrations are illustrated in Figure 7.14. The decline in scattering intensity of these modes upon incorporation of 5-FU,

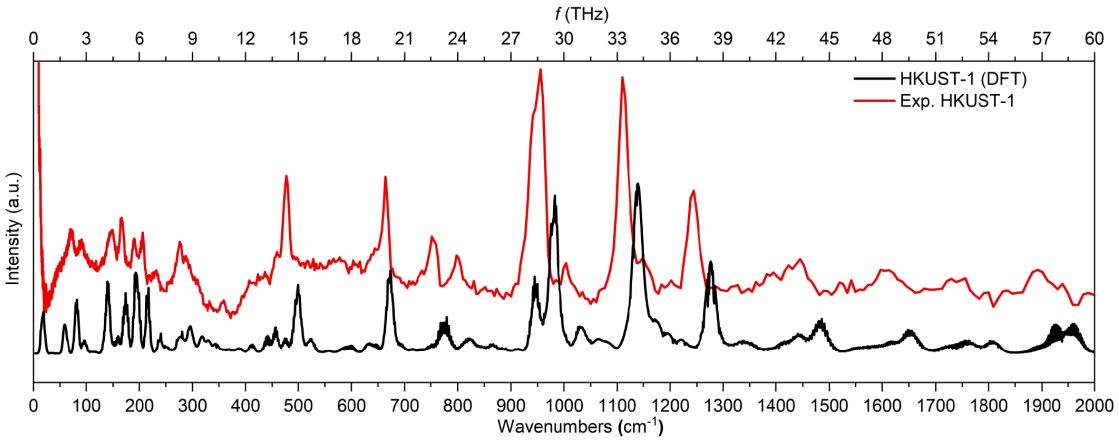

Figure 7.11: Theoretical and experimental INS spectra of HKUST-1 for comparison. Theoretical spectrum is displayed in black and experimental spectrum is shown in red.

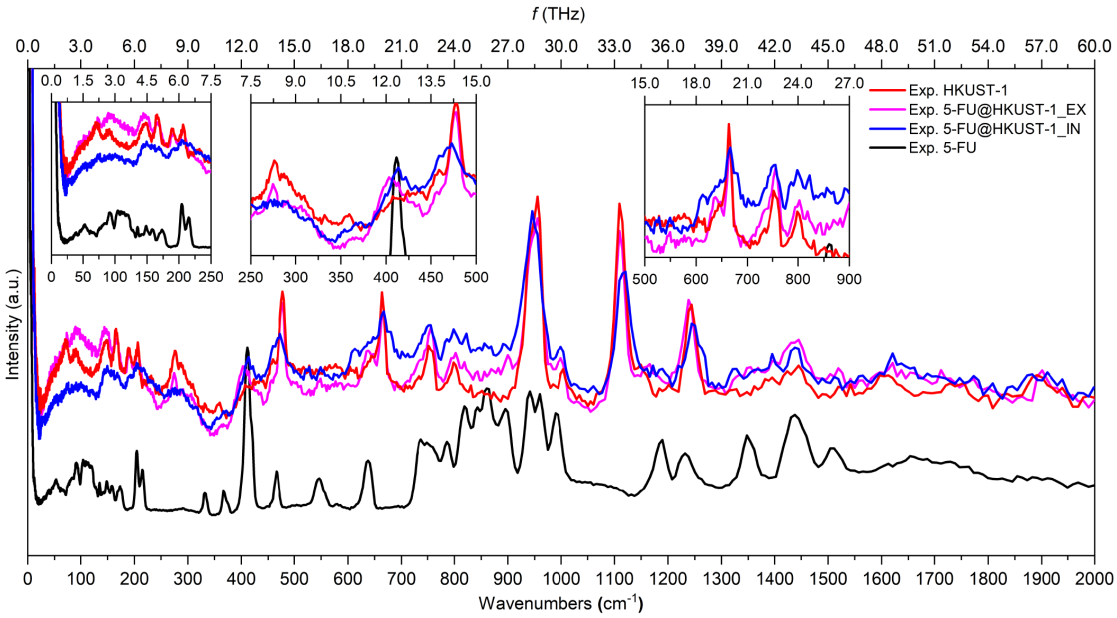

Figure 7.12: Full INS spectra of HKUST-1 samples up to ∼60 THz (2000 cm^{-1}). The experimental spectrum of 5-FU was scaled down by a factor of 5 to facilitate comparison with experimental data of HKUST-1

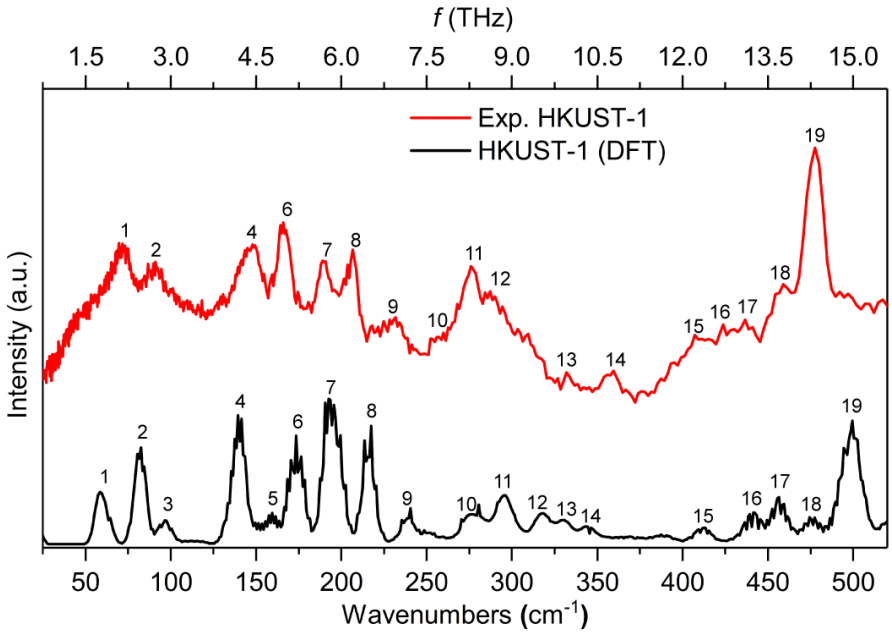

Figure 7.13: Theoretical and experimental INS spectra of HKUST-1 with vibrational modes marked as 1-19 for easy correlation between theoretical and experimental data.

Table 7.2: Description of vibrational and rotational modes of HKUST-1 identified in its INS spectrum

Mode no.	**Theo.** (cm^{-1})	**Exp.** (cm^{-1})	**Description** [120]
0	19	(hidden)	Strong paddle-wheel deformation and translational motion
1	60	70	Paddle-wheel deformation and translational motion with organic linker rotation
2	83	91	Paddle-wheel deformation and rotation with organic linker rocking
3	97	(hidden)	Organic linker trampoline-like motion
4	140	148	Paddle-wheel rocking with organic linker rocking
5	160	(hidden)	Paddle-wheel deformation
6	174	166	Paddle-wheel translational motion
7	193	190	Asymmetric Paddle-wheel deformation (Cu−Cu buckling) with linker rocking Asymmetric paddle-wheel deformation (O−Cu−O bending)
8	217	207	Paddle-wheel rotation with strong linker rocking
9	241	232	Paddle-wheel deformation (strong Cu−Cu buckling) with linker rocking
10	280	260	Asymmetric paddle-wheel deformation
11	296	276	(O−Cu−O bending andCu−Cu buckling)
12	318	288	Paddle-wheel deformation with linker rocking
13	330	332	
14	345	359	
15	411	408	In plane aromatic ring rotation with asymmetric Cu−O stretching
16	442	425	
17	457	438	
18	477	460	In plane aromatic ring deformation with partially symmetric Cu−O stretching
19	499	478	Out of plane aromatic ring deformation

seen in Figures 7.10b and 7.10c, is accompanied by not only the reduction of the integrated area under the INS spectra (Table 7.3), but also the significant broadening of these peaks in the *in situ* derived sample. The broadening was approximated

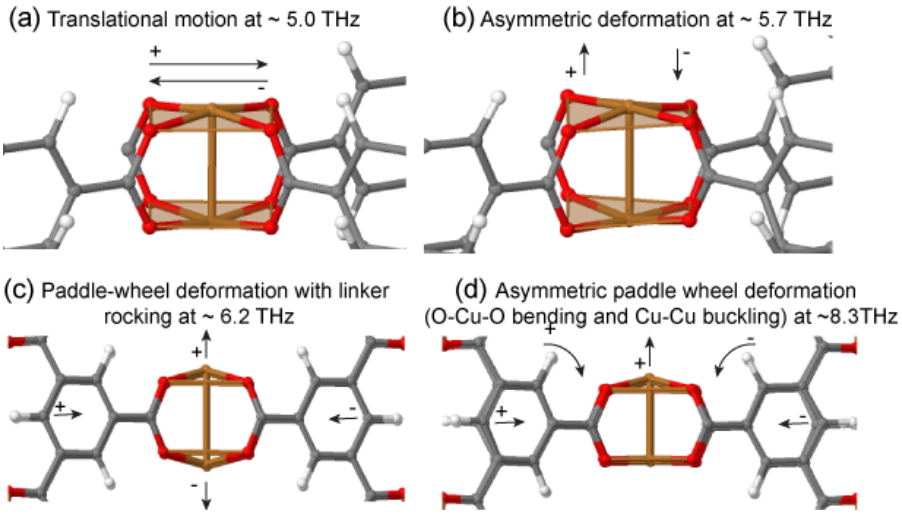

Figure 7.14: THZ modes of HKUST-1 mostly affected by the presence of 5-FU guest, showing collective vibrations at (a) ~5.0 THz, (b) ~5.7 THz, (c) ~6.2 THz, and (d) ~8.3 THz. Arrows indicate the directions of the collective deformations with +/- amplitudes computed by DFT (B3LYP, 6-31G basis set). Colour scheme: copper in orange, carbon in grey, oxygen in red, hydrogen in white, nitrogen in purple, and fluorine in green.

by values of full width at half maximum (FWHM in Figure 7.15), which reflect the changes in vibrations of aforementioned collective modes.

Data in Figure 7.10d show suppression of the paddle wheel vibrational modes in 5-FU@HKUST-1_IN, especially the peak at ~8.3 THz (276 cm^{-1}) attributed

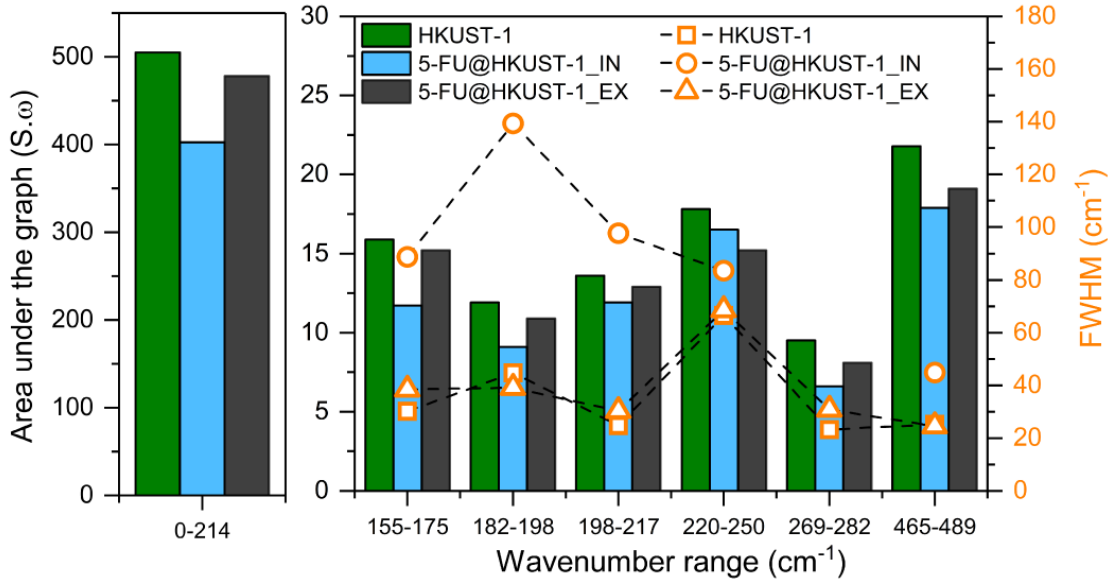

Figure 7.15: Bar plot summarizing data presented in Table 7.3. The plot demonstrates the decrease in the area and the broadening of specific peaks related to copper (II) paddle wheel vibrations in 5-FU@HKUST-1_IN sample.

to asymmetric paddle wheel deformation (O-Cu-O bending and Cu-Cu buckling). It can be seen that this mode completely vanishes upon the incorporation of 5-FU. The proposed explanation is that confinement of 5-FU molecules within the distorted host framework is responsible for the suppression of vibrational modes observed here. Suppression of this mode indicates a change in the coordination environment of the copper paddle-wheel that also affects the deformation of the organic linker. The fall in the THz intensity could be correlated to hindrance of the paddle-wheel motions, due to interaction with drug molecules positioned inside (bound to CUS) or outside the pores of the framework (hydrogen bonded

Table 7.3: Values of area under the inelastic curves and FWHM of the HKUST-1 THz mode mostly affected by the presence of 5-FU

Mode no.	**Wavenumber** (cm^{-1})	**Sample**	**Area** ($S\times\omega$)	**FWHM** (cm^{-1})
	0-214	◇	504.8	-
		○	402.6	-
		●	477.9	-
Mode 6	155-175	◇	15.9	30.1
		○	11.7	88.8
		●	15.2	38.5
Mode 7	182-198	◇	11.9	44.7
		○	9.1	139.3
		●	10.9	39.1
Mode 8	198-217	◇	13.6	24.8
		○	11.9	97.7
		●	12.9	30.3
Mode 9	220-250	◇	17.8	66.5
		○	16.5	83.5
		●	15.2	68.6
Mode 11	269-282	◇	9.5	23.2
		○	6.6	-
		●	8.1	30.8
Organic linker deformation	465-489	◇	21.8	25.3
		○	17.9	44.9
		●	19.1	24.5

◇ HKUST-1 ○ 5-FU@HKUST-1_IN ● 5-FU@HKUST-1_EX

and $\pi - \pi$ interactions); herein the *in situ* confinement approach led to a greater decline of mode intensity than the *ex situ* method.

Turning to regions-III, unambiguously, the new mode observed at ∼12 THz (410 cm^{-1}) indicates the presence of 5-FU in the measured samples (Figure 7.12 inset), as previously detected in the ATR-FTIR data (Figure 7.1c). The BTC linker deformation (∼474-478 cm^{-1}) has also been identified. The broadening of the peak attributed to organic linker vibrations reveals that framework distortion is not restricted to the CUS centers, but also affecting the walls of the cages comprising bridging organic linkers. Interestingly, the previously described modal changes are accompanied by smaller changes in the characteristic vibrational modes of the frameworks in the higher energy region of ∼950-1500 cm^{-1}, see Figure 7.11. Notable changes detected in the THz vibrations reveal the stronger guest-host intermolecular interactions present in the *in situ* derived samples, attributable to the confinement of 5-FU in the pores of HKUST-1 *via* coordination to the copper paddle-wheel. In contrast, during *ex situ* encapsulation, the drug molecules in solution will have to compete against the polar solvent for coordination to the active site and suffer from reduction in mobility from solvation effects. Consequently, the solvent molecules occupy some of the metallic active sites, thereby reducing the free binding sites available to drug molecules. Finally, propensity of forming hydrogen bonds with the external surface of the cages could mean that in the *ex situ* strategy the drug molecule has a higher likelihood to bind to framework exterior. This is hypothesized considering that, during the *ex situ* encapsulation, it is energetically preferable for 5-FU to establish π-π interactions and hydrogen bonding with the external walls of HKUST-1 cages then it is to overcome the physical barrier imposed by the small cage apertures and establish inter-pore interactions.

7.4 Summary and conclusions

By focusing on the resulting guest-host interaction exposed by INS spectroscopy, this chapter has contrasted the encapsulation performance of two confinement methods: the conventional impregnation technique and the novice *in situ* mechanochemical

method. Modifications in the THz lattice dynamics of 5-FU@HKUST-1_IN have been detected, where sharp reductions in the low-energy collective modes under ∼7.5 THz (∼250 cm^{-1}) mark the suppression of the copper paddle-wheel motions due to drug incorporation. By leveraging the mechanochemical method, the results show that *in situ* one-pot strategy can directly encapsulate molecules into the pores of host framework. The *in situ* drug encapsulation methodology may have the potential to minimize the burst effect [14], contributing to the development of improved pathways to control the binding and release of drug molecules from MOFs.

I didn't want to just know names of things.
I remember really wanting to know how it all worked.

— Elizabeth Blackburn

8

Elucidating the drug release from MOF composites *via in situ* SR-microFTIR

Contents

8.1 Background and motivation

The concept of employing MOFs as porous vessels to host drug molecules, presented in the previous chapters, holds promise as a pharmaceutically efficient way to achieve sustained release of various therapeutic molecules [10, 27, 44]. Although progress has been made in the recent years [15, 146], the prolonged, well controlled, targeted delivery of therapeutic agents remains a challenge in the field. For example, research on the delivery of anti-cancer drugs currently seeks to improve the traditional direct administration routes to mitigate any undesirable side effects and poor biodistribution [221–223].

Recently, strategies combining porous materials and organic polymers to yield a bespoke composite present an alternative way forward to avoid the burst effect [14]. As shown in Chapter 7, mechanochemistry can be successfully applied to accomplish the *in situ* encapsulation of 5-FU within HKUST-1 resulting in the 5-FU@HKUST-1 system[1]. However, HKUST-1 is a water sensitive MOF, which degrades rapidly in the presence of humidity [224, 225]. This chapter aims to demonstrate that 5-FU@HKUST-1 can be easily combined with a biocompatible polymer like polyurethane (PU) to fabricate the 5-FU@HKUST-1/PU composites [187, 226, 227]. The presence of a polymeric matrix can significantly enhance the aqueous stability of certain MOFs that have a huge potential for hosting a plethora of drug molecules, but suffer from poor water stability [228]. Specifically, HKUST-1 has been selected not only due to its poor water stability, but also due to the presence of several CUS that can act as strong binding sites for attaching different polar guest molecules. The combination of polymer and MOFs represents an effective way of providing a suitable scaffolding to the MOF while harnessing its great potential as a DDS thus creating a tunable drug@MOF/polymer platform for therapeutic applications, such as the topical treatment of skin conditions *via* the fabrication of functional wound dressing devices [45, 229].

As highlighted in Chapter 2, understanding the release of drug molecules from host frameworks has been generally carried out using *ex situ* techniques (*e.g.* sample and separate, continuous flow, diffusion methods) that are more appropriate for establishing the drug release kinetics [143]. Analytical studies to construct drug release profiles of drug@MOF systems rely on these stepwise approach where aliquots are periodically collected from the released media, and the drug concentration is determined *via* UV-Vis spectroscopy and liquid chromatography [148, 230, 231]. Although these methods yield drug release profiles, they do not reveal the underlying mechanism or chemical and physical structural transformation occurring during

[1] From the samples studied in Chapter 7, 5-FU@HKUST-1_IN (hereafter referred as 5-FU@HKUST-1) has been selected to be further studied in this chapter based on the stronger guest-host interaction detected for this assembley.

the drug release process. These dynamical changes are key to correlating the guest-host interactions of drug@MOF systems.

To address these limitations, this chapter presents an *in situ* strategy to probe the release of 5-FU from HKUST-1/PU membrane composites. SR-microFTIR was conducted in Beamline B22 at the Diamond Light Source, which allowed broadband measurements to be conducted with a high signal to noise ratio [232, 233]. The transformations of the host framework were followed through the evolution of vibrational bands that are specific to the guest and the host structure.

8.2 *In situ* drug release experiments

SR-microFTIR spectroscopy experiments were performed in two different fluid cell setups (*i.e.* static and flow liquid cells) to study the molecular structural changes of the guest-host assembly of 5-FU@HKUST-1/PU composite and its constituents during the release of drug molecules. The results of the static experiments performed under deuterated water (D_2O) exposure were considered first. DFT theoretical calculations shed light on the energetics of drug-MOF interactions responsible for the adsorption and release of the encapsulated drug molecules, Finally, the results from the flow experiments subject to a combination of D_2O/H_2O were be examined, revealing the synergy of the polymer matrix and MOF combination that enables the composites to suppress the unwanted burst effect.

8.2.1 Static-cell measurements

Figure 8.1 shows the experimental setups used in this study (see 3.3a in Chapter 3 for additional details of the experimental setup). Static fluid cell experiments were performed using samples listed in Table 8.1, individually inserted into a customized liquid cell between two zinc selenide (ZnSe) circular windows separated by a 10 µm thick Teflon spacer. 2 µL of the chosen medium (D_2O) were pipetted onto the sample and the cell was sealed. To select specific sites within the samples, images were collected under visible light *via* the IR microscope (Figure 8.2).

Table 8.1: Description of samples used in SR-microFTIR measurements

	Sample	Synthesis Method	Details
Powder Samples	HKUST-1	Manual grinding	Pristine MOF
	5-FU@HKUST-1	Manual grinding	*In situ* encapsulation
	5-FU	-	As-received
Polymer composite samples	HKUST-1/PU	Drop cast	85 wt.% / 15 wt.%
	5-FU@HKUST-1/PU	Drop cast	85 wt.% / 15 wt.%
	5-FU/PU	Drop cast	14 wt.% / 86 wt.%

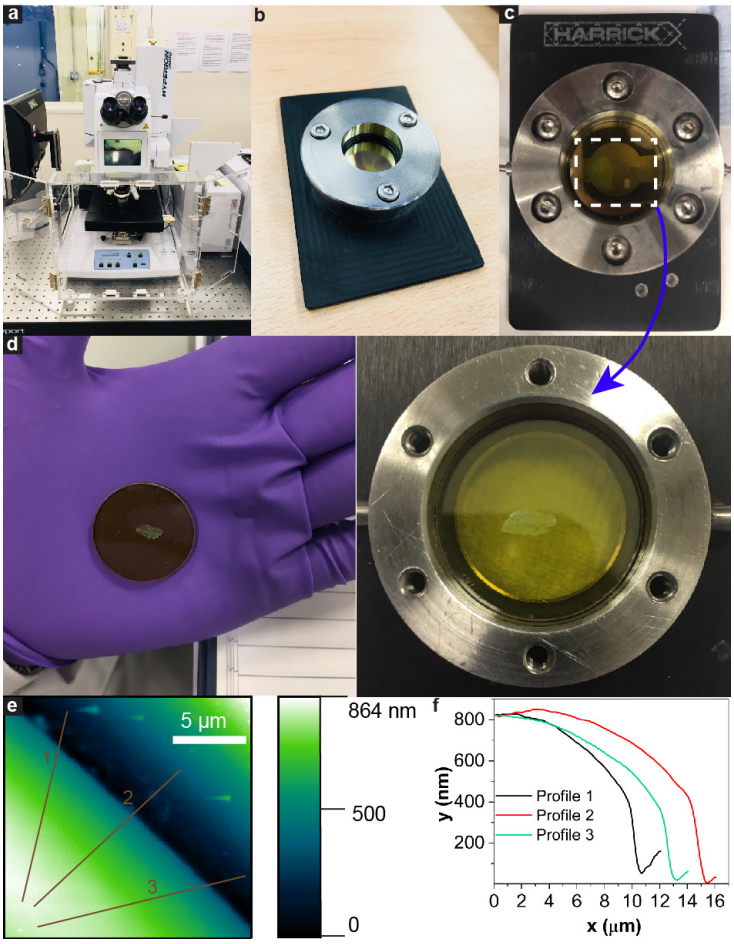

Figure 8.1: Experimental setup for *in situ* SR-microFTIR measurements.(a) Optics FTIR microscope. (b) Static liquid cell. (c) Flow liquid cell. (d) Sample deposition onto a pair of 25 mm diameter zinc selenide (ZnSe) circular windows. During the experiments, the samples remained fully attached to the ZnSe windows, as a result of the drop cast technique applied for their fabrication. (e) AFM image of membrane produced *via* drop casting. Profiles presented in (f) show that the thickness of the membranes was less than 1 µm.

For IR measurements in different media, the frequency of a molecular vibration depends on the masses of the vibrating atoms. Therefore, absorption bands of D_2O appear at lower wavenumbers than in H_2O (Figures 8.3 and 8.4). In the ranges of 1500-1750 cm^{-1} (H−O−H bending) and 1150-1300 cm^{-1} (D−O−D bending), H_2O or D_2O modes, respectively, overlap with important vibrational bands of the drug molecule present in the 5-FU@HKUST-1 samples. Therefore, the monitoring of the 5-FU drug release was carried out with a complementary set of experiments performed in H_2O and D_2O, respectively, to fully capture the evolution of drug peaks in the spectral range of interest (650-2000 cm^{-1}). Importantly, the release of the drug molecules can be tracked by the progressively decreasing intensity of

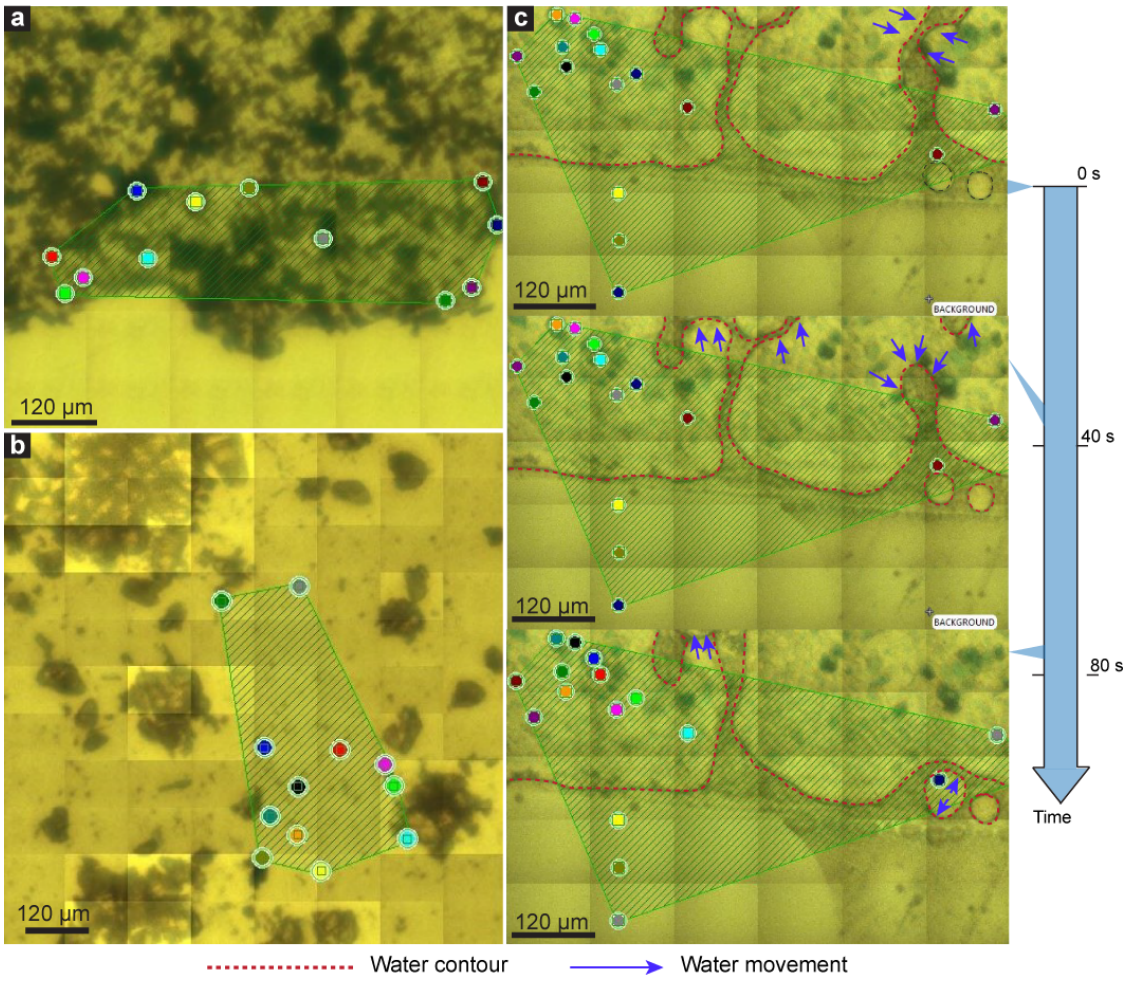

Figure 8.2: Optical micrographs showing multiple sites selected in the samples for data acquisition. (a) HKUST-1/PU membrane, (b) 5-FU crystals, and (c) 5-FU@HKUST-1/PU membrane in contact with water. The movement of the medium can be observed by contrasting the images c-top to c-bottom.

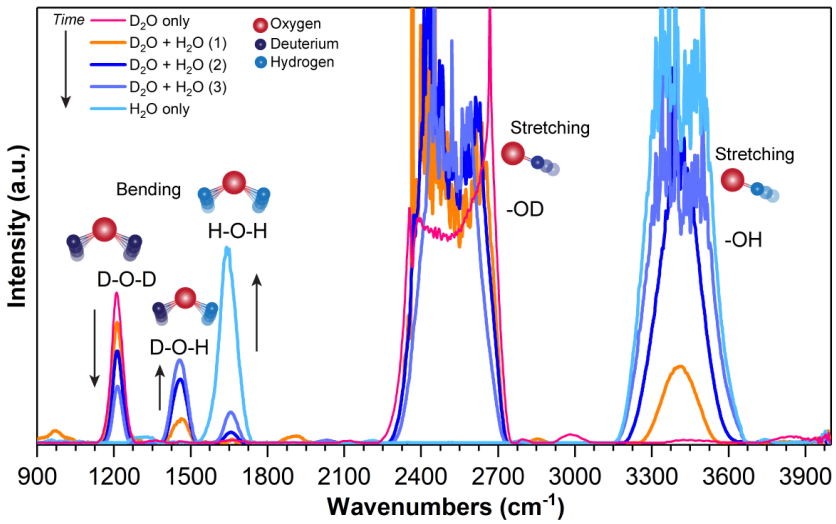

Figure 8.3: SR-microFTIR spectra of deionized water (H_2O) and deuterated water (D_2O). Specific bending and stretching modes are illustrated. Observe the saturation of –OD and –OH stretching bands due to the high signal of solvent in the range > 2000 cm^{-1}

the 5-FU peaks identified in the 5-FU@HKUST-1 samples.

The samples were characterized *via* TGA (Figures 8.5 and 8.6) where the level of drug encapsulation within HKUST-1 was determined to be ∼14.0 wt.%. Comparison of these drug loading with various other 5-FU@MOF systems is presented in

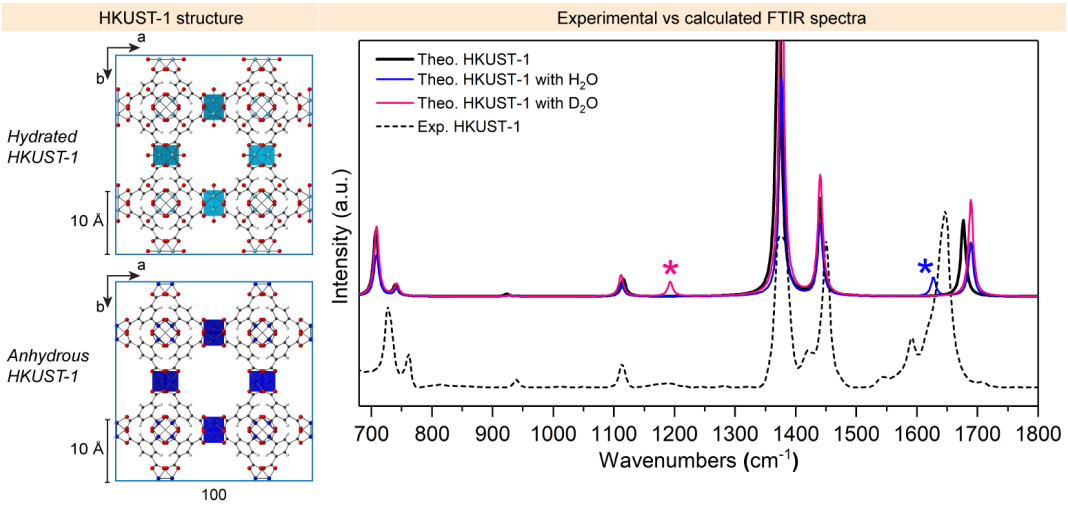

Figure 8.4: Theoretical spectra of activated and hydrated HKUST-1 (H_2O-HKUST-1 and D_2O-HKUST-1.) The comparison between the spectra shows the respective bending modes of D_2O and H_2O (observed in the experimental spectra) when coordinated to the cooper sites in HKUST-1. A scaling factor of 0.95 was applied to the theoretical spectra eliminate common shifts resulting from the *ab initio* calculations and match the frequencies against the experimental spectrum. Colour code: O in red, C in black, H in grey, hydrated Cu in light blue, and activated Cu in navy blue.

Table 8.2: Comparison of 5-FU loading in HKUST-1 and different MOF hosts

	MOF	5-FU loading (wt.%)	Reference
Copper MOFs	HKUST-1	14.0	This work
	Cu-MOF	17.3	[234]
	Cu-MOF	47.3	[235]
	HKUST-1	40.2	[212]
Various MOF systems	ZIF-8	5.0	[236]
	In-MOF	32.6	[162]
	Gd-MOF	47.0	[237]
	Zn-MOF	36.8	[238]
	Dy-MOF	47.3	[239]
	Nd-MOF	18.0	[240]
	CD-MOF	15.7	[159]
	MIL-53 (Fe)	13.1	
	MIL-88 (Fe)	28.0	[200]
	MIL-100 (Fe)	66.0	
	Zn-MOF	44.8	[241]
Other DDS	FeO nanoparticles	1.9	[242]
	Chitosan nanoparticles	29.9-69.7	[243]
	Polysacharides particles	3.0	[244]

Table 8.2. As shown in the table, the loadings varied from 1.9 wt.% to 69.7 wt.%, being the loading achieved in the 5-FU@HKUST-1 systems herein produced in good agreement with what has been achieved in recent works. It is worth noting that most of the 5-FU@MOF systems presented in Table 8.2 used conventional immersion/impregnation encapsulation technique in which the carrier was immersed into a 5-FU solution for different periods of time. However, the *in situ* technique applied herein is different from the reported literature approach, by providing optimized condition that minimize the drug molecules binding to the external wall of the host carrier (Chapter 7).

The characterization of the morphology of the 5-FU@HKUST-1/PU membranes and HKUST-1 crystals (Figure 8.7) was performed *via* SEM and AFM. The samples show a non-uniform crystal size distribution (432 ± 83 nm), product of the grinding method applied for the synthesis (Figure 8.7a-c). From the SEM images in Figure 8.7d and AFM images (Figures 8.7e) it possible to observe details

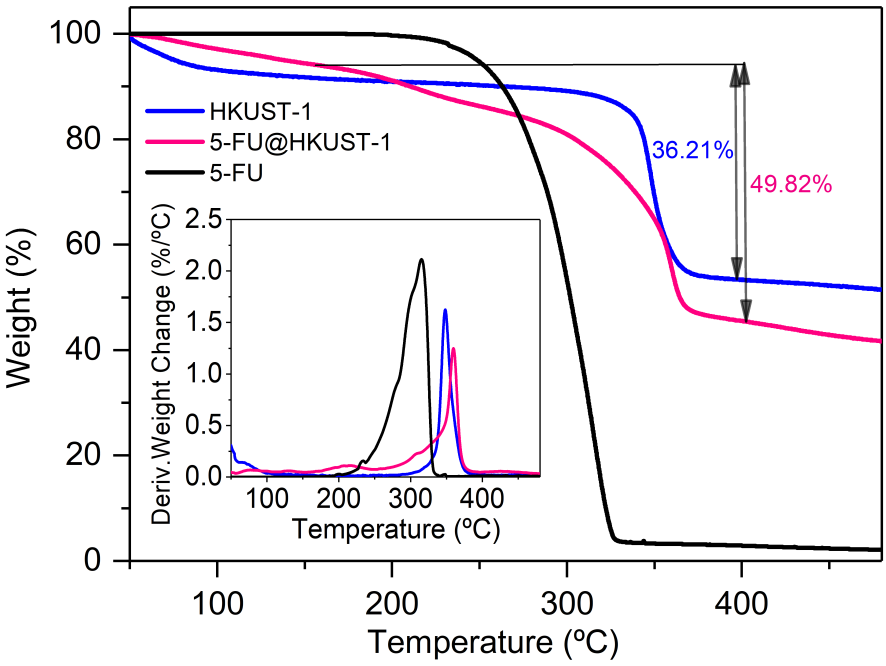

Figure 8.5: TGA of HKUST-1 (blue), 5-FU@HKUST-1 (pink), and 5-FU (black) samples with inset showing the derivative weight change with respect to temperature. Inset shows the differential material decomposition behaviour as a function of temperature.

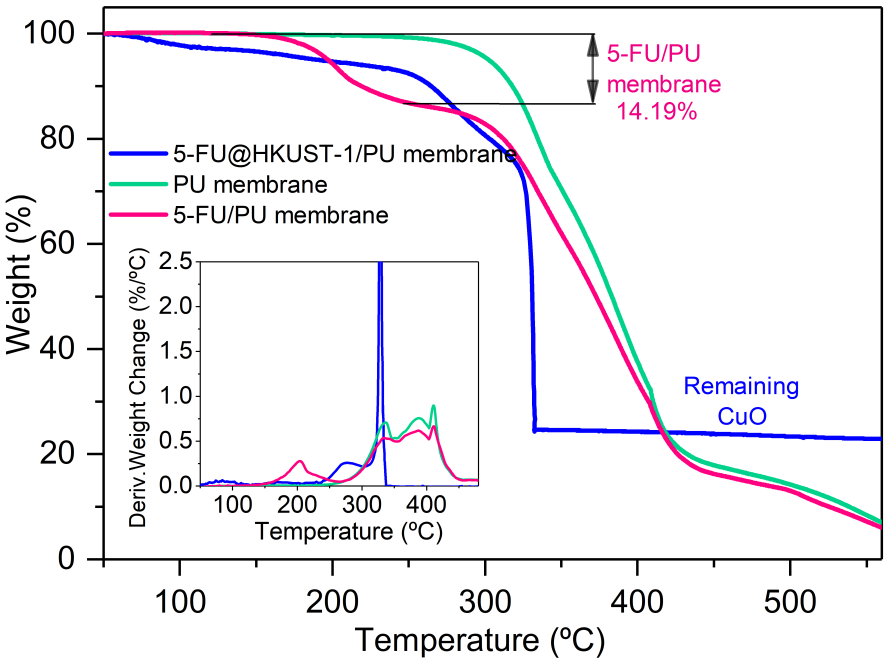

Figure 8.6: TGA of PU membrane (green) versus 5-FU@HKUST-1/PU (blue) and 5-FU/PU membrane (pink) and samples. Insets display the derivative weight change with respect to the temperature.

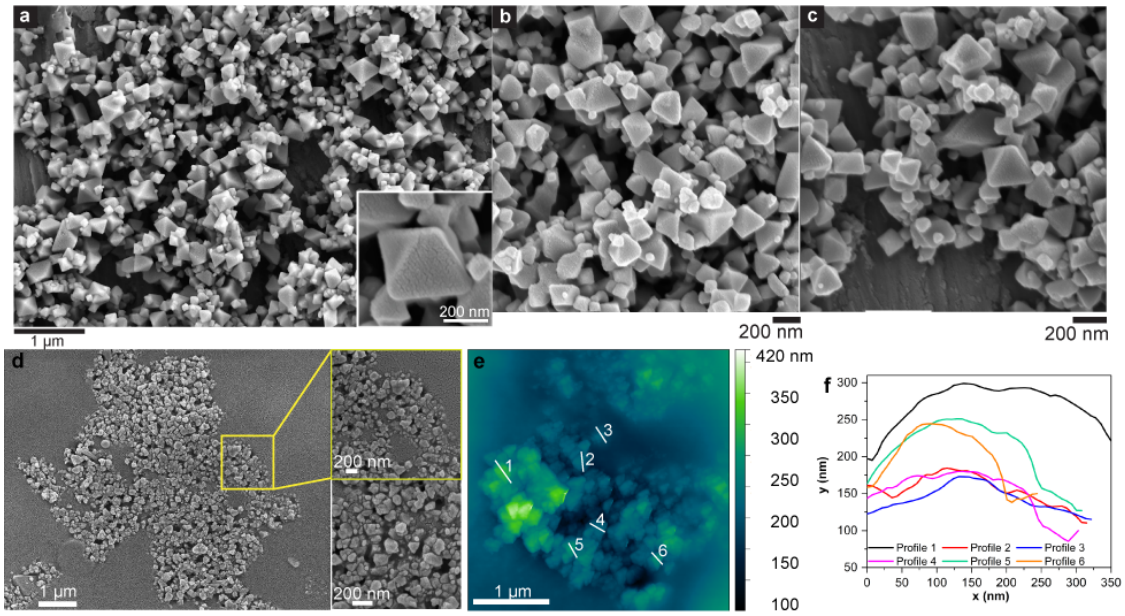

Figure 8.7: SEM micrographs of (a-b) pristine HKUST-1 (crystal size of 432 ± 83 nm (averaged of 100 measurements)), and (c) 5-FU@HKUST-1 (crystal size of 421 ± 75 nm (averaged of 100 measurements)). Note the non-uniform crystal size distribution varying from *ca.* 50 to 500 nm.(d) SEM of pristine HKUST-1 crystal embedded in the PU matrix. Zoon-ins show details of the membrane where HKUST-1 particles are coated by the polymer. (e) AFM image of HKUST-1/PU membrane for morphology characterization. (d) Height profiles from traces marked in (e). The smooth edges demonstrate the coating of the crystals by the polymer.

of the membrane where HKUST-1 particles are coated by the PU polymer. The smooth edges demonstrate the coating of the crystals by the polymer (Figure 8.7f).

Figures 8.8a-b contrast the time dependent evolution of FTIR spectra of the 5-FU@HKUST-1/PU and 5-FU/PU samples. Due to the high loading of MOF within polymer in the composites (85 wt.% of HKUST-1), the spectra of 5-FU@HKUST-1/PU were mainly dominated by the intense vibrational bands of the HKUST-1 framework. However, it is possible to distinctly identify 5-FU modes associated with the δ-ring (817 cm^{-1}) and δ(N−H) (954 cm^{-1}), ν(C−F) (1279 cm^{-1}) and ν(C−H) bonds (1349 cm^{-1}) of 5-FU, as confirmed through the analysis of powder spectra (Figure 8.9). The complete description of the vibrational modes of the composites, 5-FU, and PU is summarized in Table 8.3. Figures 8.8c-d show the time evolution of the integrated spectral area of selected HKUST-1, 5-FU, molecular water (H_2O) and PU peaks of in the composites. PU peaks were used as a reference due to the inert nature of the polymer upon water exposure.

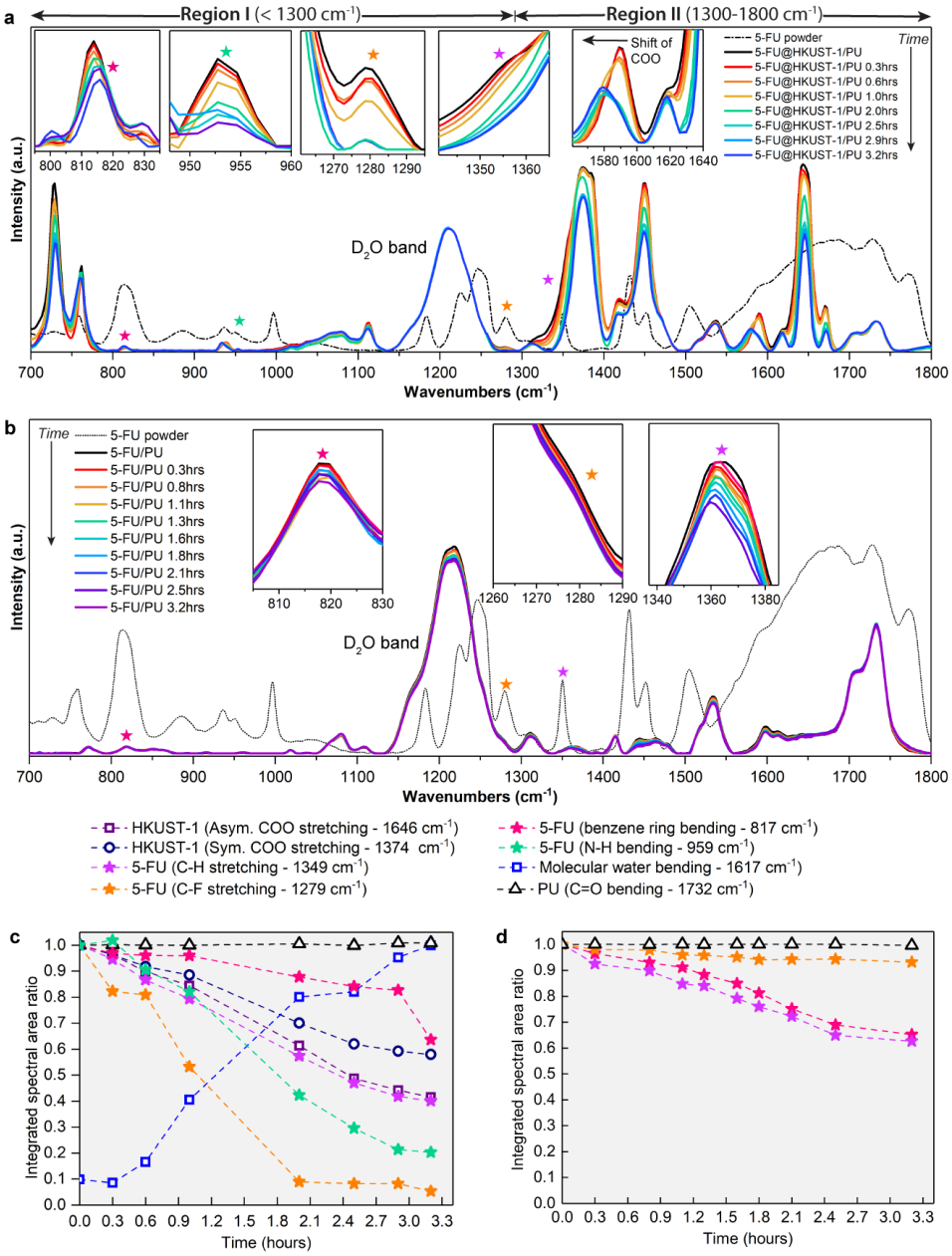

Figure 8.8: SR-microFTIR spectra obtained by static-cell measurements. Evolution of (a) 5-FU@HKUST-1/PU and (b) 5-FU/PU membranes, collected over a period of 3.2 hours. Insets show in detail the changes observed to drug molecule related peaks and important HKUST-1 peaks. 5-FU spectrum was scaled down by a factor of 0.7 to facilitate the comparison with the composite spectra. In (b) the spectra of a few time points were omitted for clarity, causing a small mismatch between the time intervals presented in (a) and (b). However, the overall time analyzed had remained the same. Integrated spectral area ratios of selected peaks of (c) 5-FU@HKUST-1/PU and (d) 5-FU/PU, demonstrating the evolution of vibrational modes intensity in HKUST-1 framework, 5-FU drug, and molecular water. The PU peak at 1732 cm^{-1} (C=O bending) was chosen as a reference due to the absence of any changes with time recorded for this band.

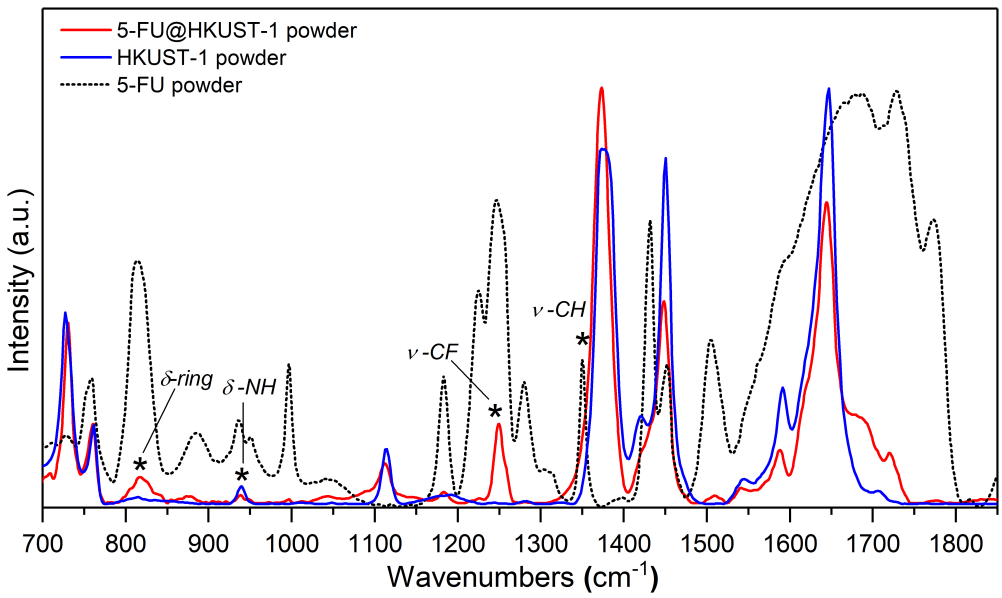

Figure 8.9: SR-microFTIR spectra of 5-FU@HKUST-1, HKUST-1, and 5-FU powder samples collected using the static fluid-cell. The asterisks denote the vibrations of 5-FU guest molecules detected in the 5-FU@HKUST-1 sample.

The values presented at different time points were normalized against the initial area value (hereafter referred only as "area"). The HKUST-1 structure is composed of dimers of Cu^{2+} ions chelated by four BTC bridges, forming the paddle-wheel moiety. With respect to the vibrational modes of HKUST-1, the spectra of the composites can be divided into two regions. Region-I ($< 1300\,cm^{-1}$), shows bands assigned to the out of plane vibrations of benzene ring while region-II (1300-1800 cm^{-1}) is mainly associated to the vibrations of the carboxylate groups. Both are parts of the BTC linker. Specifically, the bands at $1646\,cm^{-1}$ and $1590\,cm^{-1}$ and at $1450\,cm^{-1}$ and $1374\,cm^{-1}$ in region-II correspond to the asymmetric and symmetric stretching of the carboxylate groups, respectively (see Figure 8.10 and Table 8.3).

The three typical microporous sites in HKUST-1 structure (5, 11, and 13.5 Å in diameter), possessing different hydrophilic characters, are schematically represented in Figure 8.11. Water molecules can only penetrate the larger pores of the framework [41, 42], where they start hydrolyzing the Cu−O bonds in the paddle-wheel and so breaking down the crystalline structure of HKUST-1 [224]. The permeation of media through the polymer matrix was monitored by tracking the bending mode of

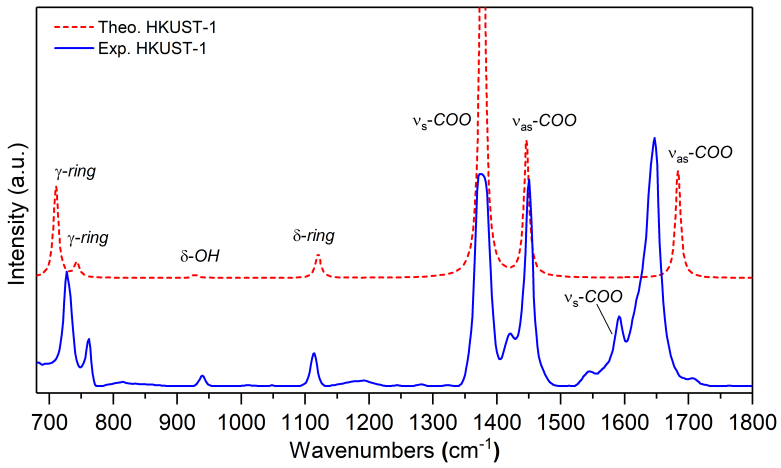

Figure 8.10: Band identification of HKUST-1 framework *via* density functional theory calculations. A scaling factor of 0.95 was applied to the theoretical spectrum to eliminate common shifts resulting from the *ab initio* calculations

Table 8.3: Details of main vibrational bands of HKUST-1, 5-FU, and PU

	Exp.(cm^{-1})	**Description**
HKUST-1	1646	ν_{as}COO
	1590	ν_{s}COO
	1450	ν_{as}COO
	1374	ν_{s}COO
	759	γC−H in the benzene ring
	729	
H_2O	1617	δ molecular water
		Modes appear when H_2O is coordinated to the Cu site
5-FU [211]	1686	δC=C
	1452	δN−H
	1430	ν ring
	1350	νC−H
	1279	νC−F
	1184	δN−H
	959	
	883	γC−H
	814	δ benzene ring
	757	
PU [245, 246]	1732	νC=O
	1532	δN−H
	1230	δC−N
	1080	δC−O−C

$\nu_{as}\backslash\nu_{s}$ = asymmetric\symmetric stretching, γ = out-of-plane bending,
δ = in-plane bending

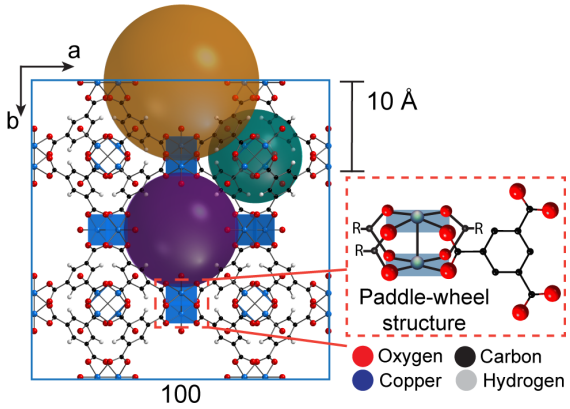

Figure 8.11: Crystal structure of HKUST-1 highlighting the three different types of pores in the structure with diameters of 5 Å (green), 11 Å (purple), and 13.5 Å (yellow), and an illustration of the paddle-wheel moiety.

molecular water at 1617 cm^{-1} (see Figure 8.4). It is important to note the increasing presence of the H_2O band in the sample during measurements performed under D_2O exposure, despite the stability of the D_2O band ($\sim$1200 cm^{-1}) throughout the experiment (*i.e.* no significant bulk D-H exchange in the liquid was detected). This observation suggests that a small amount of D-H exchange occurs within the pores of HKUST-1, with the substitution of hydrogen atoms found on the framework. As such, this confirms the ingress of D_2O into the sample, showing an increasing penetration with longer exposure, trackable with the SR-microFTIR probe.

Within regions -I and -II, three important features must be highlighted. First, in Figure 8.8a, with time progression the observed decrease in intensity of the vibrational peaks and integrated spectral area values of drug and framework peaks. Secondly, the shift of the band detected at 1590 cm^{-1} shown in the inset of Figure 8.8a, associated with the symmetric stretching of the carboxylate groups in HKUST-1. This shift can be assigned to modifications in the coordination of the carboxylate groups, indicating changes in chemical and physical interactions surrounding the HKUST-1 paddle-wheel environment. Last, in Figures 8.8c-d, the evident differences in the kinetics of the 5-FU drug molecules being released from the 5-FU/PU sample versus the 5-FU@HKUST-1/PU composite membrane.

Detailed analysis of the evolution of the FTIR spectra of 5-FU@HKUST-1/PU shows that within 1 hour of continuous exposure to D_2O, the HKUST-1 framework

was not greatly affected. After 2 hours, the decrease of the framework vibrational bands intensity was observed. These changes are accompanied by the increase in intensity of the band at 1617 cm^{-1}, showcasing penetration of water molecules into the composite and their interaction with HKUST-1. The normalized area value of the molecular water peak increased by ∼80%, accompanied by the constant decrease in the area of HKUST-1 peaks (Figure 8.8c).

According to the evolution of the spectral area presented in Figure 8.8c, the carboxylate group vibrations at 1646 cm^{-1} and 1374 cm^{-1} were primarily affected when compared to ring deformation at 725 cm^{-1}, due to the stronger effect of water on the former. Since there are overlaps between the MOF and drug molecule vibrational modes within regions -I and -II (*e.g.* peaks at 759 cm^{-1}, 1374 cm^{-1}, 1450 cm^{-1} and 1646 cm^{-1}) the decrease in the intensity of the most affected HKUST-1 peaks cannot be taken simply as the chemical decomposition of the host framework, but might also be attributed to the progressive release of the drug molecules from the HKUST-1 pores. Therefore, complementary static-cell measurements of HKUST-1/PU (Figure 8.12) and PU membranes (Figure 8.13) were performed to investigate any possible framework decomposition. It was observed that the main vibrational peaks of HKUST-1 have not suffered major degradation during the static experiments. The PU membrane remains unchanged upon media exposure. In the HKUST-1/PU spectra it is possible to observe the progressive increase in intensity of the molecular water peak (Figure 8.12b), confirming the permeation of water. A decrease in the spectral area of the symmetric and asymmetric vibrations of carboxylate groups was found at 1646 cm^{-1} and 1450 cm^{-1}. The most important observation Figure 8.12 is that the redshift of the 1590 cm^{-1} band, observed in 5-FU@HKUST-1/PU, was not detected in the spectra of HKUST-1/PU composite. This confirms that the observed shit of the symmetric stretch of the carboxylate group occurs due to the release of the drug molecule and associated changes in the guest-host interactions, instead of being related to the deuteration of the carboxylate group [247]. At this point, it is uncertain whether the amount of D_2O in contact with the sample was insufficient to

cause detectable framework degradation or if the polymer is effectively protecting the HKUST-1 crystals (since the MOF is fairly stable when a small amount of water is adsorbed) [42]. This question is fully addressed using *via* flow-cell studies, described in detail in section 8.2.5.

A closer look at the redshift of the vibrational band at 1590 cm^{-1} displays two important findings. First, it indicates changes in the environment of the carboxylate group bridging the pores of the host framework. This could be a result of structural distortions to the framework unit cell [248], resulting in a low symmetry configuration.

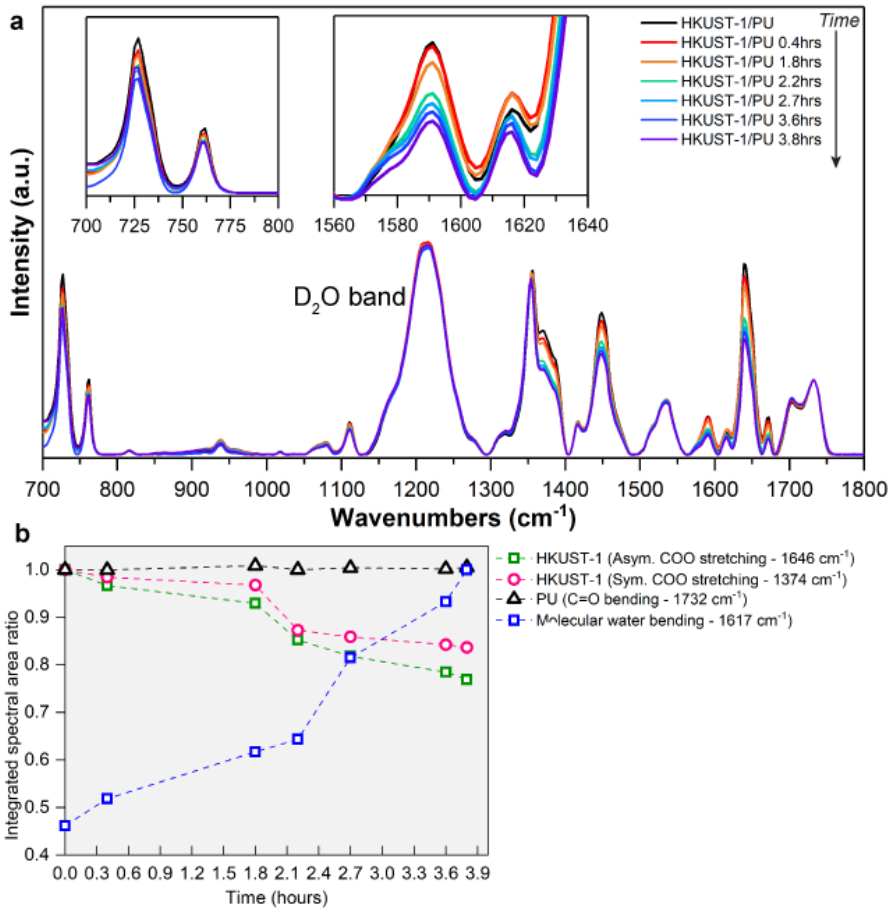

Figure 8.12: (a) Time evolution of HKUST-1/PU SR-microFTIR spectra collected during static fluid-cell experiments. (b) Evolution of integrated spectral area ratios of selected HKUST-1/PU peaks with time, upon coming into contact with water. Presented here are asymmetric and symmetric stretching modes of the carboxylate groups in HKUST-1, bending of molecular water, and PU C=O bending, used as the reference.

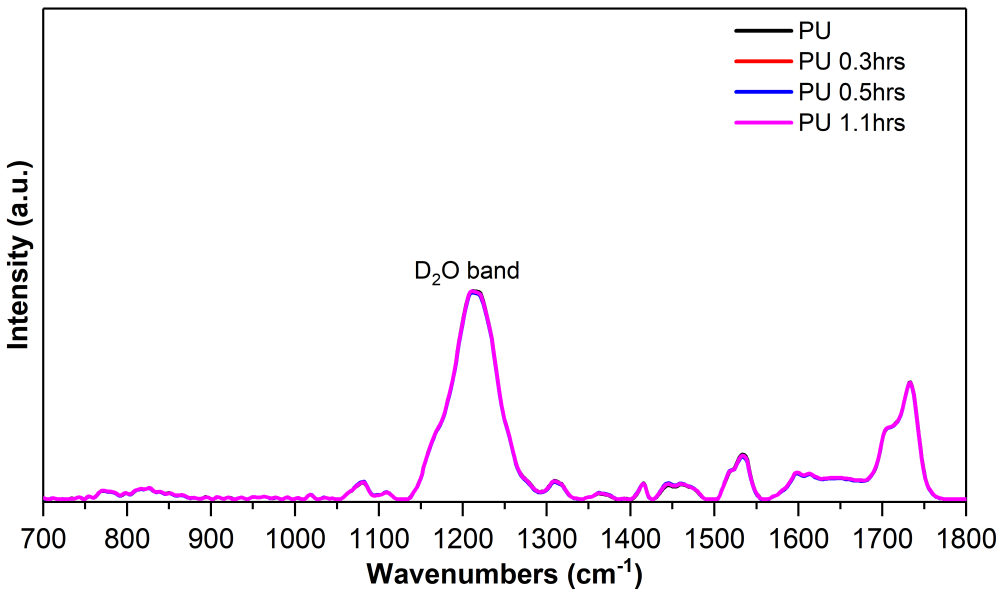

Figure 8.13: Time evolution of PU membrane SR-microFTIR spectra collected during static fluid-cell experiments, the overlapping data independent of time confirm the stability of the polymeric matrix subject to water.

Interestingly, it was established in Chapter 7 that the cubic structure of HKUST-1 is recoverable upon the release of the encapsulated drug as demonstrated by the PXRD patterns in Figure 8.14. Together, the guest-host interactions not only modify the environment of the paddle-wheel structure of HKUST-1, but also affect the preferred spatial orientation, resulting in a mechanically strained framework. The recovery of the long-range framework periodicity suggests that the coordination of the carboxylate groups is also affected by guest encapsulation and is progressively restored during the release process, as seen in Figure 8.8a. Upon the departure of 5-FU, the main HKUST-1 bands become sharper, indicating the increase in the structure symmetry and the relaxation of the structure [198, 249].

It should be emphasized that the permeation of water into the polymeric membrane was only possible due to the presence of HKUST-1 crystals embedded in these composites. It is hypothesized that HKUST-1 enables the establishment of hydrophilic "channels" that facilitate the penetration of molecular water that triggers the release of the 5-FU drug molecules, as illustrated in Figure 8.15. The role played by HKUST-1 on the water diffusion, attributed to the hydrophilic metal sites present in its structure, can be detected by contrasting the evolution of 5-FU/PU

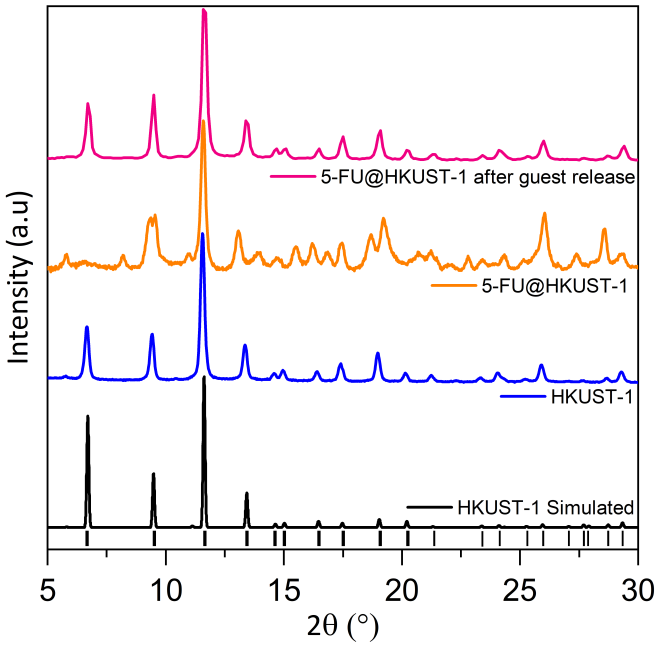

Figure 8.14: Normalized diffraction patterns of manually ground HKUST-1 (blue) and its drug loaded counterpart (orange). In pink is PXRD of 5-FU@HKUST-1 after the release of the 5-FU (guest) molecules. Recovery of cubic symmetry is clear when comparison is made between the diffraction pattern of the host framework obtained after guest release and simulated pattern of HKUST-1 (black).

and 5-FU@HKUST-1/PU spectra (see Figure 8.8a-b). During measurements of 5-FU/PU membrane under static conditions, only minor changes to the drug peaks were observed in the FTIR spectra, in which a slower and smaller decrease in the spectral area (Figure 8.8d) was captured. In the 5-FU@HKUST-1/PU spectra is possible to observe reductions of as much as 90% in the intensity of drug molecule vibrational modes; however, in the 5-FU/PU spectra, the corresponding decline reaches a maximum of ∼35%. Further verification of the role of HKUST-1 on water accessibility can be observed in a demonstration presented in Figure 8.16. The change in colour of HKUST-1/PU membrane upon heating reveals that the water molecules, coordinated to the CUS, have accessibility into and out of the membrane. This effect has been further quantified by measuring the swelling of the composite due to water uptake (Figure 8.16c) and the decline of surface contact angle (*ca.* 95° to 80°, see Figure 8.17) upon the incorporation of hydrophilic HKUST-1 to the hydrophobic PU matrix.

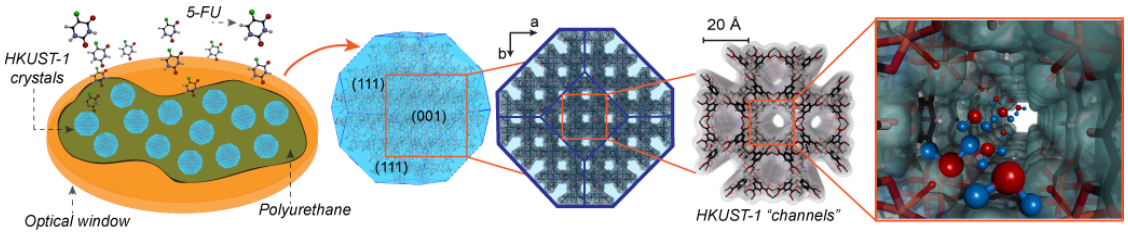

Figure 8.15: Schematic representation of HKUST-1 crystals and hydrophilic "channels" responsible for the permeation of water into the polymeric matrix and release of 5-FU molecules from the polymeric membrane. Colour code: O in red, C in black, H in grey, Cu in orange, N in purple, and F in green. Hydrogen atoms in the water molecules are shown in blue.

Before proceeding to the flow experiments, a detailed look into the synergy between 5-FU and HKUST-1 was performed *via* DFT calculations to reveal the dynamics of vibrational motions underpinning the dissociation of the drug molecule from the framework upon water exposure. The theoretical prediction will aid the understanding of the transformations presented by the material during the static and flow-cell experiments.

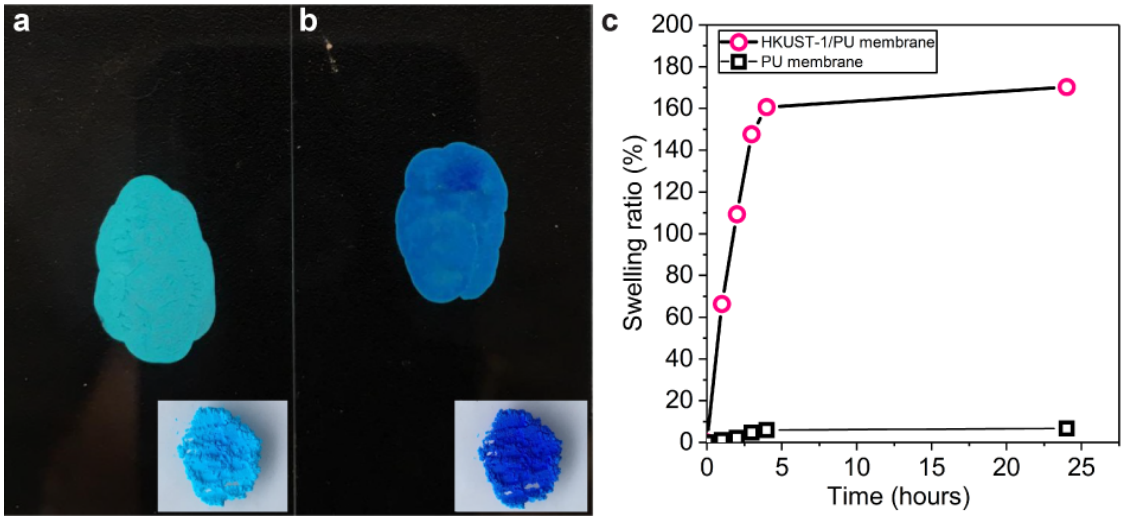

Figure 8.16: Change in colour of membranes. HKUST-1/PU membrane (a) before and (b) after sample activation at 100 °C, and insets showing the corresponding powder samples. HKUST-1 framework presents a characteristic colour switch from light blue (turquoise) to dark blue upon heating, linked to the change in coordination of the copper site. The colour change observed in the composite membrane samples confirmed the accessibility of molecular water in and out of the polyurethane matrix. (c) Swelling ratio of composites showcasing the superior absorption of water in HKUST-1/PU composite in comparison to a neat PU membrane.

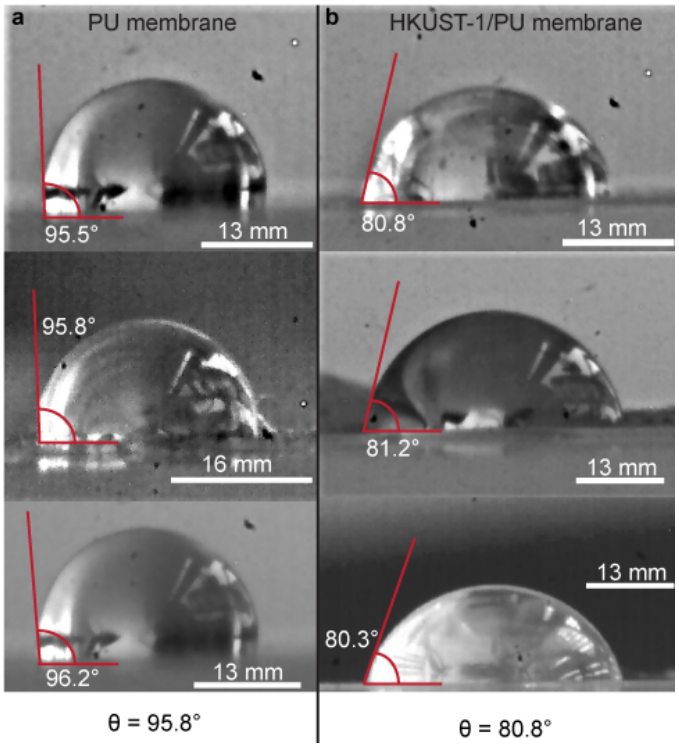

Figure 8.17: Water contact angles with (a) PU membrane and (b) HKUST-1/PU membranes displaying the increase in the wettability of the membranes by the addition of HKUST-1 particles. Attempts were made to quantity the contact angle of HKUST-1 powder. However due to the hydrophilic character and high wettability of HKUST-1 powder, no water droplet was formed to allow the quantification of contact angle.

8.2.2 DFT calculations of 5-FU@HKUST-1 assembley

As discussed in Chapter 7, the encapsulation of the drug molecules *via* the mechanochemical *in situ* strategy results in the self-assembly of drug@MOF systems, in which guest drug molecules are successfully confined in the pores of the host HKUST-1 framework. *Ab initio* DFT calculations were employed using the periodic code CRYSTAL17 [171] to reveal the nature of the guest-host interactions from different possible assemblies of 5-FU@HKUST-1 (*i.e.* adducts A-D in Figures 8.19-8.22) [2]

8.2.3 Binding energies and DFT model validation

The calculations were performed with a newly developed DFT-based 'composite method' PBEsol0-3c [250], which uses a sol-def2-mSVP basis set. This is a cost-

[2] The calculation presented in this section were developed in collaboration with scientists Professor Bartolomeo Civarelli and Ph.D. student Lorenzo Donà (University of Turin), developers of the composite DFT method used in the calculations of 5-FU@HKUST-1 assemblies.

effective HF/DFT composite method combined with a double-zeta quality basis set that is expected to provide a good trade off between accuracy and cost [250]. As a check, a comparison between this method with the benchmarked B3LYP-D3(ABC)/VTZP calculations. Figure 8.18 shows that computed binding energies for adducts A and D with both methods are very similar thus confirming the excellent accuracy of PBEsol0-3c.

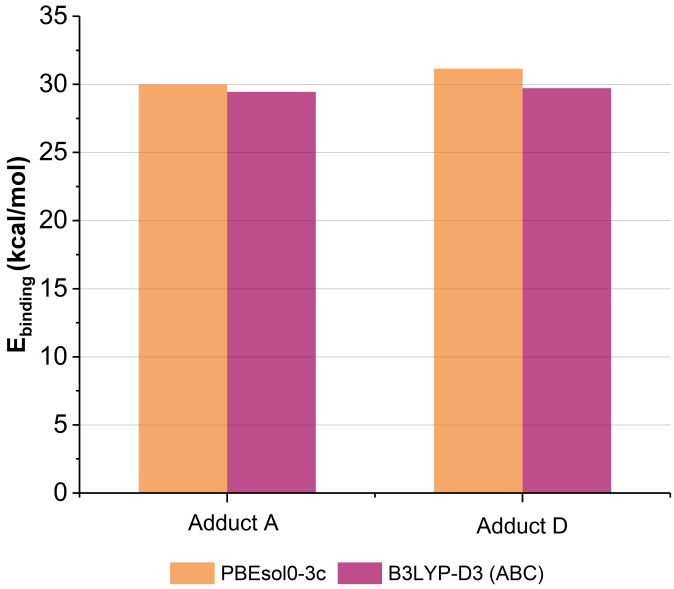

Figure 8.18: Comparison between binding energies calculated for adducts A and D configuration using PBEsol0-3c and B3LYP-D3(ABC) levels of theory and sol-def2-mSVP and Ahlrichs (VTZP) basis set, respectively. The good agreement between the computed binding energies applying both methods validating the new method developed and used in this work.

8.2.4 Analysis of adducts configurations

Four possible guest-host configurations of 5-FU encapsulated in the largest pore of HKUST-1 (*i.e.* 5-FU@HKUST-1), namely adducts A to D, as shown in Figures 8.19-8.22, were investigated in the DFT calculations with the PBEsol0-3c method [250].

In Figure 8.23a, the electrostatic potential mapped on top of a charge density isosurface for both HKUST-1 and 5-FU clearly shows that copper acts as a coordinatively unsaturated metal with a large positive region while oxygens in 5-FU molecule are surrounded by a strong negative region. The initial configurations for the four adducts have been created by matching the positive and negative regions

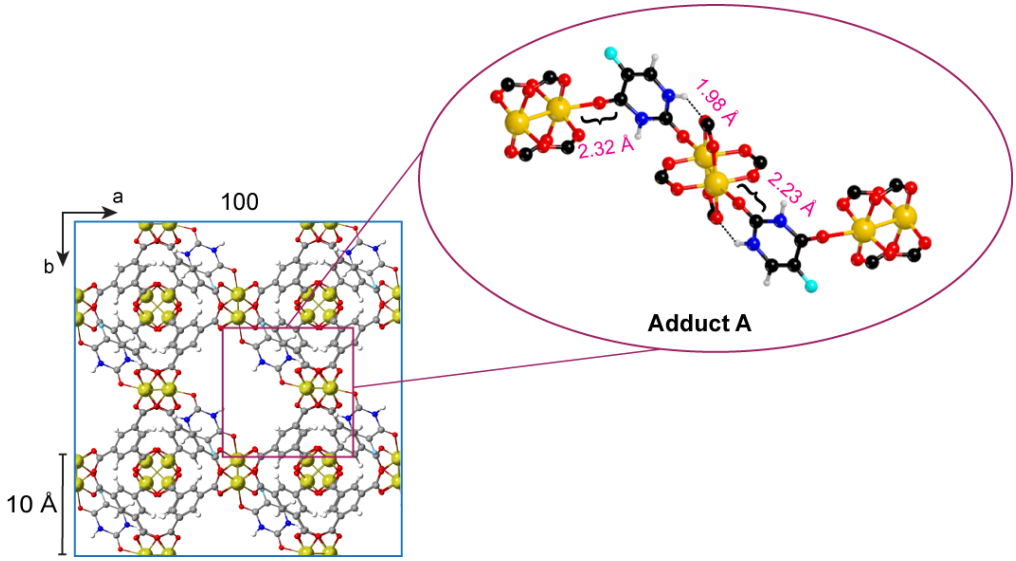

Figure 8.19: Adduct A configuration. In this adduct, 5-FU drug molecule (guest) interacts with two different paddle-wheels through its oxygen atoms. Hydrogen bonds are established between the N-H group of 5-FU and oxygen atoms in the carboxylate groups of the HKUST-1 (host) paddle-wheel. Note that in this case there are two molecules in the unit cell. Colour code: O in red, C in black, H in grey, Cu in yellow, N in navy blue, and F in turquoise.

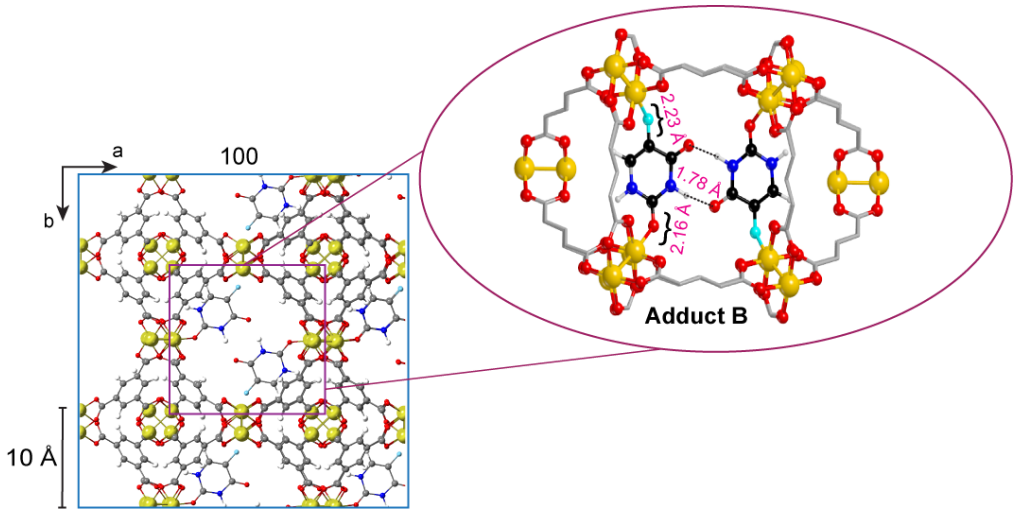

Figure 8.20: Adduct B configuration. In this adduct, the 5-FU guest is anchored to the adjacent paddle-wheels of the HKUST-1 (host) *via* its one of the oxygen atoms and fluorine, establishing NH-O hydrogen bonds with adjacent 5-FU molecules. Note that in this case there are two molecules in the unit cell. Colour code: O in red, C in grey, H in grey, Cu in yellow, N in navy blue, and F in turquoise.

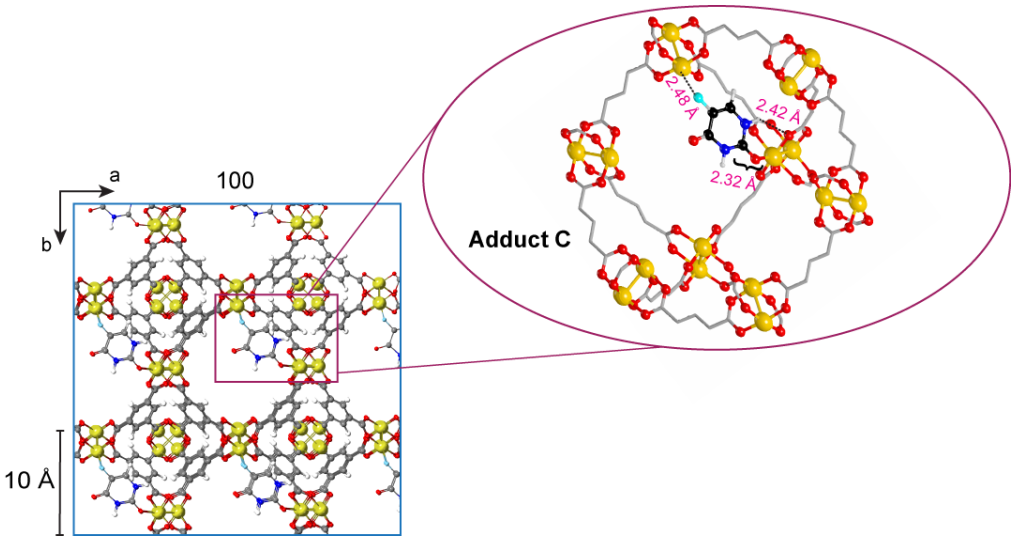

Figure 8.21: Adduct C configuration. 5-FU chelates two paddle-wheels *via* its oxygen and fluorine atoms. Note that in this case there is one molecule of 5-FU in the unit cell. Colour code: O in red, C in grey, H in grey, Cu in yellow, N in navy blue, and F in turquoise.

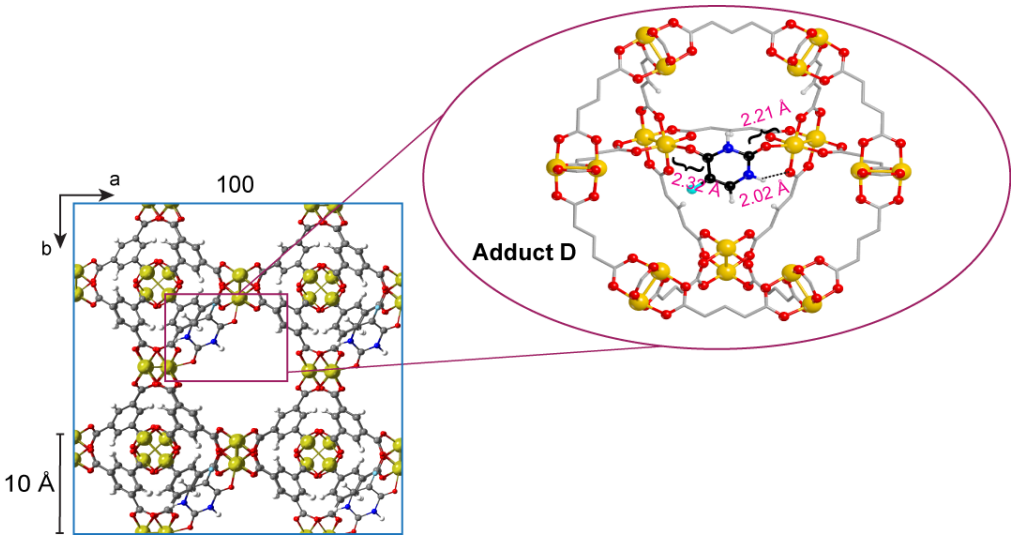

Figure 8.22: Adduct D configuration. In this configuration, 5-FU interacts with two different paddle-wheels through its oxygen atoms. Note that this geometry is similar to adduct A but there is one molecule of 5-FU in the unit cell. Colour code: O in red, C in grey, H in grey, Cu in yellow, N in navy blue, and F in turquoise.

of HKUST-1 and 5-FU and by considering the strong affinity between copper and oxygen. Therefore, a Cu−O bond was assumed as the dominant interaction in 5-FU@HKUST-1. Additionally, secondary interactions between NH groups of 5-FU and the negative regions around the carboxylate oxygens of the MOF could be envisaged, along with a less strong interaction between copper and fluorine. The Cu−Cu distances in the cage are compatible with the size of the drug molecule, thus making it possible to have the bridging geometries. Overall, the sum of these different interactions and chemical intuition have led to the four adducts shown in Figures 8.19-8.22. It is important to emphasize that the models herein proposed consider ideal drug loading within HKUST-1 pores, which can differ from the experimental sample with ∼14 wt.% loading of 5-FU in HKUST-1.

Based on the EPS of HKUST-1 and 5-FU (Figure 8.23a) it can be clearly seen that while Cu atoms in the paddle-wheel of HKUST-1 (positive regions) can act as a primary adsorption sites, oxygen atoms of 5-FU (negative regions) can strongly interact with copper through dative bonding. Instead, a less strong interaction is expected through the fluorine atom. In addition, the size of the 5-FU molecule and the Cu—Cu distances in the cage are commensurate to each other and can lead to a bridging conformation of the possible 5-FU@HKUST-1 adducts. The stabilization energy of four different drug-MOF binding configurations (*i.e.* adducts A-D in Figure 8.19-8.22) has been investigated and contrasted it against the water-MOF interactions. The theoretical spectra for each adduct configurations being considered are presented in Figure 8.24a-d and were contrasted against the experimental 5-FU@HKUST-1 ATR-FTIR spectrum.

The closer match between the experimental and theoretical spectrum of adduct A suggests that this is probably the dominant configuration in 5-FU@HKUST-1 system. The theoretical results crucially show that 5-FU is in coordination with HKUST-1 specifically *via* its CUS sites (*via* C=O$\cdots$Cu coordination). Concomitantly, 5-FU establishes hydrogen bonds with the oxygen atoms present in the carboxylate groups, as depicted in Figure 8.24e. This configuration is akin to another reported system termed: TCNQ@HKUST-1 [102]. As displayed in Figure 8.24f, the

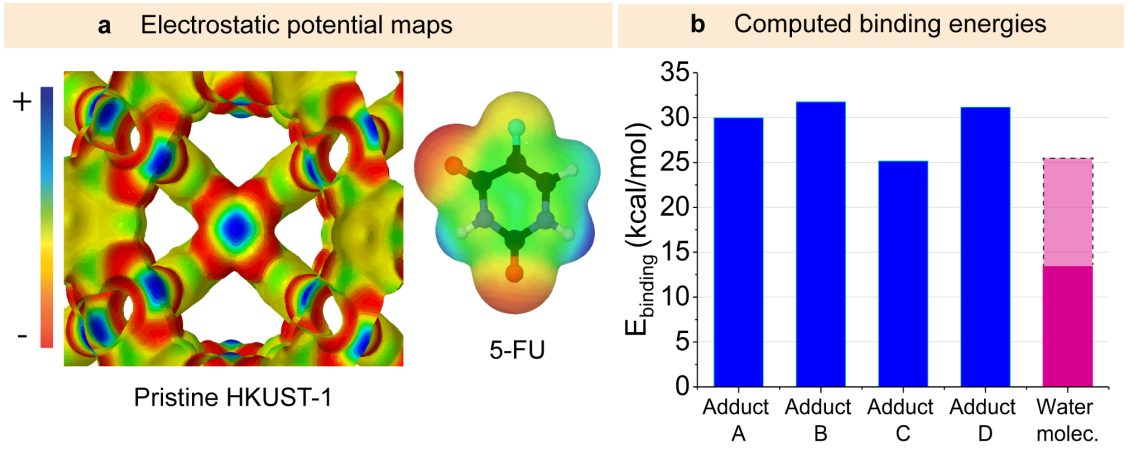

Figure 8.23: (a) Electrostatic potential maps of HKUST-1 (left) and 5-FU (right) supporting that 5-FU can strongly interact with the copper centres of HKUST-1 through its oxygen atoms generating both bridged and single site adducts. The interaction through the fluorine atom is possible but less likely due to the strength of the bond. (b) Binding energies of different adducts for the 5-FU-HKUST-1 interaction. The dashed line represent the binding energy relative to two water molecules, necessary for the release of the two 5-FU molecules encapsulated in the pores of adducts A-D.

Cu−Cu distances in two adjacent paddle-wheels is also affected by the binding of the 5-FU molecules to the CUS. This showcases the disturb to the preferred spatial orientation and relaxation upon drug release detected in Figure 8.14. However, based on the computed binding energies summarized in Figure 8.23b, and the analysis of the low energy vibrational bands (*i.e.* THz vibrations) *via* INS displayed in Figure 8.25, a coexistence between the different adduct configurations is possible in the 5-FU@HKUST-1 system. According to the binding energies calculated, it was possible to establish that D_2O and H_2O are capable of triggering the release of 5-FU, as observed experimentally (see Figure 8.23b). Table 8.4 gathers the different contributions needed to calculate the enthalpy of adsorption for the different 5-FU@HKUST-1 adducts. In details, E_L is the electronic energy from DFT calculation, E_0 is the zero-point vibration energy and E_T is the thermal contribution to enthalpy. The latter term were obtained at T = 298K. From the computed values, the enthalpies of adsorption at 298 K was obtained as reported in Table 8.4. Results confirm that adduct C is the less favoured configuration, while other adducts show similar ΔHs. In agreement with binding energies, the

adsorption enthalpies show that two water molecules are capable of competing with 5-FU for the interaction with the metal site.

It is important to emphasize that the binding energies shown in Figure 8.23b should be interpreted according to the particularities of the adduct configurations, especially when comparing these binding energies with the water binding energy. Although, adducts A and B display two 5-FU molecules in each HKUST-1 pore, and adducts C and D are comprised of one 5-FU molecule per pore, all configurations show the adsorbate as bridged between two adjacent metal sites (see

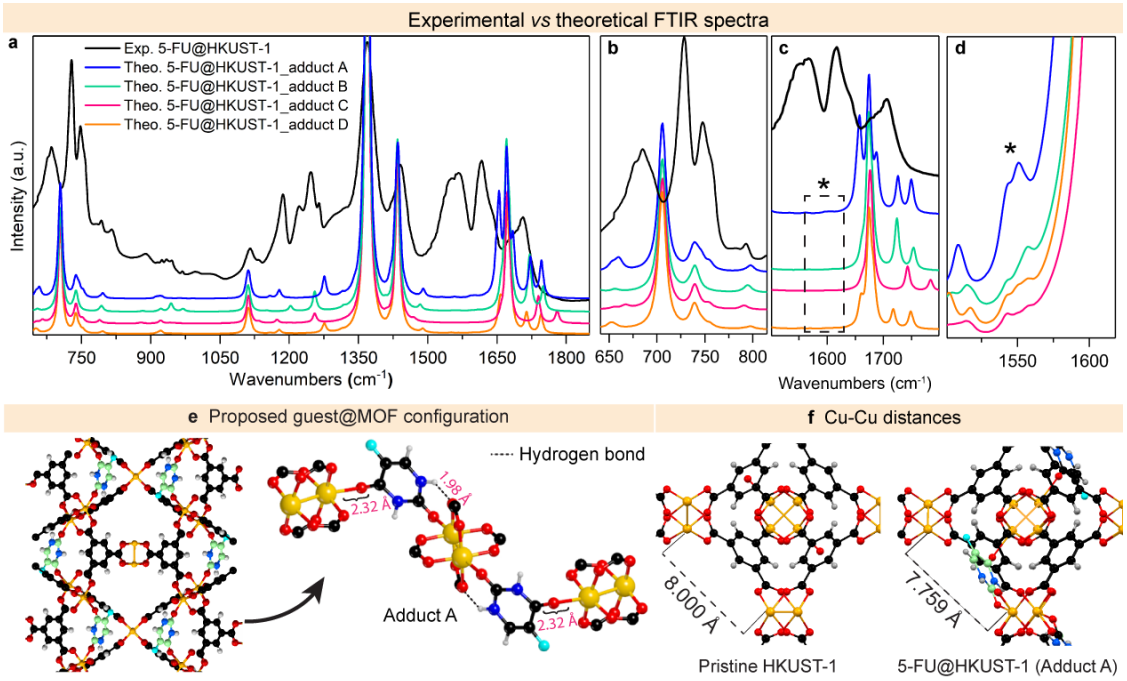

Figure 8.24: Results from DFT calculations. (a) Comparison of experimental (ATR-FTIR) and calculated spectra of 5-FU@HKUST-1 for the four possible host guest configurations, termed adducts A-D. Closer look at different spectral regions showcasing the better match between adduct A spectrum and the experimental data when contrasted with other configurations: (b) 650-810 cm^{-1}, (c) 1500-1750 cm^{-1}, and (d) zoom-in of the peak ~1550 cm^{-1}, which was presented in low intensity due to the adopted DFT basis set. Note that a scaling factor (*i.e.* 0.95) were applied to the DFT spectra in (a), (b), (c), and (d) to eliminate common shifts resulting from the *ab initio* calculations and to match the frequencies against the experimental spectrum. (e) Proposed guest-host interaction obtained from DFT. In the schematic, 5-FU interacts with two different paddle-wheel sites through oxygen atoms while establishing hydrogen bonds with the carboxylate groups. (f) DFT optimized structure showing the Cu−Cu distances between adjacent paddle-wheels in pristine HKUST-1 (left) and 5-FU@HKUST-1 (right). Colour code: O in red, C in black, H in grey, Cu in yellow, N in navy blue, and F in turquoise. Carbon atoms in the drug molecules were displayed in green to show the position of the guest molecule.

Table 8.4: Thermodynamic analysis of the different adduct configurations

	Adduct A	**Adduct B**	**Adduct C**	**Adduct D**	HKUST-1 + H_2O	HKUST-1 + D_2O
E_L (KJ/MOL)	-7.09×10^7	-7.09×10^7	-6.96×10^7	-6.96×10^7	-7.07×10^7	-7.07×10^7
E_0 (KJ/MOL)	2898.79	2898.42	2682.91	2683.84	3255.06	3047.48
E_T (KJ/MOL)	327.11	326.68	305.48	304.76	385.49	396.59
H (KJ/MOL)	-7.09×10^7	-7.09×10^7	-6.96×10^7	-6.96×10^7	-7.07×10^7	-7.07×10^7
ΔE (KCAL/MOL)	-30.01	-31.78	-25.24	-31.25	-13.41	-13.41
ΔH (KCAL/MOL)	-28.65	-30.51	-23.93	-29.88	-11.65	-11.90

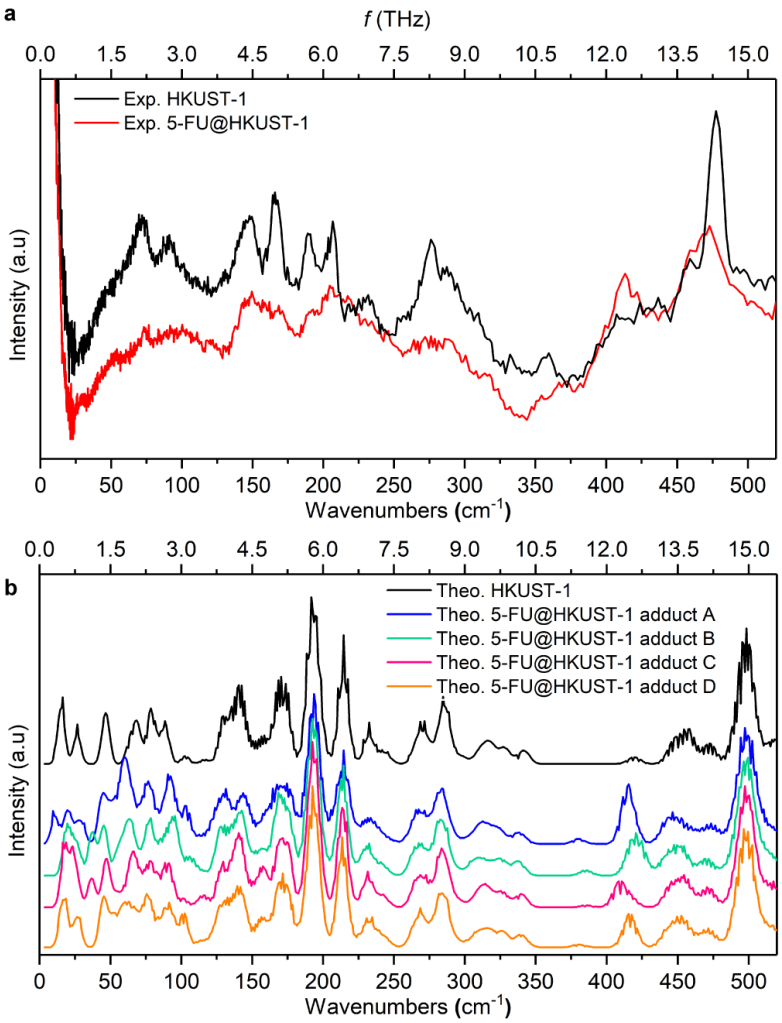

Figure 8.25: INS spectra of adduct configurations. Comparison between (a) experimental INS spectra of pristine HKUST-1, 5-FU@HKUST-1, and (b) theoretical INS spectra of pristine HKUST-1 and different adduct configurations (*i.e.* A-D)

Figures 8.19-8.22). In adducts A, B and D, for example, 5-FU is linked through oxygen-copper bonds while in adduct C the interaction involves one oxygen and the fluorine atom. It is worth noting that for the latter, not unexpectedly, the binding energy is the lowest one. As regards the competition with water, in adduct A, for example, the binding energy of each individual oxygen-copper bond might be considered to be ∼15 kcal/mol, on average, very close the water binding energy of ∼13.5 kcal/mol, and therefore highlighting the capability of water (D_2O and H_2O) to induce the release of 5-FU molecules. Additionally, because of the smaller size of water molecules in comparison with 5-FU, the configurational entropy [251] as well as entropy of stabilization [252] favour the formation of water-CUS interactions in the HKUST-1 framework.

8.2.5 Flow-cell measurements

SR-microFTIR *in situ* flow experiments using a liquid flow-cell were conducted to investigate the possible degradation of HKUST-1 and the protective role conferred by the PU matrix (Figure 8.26). For measurement in D_2O flow, the media were allowed to flow for approximately 25 minutes before starting data collection, thus allowing the system to reach D-H equilibrium. Over a total period of 2.3 hours, no clear decomposition of the framework was observed. All the main framework peaks appear to be intact, with minimal changes to the carboxylate vibrations intensity (see in Figure 8.26a). Importantly, this confirms that the polymeric matrix is able to significantly enhance the stability of HKUST-1 in aqueous conditions by providing a protective coating to the MOF structure. This can be further demonstrated by contrasting the PXRD of HKUST-1/PU membrane and HKUST-1 powder before and after immersion in H_2O (Figure 8.27). While in the polymer composite the diffraction peaks of HKUST-1 appear to be intact, those in the powder sample suffers major degradation over a much shorter period of time.

Flow experiments were also conducted on 5-FU/PU membranes to further corroborate the difficulty that 5-FU molecules face to escape the PU membrane in the absence of HKUST-1 crystals. The evolution of the vibrational spectra is

presented in Figure 8.26b showing the stabilization of the D_2O flow by the decrease in intensity of H-O-D bending mode (~1460 cm^{-1}). A closer look at the drug peaks in the composite spectra reveals that their intensity is only minimally affected over a 2-hour period (Figure 8.28). This is more evident when 5-FU/PU spectra are contrasted against the spectra of 5-FU@HKUST-1/PU membrane (Figure 8.8a), in which changes to the drug peaks intensity were observed within 1 hour (see Figure 8.8a). This observation highlights the importance of HKUST-1 embedded within the composites to yield a more sustained release of the drug. As previously discussed, the creation of the hydrophilic channels by HKUST-1 is essential for the water-CUS interactions and subsequent release of the drug molecule. The results

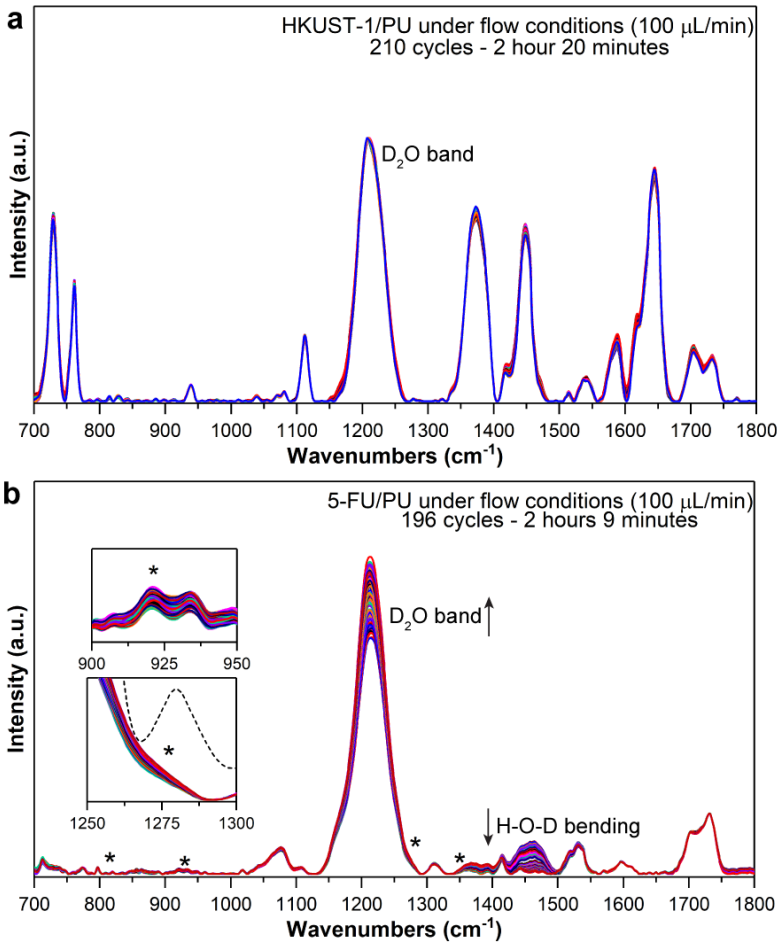

Figure 8.26: Flow-cell measurements of polymeric composites. (a) HKUST-1/PU membrane under D_2O flow shows absence of any change to MOF vibrational bands. (b) 5-FU/PU membrane spectra, showing the increase in intensity of D_2O band and decrease of H_2O which demonstrates the stabilization of D_2O flow. Asterisk marks the position of drug peaks in the composite spectra.

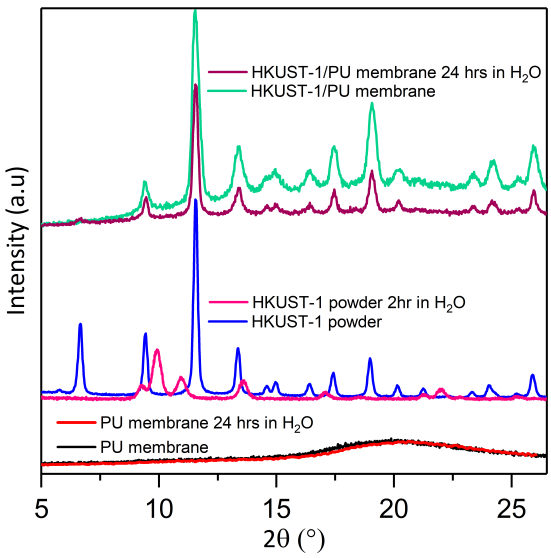

Figure 8.27: PXRD patterns of PU and HKUST-1/PU composite and HKUST-1 powder before and after immersion in water for 24 hours and 2 hours, respectively. The composites patterns show how the polymeric matrix can provide protection to the MOF, preventing hydrolysis. For HKUST-1 powder, the intensity of the diffraction peaks has decreased significantly after 2-hour immersion accompanied by emergence of new Bragg peaks suggesting phase transformation. In contrast, the diffraction pattern of HKUST-1/PU composite shows that it is considerably more stable even after 24 hours of immersion in water.

presented in this chapter suggest that the polymer coating provides not only a supporting scaffold to the framework, protecting it against water degradation, but also helps to regulate the rate of the drug release process, as evidenced in Figure 8.29. In fact, the presence of the PU, even at a high HKUST-1:PU ratio, demonstrated the potential of employing the composites to suppress the release of 5-FU by a factor of about 20 times. Crucially, since HKUST-1 plays a key role on the release kinetics of 5-FU molecules (as demonstrated in Figures 8.8 and 8.26), one can conclude that the larger the HKUST-1:PU ratio, the faster the release of the guest molecules will be. Therefore, there is scope to tune the MOF:polymer ratio in the composites to achieve a well-controlled release of 5-FU molecules in order to mitigate the unwanted burst effect (*i.e.* extending the release period to intervals longer than 3.3 hours).

In this context, Figure 8.30 presents the spectra of 5-FU@HKUST-1 powder collected during flow experiments. The combination of measurements taken under D_2O (Figure 8.30a-c) and H_2O (Figure 8.30d) flow permitted a close monitoring

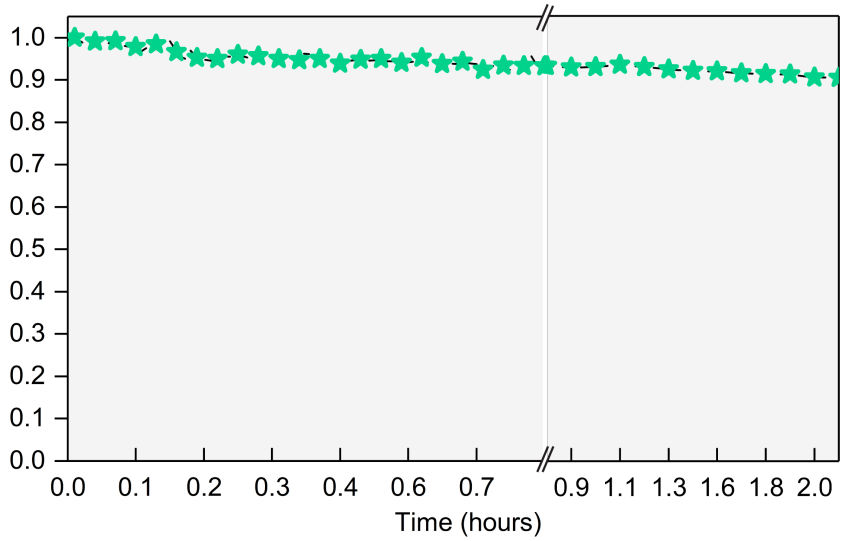

Figure 8.28: Integrated spectral area of 5-FU/PU peak (C-F stretching 1279 cm^{-1}) selected from spectra collected during the flow experiments.

of the evolution of 5-FU peaks in regions I and II of the vibrational spectra. Figure 8.30a presents the evolution of the sample over time under D_2O flow (the spectra of various time points were omitted for clarity). However, all the spectra collected have been represented for regions of interest within the spectral range in the 3D contour maps presented in Figures 8.30b and 8.30c and in the inset in

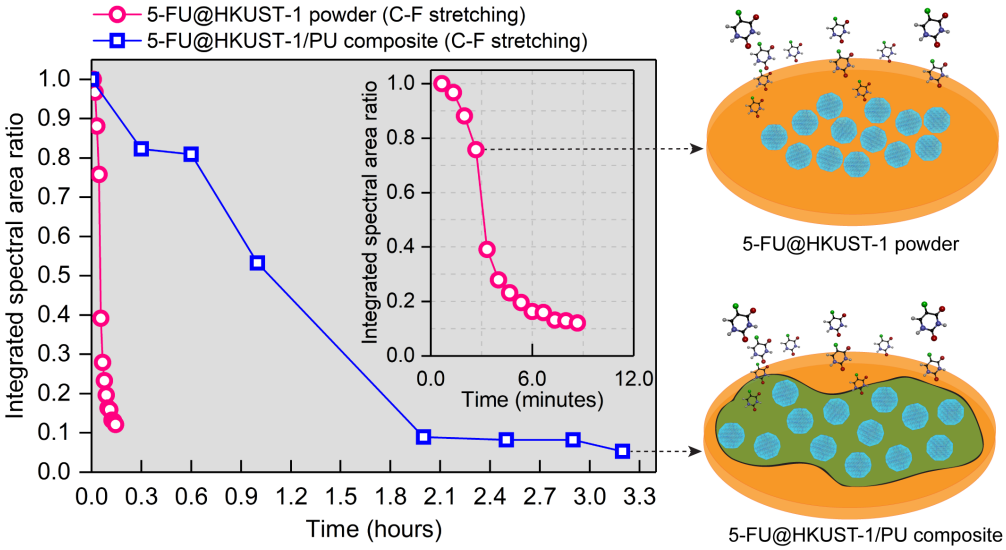

Figure 8.29: Changes in the rate of drug release due to the presence of the polymer matrix. Comparison of spectral area of 5-FU peak (C-F stretching 1279 cm^{-1}) in 5-FU@HKUST-1 powder and 5-FU@HKUST-1/PU composite demonstrating how PU aids in regulating the velocity of 5-FU release.

Figure 8.30a. Under D_2O flow, the most pronounced changes can be observed in the shoulder at ∼1620 cm^{-1} and ∼1700 cm^{-1}, which can be attributed to the C=C stretching of 5-FU. The progressive decline in the intensity of these peaks, accompanied by the sharpening of the HKUST-1 bands at 1374 cm^{-1}, 1450 cm^{-1} and 1646 cm^{-1}, respectively, indicating the release of the 5-FU molecules. Meanwhile, it is possible to observe with detail the disappearance of these shoulders with time (Figures 8.30b-c). Figure 8.30d shows the spectra of 5-FU@HKUST-1 powder collected under H_2O flow. As can be seen in the highlighted region (1160-1300 cm^{-1}) and in the 3D profile presented in the inset, the release of the drug molecules upon exposure of HKUST-1 to a moist environment happens in an accelerated manner. By monitoring the evolution of the C-F stretching mode of 5-FU at 1279 cm^{-1}, indeed the fast release of 5-FU molecules within only 10 minutes was detected. This phenomenon marks the burst effect (rapid and uncontrolled release), which could be attributed to the water-induced degradation of the HKUST-1 framework. The comparison of 5-FU@HKUST-1 powder spectra before and after exposure to a moist environment for over 9 hours shows the pronounced decomposition of the powder sample with degradation of the main framework peaks as well as the disappearance of drug peaks (marked by asterisks in Figure 8.31). The increase in intensity of the band at 1720 cm^{-1}, associated with the C=O stretching of a carboxylic acid group, indicates the presence of protonated linker (*i.e.* H_3BTC). The protonation of the organic ligand is an indicator of major framework decomposition [194, 197]. Given this strong structural degradation, it becomes evident the need of the (hydrophobic) polymeric scaffolding for the protection of the (hydrophilic) HKUST-1 framework.

8.3 *Ex situ* drug release experiments

To further evidentiate the advantages presented by the combination of a hydrophobic polymeric matrix with hydrophilic host MOF fillers, prolonged release tests (up to 7 days) were performed *ex situ* with the powder and composites samples studied in this chapter. Drug release profiles were constructed *via* UV-Vis spectroscopy, as presented in Figure 8.32. The *ex situ* release experiments were performer in H_2O.

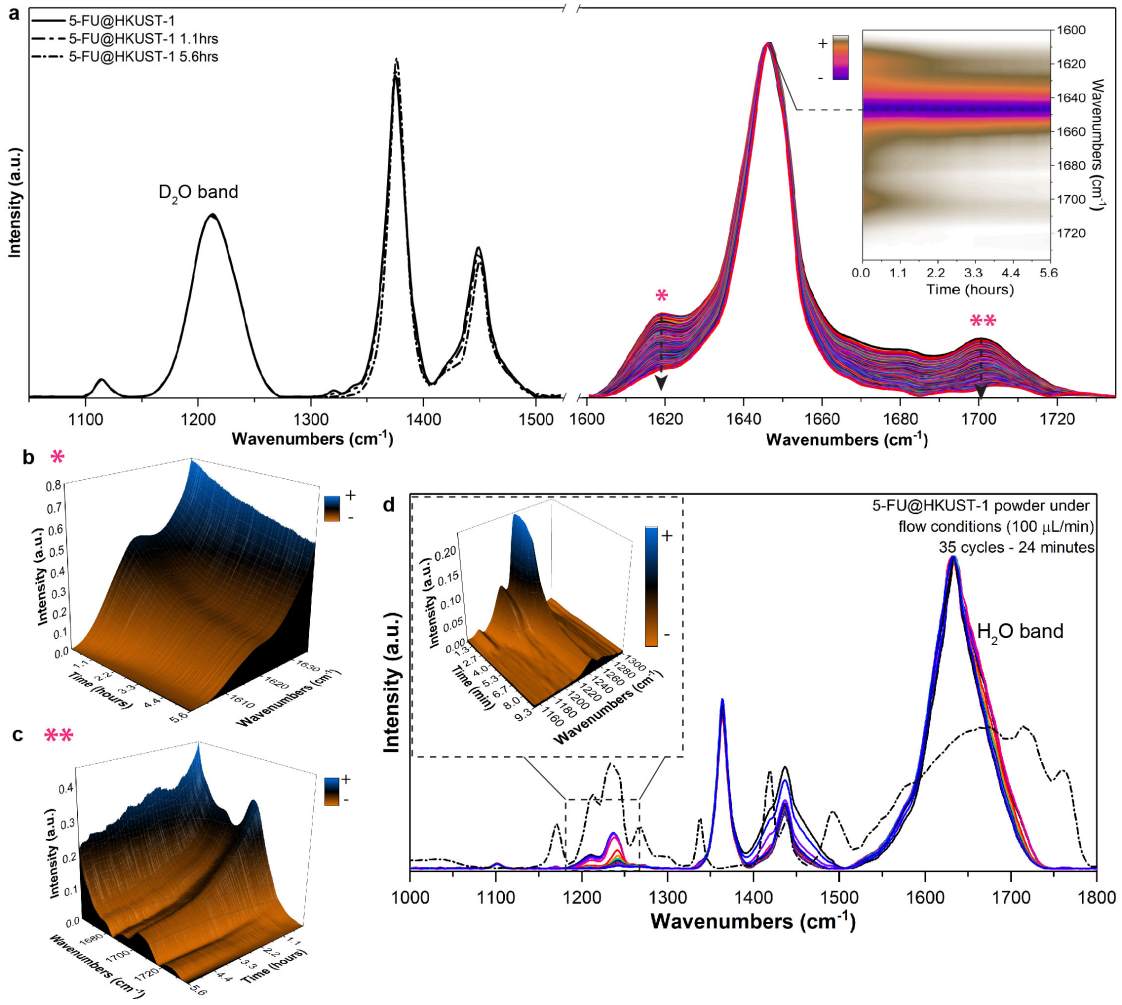

Figure 8.30: Flow-cell measurements of powder samples. (a) Time-resolved SR-microFTIR spectra of 5-FU@HKUST-1 powder sample collected under 100 µLmin^{-1} of D_2O flow. The D_2O bending mode is indicated. Inset shows the 2D profile demonstrating the progressive decrease of the 5-FU drug peaks intensity. Asterisks mark the 5-FU peaks being monitored. (b, c) 3D contour maps showing the detailed evolution of the intensity of C=C bending and N-H stretching modes of the drug molecule. (d) Spectra of 5-FU@HKUST-1 powder sample collected under 100 µLmin^{-1} H_2O flow. The H_2O bending mode is indicated. Inset displays the evolution of the C-F stretching mode ($\sim$1279 cm^{-1}) of 5-FU, indicating the fast release of a considerable amount of the drug molecule within 10 minutes. 5-FU spectrum was scaled down by a factor of 0.6 to facilitate the comparison with the spectra of the composite membranes molecules.

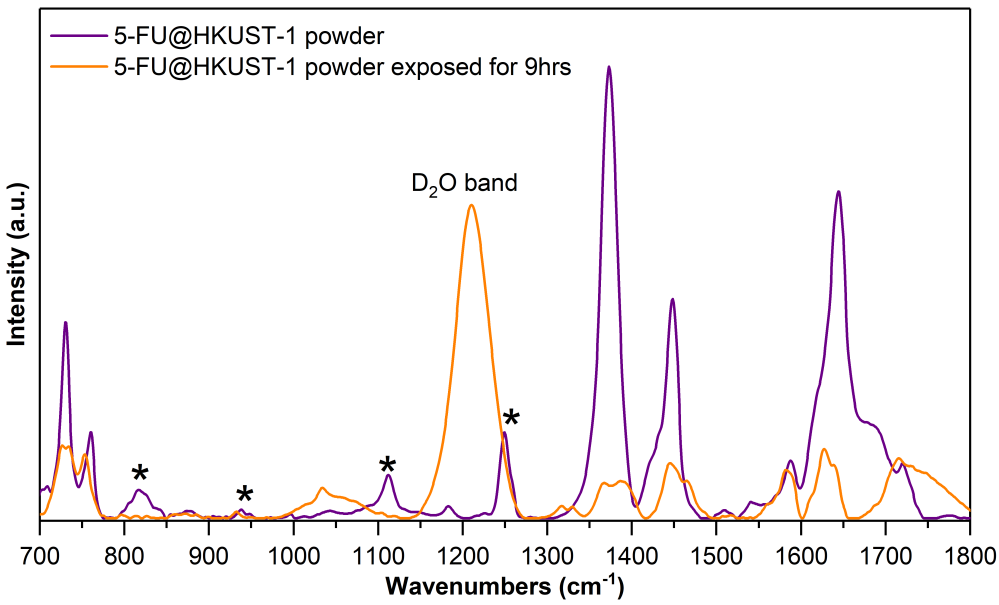

Figure 8.31: Comparison of 5-FU@HKUST-1 powder spectra before and after long exposure to moist environment. The spectra show the pronounced decomposition of the powder sample with degradation of main framework peaks as well as the disappearance of drug peaks, the latter marked by asterisks. The increase in intensity of the band at 1720 cm^{-1} indicates the presence of the acidic form of BTC.

The evolution of the 266 nm absorption band of 5-FU was monitored to determine and compare the cumulative release of the drug molecules from 5-FU@HKUST-1 powder, and 5-FU@HKUST-1/PU and 5-FU/PU membranes. Fitted curves of the release profiles revealed that the release process follows a generalized hyperbolic curve for all the samples (see Table 8.5).

During the first release stage (initial 5 hours), a drug release of ∼56% was detected from 5-FU@HKUST-1 powder sample in the first 15 minutes, going up to a total of ∼84% after 5 hours of continuous exposure to an aqueous environment. As previously mentioned, this can be characterized as the burst effect attributed to the fast degradation of the HKUST-1 host structure when exposed to bulk amounts of H_2O. Comparatively, only ∼10% of 5-FU were released from 5-FU@HKUST-1/PU membrane in the initial 15 minutes, with a maximum of ∼40% released after 5 hours.

Table 8.5: Fitting equations: 5-FU release profiles from HKUST-1/PU composites

Sample	Fitted equation	R^2
5-FU@HKUST-1 powder	$5\text{-FU}(\%) = 110.8 - \frac{372.5}{1+4214x^{1/0.475}}$	0.97388
5-FU@HKUST-1/PU memb.	$5\text{-FU}(\%) = 53.3 - \frac{48.3}{1+0.38x^{1/0.83}}$	0.99891
5-FU/PU memb.	$5\text{-FU}(\%) = 6.37 - \frac{4.33}{1+0.85x^{1/1.06}}$	0.9977

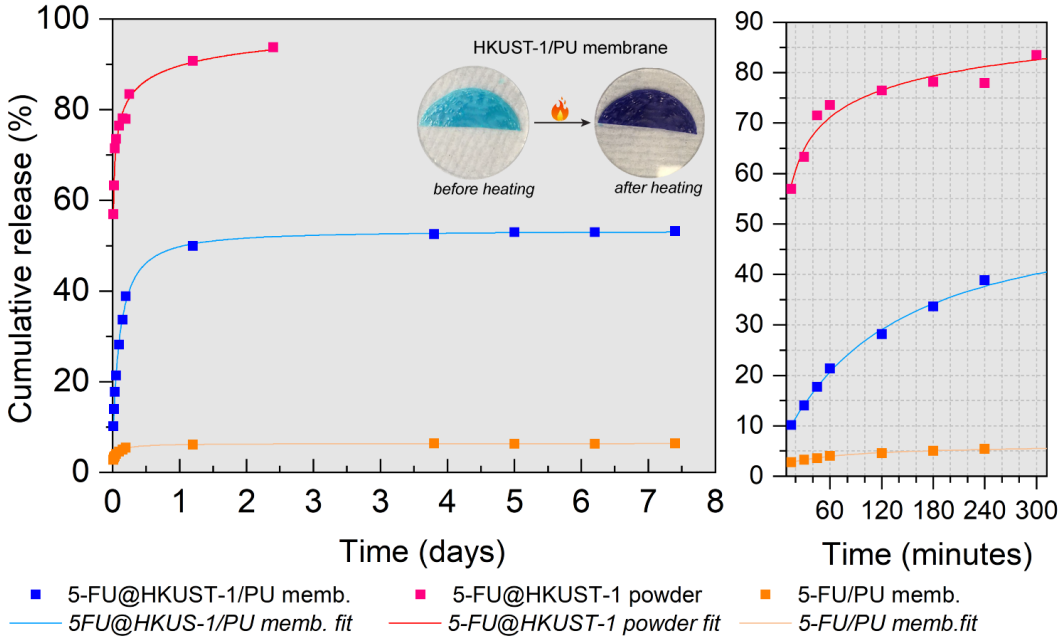

Figure 8.32: Drug release profiles of 5-FU@HKUST-1 powder (red trace fit), 5-FU@HKUST-1/PU membrane (blue trace fit), and 5-FU/PU (orange trace fit) revealing the cumulative release over a period of 7 days. The drug release profiles were constructed *via* UV-Vis measurements. The percentages were calculated by considering the total loading of the drug in the drug@MOF systems, determined by TGA. Insets show photographs of HKUST-1/PU membrane after it has been immersed in H_2O for the 7-day release period.The evident change in colour of the membrane upon heating indicates the survival of HKUST-1 MOF when protect by the PU coating

Conversely, for the same time intervals, the amounts of ∼2.5% and ∼5.0% were released from 5-FU/PU composite. In the second release stage (*i.e.* up to 7 days), a deceleration of the release was noted, which stabilized after 24 hours. ∼53.2%, and ∼6.3% of the 5-FU loaded into 5-FU@HKUST-1/PU, and 5-FU/PU were respectively released after 7 days. In contrast, ∼95.5% of 5-FU was release from

5-FU@HKUST-1 powder after 48 hours, in which period the complete decomposition of the host structure was detected.

Three key facts should be highlighted from the prolonged drug release results. First, as demonstrated by the *in situ* drug release experiments discussed earlier in this chapter, the presence of HKUST-1 is essential for the effective release of 5-FU. The hydrophilic channels created by the host MOF allowed for a release 8 times more effective than the one observed for its MOF-free counterpart. Secondly, the role played by the hydrophobic polymer on the regulation of the release rate over an extended period is very clear. This is evidenced by the stabilisation of the release after 24 hours and the continuous delivery of 5-FU up to 7 days. Specifically, during the critical first 15 minutes, the polymeric matrix acted to highly suppress the release of 5-FU. Last, the protective character of the polymer coating is also evidenced in the release profile of 5-FU@HKUTS-1 powder. The release pf 5-FU from the powder sample was almost complete in the first 48 hours, effect attributed to HKUST-1 degradation. As noted in the inset of Figure 8.32, the change in colour of the 5-FU@HKUST-1/PU membrane upon heating, recorder after the 7-day release experiment, demonstrated the survival of the HKUST-1 host MOF when protect by the PU coating.

8.4 Summary and conclusions

HKUST-1 plays a significant role in the basic and applied fields of MOFs research, due to not only its ease of synthesis and scalability, but also because it is a reference material for the study of many general properties of MOFs. This chapter has demonstrated the power of high resolution synchrotron microspectroscopy technique to track the local chemical and physical transformations taking place in the guest@MOF assembly and guest@MOF/Polymer composite during the dynamic release of guest molecules. It has been shown that while PU effectively and efficiently protects the moisture-sensitive MOF structure against water degradation, the incorporation of HKUST-1 is important to facilitate the release of the 5-FU molecules. To this end, the combination of a hydrophilic MOF with a hydrophobic

polymeric matrix is a highly promising strategy to overcome the burst effect. The presented DFT calculations uncover the preferred 5-FU@HKUST-1 configurations and elucidate the energetics behind the guest-host interactions. Furthermore, the theory sheds light on how the HKUST-1 recovers its symmetry upon the release of the encapsulated drug molecules, helping to confirm the efficacy of the solvent-free mechanochemical approach to manufacture drug@MOF assemblies in a green chemical process. Finally, the general concept of tunable composite systems coupled with facile encapsulation of guests is a promising way forward to controlling the binding and release of drug molecules confined in a range of microporous materials.

Certain people – men, of course – discouraged me,
saying [science] was not a good career for women.
That pushed me even more to persevere

— Francoise Barré

9 Conclusions and Future Outlook

This thesis was devoted to propelling the practical biotechnological applications of MOF materials. The results herein presented focused on three main aspects related to the use of MOFs as DDS, which are extendable to the development of MOF-based technology for a variety of industry related applications:

I. The development of environmentally friendly MOF fabrication methods and drug encapsulation approaches, focusing on enhancing energy efficiency and the material's life cycle and biocompatibility.

II. The improvement of the general understanding regarding guest-host intermolecular interactions arising from drug confinement into MOF pores, specifically targeting the results of *in situ* encapsulation.

III. The in-depth understanding of the physicochemical behavior, material characteristics, and molecular mechanisms behind the dissociation of drug molecules from the host MOF structure.

The interpretation of results allowed the collection of intertwining conclusions detailed in the following paragraphs. This concluding chapter provides an overview of the results and discoveries made throughout this work and presents perspectives of future areas for exploration in the field.

Chapters 4, 5, and 6 took steps towards addressing the existing gap in the sustainable synthesis of drug@MOF systems using HKUST-1 and MIL-100 (Fe) as prototypical host structures. By leveraging the use of mechanochemistry and

water-based methodologies for the fabrication of various drug@MOF systems, the work presented in these chapters elucidate new strategies for the 'green' preparation of nanoporous 3D frameworks.

Chapter 4 presented the use of two mechanochemical based techniques for the encapsulation of 5-FU in MIL-100 (Fe). The easily accessible and low-cost manual grinding technique was contrasted to the automated vortex grinding. Vibrational spectroscopy of each drug@MOF assembly revealed the sustaining intermolecular interactions arising from each encapsulation technique. Both methods were equally effective for the preparation of pristine MIL-100 (Fe), yielding a highly crystalline material. However, the more homogenous distribution of grinding force over a larger contact area presented by manual grinding is more effective for the *in situ* encapsulation of 5-FU. It was determined that this approach permits the simultaneous formation of adjacent SBUs, which could explain the efficacy of manual grinding in achieving the confinement of 5-FU guest molecules. Conversely, in the vortex grinding process, the synchronized formation of adjacent SBUs is anticipated to be relatively slower due to the reduced region of contact from the impact collision of the stainless steel balls. Consequently, the resulting stronger guest-host interactions of the manually ground sample translates into a slower release of 5-FU from the MIL-100 (Fe) host.

The reported findings serve as a proof of concept, to illustrate how different mechanochemical environments can result in significantly different outcomes in the fabrication of drug@MOF systems. Crucially, one should appreciate the complexity underpinning the mechanochemical route, where a deeper understanding of the mechanism of incorporation and the role of mechanical stresses (*e. g.* shear, collision impact, and viscous response) are warranted to precisely control the capture of drugs and other bulky guest molecules. Nevertheless, the limitations imposed by the manual grinding process herein utilized, specifically in terms of reproducibility need to be acknowledged. However, the advantages presented by this method and its simplicity (*i.e.* low associated cost and easy accessibility) could be exploited for the rapid fabrication of novel guest@host systems at lab scale.

Chapter 5 continued the mission of using mechanochemistry to achieve MOF pore confinement by extending the candidate list of 'guest' drug molecules encapsulated within MIL-100 (Fe). This chapter presented a feasibility investigation to show how 5-FU and caffeine could function as a 'modulator', triggering the fabrication of highly crystalline MIL-100 (Fe) material, while aspirin yielded the formation of an amorphous MIL-100 (Fe) phase. These results can play a big role in advancing the sustainable fabrication of MIL-100 (Fe), by showing the innovative use of benign modulators, such as caffeine, to replace highly toxic mineralizers (*e.g.* HF) commonly used in the preparation of MIL-100 (Fe). Nevertheless, this process not only led to the fabrication of robust MIL-100 (Fe), but also allowed the environmentally friendly preparation of drug-encapsulated MOF systems, thereby addressing the continuous search for low-cost and scalable methodologies for encapsulation of guest molecules.

Chapter 5 further introduced the use of high-resolution INS spectroscopy as a new approach to study drug-MOF interactions, and more generally, the drug confinement effects from a molecular vibrational point of view. The potential offered by INS for the study of drug@MOF system is attributed to its high sensitivity to probe intermolecular interactions and its enhanced sample penetration, which had not yet been fully realized. However, this chapter demonstrated how neutron vibrational spectroscopy can be utilized to reveal intrinsic guest-host coupling, pointing to the successful confinement of drug molecules. This result was accomplished through the study of unique MOF collective vibrations observed in the low energy THz region ($<$100 cm^{-1}). THz studies *via* INS permitted the detection of strong differences in the vibrational behaviour of the isolated drug molecules when compared to drug molecules confined within the MOF pores.

Chapter 6 explored the development of a novel water-reconstruction process applied to the fabrication of the highly crystalline MIL-100 (Fe) material. One attraction of the proposed approach is its extension to the nano-caging of various guest drug molecules. This has led to the fabrication of drug@MIL-100 systems with a high loading of the encapsulated guest molecules, reaching the theoretical hosting potential of MIL-100 (Fe), not previously attained using conventional

encapsulation techniques. Indeed improving the encapsulation performance and overall drug-loading through green confinement techniques is paramount to the field of guest@MOF systems and the biomedical application of MOFs nanoparticles. Nevertheless, the high selectivity of INS spectroscopy to hydrogens has proven essential for unrevealing the mechanism behind the unconventional MIL-100 (Fe) reconstruction process. It was revealed that the reconstruction phenomenon is governed by the continuous deprotonation of the organic linkers, allowing the assembly of the extended 3D framework structure. Exceptionally, the reconstruction process was highly effective in the recovery of time degraded (aged) and mechanically amorphized samples. These are important findings that pave the way for the regeneration and recycling of MIL-100 materials, thereby addressing one of the main challenges preventing their industrial applications. As such, the results presented in this chapter form the basis of future investigations exploring the used of this method for the design and mitigation of crystalline defects to tailor properties and cyclic use of MOF materials. Moreover, this work provides a much-needed approach towards the eco-friendly and scalable synthesis of mesoporous MIL-100 (Fe) and guest@MIL-100 systems for future commercialization. Further assessments and careful synergetic analysis to better model the energetic cost of the reconstruction under large-scale conditions are strongly encouraged. Additionally, it is also appealing to advance the studies of the sustainably improved guest encapsulation methods, presented in Chapters 5 and 6, in follow-on work to include the detailed investigation of the drug release from the drug@MIL-100 (Fe). The confinement effects resulting from the modulator and reconstruction effects can be, then, assessed systematically and in detail.

Chapter 7 presented a comprehensive examination of the encapsulation performance of two confinement methods: the conventional and broadly applied impregnation technique and the novel *in situ* mechanochemical method. The use of INS spectroscopy revealed clear differences in the nature of the guest-host interactions, where modifications in the THz lattice dynamics of the *in situ* derived sample highlighted the suppression of the copper paddle-wheel motions due to

the drug-CUS coordination. By leveraging of the mechanochemical method, it was confirmed that the *in situ* strategy leads to a stronger drug-MOF coupling. Conversely, in the *ex situ* encapsulation, the drug molecules in solution face strong competition with the polar solvent for coordination to the MOF active sites. Thereby, this approach can reduce the free binding sites available to drug molecules and increase the propensity of drug adsorption on pore walls. Nevertheless, it is necessary to emphasize the dependence of the impregnation method on the type of solvent used and the length of the immersion time, thus limiting the encapsulation of guests with a low solubility. Such shortcomings are eliminated with the use of the *in situ* method.

Subsequently, the results in Chapter 7 shed light on the potential presented by the solvent-free *in situ* encapsulation to minimize the long-standing unwanted burst effect, contributing to the development of improved pathways to control the binding and release of drug molecules from MOFs. Follow-on studies can expand on the scope of employing HKUST-1 mechanochemical encapsulation of guest molecules with different physicochemical characteristics (*e.g.* oxides and metal complexes for sensing devices). These lines of inquiry could further exploit the hosting potential of HKUST-1, a framework with a significant role in the basic and applied fields of MOFs research, can be additionally explored *via* mechanochemical encapsulation towards the fabrication of novel guest@MOF systems.

Finally, Chapter 8 demonstrated how high-resolution synchrotron microspectroscopy can be used to track the dynamic chemical and physical transformations occurring in drug@MOF and drug@MOF/Polymer composites during the release of guest molecules. The results laid out on this chapter evidenced the protective role played by the PU matrix, not only protecting the HKUST-1 against water-decomposition but also regulating the release rate of the 5-FU molecules. At the same time, the presence of HKUST-1 in the composites was essential for the effective release of the drug molecules. In a wider scope, Chapter 8 tackled the importance of the hydrophilic/hydrophobic balance established between the embedded MOF filler and the supporting matrix. The overall concept of tunable composite systems coupled with the facile encapsulation of guests is a promising way

forward to controlling the binding and release of drug molecules confined in a range of nanoporous materials. More importantly, the experimental methods and results presented in Chapter 8 illuminate the importance of the dynamic monitoring of the drug release process to fully understand its underlying mechanisms. The methods and insights detailed in this chapter can, therefore, be extended to the examination of other combinations of MOF/polymer nanocomposite systems, with work in this direction already being under way. Specifically, the grouping of 5-FU@HKUST-1 with other polymeric materials possessing different degrees of hydrophobicity can be paired with the elucidation of the hydrophobic-release rate dependency.

The extent of topics explored in this thesis – notably, the optimization of mechanochemical procedures to facilitate future scaling-up, the development of molecular encapsulation strategies with an enhanced understanding of the guest-host interactions, and a deeper scrutiny of the guest release mechanisms – are demonstrative of the multitudinous lines of inquiry that are topical within the MOF research field. Therefore, this thesis mutually contributes to the practical development of MOF-based drug delivery platforms and expands on the novel synthetic and characterisation techniques of guest@MOF systems, all of which are central to the rational design and engineering of advanced functional materials for real-world applications. Looking back, however, to the extensive research done in the realm of MOF and the important advances achieved in the past two decades, one of the main weaknesses in the field still resides in the limited biomedical expertise when designing the experiments behind the preparation of MOF and guest@MOF systems. This hinders the translation of the advances to the clinic. To better leverage the implications of the results presented within this thesis, future investigation is needed in a few areas to determine pathways for the effective use of MOF materials as a toolbox for biomedicine. First of all, studies that transcend the proof-of-concept stage, as presented in the results chapters of this thesis, moving towards *in vivo* drug delivery and biocompatibility studies are needed. To attain this, expressively more cell-based studies are essential, requiring MOF researchers to establish stronger collaborations in the natural and pharmaceutical

sciences. Additionally, thorough *in vivo* studies can help fill in the gap in the literature surrounding the integral comparison of the MOFs carriers' performance with solutions and technology presently available in the market.

Subsequently, follow-on studies should further assess the implications of the newly developed synthetic methods, detailed in Chapters 4-6, on the kinetics and dynamics of drug release process from MOF carriers, *via in vitro* and *in vivo* essays. In the majority of the studies present in the literature, the understanding of the guest release process from guest@MOF systems has been largely reliant on permeation and retention mechanisms. However, the findings and methodologies presented in Chapter 8 highlight the importance of examining carefully the dynamic behaviour of the guest@MOF system. While the methodology has been applied herein to examine the release *in vitro*, the SR-microFTIR set-up can be applied to *in vivo* release studies as it offers a unique capability to examine live cells with high-resolution. As a result, new insights can be offered to the *in vivo* behaviour of the produced guest@MOF systems.

Further, expanding the examination of the bespoke newly presented synthetic methods with a cost-effectiveness analysis on their manufacturing parameters for MOF systems (*e.g.* the mechanochemical *in situ* encapsulation kinetics) are highly desirable to further the evaluation of their scalability for industrial production. Together with the translational biocompatibility studies, these new investigations can help to clarify the critical features MOF-based formulation must present achieved their practical application in biomedicine.

As these issues are addressed in follow-on studies, new findings can propel the research on MOFs forward to uncover if this class of materials is capable of reaching the end-user as novel and more effective treatments for various hard-to-treat diseases.

The language of friendship is not words but meanings...

— Henry David Thoreau

References

[1] T. Tian et al. "A sol-gel monolithic metal-organic framework with enhanced methane uptake". *Nat. Mater.* 17 (2) (2018), 174–179.

[2] Y. Sun, Y. Li, and J. C. Tan. "Framework flexibility of ZIF-8 under liquid intrusion: discovering time-dependent mechanical response and structural relaxation". *Phys. Chem. Chem. Phys.* 20 (15) (2018), 10108–10113.

[3] A. K. Chaudhari and J. C. Tan. "Mechanochromic MOF nanoplates: spatial molecular isolation of light-emitting guests in a sodalite framework structure". *Nanoscale.* 10 (8) (2018), 3953–3960.

[4] A. K. Chaudhari and J. C. Tan. "A mechano-responsive supramolecular metal-organic framework (supraMOF) gel material rich in ZIF-8 nanoplates". *Chem. Comm.* 53 (61) (2017), 8502–8505.

[5] P. Horcajada et al. "Metal-organic frameworks in biomedicine". *Chem. Rev.* 112 (2) (2012), 1232–1268.

[6] P. Horcajada et al. "Porous metal-organic-framework nanoscale carriers as a potential platform for drug delivery and imaging". *Nat. Mater.* 9 (2) (2010), 172–178.

[7] L. Wang, M. Zheng, and Z. Xie. "Nanoscale metal–organic frameworks for drug delivery: a conventional platform with new promise". *J. Mater. Chem. B* 6 (5) (2018), 707–717.

[8] Y. Liu, Y. L. Zhao, and X. Y. Chen. "Bioengineering of Metal-organic Frameworks for Nanomedicine". *Theranostics.* 9 (11) (2019), 3122–3133.

[9] S. Keskin and S. Kızılel. "Biomedical Applications of Metal Organic Frameworks". *Ind. Eng. Chem. Res.* 50 (4) (2011), 1799–1812.

[10] A. G. Márquez et al. "Biocompatible polymer–metal–organic framework composite patches for cutaneous administration of cosmetic molecules". *J. Mater. Chem. B* 4 (43) (2016), 7031–7040.

[11] J. Mehta et al. "Recent advances in enzyme immobilization techniques: Metal-organic frameworks as novel substrates". *Coord. Chem. Rev.* 322 (2016), 30–40.

[12] M. C. Bernini et al. "Screening of bio-compatible metal-organic frameworks as potential drug carriers using Monte Carlo simulations". *J. Mater. Chem. B* 2 (7) (2014), 766–774.

[13] D. Cunha et al. "Rationale of Drug Encapsulation and Release from Biocompatible Porous Metal–Organic Frameworks". *Chem. Mater.* 25 (14) (2013), 2767–2776.

[14] X. Huang and C. S. Brazel. "On the importance and mechanisms of burst release in matrix-controlled drug delivery systems". *J. Control. Release* 73 (2) (2001), 121–136.

[15] C. Orellana-Tavra et al. "Amorphous metal-organic frameworks for drug delivery". *Chem. Comm.* 51 (73) (2015), 13878–13881.

[16] A. Schaate et al. “Modulated synthesis of Zr-based metal-organic frameworks: from nano to single crystals”. *Chemistry.* 17 (24) (2011), 6643–6651.

[17] S. Behzadi et al. “Cellular uptake of nanoparticles: journey inside the cell”. *Chem. Soc. Rev.* 46 (14) (2017), 4218–4244.

[18] M. Sajid. “Toxicity of nanoscale metal organic frameworks: a perspective”. *Environ. Sci. Pollut. Res. Int.* 23 (15) (2016), 14805–14807.

[19] C. Y. Sun et al. “Zeolitic Imidazolate framework-8 as efficient pH-sensitive drug delivery vehicle”. *Dalton Trans.* 41 (23) (2012), 6906–6909.

[20] Y. Wang and D. S. Kohane. “External triggering and triggered targeting strategies for drug delivery”. *Nat. Rev. Mater.* 2 (6) (2017), 17020.

[21] B. Yang et al. “Post-Synthetic Modification Nanoscale Metal-Organic Frameworks for Targeted Drug Delivery in Cancer Cells”. *Pharm. Res.* (2017), 2440–2450.

[22] C. Carvalho et al. “Doxorubicin: The Good, the Bad and the Ugly Effect”. *Curr. Med. Chem.* 16 (25) (2009), 3267–3285.

[23] D. Peer et al. “Nanocarriers as an emerging platform for cancer therapy”. *Nat. Nanotechnol.* 2 (12) (2007), 751–760.

[24] F. Bray et al. “Global cancer statistics 2018: GLOBOCAN estimates of incidence and mortality worldwide for 36 cancers in 185 countries”. *CA Cancer J. Clin.* 68 (6) (2018), 394–424.

[25] S. Muro. “Challenges in design and characterization of ligand-targeted drug delivery systems”. *J. Control. Release* 164 (2) (2012), 125–137.

[26] X. Zhu et al. “Inherent anchorages in UiO-66 nanoparticles for efficient capture of alendronate and its mediated release”. *Chem. Comm.* 50 (63) (2014), 8779–8782.

[27] K. Deng et al. “Aptamer-mediated up-conversion core/MOF shell nanocomposites for targeted drug delivery and cell imaging”. *Sci. Rep.* 5 (2015), 7851.

[28] Y. Zhang et al. “Challenges and recent advances in MOF–polymer composite membranes for gas separation”. *Inorg. Chem. Front.* 3 (7) (2016), 896–909.

[29] R. Lin et al. “Metal organic framework based mixed matrix membranes: An overview on filler/polymer interface”. *J. Mater. Chem. A* (2017), 293–312.

[30] Xia Wei Ch.and Li et al. “Metal organic framework-derived anthill-like Cu@carbon nanocomposites for nonenzymatic glucose sensor”. *Anal. Methods* 6 (5) (2014), 1550–1557.

[31] S. Schreml and M. Berneburg. “The global burden of diabetic wounds”. *Brit. J. Dermatol.* 176 (4) (2017), 845–846.

[32] A. Raghav et al. “Financial burden of diabetic foot ulcers to world: a progressive topic to discuss always”. *Ther. Adv. Endocrinol.* 9 (1) (2018), 29–31.

[33] M. K. Strecker-McGraw, T. R. Jones, and D. G. Baer. “Soft tissue wounds and principles of healing”. *Emerg. Med. Clin. N. Am.* 25 (1) (2007), 1–22.

[34] H. J. Degreef. “How to heal a wound fast”. *Dermatol. Clin.* 16 (2) (1998), 365–375.

[35] R. Karimi-Alavijeh et al. “Investigation of reasons for metal–organic framework’s antibacterial activities”. *Polyhedron.* 156 (2018), 257–278.

[36] A. García-Márquez et al. "Green Microwave Synthesis of MIL-100(Al, Cr, Fe) Nanoparticles for Thin-Film Elaboration". *Eur. J. Inorg. Chem.* 2012 (32) (2012), 5165–5174.

[37] C. F. Zhang et al. "A novel magnetic recyclable photocatalyst based on a core-shell metal-organic framework Fe_3O_4@MIL-100(Fe) for the decolorization of methylene blue dye". *J. Mater. Chem. A* 1 (45) (2013), 14329–14334.

[38] H. Tian et al. "One-pot sustainable synthesis of magnetic MIL-100(Fe) with novel Fe_3O_4 morphology and its application in heterogeneous degradation". *Dalton Trans.* (2018), 3417–3424.

[39] T. Baati et al. "In depth analysis of the in vivo toxicity of nanoparticles of porous iron(III) metal–organic frameworks". *Chem. Sci.* 4 (4) (2013), 1559–1607.

[40] E. Bellido et al. "Understanding the colloidal stability of the mesoporous MIL-100(Fe) nanoparticles in physiological media". *Langmuir.* 30 (20) (2014), 5911–5920.

[41] N. R. Dhumal et al. "Molecular Interactions of a Cu-Based Metal–Organic Framework with a Confined Imidazolium-Based Ionic Liquid: A Combined Density Functional Theory and Experimental Vibrational Spectroscopy Study". *J. Phys. Chem. C.* 120 (6) (2016), 3295–3304.

[42] J. A. Mason, M. Veenstra, and J. R. Long. "Evaluating metal–organic frameworks for natural gas storage". *Chem. Sci.* 5 (1) (2014), 32–51.

[43] A. C. McKinlay et al. "BioMOFs: Metal-Organic Frameworks for Biological and Medical Applications". *Angew. Chem. Int. Ed.* 49 (36) (2010), 6260–6266.

[44] X. Li et al. "New insights into the degradation mechanism of metal-organic frameworks drug carriers". *Sci. Rep.* 7 (1) (2017), 13142.

[45] J. Xiao et al. "Copper Metal-Organic Framework Nanoparticles Stabilized with Folic Acid Improve Wound Healing in Diabetes". *ACS Nano* (2018), 1023–1032.

[46] J. Jiang, Y. Zhao, and O. M. Yaghi. "Covalent Chemistry beyond Molecules". *J. Am. Chem. Soc.* 138 (10) (2016), 3255–65.

[47] B. Supronowicz, A. Mavrandonakis, and T. Heine. "Interaction of Biologically Important Organic Molecules with the Unsaturated Copper Centers of the HKUST-1 Metal–Organic Framework: an Ab-Initio Study". *J. Phys. Chem. C.* 119 (6) (2015), 3024–3032.

[48] C. Chiericatti et al. "Novel application of HKUST-1 metal–organic framework as antifungal: Biological tests and physicochemical characterizations". *Microporous Mesoporous Mat.* 162 (2012), 60–63.

[49] J. Hou et al. "Study on hydrophilic 5-fluorouracil release from hydrophobic poly(epsilon-caprolactone) cylindrical implants". *Drug. Dev. Ind. Pharm.* 37 (9) (2011), 1068–1075.

[50] N. Liédana et al. "The template role of caffeine in its one-step encapsulation in MOF NH_2-MIL-88B(Fe)". *J. Mater. Chem. B* 2 (9) (2014), 1144–1151.

[51] B. Singco et al. "Approaches to drug delivery: Confinement of aspirin in MIL-100(Fe) and aspirin in the de novo synthesis of metal–organic frameworks". *Microporous Mesoporous Mat.* 223 (2016), 254–260.

[52] C. Doonan et al. “Metal-Organic Frameworks at the Biointerface: Synthetic Strategies and Applications”. *Acc Chem. Res.* 50 (6) (2017), 1423–1432.

[53] M. Rubio-Martinez et al. “New synthetic routes towards MOF production at scale”. *Chem. Soc. Rev.* 46 (11) (2017), 3453–3480.

[54] N. Stock and S. Biswas. “Synthesis of Metal-Organic Frameworks (MOFs): Routes to Various MOF Topologies, Morphologies, and Composites”. *Chem. Rev.* 112 (2) (2012), 933–969.

[55] J. F. Fernandez-Bertran. “Mechanochemistry: an overview”. *Pure Appl. Chem.* 71 (4) (1999), 581–586.

[56] T. Friščić. “Metal-Organic Frameworks: Mechanochemical Synthesis Strategies”. In: *Encyclopedia of Inorganic and Bioinorganic Chemistry*. 2014.

[57] S. L. James et al. “Mechanochemistry: opportunities for new and cleaner synthesis”. *Chem. Soc. Rev.* 41 (1) (2012), 413–447.

[58] T. Friščić. “New opportunities for materials synthesis using mechanochemistry”. *J. Mater. Chem.* 20 (36) (2010), 7599–7605.

[59] T. R. Musgrave and C. E. Mattson. “Coordination Chemistry of 4,4’-Bipyridine”. *Inorg. Chem.* 7 (7) (1968), 1433–1436.

[60] A. Pichon, A. Lazuen-Garay, and S. L. James. “Solvent-free synthesis of a microporous metal-organic framework”. *CrystEngComm* 8 (3) (2006), 211–214.

[61] W. Yuan et al. “Study of the mechanochemical formation and resulting properties of an archetypal MOF: $Cu_3(BTC)_2$ (BTC = 1,3,5-benzenetricarboxylate)”. *CrystEngComm* 12 (12) (2010), 4063–4065.

[62] T. Friščić et al. “Ion- and liquid-assisted grinding: improved mechanochemical synthesis of metal-organic frameworks reveals salt inclusion and anion templating”. *Angew. Chem. Int. Ed.* 49 (4) (2010), 712–715.

[63] L. Han et al. “A facile and green synthesis of MIL-100(Fe) with high-yield and its catalytic performance”. *New J. Chem.* 41 (22) (2017), 13504–13509.

[64] K. Leng et al. “Rapid Synthesis of Metal–Organic Frameworks MIL-101(Cr) Without the Addition of Solvent and Hydrofluoric Acid”. *Cryst. Growth Des.* 16 (3) (2016), 1168–1171.

[65] M. Pilloni et al. “Liquid-assisted mechanochemical synthesis of an iron carboxylate Metal Organic Framework and its evaluation in diesel fuel desulfurization”. *Microporous Mesoporous Mat.* 213 (2015), 14–21.

[66] J. Yang et al. “NaCl as a solid solvent to assist the mechanochemical synthesis and post-synthesis of hierarchical porous MOFs with high I_2 vapour uptake”. *Dalton Trans.* 47 (14) (2018), 5065–5071.

[67] S. Tanaka et al. “Hierarchical Pore Development of ZIF-8 MOF by Simple Salt-Assisted Mechanosynthesis”. *Cryst. Growth Des.* 18 (1) (2017), 274–279.

[68] M. Bellusci et al. “Magnetic Metal-Organic Framework Composite by Fast and Facile Mechanochemical Process”. *Inorg. Chem.* (2018), 1806–1814.

[69] M. Wilke et al. “Fast and efficient synthesis of a host guest system: a mechanochemical approach”. *CrystEngComm* 18 (7) (2016), 1096–1100.

[70] Y. Tang et al. "Solid-phase hot-pressing synthesis of POMOFs on carbon cloth and derived phosphides for all pH value hydrogen evolution". *J. Mater. Chem. A* 6 (44) (2018), 21969–21977.

[71] Y. Chen et al. "Roll-to-Roll Production of Metal-Organic Framework Coatings for Particulate Matter Removal". *Adv. Mater.* 29 (15) (2017), 1606221.

[72] Y. Chen et al. "A Solvent-Free Hot-Pressing Method for Preparing Metal-Organic-Framework Coatings". *Angew. Chem. Int. Ed.* 55 (10) (2016), 3419–3423.

[73] M. Samal et al. "Kitchen grinder: a tool for the synthesis of metal–organic frameworks towards size selective dye adsorption". *CrystEngComm* 20 (18) (2018), 2486–2490.

[74] J. Stojakovic, B. S. Farris, and L. R. MacGillivray. "Vortex grinding for mechanochemistry: application for automated supramolecular catalysis and preparation of a metal-organic framework". *Chem. Comm.* 48 (64) (2012), 7958–7960.

[75] D. Crawford et al. "Synthesis by extrusion: continuous, large-scale preparation of MOFs using little or no solvent". *Chem. Sci.* 6 (3) (2015), 1645–1649.

[76] B. Karadeniz et al. "Benign by Design: Green and Scalable Synthesis of Zirconium UiO-Metal–Organic Frameworks by Water-Assisted Mechanochemistry". *ACS. Sustain. Chem. Eng.* 6 (11) (2018), 15841–15849.

[77] S. Waitschat, H. Reinsch, and N. Stock. "Water-based synthesis and characterisation of a new Zr-MOF with a unique inorganic building unit". *Chem. Comm.* 52 (86) (2016), 12698–12701.

[78] R. Chen et al. "A two-dimensional zeolitic imidazolate framework with a cushion-shaped cavity for CO_2 adsorption". *Chem. Comm.* 49 (82) (2013), 9500–9502.

[79] M. P. Jian et al. "Water-based synthesis of zeolitic imidazolate framework-8 with high morphology level at room temperature". *RSC Adv.* 5 (60) (2015), 48433–48441.

[80] F. Jeremias, S. K. Henninger, and C. Janiak. "Ambient pressure synthesis of MIL-100(Fe) MOF from homogeneous solution using a redox pathway". *Dalton Trans.* 45 (20) (2016), 8637–8644.

[81] D. DeSantis et al. "Techno-economic Analysis of Metal-Organic Frameworks for Hydrogen and Natural Gas Storage". *Energ. Fuel.* 31 (2) (2017), 2024–2032.

[82] M. D. Allendorf et al. "Guest-Induced Emergent Properties in Metal-Organic Frameworks". *J. Phys. Chem. Lett.* 6 (7) (2015), 1182–1195.

[83] M. T. Simon-Yarza et al. "Antineoplastic busulfan encapsulated in a metal organic framework nanocarrier: first in vivo results". *J. Mater. Chem. B* 4 (4) (2016), 585–588.

[84] A. C. McKinlay et al. "Multirate delivery of multiple therapeutic agents from metal-organic frameworks". *APL Mater.* 2 (12) (2014), 124108.

[85] C. Gaudin et al. "A quantitative structure activity relationship approach to probe the influence of the functionalization on the drug encapsulation of porous metal-organic frameworks". *Microporous Mesoporous Mat.* 157 (2012), 124–130.

[86] D. Cunha et al. “Rationale of Drug Encapsulation and Release from Biocompatible Porous Metal–Organic Frameworks”. *Chem. Mater.* 25 (14) (2013), 2767–2776.

[87] S. Rojas et al. “Toward Understanding Drug Incorporation and Delivery from Biocompatible Metal-Organic Frameworks in View of Cutaneous Administration”. *ACS Omega* 3 (3) (2018), 2994–3003.

[88] Y. J. Sun et al. “Metal-Organic Framework Nanocarriers for Drug Delivery in Biomedical Applications”. *Nano-Micro Lett.* 12 (1) (2020), 103.

[89] N. Liedana et al. “CAF@ZIF-8: One-Step Encapsulation of Caffeine in MOF”. *ACS Appl. Mater. Inter.* 4 (9) (2012), 5016–5021.

[90] X. R. Chen et al. “MOF Nanoparticles with Encapsulated Autophagy Inhibitor in Controlled Drug Delivery System for Antitumor”. *ACS Appl. Mater. Inter.* 10 (3) (2018), 2328–2337.

[91] M. Zheng et al. “One-Step Synthesis of Nanoscale Zeolitic Imidazolate Frameworks with High Curcumin Loading for Treatment of Cervical Cancer”. *ACS Appl. Mater. Interfaces* 7 (40) (2015), 22181–22187.

[92] H. Zheng et al. “One-pot Synthesis of Metal-Organic Frameworks with Encapsulated Target Molecules and Their Applications for Controlled Drug Delivery”. *J. Am. Chem. Soc.* 138 (3) (2016), 962–968.

[93] J. Nawrocki et al. “Development of an SBU-Based Mechanochemical Approach for Drug-Loaded MOFs”. *Eur. J. Inorg. Chem.* 2020 (10) (2020), 796–800.

[94] X. L. Wu et al. “Facile synthesis of multiple enzyme-containing metal-organic frameworks in a biomolecule-friendly environment”. *Chem. Comm.* 51 (69) (2015), 13408–13411.

[95] G. C. Yu and X. Y. Chen. “Host-Guest Chemistry in Supramolecular Theranostics”. *Theranostics.* 9 (11) (2019), 3041–3074.

[96] C. L. Hobday et al. “Understanding the adsorption process in ZIF-8 using high pressure crystallography and computational modelling”. *Nat. Commun.* 9 (9) (2018), 1429.

[97] J. E. Zuckerman and M. E. Davis. “Clinical experiences with systemically administered siRNA-based therapeutics in cancer”. *Nat. Rev. Drug. Discov.* 14 (12) (2015), 843–856.

[98] J. H. Tang et al. “Single-molecule level control of host-guest interactions in metallocycle-C60 complexes”. *Nat. Commun.* 10 (1) (2019), 4599.

[99] M. D. Allendorf and V. Stavila. “Crystal engineering, structure–function relationships, and the future of metal–organic frameworks”. *CrystEngComm* 17 (2) (2015), 229–246.

[100] M. I. Gonzalez et al. “Structural characterization of framework-gas interactions in the metal-organic framework Co-2(dobdc) by in situ single-crystal X-ray diffraction”. *Chem. Sci.* 8 (6) (2017), 4387–4398.

[101] G. P. Dangi et al. “A density functional theory study on the interaction of hydrogen molecule with MOF-177”. *Mol. Simulat.* 36 (5) (2010), 373–381.

[102] A. A. Talin et al. "Tunable electrical conductivity in metal-organic framework thin-film devices". *Science.* 343 (6166) (2014), 66–69.

[103] X. Y. Liu et al. "Using a Multi-Shelled Hollow Metal-Organic Framework as a Host to Switch the Guest-to-Host and Guest-to-Guest Interactions". *Angew. Chem. Int. Ed.* 57 (8) (2018), 2110–2114.

[104] Z. C. Hu et al. "A Luminescent Mg-Metal-Organic Framework for Sustained Release of 5-Fluorouracil: Appropriate Host-Guest Interaction and Satisfied Acid-Base Resistance". *ACS Appl. Mater. Inter.* 12 (13) (2020), 14914–14923.

[105] R. Anand et al. "Host-guest interactions in Fe(III)-trimesate MOF nanoparticles loaded with doxorubicin". *J. Phys. Chem. B* 118 (29) (2014), 8532–8539.

[106] I. Tibbetts and G. E. Kostakis. "Recent Bio-Advances in Metal-Organic Frameworks". *Molecules.* 25 (6) (2020), 1291.

[107] T. Chalati et al. "Porous metal organic framework nanoparticles to address the challenges related to busulfan encapsulation". *Nanomedicine. Lond.* 6 (10) (2011), 1683–1695.

[108] O. M. Yaghi, G. M. Li, and H. L. Li. "Selective Binding and Removal of Guests in a Microporous Metal-Organic Framework". *Nature.* 378 (6558) (1995), 703–706.

[109] M. Kotzabasaki and G. E. Froudakis. "Review of computer simulations on anti-cancer drug delivery in MOFs". *Inorg. Chem. Front.* 5 (6) (2018), 1255–1272.

[110] P. R. Haseth and J. A. Griffiths. "Theoretical Background". In: *Fourier Transform Infrared Spectrometry.* John Wiley Sons, Inc., 2007, 19–55.

[111] B. Chase. "Fourier Transform Raman Spectroscopy". *Anal. Chem.* 59 (14) (1987), 881A–889A.

[112] A. Borgschulte et al. "Inelastic neutron scattering evidence for anomalous H-H distances in metal hydrides". *Proc. Natl. Acad. Sci.* 117 (8) (2020), 4021–4026.

[113] F. Foglia et al. "In Vivo Water Dynamics in Shewanella oneidensis Bacteria at High Pressure". *Sci. Rep.* 9 (2019), 8716.

[114] S. Datta et al. "Self-assembled poly-catenanes from supramolecular toroidal building blocks". *Nature.* 583 (7816) (2020), 400–405.

[115] H. Naseri et al. "Turbulence and Cavitation Suppression by Quaternary Ammonium Salt Additives". *Sci. Rep.* 8 (2018), 7636.

[116] X. Z. Hu et al. "How does solubilisation of plant waxes into nonionic surfactant micelles affect pesticide release?" *J. Colloid Interface Sci.* 556 (2019), 650–657.

[117] J. Eckert. "Theoretical Introduction to Neutron-Scattering Spectroscopy". *Spectroc. Acta A* 48 (3) (1992), 271–283.

[118] M. Grimaldo et al. "Dynamics of proteins in solution". *Q. Rev. Biophys.* 52 (2019), 1–63.

[119] F. Fernandez-Alonso and D. L. Price. *Neutron Scattering - Applications in Biology, Chemistry, and Materials Science Preface.* New York, USA: Academic Press, 2017.

[120] M. R. Ryder et al. "Discovering connections between terahertz vibrations and elasticity underpinning the collective dynamics of the HKUST-1 metal–organic framework". *CrystEngComm* 18 (23) (2016), 4303–4312.

[121] Science and Technology Facility Council: "ISIS Neutron and Muon Source - How ISIS works". *https://www.isis.stfc.ac.uk/Pages/How-ISIS-works.aspx* (Access date: Sep 2020).

[122] N. L. Rosi et al. "Hydrogen storage in microporous metal-organic frameworks". *Science.* 300 (5622) (2003), 1127–1129.

[123] J. L. Rowsell, J. Eckert, and O. M. Yaghi. "Characterization of H2 binding sites in prototypical metal-organic frameworks by inelastic neutron scattering". *J. Am. Chem. Soc.* 127 (42) (2005), 14904–14910.

[124] P. Nugent et al. "Dramatic effect of pore size reduction on the dynamics of hydrogen adsorbed in metal–organic materials". *J. Mater. Chem. A* 2 (34) (2014), 13884–13891.

[125] S. Yang, A. Ramirez-Cuesta, and M. Schröder. "Inelastic neutron scattering study of binding of para-hydrogen in an ultra-microporous metal–organic framework". *Chem. Phys.* 428 (2014), 111–116.

[126] D. J. Tranchemontagne et al. "Hydrogen Storage in New Metal–Organic Frameworks". *J. Phys. Chem. C.* 116 (24) (2012), 13143–13151.

[127] S. K. Callear et al. "High-resolution inelastic neutron scattering and neutron powder diffraction study of the adsorption of dihydrogen by the Cu(II) metal–organic framework material HKUST-1". *Chem. Phys.* 427 (2013), 9–17.

[128] S. Yang et al. "Pore with gate: modulating hydrogen storage in metal-organic framework materials via cation exchange". *Faraday Discuss.* 151 (2011), 19–36.

[129] T. Pham et al. "Exceptional H_2 sorption characteristics in a Mg^{2+} -based metal-organic framework with small pores: insights from experimental and theoretical studies". *Phys. Chem. Chem. Phys.* 18 (3) (2016), 1786–1796.

[130] T. Pham et al. "Dynamics of H_2 adsorbed in porous materials as revealed by computational analysis of inelastic neutron scattering spectra". *Phys. Chem. Chem. Phys.* 18 (26) (2016), 17141–17158.

[131] K. A. Forrest et al. "Inelastic Neutron Scattering and Theoretical Studies of H_2 Sorption in a Dy(III)-Based Phosphine Coordination Material". *Chem. Mater.* 27 (22) (2015), 7619–7626.

[132] K. A. Forrest et al. "Investigating H_2 Sorption in a Fluorinated Metal-Organic Framework with Small Pores Through Molecular Simulation and Inelastic Neutron Scattering". *Langmuir.* 31 (26) (2015), 7328–7336.

[133] C. M. Brown et al. "Hydrogen adsorption in HKUST-1: a combined inelastic neutron scattering and first-principles study". *Nanotechnology* 20 (20) (2009), 204025.

[134] M. E. Casco et al. "Gate-opening effect in ZIF-8: the first experimental proof using inelastic neutron scattering". *Chem. Comm.* 52 (18) (2016), 3639–3642.

[135] T. Pham et al. "Investigating the Gas Sorption Mechanism in an rht-Metal–Organic Framework through Computational Studies". *J. Phys. Chem. C.* 118 (1) (2013), 439–456.

[136] M. E. Casco et al. "Understanding ZIF-8 Performance upon Gas Adsorption by Means of Inelastic Neutron Scattering". *ChemistrySelect* 2 (9) (2017), 2750–2753.

[137] J. D. Humby et al. "Host-guest selectivity in a series of isoreticular metal-organic frameworks: observation of acetylene-to-alkyne and carbon dioxide-to-amide interactions". *Chem. Sci.* 10 (4) (2019), 1098–1106.

[138] N. Lock et al. "Scrutinizing negative thermal expansion in MOF-5 by scattering techniques and ab initio calculations". *Dalton Trans.* 42 (6) (2013), 1996–2007.

[139] M. R. Ryder et al. "Detecting Molecular Rotational Dynamics Complementing the Low-Frequency Terahertz Vibrations in a Zirconium-Based Metal-Organic Framework". *Phys. Rev. Lett.* 118 (25) (2017), 255502.

[140] M. R. Ryder et al. "Identifying the role of terahertz vibrations in metal-organic frameworks: from gate-opening phenomenon to shear-driven structural destabilization". *Phys. Rev. Lett.* 113 (21) (2014), 215502.

[141] K. Titov et al. "OX-1 Metal–Organic Framework Nanosheets as Robust Hosts for Highly Active Catalytic Palladium Species". *ACS. Sustain. Chem. Eng.* 7 (6) (2019), 5875–5885.

[142] J. Shen and D. J. Burgess. "In vitro dissolution testing strategies for nanoparticulate drug delivery systems: recent developments and challenges". *Drug. Deliv. Transl. Re.* 3 (5) (2013), 409–415.

[143] S. D'Souza. "A Review of In Vitro Drug Release Test Methods for Nano-Sized Dosage Forms". *Int. J. Adv. Pharm* 22 (24) (2014), 29304–29313.

[144] M. N. Martinez et al. "Breakout session summary from AAPS/CRS joint workshop on critical variables in the in vitro and in vivo performance of parenteral sustained release products". *J. Control. Release* 142 (1) (2010), 2–7.

[145] P. Horcajada et al. "Influence of pore size of MCM-41 matrices on drug delivery rate". *Microporous Mesoporous Mat.* 68 (1-3) (2004), 105–109.

[146] P. Horcajada et al. "Flexible porous metal-organic frameworks for a controlled drug delivery". *J. Am. Chem. Soc.* 130 (21) (2008), 6774–6780.

[147] S. R. Miller et al. "Biodegradable therapeutic MOFs for the delivery of bioactive molecules". *Chem. Comm.* 46 (25) (2010), 4526–4528.

[148] S. Rojas et al. "Metal-Organic Frameworks as Efficient Oral Detoxifying Agents". *J. Am. Chem. Soc.* 140 (30) (2018), 9581–9586.

[149] X. Sun et al. "A novel mechanochemical method for reconstructing the moisture-degraded HKUST-1". *Chem. Comm.* 51 (54) (2015), 10835–10838.

[150] C. Orellana-Tavra et al. "Drug delivery and controlled release from biocompatible metal-organic frameworks using mechanical amorphization". *J. Mater. Chem. B* 4 (47) (2016), 7697–7707.

[151] X. C. Gao et al. "Fabrication of functional hollow microspheres constructed from MOF shells: Promising drug delivery systems with high loading capacity and targeted transport". *Sci. Rep.* 6 (2016), 37705.

[152] L. Y. Lu et al. "Metal Organic Framework@Polysilsesequioxane Core/Shell-Structured Nanoplatform for Drug Delivery". *Pharmaceutics.* 12 (2) (2020), 98.

[153] G. Osorio-Toribio et al. "Controlled Transdermal Release of Antioxidant Ferulate by a Porous Sc(III) MOF". *iScience* 23 (6) (2020), 101156.

[154] L. Salmela and C. Washington. "A continuous flow method for estimation of drug release rates from emulsion formulations". *Int. J. Pharm.* 472 (1) (2014), 276–281.

[155] D. F. Andrade et al. "Assessing the In Vitro Drug Release from Lipid-Core Nanocapsules: a New Strategy Combining Dialysis Sac and a Continuous-Flow System". *AAPS PharmSciTech* 16 (6) (2015), 1409–1417.

[156] N. Dimov et al. "Formation and purification of tailored liposomes for drug delivery using a module-based micro continuous-flow system". *Sci. Rep.* 7 (2017), 12045.

[157] Yi. Chen et al. "Identification and quantification of microplastics using Fourier-transform infrared spectroscopy: Current status and future prospects". *Curr. Opin. Environ. Sci. Health.* 18 (2020), 14–19.

[158] J. L. Perez-Rodriguez et al. "Gildings from Andalusia: Materials used in different types of artworks along centuries". *J. Cult. Herit.* 31 (2018), 112–121.

[159] Y. Han et al. "Cyclodextrin-Based Metal-Organic Frameworks (CD-MOFs) in Pharmaceutics and Biomedicine". *Pharmaceutics.* 10 (4) (2018), 271.

[160] A. Greenaway et al. "In situ synchrotron IR microspectroscopy of CO_2 adsorption on single crystals of the functionalized MOF Sc2(BDC-NH2)3". *Angew. Chem. Int. Ed.* 53 (49) (2014), 13483–13487.

[161] M. Savage et al. "Selective Adsorption of Sulfur Dioxide in a Robust Metal-Organic Framework Material". *Adv. Mater.* 28 (39) (2016), 8705–8711.

[162] H. T. Li et al. "A InIII-MOF with Imidazole Decorated Pores as 5-FU Delivery System to Inhibit Colon Cancer Cells Proliferation and Induce Cell Apoptosis in vitro and in vivo". *Z. Anorg. Allg. Chem.* 645 (11) (2019), 801–809.

[163] J. D. Humby et al. "Host-guest selectivity in a series of isoreticular metal-organic frameworks: observation of acetylene-to-alkyne and carbon dioxide-to-amide interactions". *Chem. Sci.* 10 (4) (2019), 1098–1106.

[164] H. G. W. Godfrey et al. "Analysis by synchrotron X-ray scattering of the kinetics of formation of an Fe-based metal-organic framework with high CO_2 adsorption". *APL Mater.* 7 (11) (2019), 111104.

[165] B. Civalleri et al. "Ab-initio prediction of materials properties with CRYSTAL: MOF-5 as a case study". *CrystEngComm* 8 (5) (2006), 364–371.

[166] W. Zhou and T. Yildirim. "Lattice dynamics of metal-organic frameworks: Neutron inelastic scattering and first-principles calculations". *Phys. Rev. B* 74 (18) (2006), 180301.

[167] M. S. Denny and S. M. Cohen. "In Situ Modification of Metal-Organic Frameworks in Mixed-Matrix Membranes". *Angew. Chem. Int. Ed.* 54 (31) (2015), 9029–9032.

[168] S. F. Parker et al. "Recent and future developments on TOSCA at ISIS". *J. Phys. Conf. Ser.* 554 (2014), 012003.

[169] O. Arnold et al. "Mantid—Data analysis and visualization package for neutron scattering and μ SR experiments". *Nucl. Instrum. Methods Phys. Res.* 764 (2014), 156–166.

[170] R. S. Pinna et al. "The neutron guide upgrade of the TOSCA spectrometer". *Nucl. Instrum. Methods Phys. Res.* 896 (2018), 68–74.

[171] R. Dovesi et al. "Quantum-mechanical condensed matter simulations with CRYSTAL". *Wiley Interdiscip. Rev. Comput. Mol. Sci.* 8 (4) (2018), e1360.

[172] C. Lee, W. Yang, and R. G. Parr. "Development of the Colle-Salvetti correlation-energy formula into a functional of the electron density". *Phys. Rev. B. Condens. Matter.* 37 (2) (1988), 785–789.

[173] A. D. Becke. "Perspective: Fifty years of density-functional theory in chemical physics". *J. Chem. Phys.* 140 (18) (2014), 18A301.

[174] S. Grimme et al. "A consistent and accurate ab initio parametrization of density functional dispersion correction (DFT-D) for the 94 elements H-Pu". *J. Chem. Phys.* 132 (15) (2010), 154104.

[175] A. Schäfer et al. "Fully optimized contracted Gaussian basis sets for atoms Li to Kr". *J. Chem. Phys.* 97 (4) (1992), 2571–2577.

[176] F. Pascale et al. "The calculation of the vibrational frequencies of crystalline compounds and its implementation in the CRYSTAL code". *J. Comput. Chem.* 25 (6) (2004), 888–897.

[177] C. M. Zicovich-Wilson et al. "Ab initio simulation of the IR spectra of pyrope, grossular, and andradite". *J. Comput. Chem.* 29 (13) (2008), 2268–2278.

[178] M. J. Frisch et al. *Gaussian~16 Revision C.01.* Gaussian Inc. Wallingford CT. 2016.

[179] K. Dymkowski et al. "AbINS: The modern software for INS interpretation". *Phys. B Cond. Mat.* 551 (2018), 443–448.

[180] V. Guillerm et al. "A series of isoreticular, highly stable, porous zirconium oxide based metal-organic frameworks". *Angew. Chem. Int. Ed.* 51 (37) (2012), 9267–9271.

[181] BIOVIA. "Dassault Systèmes, Discovery Studio, 2017 R2". *Dassault Systèmes,* San Diego, USA (2020).

[182] W.S. Rasband. "ImageJ, U. S. National Institutes of Health, Bethesda". *https://imagej.nih.gov/ij/,* Maryland, USA (1997-2018).

[183] R. Kuroda et al. "Annealing assisted mechanochemical syntheses of transition-metal coordination compounds and co-crystal formation". *CrystEngComm* 11 (2009), 427–432.

[184] H. Lv et al. "Efficient degradation of high concentration azo-dye wastewater by heterogeneous Fenton process with iron-based metal-organic framework". *J. Mol. Catal. A-Chem* 400 (2015), 81–89.

[185] F. Zhang et al. "Facile synthesis of MIL-100(Fe) under HF-free conditions and its application in the acetalization of aldehydes with diols". *Chem. Eng. J.* 259 (2015), 183–190.

[186] G. Chen et al. "In Vitro Toxicity Study of a Porous Iron(III) MetalOrganic Framework". *Molecules.* 24 (7) (2019), 1211.

[187] F. Zhang et al. "Peptide-/Drug-Directed Self-Assembly of Hybrid Polyurethane Hydrogels for Wound Healing". *ACS Appl. Mater. Interfaces* 11 (40) (2019), 37147–37155.

[188] G. Chaturvedi et al. "Removal of fluoroquinolone drug, levofloxacin, from aqueous phase over iron based MOFs, MIL-100(Fe)". *J. Solid State Chem.* 281 (2020), 121029.

[189] S. D. Taherzade et al. "Application of Metal-Organic Framework Nano-MIL-100 (Fe) for Sustainable Release of Doxycycline and Tetracycline". *Nanomaterials* 10 (8) (2017), 215.

[190] D. Crawford et al. "Organic synthesis by Twin Screw Extrusion (TSE): continuous, scalable and solvent-free". *Green. Chem.* 19 (6) (2017), 1507–1518.

[191] V. Agostoni et al. "Towards an improved anti-HIV activity of NRTI via metal-organic frameworks nanoparticles". *Adv. Healthc. Mater.* 2 (12) (2013), 1630–1637.

[192] P. Horcajada et al. "Synthesis and catalytic properties of MIL-100(Fe), an iron(III) carboxylate with large pores". *Chem. Comm.* 27 (2007), 2820–2822.

[193] B. Yuan et al. "Novel room-temperature synthesis of MIL-100(Fe) and its excellent adsorption performances for separation of light hydrocarbons". *Chem. Eng. J.* 355 (2019), 679–686.

[194] N. Mohammad Mahmoodi et al. "Metal-organic framework (MIL-100 (Fe)): Synthesis, detailed photocatalytic dye degradation ability in colored textile wastewater and recycling". *Mater. Res. Bull.* 100 (2018), 357–366.

[195] Y. K. Seo et al. "Large scale fluorine-free synthesis of hierarchically porous iron(III) trimesate MIL-100(Fe) with a zeolite MTN topology". *Microporous Mesoporous Mat.* 157 (2012), 137–145.

[196] Y. Fang et al. "Effect of mineralizing agents on the adsorption performance of metal–organic framework MIL-100(Fe) towards chromium(VI)". *Chem. Eng. J.* 337 (2018), 532–540.

[197] S. Lin et al. "Adsorption behavior of metal–organic frameworks for methylene blue from aqueous solution". *Microporous Mesoporous Mat.* 193 (2014), 27–34.

[198] C. Petit. *Factors Affecting the Removal of Ammonia from Air on Carbonaceous Materials: Investigation of Reactive Adsorption Mechanism.* New York, USA: Springer Science Business Media, 2012.

[199] D. S. Sivia. *Elementary scattering theory : for X-ray and neutron users.* Oxford, UK: Oxford University Press, 2011.

[200] N. Đ. H. Nguyn. "Investigation in Loading 5-Fluorouracil Ability of Iron-Organic Frameworks". *Vietnam. J. Sci. Technol.* 56 (2018), 219–227.

[201] A. Griffin and H. Jobic. "Theory of the effective Debye–Waller factor in neutron scattering from high frequency molecular modes". *J. Chem. Phys.* 75 (12) (1981), 5940–5943.

[202] S. Han and M. S. Lah. "Simple and Efficient Regeneration of MOF-5 and HKUST-1 via Acid–Base Treatment". *Cryst. Growth Des.* 5568-5572 (11) (2015), 5568–5572.

[203] J. F. Fernández-Bertrán et al. "Characterization of mechanochemically synthesized imidazolates of Ag^{+1}, Zn^{+2}, Cd^{+2}, and Hg^{+2}: Solid state reactivity of nd10 cations". *J. Phys. Chem. Solids* 67 (8) (2006), 1612–1617.

[204] M. Thommes et al. "Physisorption of gases, with special reference to the evaluation of surface area and pore size distribution (IUPAC Technical Report)". *Pure Appl. Chem.* 87 (9) (2015), 1051–1069.

[205] L. Wang et al. "Ethylenediamine-functionalized metal organic frameworks MIL-100(Cr) for efficient CO_2/N_2O separation". *Sep. Purif. Technol.* 235 (2020), 116219.

[206] J. Yang et al. "Effects of Activation Temperature and Densification on Adsorption Performance of MOF MIL-100(Cr)". *J. Chem. Eng. Data* 64 (12) (2019), 5814–5823.

[207] G. Mahalakshmi and V. Balachandran. "FT-IR and FT-Raman spectra, normal coordinate analysis and ab initio computations of Trimesic acid". *Spectrochim. Acta A. Mol. Biomol. Spectrosc.* 124 (2014), 535–547.

[208] *Neutron Scattering Fundamentals, Experimental Methods in the Physical Sciences*. New York, USA: edited by F. Fernandez-Alonso and D. L. Price, Academic Press, 2013.

[209] B. E. Souza et al. "Guest-host interactions of nanoconfined anti-cancer drug in metal-organic framework exposed by terahertz dynamics". *Chem. Comm.* 55 (27) (2019), 3868–3871.

[210] A. K. Chaudhari et al. "Optochemically Responsive 2D Nanosheets of a 3D Metal-Organic Framework Material". *Adv. Mater.* 29 (27) (2017), 1701463.

[211] V. K. Rastogi and M. A. Palafox. "Vibrational spectra, tautomerism and thermodynamics of anticarcinogenic drug: 5-fluorouracil". *Spectrochim. Acta A. Mol. Biomol. Spectrosc.* 79 (5) (2011), 970–977.

[212] Y. Li et al. "Strategy for chemotherapeutic delivery using a nanosized porous metal-organic framework with a central composite design". *Int. J. Nanomedicine* 12 (2017), 1465–1474.

[213] M. Klimakow et al. "Mechanochemical Synthesis of Metal-Organic Frameworks: A Fast and Facile Approach toward Quantitative Yields and High Specific Surface Areas". *Chem. Mater.* 22 (18) (2010), 5216–5221.

[214] R. Babarao Jiang and Jianwen. "Unraveling the Energetics and Dynamics of Ibuprofen in Mesoporous Metal-Organic Frameworks". *J. Phys. Chem.* 42 (113) (2009), 18287–18291.

[215] M. Kondo et al. "Three-dimensional framework with channeling cavities for small molecules: [M-2(4,4'-bpy)(3)(NO_3)(4)]center dot xH_2O(n) (M = Co, Ni, Zn)". *Angew. Chem. Int. Ed.* 36 (16) (1997), 1725–1727.

[216] D. Venkataraman et al. "Zeolite-Like Behavior of a Coordination Network". *J. Am. Chem. Soc.* 117 (46) (1995), 11600–11601.

[217] B. Yuan et al. "Enhanced Hydrothermal Stability and Catalytic Performance of HKUST-1 by Incorporating Carboxyl-Functionalized Attapulgite". *ACS Appl. Mater. Interfaces* 8 (25) (2016), 16457–16464.

[218] M. Schlesinger et al. "Evaluation of synthetic methods for microporous metal–organic frameworks exemplified by the competitive formation of $[Cu_2(BTC)_3(H_2O)_3]$ and $[Cu_2(BTC)(OH)(H_2O)]$". *Microporous Mesoporous Mat.* 132 (1) (2010), 121–127.

[219] F. A. Sofi, K. Majid, and O. Mehraj. "The visible light driven copper based metal-organic-framework heterojunction:HKUST-1@Ag-Ag_3PO_4 for plasmon enhanced visible light photocatalysis". *J. Alloys Compd.* 737 (2018), 798–808.

[220] W. W. Lestari et al. "Solvothermal and electrochemical synthetic method of HKUST-1 and its methane storage capacity". *IOP Conf. Ser. Mat. Sci. Eng.* 107 (2016), 012030.

[221] S. Senapati et al. "Controlled drug delivery vehicles for cancer treatment and their performance". *Signal Trans. Target. Ther.* 3 (2018), 7.

[222] R. Ferrari et al. "Polymer nanoparticles for the intravenous delivery of anticancer drugs: the checkpoints on the road from the synthesis to clinical translation". *Nanoscale.* 10 (48) (2018), 22701–22719.

[223] W. Fan et al. "Generic synthesis of small-sized hollow mesoporous organosilica nanoparticles for oxygen-independent X-ray-activated synergistic therapy". *Nat. Commun.* 10 (1) (2019), 1241.

[224] M. Todaro et al. "Decomposition Process of Carboxylate MOF HKUST-1 Unveiled at the Atomic Scale Level". *J. Phys. Chem. C.* 120 (23) (2016), 12879–12889.

[225] A. Doman et al. "Role of water molecules in the decomposition of HKUST-1: Evidence from adsorption, thermoanalytical, X-ray and neutron scattering measurements". *Appl. Surf. Sci.* 480 (2019), 138–147.

[226] W. Wang and C. Wang. "Polyurethane for biomedical applications: A review of recent developments". In: *The Design and Manufacture of Medical Devices.* 2012, 115–151.

[227] X. Chen et al. "Preparation and characterization of PEG-modified polyurethane pressure-sensitive adhesives for transdermal drug delivery". *Drug Dev. Ind. Pharm.* 35 (6) (2009), 704–711.

[228] Y. H. Shih et al. "A Simple Approach to Enhance the Water Stability of a Metal-Organic Framework". *Chemistry.* 23 (1) (2017), 42–46.

[229] X. Ren et al. "Copper Metal-Organic Framework Loaded on Chitosan Film for Efficient Inhibition of Bacteria and Therapy of Local Infection". *Nanoscale.* 11 (24) (2019), 11830–11838.

[230] K. R. Stefaniak et al. "Photo-triggered release of 5-fluorouracil from a MOF drug delivery vehicle". *Chem. Comm.* 54 (55) (2018), 7617–7620.

[231] S. Rojas, N. Guillou, and P. Horcajada. "Ti-Based nanoMOF as an Efficient Oral Therapeutic Agent". *ACS Appl. Mater. Interfaces* 11 (25) (2019), 22188–22193.

[232] J. Doherty et al. "Live single cell analysis using synchrotron FTIR microspectroscopy: development of a simple dynamic flow system for prolonged sample viability". *Analyst* 144 (3) (2019), 997–1007.

[233] H. M. Elsheikha et al. "Label-free characterization of biochemical changes within human cells under parasite attack using synchrotron based micro-FTIR". *Anal. Methods* 11 (19) (2019), 2518–2530.

[234] R. Li et al. "Encapsulation of 5-Fluorouracil in a Copper(II)-based Porous Metal-organic Framework: Drug Delivery and Inhibiting Human Spinal Cord Tumor Cells". *Z. Anorg. Allg. Chem.* 644 (5) (2018), 317–321.

[235] E. H. Zhou et al. "A 3D polyhedral metal–organic framework as drug carrier for controllable release". *B. Chem. Soc. Ethiopia* 31 (3) (2018), 457–463.

[236] P. H. Ho et al. "One-pot synthesis of 5-FU@ZIF-8 and ibuprofen@ZIF-8 nanoparticles". *Inorg. Chim. Acta* 500 (2020), 119229.

[237] D. Wei et al. "A Mesoporous Gd-MOF with Lewis Basic Sites for 5-FU Delivery and Inhibition of Human Lung Cancer Cells In Vivo and In Vitro". *J. Inorg. Organomet. Polym.* 30 (2019), 1121–1131.

[238] B. H. Song et al. "Efficient drug delivery of 5-fluorouracil by a biocompatible Zn-metal–organic framework nanostructure and anti-liver cancer activity study". *J. Iran. Chem. Soc.* 16 (2) (2018), 333–340.

[239] L. C. Zhao et al. "Fabrication of a Porous Metal-Organic Framework with Polar Channels for 5-FU Delivery and Inhibiting Human Osteosarcoma Cells". *J. Chem.* 2018 (2018), 1523154.

[240] P. Y. Du, W. Gu, and Xin Liu. "A three-dimensional Nd(III)-based metal–organic framework as a smart drug carrier". *New J. Chem.* 40 (11) (2016), 9017–9020.

[241] K. Xing et al. "Dual-Stimulus-Triggered Programmable Drug Release and Luminescent Ratiometric pH Sensing from Chemically Stable Biocompatible Zinc Metal-Organic Framework". *ACS Appl. Mater. Interfaces* 10 (26) (2018), 22746–22756.

[242] S. Tummala, M. Kumar, and A. Prakash. "Formulation and characterization of 5-Fluorouracil enteric coated nanoparticles for sustained and localized release in treating colorectal cancer". *Saudi Pharm. J.* 23 (3) (2015), 308–314.

[243] R. Seda and M. Pulat. "5-Fluorouracil Encapsulated Chitosan Nanoparticles for pH-Stimulated Drug Delivery: Evaluation of Controlled Release Kinetics". *J. Nanomater.* 2012 (2012), 313961.

[244] J. L. Arias. "Novel strategies to improve the anticancer action of 5-fluorouracil by using drug delivery systems". *Molecules.* 13 (10) (2008), 2340–2369.

[245] F. C. Wang et al. "FTIR analysis of hydrogen bonding in amorphous linear aromatic polyurethanes. I. Influence of temperature". *J. Polym. Sci. Part B: Polym. Phys.* 32 (8) (1994), 1305–1313.

[246] F. C. Wang et al. "FTIR analysis of hydrogen bonding in amorphous linear aromatic polyurethanes. II. Influence of styrene solvent". *J. Polym. Sci. Part B: Polym. Phys.* 32 (8) (1994), 1315–1320.

[247] T. Resler et al. "Kinetic and vibrational isotope effects of proton transfer reactions in channelrhodopsin-2". *Biophys. J.* 109 (2) (2015), 287–297.

[248] C. C. Sutton, G. Silva, and G. V. Franks. "Modeling the IR spectra of aqueous metal carboxylate complexes: correlation between bonding geometry and stretching mode wavenumber shifts". *Chemistry.* 21 (18) (2015), 6801–6805.

[249] Y. K. Seo et al. "Microwave synthesis of hybrid inorganic–organic materials including porous $Cu_3(BTC)_2$ from Cu(II)-trimesate mixture". *Microporous Mesoporous Mat.* 119 (1) (2009), 331–337.

[250] L. Dona, J. G. Brandenburg, and B. Civalleri. "Extending and assessing composite electronic structure methods to the solid state". *J. Chem. Phys.* 151 (12) (2019), 121101.

[251] M. Fleck and B. Zagrovic. "Configurational Entropy Components and Their Contribution to Biomolecular Complex Formation". *J. Chem. Theory Comput.* 15 (6) (2019), 3844–3853.

[252] C. M. Rost et al. "Entropy-stabilized oxides". *Nat. Commun.* 6 (2015), 8485.